



JP9701026

KEK-PROC--96-4

# RADIATION DETECTORS AND THEIR USES

Proceedings of the 10th Workshop  
on Radiation Detectors and Their Uses

23-25 January, 1996  
KEK, Tsukuba, Ibaraki  
JAPAN

Edited by

M.Miyajima and S.Sasaki  
National Laboratory for High Energy Physics

T.Iguchi and M.Nakazawa  
Tokyo University

2

**National Laboratory for High Energy Physics, 1996**

KEK Reports are available from:

Technical Information & Library  
National Laboratory for High Energy Physics  
1-1 Oho, Tsukuba-shi  
Ibaraki-ken, 305  
JAPAN

Phone: 0298-64-5136  
Telex: 3652-534 (Domestic)  
(0)3652-534 (International)  
Fax: 0298-64-4604  
Cable: KEK OHO  
E-mail: [Library@kekvox.kek.jp](mailto:Library@kekvox.kek.jp) (Internet Address)  
Internet: <http://www.kek.jp>

## PREFACE

The 10th workshop on "Radiation Detectors and Their Uses" was held on the January 23, 24 and 25, 1996 at National Laboratory for High Energy Physics (KEK) in Tsukuba. This workshop has been hosted by the Radiation Safety Control Center in KEK under the supports of the Nuclear Engineering Research Laboratory of Tokyo University and the Society of Radiation Science, the affiliate of Japan Society of Applied Physics.

More than one hundred participants registered to the workshop. Thirty-five papers were presented from various fields in the workshop, which included two invited talks focused on the basics of the charge-sensitive amplifiers and the signal processing for position-sensitive detectors, respectively. In the workshop, we had also two special sessions: one was the short-course program entitled "Recent Development on Micro-channel Plate (MCP)" in which topics and experimental techniques related to MCPs were presented, and the other was the poster session where impassioned presentations were made by young researchers from the graduate schools.

Among those contributions, thirty-three papers were published in this proceedings as the fruits of the workshop.

Mitsuhiro Miyajima  
Shinichi Sasaki  
Tetsuo Iguchi  
Masaharu Nakazawa

## TABLE OF CONTENT

<b>ANGLE-RESOLVED ION TOF SPECTROMETER WITH A POSITION SENSITIVE DETECTOR</b> N.Saito, F.Heiser, K.Wieliczec and U.Becker .....	1
<b>LOW ENERGY RBS-CHANNELING MEASUREMENT SYSTEM WITH THE USE OF A TIME-OF-FLIGHT SCATTERED ION DETECTOR</b> M.Hasegawa, N.Kobayashi and N.Hayashi .....	8
<b>SINGLE ION COUNTING WITH A MCP DETECTOR</b> H.Tawara, S.Sasaki, E.Shibamura and M.Miyajima .....	17
<b>SUPERHEATED LIQUID DROP DETECTOR RESPONSE TO LOW LET RADIATION</b> T.Sawamura, T.Joji, S.Tsuda and M.Narita .....	31
<b>TRITON, DEUTERON AND PROTON RESPONSES OF THE CR-39 TRACK DETECTOR</b> T. Yamauchi, H. Matsumoto and K. Oda .....	41
<b>CHARGE SENSITIVE AMPLIFIER -The State of Arts-</b> K.Mori .....	50
<b>SIGNAL PROCESSORS FOR POSITION-SENSITIVE DETECTORS</b> K.Hasegawa .....	77
<b>TIME- AND DEPTH-RESOLVED MEASUREMENT OF ION TRACKS IN CONDENSED MATTER</b> K.Kimura .....	84
<b>GAS-MULTIPLICATION FACTOR OF A PROPORTIONAL COUNTER OPERATED AT LOW TEMPERATURE DESCRIBED WITH THE DIETHORN, ROSE-KORFF and TOWNSEND EXPRESSIONS</b> K.Fukumura, A.Nakanishi and T.Kobayashi .....	87
<b>DESIGN OF AN EFFICIENT PULSING SYSTEM FOR A SLOW-POSITRON BEAM</b> N.Oshima, T.Suzuki, I.Kanazawa and Y.Ito .....	97
<b>DEVELOPMENT OF A DISTRIBUTED RADIATION DETECTION SYSTEM USING OPTICAL FIBERS</b> F.Jensen, G.Inouchi, E.Takada, H.Takahashi, T.Iguchi, M.Nakazawa and T.Kakuta .....	104
<b>DEVELOPMENT OF OPTIMAL CHARGE SENSITIVE PREAMPLIFIER FOR SUPERCONDUCTING TUNNEL JUNCTION</b> M.Ukibe, M.Nakazawa, M.Kisimoto, M.Katagiri, and M.Kurakado .....	114

<b>SYSTEM OF PATTERN ANALYSIS OF PIXE SPECTRA</b> K.Murozono, S.Iwasaki, J.Inoue, K.Ishii, M.Kitamura, K.Sera, and S.Futatsugawa .....	118
<b>DIGITAL SIGNAL PROCESSING FOR CdTe DETECTORS USING VXIBUS DATA COLLECTION SYSTEMS</b> D.Fukuda, H.Takahashi, T.Kurahashi, T.Iguchi and M.Nakazawa .....	124
<b>ESTIMATE OF PULSE-SEQUENCE DATA AQUISITION SYSTEM FOR MULTI-DIMENSIONAL MEASUREMENT</b> Y.Kitamura, T.Sakae, A.Nohtomi, M.Matoba and Y.Matsumoto .....	130
<b>CHARACTERIZATION OF NEUTRON DETECTOR COMBINED WITH NE213 AND CaF<sub>2</sub>(Eu)</b> M.Takada, T.Nakamura and T.Sibata .....	138
<b>SIMULATION OF THE PEAK EFFICIENCY FOR A STACKED NaI(Tl) SPECTROMETER</b> H.Yoshida, H.Murohka, K.Anami, A.Nohtomi, Y.Uozumi, T.Sakae, M.Matoba, N.Koori and T.Maki .....	148
<b>USE OF Si-PIN PHOTODIODE X-RAY DETECTOR FOR PIXE</b> J.Inoue, S.Iwasaki, K.Murozono, K.Ishii and M.Kitamura .....	157
<b>GAS GAIN CHARACTERISTICS OF PARALLEL PLATE AVALANCHE COUNTER</b> K.Nishio, H.Yamamoto, I.Kanno, I.Kimura and Y.Nakagome .....	161
<b>ESR (ELECTRON SPIN RESONANCE) RADIATION DOSIMETER</b> Y.Kinoshita, S.Takaki, C.Yamanaka and M.Ikeya .....	168
<b>ANALYSIS OF TIME VARIANT FILTERS MEANS OF THE FOURIER TRANSFORM</b> K.Husimi and M.Kuwata .....	173
<b>PERFORMANCE COMPARISON OF VARIOUS TIME VARIANT FILTERS</b> M.Kuwata and K.Husimi .....	180
<b>A RESPONSE OF THE IMAGING PLATE TO RADIATION PROPERTIES AND A DISCRIMINATED RADIATION IMAGE</b> M.Takebe, K.Abe, Y.Kondo, Y.Satoh, M.Souda, Y.Kokubun, M.Miyazaki, Y.Hori and Y.Murakami .....	189
<b>IMAGING PLATE-ASSISTED RADIOGRAPHIES WITH 3.7 MBq OR LESS SOURCE</b> K.Abe, M.Takebe, Y.Kondo, Y.Satoh, M.Souda, Y.Kokubun, M.Miyazaki, Y.Hori and Y.Murakami .....	192
<b>HIGH GAMMA-RAY MEASUREMENT USING OPTICAL EMISSION OF CERAMIC MATERIAL</b> T.Kakuta, K.Sakasai, H.Yamagishi and M.Nakazawa .....	197

<b>IS RADIATION DOSIMETRY POSSIBLE USING SUGAR DECOMPOSITION ?</b> H.Kawai, H.Morishita, T.Koga and K.Nakamura .....	202
<b>POPTOP-TYPE GERMANIUM DETECTOR COOLED BY STIRLING REFRIGERATORS</b> M.Katagiri, Y.Kobayashi, K.Takahashi, Y.Taguchi and T.Uchida .....	209
<b>CORRECTION OF DIAGNOSTIC X-RAY SPECTRA MEASURED WITH CdTe AND CdZnTe DETECTORS</b> M.Matsumoto, H.Kanamori, T.Toragaito and A.Taniguchi .....	214
<b>FABRICATION OF RADIATION DETECTOR USING PbI<sub>2</sub> CRYSTAL</b> T.Shoji, K.Sakamoto, K.Ohba, T.Suehiro and Y.Hiratate .....	224
<b>IMPROVEMENT OF THE SENSITIVITY OF CdTe DETECTORS IN THE HIGH ENERGY REGIONS</b> H.Nishizawa, K.Ikegami, K.Takashima, T.Usami and T.Yamamoto .....	230
<b>DISCRIMINATION OF THE WALL EFFECT IN A THIN COUNTER WITH MICRO-GAP STRUCTURE FOR NEUTRON POSITION SENSING</b> T.Sakae, T.Manabe, Y.Kitamura, A.Nohtomi and S.Sakamoto .....	240
<b>A NRESPG MONTE CARLO CODE FOR THE CALCULATION OF NEUTRON RESPONSE FUNCTIONS FOR GAS COUNTERS</b> K.Kudo, N.Takeda, A.Fukuda, T.Torii, M.Hashimoto, T.Sugita, X.Yang, and G.Dietze .....	248
<b>DEVELOPMENT OF A DIRECTIONAL NEUTRON DETECTOR FOR NEUTRON EMISSION PROFILE MONITOR</b> J.Kaneko, M.Katagiri, Y.Ikeda, K.Ara, T.Iguchi and M.Nakazawa .....	259
<b>List of Participants</b>	264

# ANGLE-RESOLVED ION TOF SPECTROMETER WITH A POSITION SENSITIVE DETECTOR

Norio Saito

Electrotechnical Laboratory, 1-1-4, Umezono, Tsukuba-shi 305 Japan

Franz Heiser, Kornel Wieliczec, Uwe Becker

Fritz-Haber-Institut der MPG, Faradayweg 4-6, 14195 Berlin, Germany

A angle-resolved ion time-of-flight mass spectrometer with a position sensitive anode has been investigated. Performance of this spectrometer has been demonstrated by measuring an angular distribution of a fragment ion pair,  $C^{++}O^{+}$ , from CO at the photon energy of 287.4 eV. The obtained angular distribution is very close to the theoretically expected one.

## 1. INTRODUCTION

Angular distribution measurements of fragment ions from molecules are powerful tool for investigating molecular dynamics following a core hole excitation. Angular distributions of fragment ions reflect the orientation of the molecular bond axis at the moment of the initial electronic excitation, which is determined from the electronic symmetry of the excitation. Therefore, angular distribution measurements provide the electronic symmetry of the excited molecules. Two different techniques were previously used to obtain angular distributions of fragment ions. (A) Ion time-of-flight spectra were measured with the axis of the flight tube oriented at  $0^{\circ}$ ,  $90^{\circ}$  and  $54.7^{\circ}$  with respect to the polarization vector of the incident soft X-rays. The angular distributions were determined by deconvolution of the shapes of the ion TOF spectra<sup>(1,2)</sup>. (B) The total ion intensity was measured at several angles to determine the angular dependence of the flux of the fragment ions<sup>(3,4,5,6)</sup>. Method (A) can resolve the mass/charge ratios of ions and their kinetic energies but the uncertainty in angular distributions is greater than that of method (B). Method (B) can resolve neither the mass/charge ratios nor the kinetic energies of the fragment ions. Ions with low kinetic energies were, however, discriminated by applied reverse fields. To our knowledge, mass/charge

ratio resolved and kinetic energy resolved angular distribution measurements have not been previously reported. In this paper, we investigate a technique to measure mass/charge ratio resolved and kinetic energy resolved angular distributions using a newly developed angle-resolved time-of-flight (TOF) mass spectrometer with a position sensitive detector.

## 2. ANGLE-RESOLVED TOF MASS SPECTROMETER

A newly developed angle-resolved TOF mass spectrometer with a multihit-type position sensitive anode is shown in Fig.1<sup>(7,8)</sup>. The lengths among the pusher, the extractor, and the drift tube in the spectrometer are 15mm and 5mm, respectively. The length of the drift tube is 32.5mm. The grid  $G_1$  is positioned at the middle between the drift tube and the micro-channel plates (MCPs), which separation is 8mm. The Au-coated meshes with diameters of 15mm, 20mm, 40mm, and 40mm are mounted on the extractor, the face and end of the drift tube, and the  $G_1$ , respectively. The voltage on the pusher, the extractor, the drift tube, the surface of the MCP, and the anode in the TOF mass spectrometer was set to be 800, -800, -1605, -3752V, and 0 V, respectively, to satisfy the required space focusing condition.

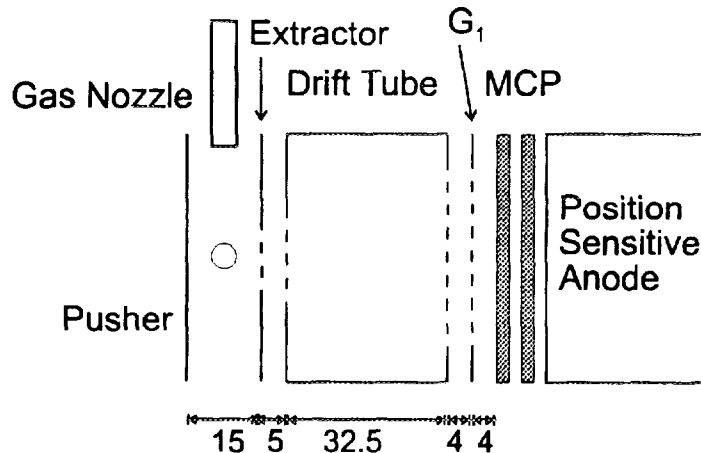


Figure 1 An angle-resolved ion TOF mass spectrometer with a position sensitive anode.

The ions were detected by MCPs with a position sensitive anode. Figure 2 shows the patterns of the position sensitive anode. The patterns of A and B correspond to pixels of x and y direction, respectively. The pixels of A and B are mounted on a anode plate as illustrated in the left hand side of Fig.2. The pixels of A are connected by narrow wires on the back of the plate from right to left. The pixels of B are connected by narrow wires on the front of the plate from top to bottom. Each wire is connected to a fast preamplifier.

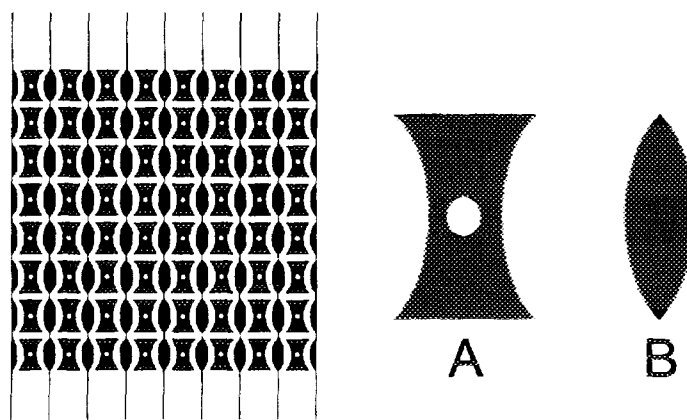


Figure 2 Pattern of the position sensitive anode in the left hand side. Patterns A and B show pixels for x and y direction, respectively.

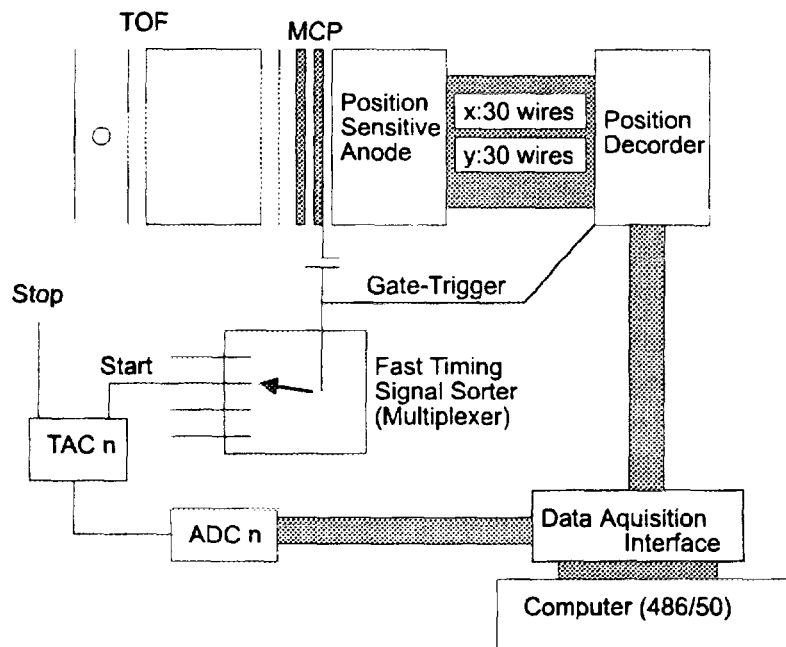


Figure 3 Electronic set up for data registration

The electronic set up used to detect ion TOF and ion positions is illustrated in Fig.3. The pulses from the end of the second MCP were utilized to determine the ion TOF and timing signals for the position decoder. Since the pulses from the second MCP were positive, these pulses were inverted in order to fit the NIM standard. Following this inversion, ion signals were selected by a fast timing signal sorter (Multiplexer) placing them into first, second, third, and fourth positions. Each selected signal was channeled into the start connector of a time-to-amplitude converter (TAC). The TAC signals were put into analog-to-digital converters (ADCs) and from there transferred into a 486 personal computer. When two ions were detected at the anode in a given time window, the TOF and the position signal on the anode for each pair of ions were recorded in the personal computer.

### 3. EXPERIMENTAL

In order to investigate performance of the spectrometer, we have measured the known angular distribution of the fragment ion pair,  $C^+O^+$ , from CO at the photon energy of 287.4 eV, which corresponds to the excitation of C1s to  $2p\pi$ , using linearly polarized light. At this photo-excitation, the molecule CO is preferentially oriented perpendicular to the electric field vector of the light at the instant of the initial electric excitation, resulting that the fragmentation occurs preferentially perpendicular to the electric field vector.

The experiments were performed at beamline BW3 of the Hamburger Synchrotronstrahlungslabor (HASYLAB) of DESY<sup>(9)</sup>. This beamline is a triple N-pole undulator beamline (N=21, 33, 44) equipped with a high resolution SX700 plane grating monochromator modified for high photon throughput. This instrument has a routinely achievable resolution of 3000 with a photon flux of  $10^{12}$  photons/sec. The degree of linear polarization of the light was determined to be 98% at 300 eV by measuring the angular distributions of the Ne 2s and 2p photoelectrons.

The spectrometer was positioned at an angle of  $55^\circ$  with respect to the electric field vector of the photon beam. The ion TOF was measured with respect to the bunch marker of the storage ring, which was operated in the single-bunch or double-bunch modes with time windows of 964 or 482 nsec, respectively. The partial CO pressure was better than  $3 \times 10^{-6}$  mbar. The ion TOF and the ion position on the anode for the ion pairs of  $C^+O^+$  have been measured using this

experimental set up.

#### 4. RESULTS

In order to get information on the angular distribution of the fragment ion pair of  $C^+O^+$ , the obtained data about the ion TOF and positions should be analyzed using the following equation<sup>(8)</sup>. This equation gives the original orientation and kinetic energy release of the dissociating molecule using the obtained data.

$$p^2 = \left[ \frac{d}{T_1/m_1 + T_2/m_2} \right]^2 + \left[ \frac{E}{1/q_1 + 1/q_2} \right]^2 \{ (T_1 - T_2) - (T_{01} - T_{02}) \} \quad (1)$$

$$\theta = \cos^{-1} \left[ \frac{d}{p \left( T_1/m_1 + T_2/m_2 \right)} \right]$$

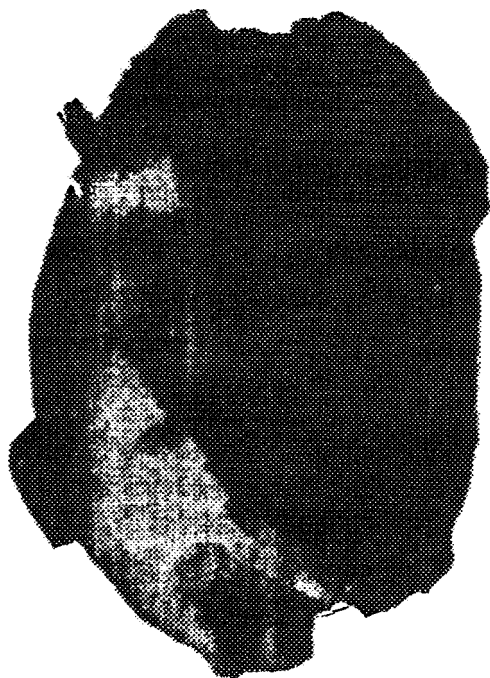


Figure 4 Three dimensional representation of the angular distribution for  $C^+O^+$  ion pairs with total kinetic energies between 12 eV and 18 eV.

where,  $p$  and  $\theta$  denote the momentum and the angle between the molecular axis and the electric field vector of the photon beam, respectively.  $T_{1,2}$ ,  $T_{01,02}$ ,  $q_{1,2}$ , and  $m_{1,2}$  represent the flight time, the flight time for zero kinetic energy, the electric charge, and mass of the first detected ions and the second detected ions, respectively. Here,  $d$  is the distance between the first detected ion and the second detected ion on the anode and  $E$  is the electric field in the collision region. In Eq.(1), the momentum conservation law is adopted and it gives the momentum vector for each event. The summation of the momentum vectors of all events in steps of 10 degrees for the angular distribution creates a three dimensional image of the process.

Figure 4 shows the three dimensional representation of the angular distribution for  $C^+O^+$  ion pairs with total kinetic energies between 12 eV and 18 eV. The electric field vector of the incident light is the horizontal direction. This three dimensional pattern shows that the fragmentation of  $C^+O^+$  occurs preferentially perpendicular to the electric field vector of the incident photon, which is very close to the theoretically expected fragmentation pattern.

## 5. SUMMARY

The performance of the newly developed angle-resolved ion TOF mass spectrometer has been demonstrated by measuring the angular distribution of the fragment ion pairs  $C^+O^+$  from CO at the photon energy of 287.4 eV. The three dimensional pattern of the angular distribution of the fragment ion pairs shows that the fragmentation occurs preferentially perpendicular to the electric vector of the photon beam, which is very close to the theoretically expected one. It becomes possible to measure Mass/charge ratio resolved and kinetic energy resolved angular distributions of fragment ions can be measured using this spectrometer.

This research was funded by the Bundesminister für Bildung, Wissenschaft, Forschung und Technologie (BMBF) and by the Deutsche Forschungsgemeinschaft. N.S. is grateful to the Alexander von Humboldt foundation for a fellowship. F.H. acknowledges financial support by the Deutscher Akademischer Austauschdienst.

---

## References

- (1) N.Saito and I.H.Suzuki, *Phys. Rev. Lett.*, **61** (1989) 2740.
- (2) J.D.Bozek, N.Saito, and I.H.Suzuki, *J. Chem. Phys.*, **100** (1994) 393.
- (3) A.Yagishita, H.Maezawa, M.Ukai, and E.Shigemasa, *Phys. Rev. Lett.*, **62** (1989) 36.
- (4) N.Kosugi, J.Adachi, E.Shigemasa, and A.Yagishita, *J. Chem. Phys.*, **97** (1993) 8842.
- (5) K.Lee, D.Y.Kim, I.Ma, D.A.Lapiano-Smith, and D.A.Hanson, *J. Chem. Phys.*, **93** (1990) 7936.
- (6) O.Hemmers, F.Heiser, J.Eiben, R.Wehlitz, and U.Becker, *Phys. Rev. Lett.*, **71** (1993) 987.
- (7) N.Saito, F.Heiser, O.Hemmers, A.Hempelmann, K.Wieliczek, J.Viefhaus, and U.Becker, *Phys. Rev. A*, **51**, R4313 (1995).
- (8) N.Saito, F.Heiser, O.Hemmers, K.Wieliczek, J.Viefhaus, and U.Becker, *Phys. Rev. A*, submitted.
- (9) A.R.B. de Castro and R. Reininger, *Rev. Sci. Instrum.* **63** (1992) 1317; C.U.S. Larsson, A. Beutler, O. Björneholm, F. Federmann, U. Hahn, A. Rieck, S. Verbin, T. Möller, *Nucl. Instrum. Methods A* **337** (1994) 603.

# LOW ENERGY RBS-CHANNELING MEASUREMENT SYSTEM WITH THE USE OF A TIME-OF-FLIGHT SCATTERED ION DETECTOR

Masataka Hasegawa, Naoto Kobayashi and Nobuyuki Hayashi,  
Electrotechnical Laboratory, 1-1-4 Umezono, Tsukuba, Ibaraki, 305 Japan

## 1. INTRODUCTION

Rutherford backscattering spectrometry (RBS) and the ion channeling have been used extensively as a powerful analysis tool for composition, impurity distribution, and structure of thin films and solid surfaces for many years. This technique usually employs He and other heavier ions as probe ions with typical incident energies ranging from several hundreds keV to several MeV. Silicon surface barrier (SSB) detector is commonly used for the detection of scattered ions. The energy resolution of the SSB detector is typically 10 keV for helium and hydrogen ions, and is worse for heavier ions. Thus in the case of the measurement of helium and hydrogen ions with energy of several hundreds keV or lower the SSB detector is not appropriate because of its energy resolution, and other detection methods with better energy resolution is expected for heavy ions. Recently Mendenhall and Weller have developed a new time-of-flight (TOF) detector, and have demonstrated the performance of the detector for He and other heavy ions.<sup>(1,2)</sup> With the use of 100 - 500 keV energy range this TOF detector is able to provide better depth resolution than that of conventional MeV RBS with a SSB detector.

We have utilized this TOF detector for our RBS-channeling measurement system which utilizes several tens keV hydrogen ions. This system is for in-situ analysis of thin films and solid surfaces which are prepared in UHV chamber. The advantages of the usage of hydrogen ions with this energy range are (1) much larger sensitivity than conventional RBS with MeV helium ions because of the larger scattering cross section, (2) smaller and simpler ion accelerator can be available compared to the usage of MeV ions, and (3) possible analysis of single crystalline samples with the use of ion channeling effect. In this paper we will report the performance of our ion scattering spectroscopy system with the use of TOF detector and several tens keV hydrogen ions to the analysis of solid materials by RBS-channeling measurements.

## 2. LOW ENERGY RBS-CHANNELING MEASUREMENT SYSTEM

### 2-1. TOF DETECTOR

For the energy analysis of several tens keV hydrogen we have utilized the TOF ion detector which was demonstrated by Mendenhall and Weller.<sup>(1,2)</sup> In fig.1 we show the schematic of the TOF detector. An annular type microchannel plate (MCP), which was called the start MCP, was adopted and installed 6mm downstream the carbon foil coaxially on the flight path of

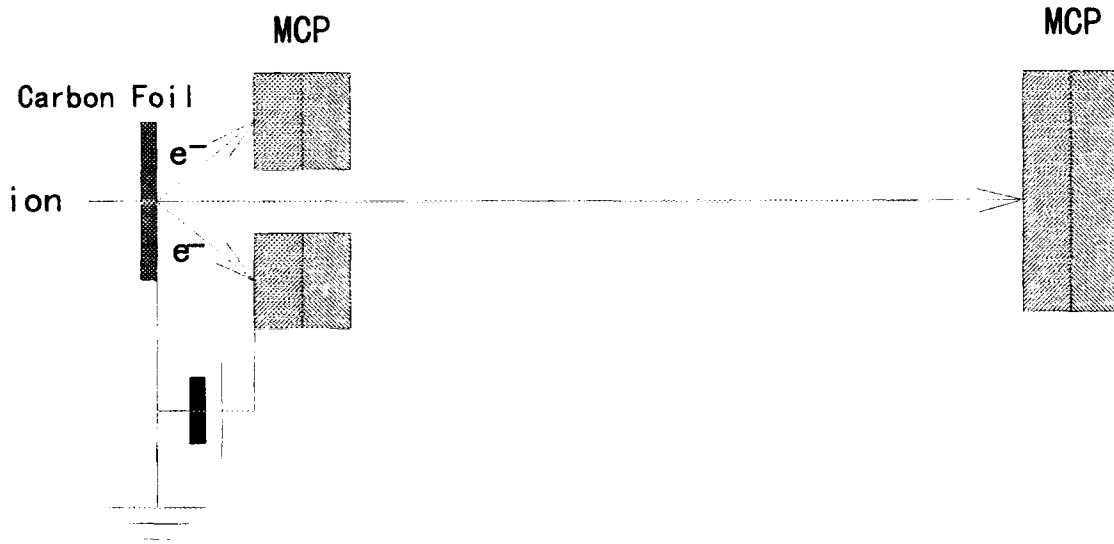


Fig.1 Schematic of time-of-flight (TOF) scattered ion detector.

the ion. Another MCP was at 455mm downstream the carbon foil (called stop MCP). The thickness of the carbon foil was  $1 \mu \text{ g/cm}^2$ , and is mounted on a tungsten mesh whose transmission coefficient is 94%. The scattered ion penetrates the carbon foil and emits secondary electrons which are detected by the start MCP and produce the start signal of the TOF measurement. The ion passes the center hole of the start MCP, and generates a stop signal the stop MCP after the flight through the length of the detector. In this detection method we do not need the pulsing of the primary ion beam to trigger the flight time measurements. In the original scheme which was demonstrated by Mendenhall and Weller the start MCP was at the off-axis of the flight pass of the ion. We have modified the arrangement of the start MCP, the stop MCP and the carbon foil to the coaxial arrangement, as shown in the figure. Because of the coaxial arrangement, whole parts of the detector are putted into single pipe with ICF114mm flanges. This arrangement is very convenient when we want to change the distance between the sample and the carbon foil to alter the detector solid angle. The carbon foil is at the ground potential,

and the input of the start MCP is biased between positive 80 and 100 volts to absorb the secondary electrons.

## 2-2. SYSTEM CONFIGURATION

In fig.2 we present a schematic of our TOF RBS-channeling measurement system. It consists of small ion accelerator, ion beam transport and UHV scattering chamber. The acceleration voltage is ranging from 5 to 30kV. We have utilized a small ECR microwave ion source (Nissin Electric

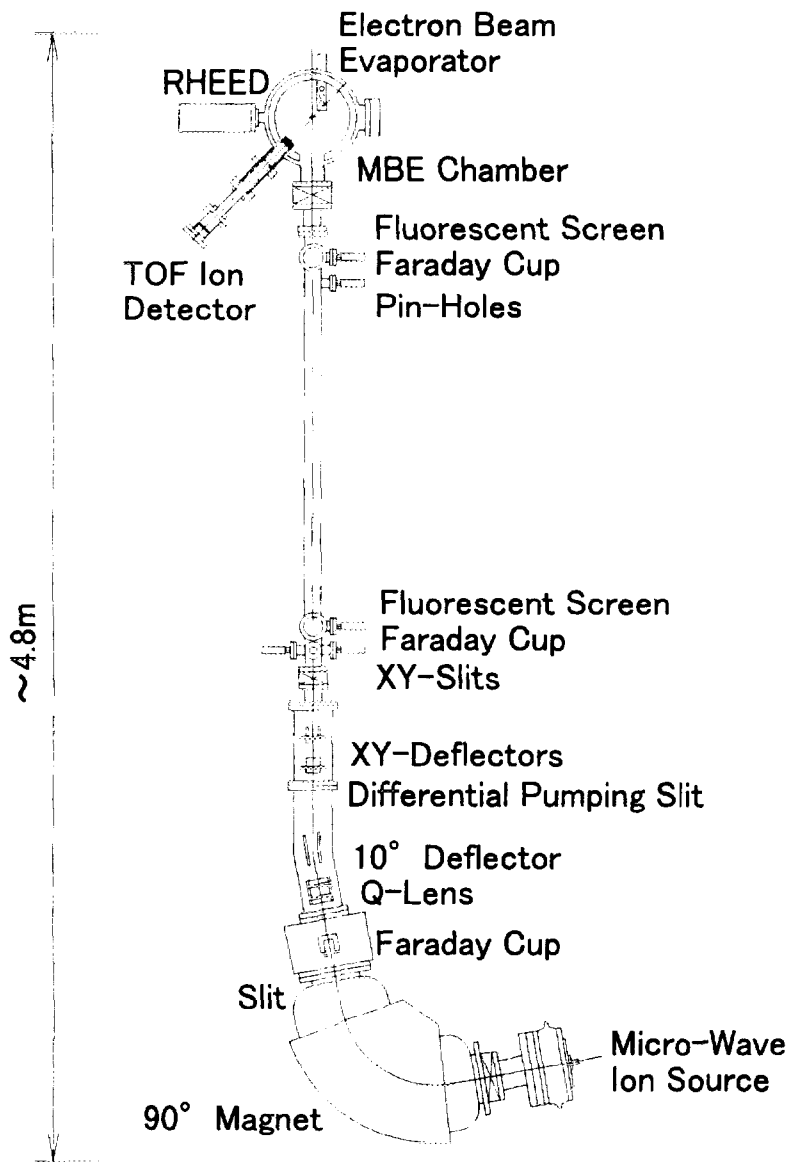


Fig.2 Schematic of TOF RBS-channeling measurement system with several tens keV hydrogen ions.

Co.), which is originally developed by Ishikawa et al. at Kyoto university.<sup>(3)</sup> Although it is not designed for light ions we are able to obtain more than  $15 \mu A H^+$  ion beam downstream the mass analyzing magnet. We should feed Ar gas to the ion source in addition to the hydrogen gas to keep the hydrogen plasma. We have 10 degree electrostatic deflector downstream the analyzing magnet to remove the neutral ions. The pressure in the beam transport duct which is differentially pumped is  $1 \times 10^{-9}$  Torr. Two sets of apertures which are separated by

a distance 1200mm are equipped in the beam transport duct. We can collimate the ion beam to a divergence angle less than 1mrad. The ion beam with low dispersion is essential for the ion channeling measurement, because the dispersion angle of the ion beam should be much smaller than the critical angle of the ion channeling.<sup>(4)</sup> For example the critical angle of Si <100> axial channeling for 25keV hydrogen ions is 54mrad.<sup>(4)</sup> The ion scattering chamber is a molecular beam epitaxy machine, which is equipped with electron-beam evaporator and reflection high energy electron diffraction apparatus. The base pressure in the scattering chamber is  $2 \times 10^{-10}$  Torr. The pressure in the chamber during the ion scattering measurement is less than  $2 \times 10^{-9}$  Torr. The sample is mounted on a 6-axis (3 axis for rotations and 3 axis for parallel movements) precision goniometer in the chamber. The dimension of whole facility is less than 5m, which is very smaller than conventional RBS-channeling facility with MeV helium ions.

### 3.DETECTOR CHARACTERISTICS

To evaluate the characteristics of our TOF ion detector for several tens keV hydrogen ions we measured the spectra of the primary ion beam directly, and of the backscattered ions from Au foil. In fig.3 we show a TOF spectrum of 24.4keV H<sup>+</sup> ions which was observed at 0 degree with respect to the incident ion direction. We observed an almost symmetrical, and low-background spectrum. Also shown is the fitting curve with the use of the Gaussian distribution whose standard deviation ( $2 \sigma$ ) is 4.3nsec. Fig.4 presents the spectrum of the backscattered ions

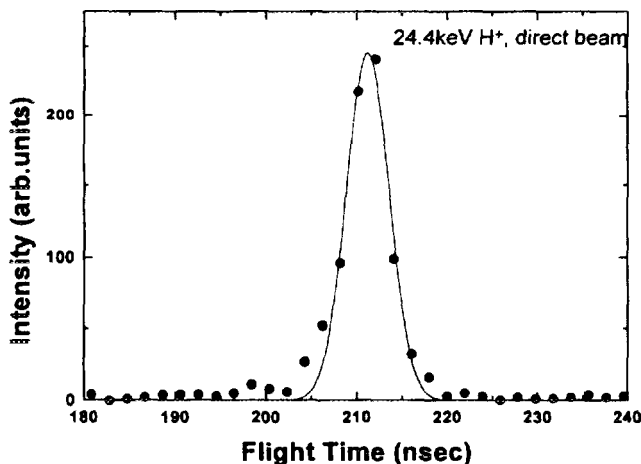


Fig.3 A time-of-flight spectrum of 24.4 keV H<sup>+</sup> ions measured directly by the TOF spectrometer at 0 degree. The fitting curve with Gaussian distribution is also shown by a solid line.

from Au foil which was observed at 135 degree with respect to the direction of the incident ions. The distance between the sample and the carbon foil of the detector is 150mm, and the aperture of the detector is 2mm  $\phi$ . In the present configuration the detector has a geometric solid angle of  $1.4 \times 10^{-4}$ sr. The intensity of the primary ion beam was

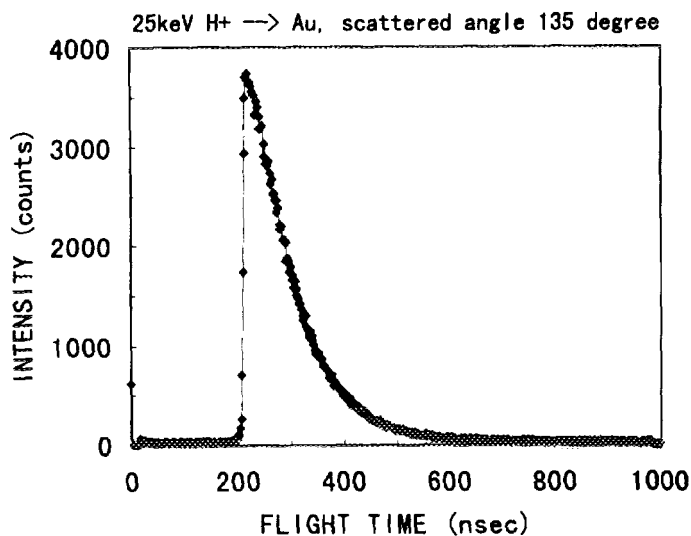


Fig.4 A time-of-flight spectrum of hydrogen ions scattered from Au foil. The energy of the incident ions is 25 keV, and the scattered angle is 135 degree with respect to the direction of the incident ion beam.

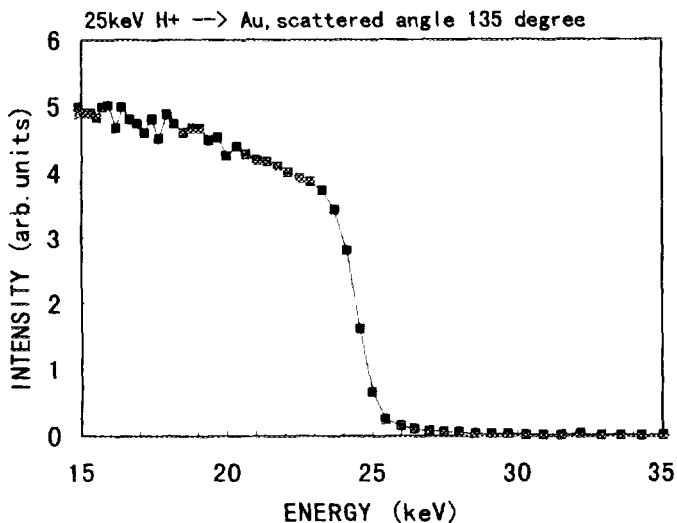


Fig.5 The energy spectrum of hydrogen ions scattered from Au, which is obtained by conversion from the time-of-flight spectrum of fig.4.

about 3nA. The counting rate of the start MCP was 7.0kcps, and that of the stop MCP was 2.2kcps. The measurement duration was 600sec. We are able to measure spectra of good statistics with low intensity primary beams on account of high scattering intensity of low energy ions compared to the MeV light ions. In fig.5 we show the conventional energy spectrum which was obtained by transformation from the TOF spectrum shown in fig.4. We evaluated the energy resolution of the TOF detector by measuring the energy width corresponding to 16~86% of the edge of the spectrum. The energy resolution for 25 keV hydrogen ions is 4.1% which is correspond to the depth resolution of 4.8nm for silicon. In the case of conventional RBS

measurement with MeV helium ions and solid state detector typical depth resolution is about 10nm for silicon. Thus the depth resolution of our system with 25 keV hydrogen ions and the TOF detector is superior to that of conventional RBS.

We also demonstrated how the TOF detector works for 25 keV Ar ions. Fig.6 presents the TOF spectrum of Ar ions scattered from Au foil to 135 degree. The flight time of Ar ion which is scattered at the surface of Au foil is 2.2  $\mu$  sec. The edge of the spectrum is not sharp

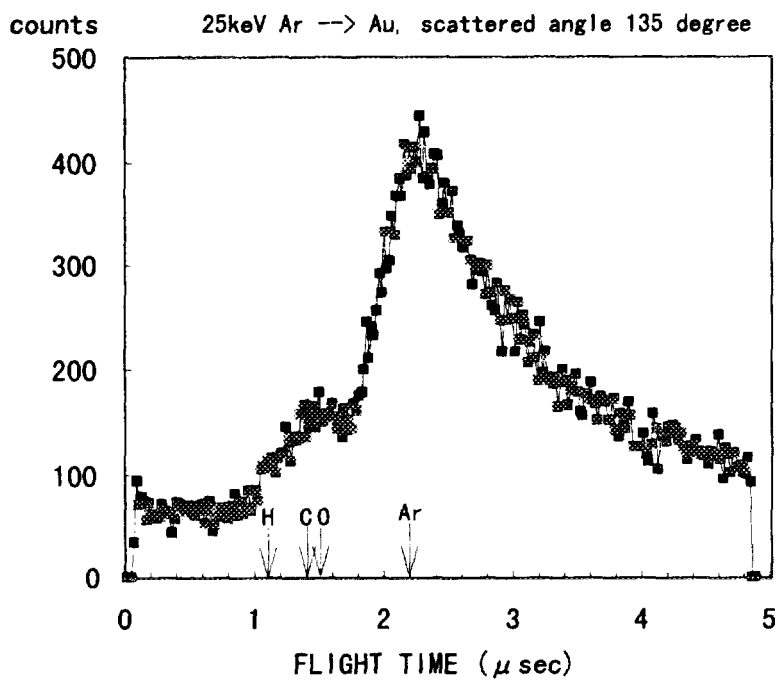


Fig.6 A time-of-flight spectrum of Ar ions scattered from Au. The energy of the incident ions is 25keV, and the scattered angle is 135 degree. Hydrogen, carbon and oxygen, which were recoiled by the Ar ions from the carbon foil, were also observed.

because of larger energy straggling of the Ar ions in the carbon foil compared to that of hydrogen ions. Also we noticed the small and wide hump in the flight time region smaller than the scattered Ar edge. It can be attributed to the signals of H, C and O ions which were recoiled from the carbon foil by the Ar ions. The recoiled ions have larger velocity than the primary ones, and they are observed in the smaller flight time region in the TOF spectrum. The H and O comes from the water over which we float the

carbon foil when we prepare the self-supporting foil on the tungsten mesh.

#### 4.RBS-CHANNELING MEASUREMENTS

One of the advantages of the usage of several tens keV hydrogen ions is the possible ion channeling measurement for the analysis of single crystalline samples. In this section we demonstrate the channeling measurements with our TOF scattered ion detection system with the use of 25keV hydrogen ions. Channeling is the steering of a beam of energetic ions into open spaces (channels) between closed-packed rows of planes of atoms in a crystal. The channeled ions do not penetrate closer than the screening distance of the vibrating atomic nuclei, and the probability of large-angle Rutherford collisions, nuclear reactions, or inner-shell x-ray excitation is greatly reduced compared with the probability of such interactions from a non-channeled (random) beam of ions. Because of the reduction of such probability, the sensitivity to the imperfection of the crystals such as point defect, dislocations, foreign atoms at interstitial

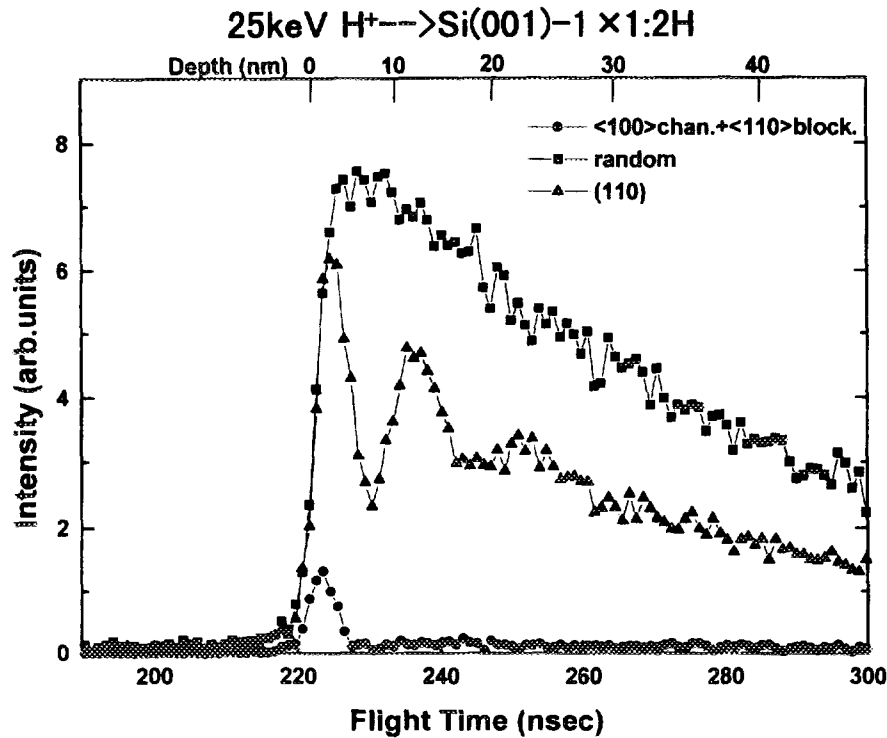


Fig.7 Time-of-flight spectra of hydrogen ions scattered from silicon crystal. The incident energy of the ions was 25 keV, and the scattered angle was 135 degree with respect to the direction of the incident ion beam. The direction of the incident ion beam was along  $\langle 100 \rangle$  axis of silicon crystal (●, axial channeling), along (110) plane (▲, planar channeling), and random orientation (■). The oscillatory feature in the spectrum, which is characteristic to the planar channeling, was clearly observed.

positions are greatly enhanced by ion channeling. Thus channeling has often been used to measure such kind of imperfections of crystals with high sensitivity.<sup>(4)</sup>

In fig.7 we show the TOF ion channeling spectra of 25 keV hydrogen ions in silicon crystal. When the direction of the incident beam is along the  $\langle 100 \rangle$  axis of silicon substrate the intensity of the scattered ions from the sample is reduced to the order of a few percent of that of random direction, which shows the ion channeling occurs and the crystal has very high quality. We also show the spectrum when the direction of the incident beam is along the (110) plane of the crystal, which is usually called “planar channeling”. When planar channeling occurs the ion traces the oscillatory trajectory between the adjacent atomic planes. The probability of the scattering increases when the ion approaches to the atomic plane. Thus the spectrum of the scattered ions shows oscillatory features when planar channeling occurs. When the direction of the incident beam is along the (110) plane of the crystal the spectrum of scattered ions clearly shows the characteristic oscillatory shape of planar channeling, as shown in fig.7. As found

from this figure our 25 keV hydrogen ion scattering spectroscopy system with the TOF detector can be available for the analysis of thin films and solid surfaces by low energy ion channeling effect.

## 5. APPLICATION TO THE MEASUREMENT OF SURFACE REACTION

In fig.8 we demonstrate the *in-situ* observation of the thermal reaction between Fe and Si substrate with the use of the TOF RBS-channeling measurement system by 25 keV hydrogen ions in UHV sample preparation chamber. Very thin Fe layer was deposited on hydrogen

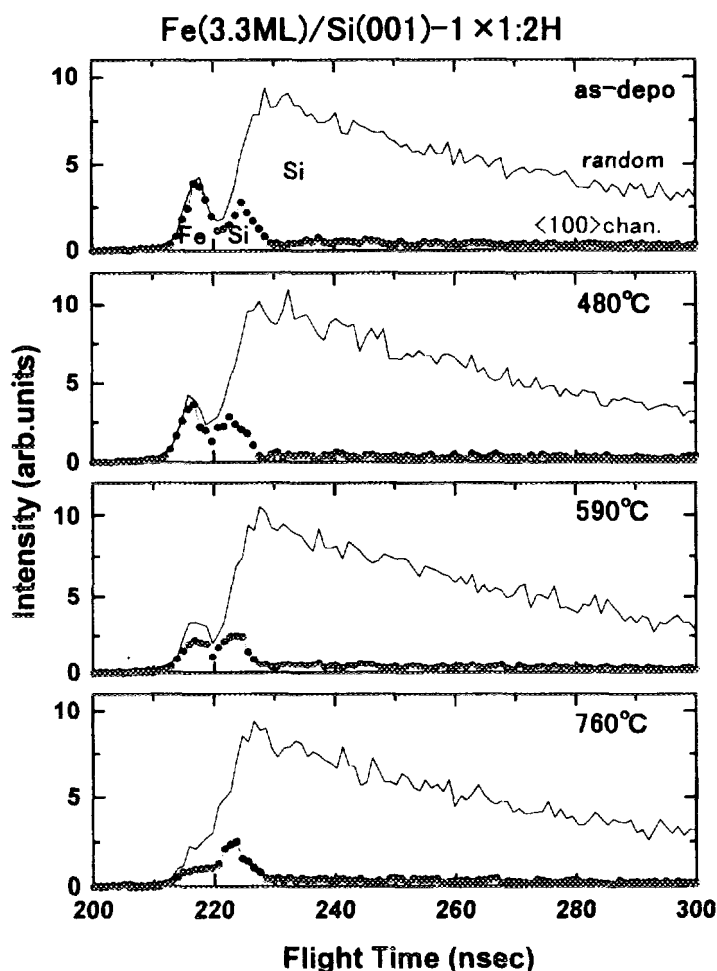


Fig.8 Time-of-flight spectra of hydrogen ions scattered from 3.3ML Fe deposited Si(001)-dihydride surface before and after various annealing temperatures. The incident energy of the ion was 25keV, and detection angle was 135degree with respect to the direction of the incident ion beam.

terminated Si(001) substrate in UHV by electron beam evaporator. Subsequent thermal reaction between deposited Fe and Si substrate was caused by the direct current heating in UHV. The amount of the deposited Fe was able to be measured precisely by our TOF RBS system to be 3.3 monolayer. There was no remarkable difference in the profile of the spectra observed before and after 480°C annealing. After the 590 °C annealing the scattering intensity from Fe became smaller than those of as-deposited film, which indicates the diffusion of Fe atoms into the Si substrate. The diffusion of the deposited Fe has proceeded by 760 °C annealing. We

also have observed the Fe-Si reaction on Si(001) clean surface. In the case of the clean surface the diffusion of the deposited Fe was observed after 380°C annealing, which is rather lower temperature compared with the case of hydrogen terminated surface. We have found from these observations that the hydrogen termination of the silicon surface works as a barrier which prevents the deposited Fe from diffusing into the silicon substrate.

## 6. SUMMARY AND CONCLUSION

We have developed a low energy Rutherford backscattering spectrometry-ion channeling measurement system for the analysis of thin films and solid surfaces with the use of several tens keV hydrogen ions and a time-of-flight particle energy spectrometer. For the detection of the scattered ions new TOF spectrometer has been developed, which consists of two micro-channel-plate detectors. The pulsing of the primary ion beam is not necessary for this type of TOF measurement, and it is possible to observe continuous scattered ion beams. The dimension of whole system is very compact compared to the conventional RBS-channeling measurement system with the use of MeV He ions. The energy resolution,  $\delta E/E$ , for 25 keV  $H^+$  was 4.1%, which corresponds to the depth resolution of 4.8 nm for silicon. The depth resolution of our system is better than that of conventional RBS system with MeV helium ions and solid state detectors. We have demonstrated the ion channeling measurement by this system with 25 keV hydrogen ions. The system can be available well to the analysis of thin films and solid surfaces with the use of the ion channeling effect. The observation of the reaction between Fe and hydrogen terminated silicon surface was also demonstrated.

## References

- (1) M.H. Mendenhall and R.A. Weller, Nucl. Instr. and Meth. **B40/41**(1989)1239.
- (2) M.H. Mendenhall and R.A. Weller, Nucl. Instr. and Meth. **B47**(1990)193.
- (3) J. Ishikawa, Y. Takeiri and T. Takagi, Rev. Sci. Instrum. **55**(1984)449.
- (4) D.S. Gemmell, Rev. Mod. Phys. **46**(1974)129.

# SINGLE ION COUNTING WITH A MCP DETECTOR

Hiroko Tawara, Shinichi Sasaki, Mitsuhiro Miyajima  
National Laboratory for High Energy Physics,  
Oho1-1, Tsukuba, Ibaraki 305, Japan

Eido Shibamura  
Saitama College of Health,  
Kamiokubo 519, Urawa, Saitama 338, Japan

## 1 Introduction

The projects to search for double beta decay of  $^{136}\text{Xe}$  are in progress in our laboratory of the National Laboratory for High Energy Physics. In order to determine the half-life of double beta decay of  $^{136}\text{Xe}$ , one of the projects aims at absolutely measuring the number of  $^{136}\text{Ba}$  ions, which are produced from  $^{136}\text{Xe}$  atoms through the nuclear double beta decay, by using a single ion counting technique.

The experimental methods and the preliminary results have been described in detail in other publications<sup>(1, 2, 3)</sup>. It should be emphasized that the experimental methods to determine the absolute number of  $^{136}\text{Ba}$  ions are required to be characterized for a ultra trace analysis. Since the half life of the double beta decay of  $^{136}\text{Xe}$  is expected to be beyond  $10^{20}$  years ( $2\nu$  mode)<sup>(4)</sup>, the number of  $^{136}\text{Ba}$  ions accumulated in the laboratory is less than a few thousands  $\text{y}^{-1}$  in 1-kg xenon with natural abundance.

The  $^{136}\text{Ba}$  ions are detected through six processes as follows: (1) collection of  $^{136}\text{Ba}$  ions in xenon onto an electrode of a positive ion collector (PIC)<sup>(1, 2)</sup>, (2) liberation from the electrode surface by a first pulsed laser, (3) sampling and (4) ionization by a second pulsed laser for element selection, (5) acceleration and drift in a time-of-flight mass spectrometer (TOF-MS) for mass separation and (6) detection by an ion detector of the TOF-MS. The efficiency of the process from (1) to (6) is required to be known absolutely to determine the number of  $^{136}\text{Ba}$  ions accumulated.

A two-stage microchannel plate (MCP) is used as the ion detector in the TOF-MS. We intend to detect  $^{136}\text{Ba}$  ions quantitatively, even if the number of  $^{136}\text{Ba}$  ions incident on the MCP per laser shot is of the order of unity. Therefore, a precise single-ion counting method is essentially needed and the detection efficiency of the MCP should be determined under the condition of a surely *single* ion incidence on the MCP at counting rate of unity or less.

A purpose of this study is to determine an intrinsic detection efficiency of the MCP for a single ion at an incident energy of several keV, which is a typical acceleration energy in the TOF-MS. The intrinsic detection efficiency of the MCP,  $\epsilon_{mcp}$  is defined as follows:

$$\epsilon_{mcp} = \frac{\text{number of output pulses of the MCP}}{\text{number of incident ions on the MCP}}. \quad (1)$$

So far,  $\epsilon_{mcp}$ s of two-stage MCPs have been measured absolutely for ions with atomic numbers ranging from 1 to 18<sup>(5, 6, 7, 8)</sup>. While the measured  $\epsilon_{mcp}$ s seem to be saturated above an incident energy of about 3 keV, they are widely scattered from 35 % to 85 %. Those measurements were performed at the counting rates of ions from  $10^2$  to  $10^6$   $\text{s}^{-1}\cdot\text{cm}^{-2}$ . It has been reported that the gain and the dead time of MCPs depended on particle counting rate<sup>(5, 6, 7, 9, 10)</sup>. Such the counting-rate dependence would cause the discrepancy among the absolute measurements of  $\epsilon_{mcp}$ .

In this study, a single-ion-counting method using alpha-particle-impact ionization of Ar atoms is demonstrated and the preliminary  $\epsilon_{mcp}$  for Ar ions with incident energies of 3 to 4.7 keV is determined. The single-ion counting by the MCP is aimed to be performed under experimental conditions as follows: (1) A signal from the MCP is reasonably identified as incidence of single Ar-ion. (2) The counting rate of Ar ions is less than  $1 \text{ s}^{-1}$ . (3) The incident Ar ions are not focused on a small part of an active area of the MCP, namely,  $\epsilon_{mcp}$  is determined with respect to the whole active area of the MCP. So far, any absolute detection efficiency has not been reported under these conditions.

## 2 Experiment

### 2.1 Principle of the single-ion-counting method

In order to measure  $\epsilon_{mcp}$  for a single ion, alpha-particle-impact ionization in a much rarefied argon target-gas is used, namely,



where  $\alpha$  is an alpha particle,  $Ar$  an argon atom and  $Ar^+$  a single-charged argon ion. The alpha particle is detected by a silicon detector with the detection efficiency of unity. The Ar ion is accelerated and is incident on the MCP. The MCP signal due to the Ar-ion incidence is measured in coincidence with the alpha-particle signal from the silicon detector. It is well known that such the coincidence technique is able to greatly reduce backgrounds in low-counting measurements.

After here, the term *alpha-particle beam* represents alpha particles detected by the silicon detector. An *ionization volume* is defined as a region from which Ar ions, produced

by the alpha particle beam, can be incident on an active area of the MCP. Also, an *interaction length*  $L$  is defined as path length of the alpha-particle beam in the ionization volume.

The ionization probability for an alpha particle within  $L$  is given by

$$n_a = \sigma \rho L, \quad (3)$$

where  $\sigma$  is an ionization cross section and  $\rho$  a density of Ar atoms in the ionization volume. Therefore, the incident rate of Ar ions on the MCP is given by

$$n_i = n_a I S K = \sigma \rho L I S K \quad (\text{s}^{-1}), \quad (4)$$

where  $I$  and  $S$  are a flux and a cross section of alpha-particle beam, respectively, and  $K$  transmission efficiency between the ionization volume and the MCP. From the definition of  $\epsilon_{mcp}$  by Eq. (1), the counting rate of Ar ions in the MCP can be written as

$$n_s = n_i \epsilon_{mcp} \quad (\text{s}^{-1}). \quad (5)$$

From Eqs. (4) and (5),  $\epsilon_{mcp}$  is obtained by the following equation.

$$\epsilon_{mcp} = n_s (\sigma I \rho L S K)^{-1}. \quad (6)$$

## 2.2 The MCP

The MCP has the following advantages: high sensitivity for ions, a large active area with high gain, a peaked pulse height distribution with maximum operating voltage, a fast response and compactness.

A MCP assembly tested in this experiment is a positive-ion detector in a TOF-MS supplied by the manufacturer (Jordan). Therefore, a grounded plate (grid plate) is mounted in a front of the MCP to form a field-free drift region in the TOF-MS. The plate has a grid at the center for incidence of ions. The open area ratio of the grid is 82 % and its diameter is 1.9 cm  $\phi$ , which is slightly smaller than that of the active area of the MCP. The distance between the grid and a front surface of the MCP is 1.3 cm. An anode of the MCP assembly mounted on a vacuum flange is connected to a signal feedthrough having 50  $\Omega$  matched output impedance.

The two-stage MCP consists of two microchannel plates (Galileo MCP-18B) with the specifications as shown in Fig. 1. The two plates have gains of  $8.7 \times 10^3$  and  $7 \times 10^3$ , respectively, at the maximum bias voltage of  $-1$  kV. Those gains were measured by the manufacturer for electrons with the incident energy of 300 eV, where an input current is typically  $1 \times 10^{-11}$  A $\cdot$ cm $^{-2}$ . In this experiment, each plate was also biased at  $-1$  kV.

The potentials of the front surface of the MCP and the anode were  $-2.2$  kV and  $-200$  V, respectively.

The Ar ions directly hit the active area of the MCP and produce secondary electrons. An open area ratio (OAR) of channels to whole active area of the MCP is about 65 % for normal incidence with respect to the front surface of the MCP. If the production rate and collection efficiency of secondary electrons is small in the active area except channels, the intrinsic detection efficiency would be limited by the OAR.

### 2.3 Experimental apparatus

A experimental apparatus is illustrated in Fig. 2. The vacuum chamber was evacuated to less than  $10^{-5}$  Pa for a few days by a turbomolecular pump to fully decrease a residual gas in channels of the MCP. Measurements were made at several different pressures less than 1 mPa. While operating the turbomolecular pump, argon gas is continuously introduced into the chamber through a needle valve during measurements. The pressure of argon in the chamber is kept constant adjusting the gas flow rate by the needle valve. An ionization gauge (B-A gauge) is used to measure the pressures before and after each measurement. Because the ionization gauge produces a large number of ions as backgrounds, it turns off during measurements.

An alpha-particle source of  $^{241}\text{Am}$  has an active area of  $8\text{ mm} \times 8\text{ mm}$  and activity of  $3 \times 10^6\text{ Bq}(2\pi)^{-1}$ . A gate valve is used to stop alpha particles during measurements of backgrounds due to dark current of the MCP. The silicon detector with an active area of  $1.2\text{ cm } \phi$  in diameter is mounted at a distance 41 cm apart from the alpha-particle source. Alpha particles are not collimated to keep the counting rate as high as possible. The path of alpha particle beam contributing the coincidence measurements is limited only by the active area of source and that of the silicon detector, as illustrated in Fig. 2.

The electrode system to accelerate Ar ions consists of an acceleration plate and the grid plate with outer diameters of  $8\text{ cm } \phi$  and  $6.35\text{ cm } \phi$ , respectively. The gap between both the plates is 3.2 cm and the acceleration plate is kept at +3 kV.

When an Ar ion is accelerated by a static electric field ( $E_{acc}$ ) formed between the acceleration plate and the grid, acceleration energy is a function of a distance from the grid plate to the position of ionization. A maximum and minimum distance are 2.7 cm and 0.8 cm, respectively, which are limited by the cross section of alpha-particle beam. Therefore, the acceleration energies of  $\text{Ar}^+$  ions lie in a range of 0.8 keV to 2.5 keV. After passing through the grid, Ar ions are accelerated again by a static electric field ( $E_{mcp}$ ) between the grid and the front surface of the MCP kept at  $-2.2$  kV. The incident energies of Ar ions on the MCP become to lie in a range from 3 keV to 4.7 keV. The field ratio

$E_{mcp} / E_{acc}$  is 1.8. The field-free drift region, which is desirable to define incident energy accurately as well as to separate multi-charged ions, is not introduced in order to prevent a decrease of transmission efficiency resulting from an additional grid electrode.

Figure 3 shows a schematic diagram of the detector system for single-ion countings using the coincidence technique. Fast responses from the MCP are analyzed with a digital signal analyzer (DSA, Tektronix 602A) at the sampling rate of 1 GHz. Signals from the silicon detector are fed to a charge-sensitive preamplifier. Then, they are shaped by a main amplifier with shaping time of  $0.5 \mu s$  and are fed to the DSA.

The coincidence measurement by the DSA is performed triggering by alpha-particle signals. The trigger level is set at 70% of the mean height of pulses due to 5.5-MeV alpha-particles in order to eliminate contribution of alpha particles incident near the edge of active area of the silicon detector and those incident on the active area after scattering from a chamber wall and electrodes. For the measurement of backgrounds due to dark current of the MCP, the pulses from a random pulse generator are used for triggering instead of the alpha-particle signals.

Whenever the DSA is triggered, it acquires simultaneously both waveforms of a trigger signal and from a MCP by a preset time period of  $2 \mu s$ . Because the frequency of occurrence of MCP signal per trigger is quite low, the waveform acquisition is repeated by a preset number (typically 500 times) in order to save the time required for measurement. When the DSA completes the preset number of waveform acquisitions, the waveform of MCP signal appeared during these successive acquisitions and the waveform averaged from all trigger signals remain in a record of the DSA.

If a pulse height of recorded MCP-signal is larger than a preset discrimination-level, the DSA also measures a time interval between the MCP signal and the averaged trigger signal. The discrimination level was set  $-8 \text{ mV}$  typically, which was slightly larger than the electronic noise level.

The measured values by the DSA are sent to a computer for data analysis. Then, the DSA resets all the memory and starts the next successive acquisitions. The successive acquisitions were also repeated several thousand times every measurement in order to accumulate more than a hundred of coincidence events in the computer.

## 3 Results and Discussion

### 3.1 Incident rate of Ar ions

In an energy region of MeV, the ionization cross sections of bare ions with charge  $Z$  are approximately  $Z^2$  times those of proton at the same velocity. The  $\sigma$  of 5.5 MeV alpha

particle for Ar is calculated to be  $4.4 \times 10^{-16} \text{ cm}^2$  from the total ionization cross section of proton recommended by Rudd et al<sup>(11)</sup>.

The ionization volume as illustrated roughly in Fig. 2 is estimated to be  $3.5 \text{ cm}^3$ . The interaction length  $L$  is estimated to be  $1.26 \text{ cm}$  by taking an average over the ionization volume. The transmission efficiency  $K$  is taken to be  $0.82$  from the open area ratio of the grid. The atomic density of 1-mPa argon gas is  $2.45 \times 10^{11} \text{ cm}^{-3}$  at  $23^\circ$ , which is the maximum atomic density in this experiment. The intensity of alpha particle beam, that is,  $IS$  was measured to be about  $350 \text{ s}^{-1}$ . From the values mentioned above and Eq. (4), the maximum incident rate of Ar ions is about  $0.04 \text{ s}^{-1}$ .

### 3.2 Response of the MCP for a single Ar ion

Using the DSA, the temporal response of the MCP was observed. Figure 4 depicts a typical response having the width of  $2 \text{ ns}$  in FWHM, followed by after-pulses due to ionic feedback. In case of large pulses as typically shown in Fig. 4, the baseline was often unstable for a duration of several tens ns. The observed signal is considered to be due to a surely single Ar-ion because the ionization probability  $n_a$  is of the order of  $10^{-4}$  and the probability of signal pile-up per alpha particle is negligible in this experiment.

### 3.3 Coincidence measurement of single Ar-ions and alpha particles

Figure 5 shows the results of coincidence measurement recorded on a display of the DSA at full time scale of  $10 \mu\text{s}$ . Only few hundred pulses from the MCP are recorded as shown at the upper side of Fig. 5, though the total number of triggering by alpha-particle signals is several millions. The lower waveform in Fig. 5 shows an averaged one from all alpha-particle signals used for triggering of the coincidence measurement. An arrow indicates the trigger-level.

As typically shown in Fig. 5, there are two types of MCP signals; pulses localized within short period and those appeared at random in time. Considering the flight time of Ar ion, the localized pulses are supposed to be due to Ar ion. Those pulses, of course, disappeared when the gate valve stopped alpha particles. The pulse height distribution of the random pulses exponentially decreased as a function of the pulse height. Such the tendency of random pulse did not depend on the pressure of argon gas. They should be considered as backgrounds occurring at random in time.

A typical time distribution of the MCP pulses is shown in Fig. 6. The horizontal axis of Fig. 6 indicates the time difference between the alpha-particle signal and the MCP signal. As shown in Fig. 5, alpha-particle signals are delayed from MCP signals due to Ar ion because of a delay in shaping time of  $0.5 \mu\text{s}$  for signals from the silicon detector.

Namely, a larger delay time means a shorter flight time of Ar ions in the time distribution of Fig. 6. Almost all the counts localize within about 500 ns, however, the distribution is not symmetrical and follows a tail. The time jitter was obtained to be 10 ns or less in the coincidence measurements using the DSA. The pulses in the tail seem to correspond to multi-charged Ar ions.

In the present experimental set up, however, the Ar<sup>+</sup> ions can not be separated from the multi-charged Ar ions. We count all the pulses observed within the time period of 500 ns in order to estimate the counting rate of signals, though it includes pulses due to multi-charged ions. The systematic errors resulting from this treatment are evaluated in the section 3.6.

A counting rate of backgrounds is determined from the number of random pulses in time distribution except the 500-ns signal region. Subtracting the counting rate of backgrounds from the total counting rate in the signal region, a counting rate of Ar ions is obtained. The counting rates of backgrounds were in a range of 4 to 8 s<sup>-1</sup>. The signal to background ratio were calculated to be 10 to 25 depending on the experimental condition.

### 3.4 Pulse height distribution

Figure 7 shows a pulse height distribution of signals measured at 0.36 mPa. The most probable value and the resolution of the distribution are 130 mV and 120 % in FWHM, respectively.

In this measurement, the discrimination level is 8 mV and the signal to background ratio is almost 10. Therefore, the distribution does not show clearly existence of backgrounds, which exponentially decrease as a function of the pulse height. The loss of signal due to the discrimination of 8 mV seems to be negligible.

The output charge corresponding to 130 mV is roughly estimated to be 7 pC. This value is smaller than 9.7 pC expected from the gains for 300-eV electrons as mentioned in the section 2.2. The critical counting rate, at which the gain decreases to the half, is of the order of 10<sup>5</sup> to 10<sup>6</sup>(12). In this experiment, the counting rate is far lower than the critical value. Therefore, the deterioration of gain due to the dead time should be negligible. On the other hand, the sampling interval of waveform by the DSA is 1 ns. It is not so enough to accurately measure the height of pulse having the width of 2 ns in FWHM. The measured pulse heights are expected to become smaller than the original one in many case. Therefore, the gain for Ar ions with the energy of keV may be larger than 7 pC.

### 3.5 Pressure dependence of signal counting rate

In Fig. 8, the counts of Ar ions per alpha-particle are plotted as a function of argon pressure. The error bars are the statistical one calculated from the total number of counts. A straight line (a solid line in Fig.8) is obtained from a least-square fitting of the data points. The data points show a good linearity but the straight line has some intercept on the horizontal axis. This intercept seems to be caused from a counting loss of the MCP signals and ambiguity of pressure measurement.

In this experiment, the DSA always measures the largest pulse, even if there are two or more pulses in the record every 500 triggerings. Counting loss rates are calculated to be 2 to 11 % for all the coincidence measurements. The counting rates of signals are corrected using the loss rates. The gas flow in the chamber might make the pressure difference between the ionization volume and the ionization gauge. The systematic error due to the pressure difference is take into consideration in the section 3.6

From the linear fitting of the data points,  $n_s(I\rho S)^{-1}$  in Eq.(6) and the error is obtained to be  $(2.7 \pm 0.2) \times 10^{-16}$  alpha particle<sup>-1</sup> Ar atom<sup>-1</sup> cm<sup>3</sup>.

### 3.6 The intrinsic detection efficiency

From  $2.7 \times 10^{-16}$  alpha particle<sup>-1</sup> Ar atom<sup>-1</sup> cm<sup>3</sup> and the values described in the section 3.1, the detection efficiency is obtained to be 0.59 using Eq.(6). The statistical error is evaluated to be 0.09 from those of  $n_s(I\rho S)^{-1}$ ,  $\sigma$ ,  $L$ , and  $K$ .

The systematic errors should be considered at least for  $\rho$ ,  $\sigma$  and  $n_s$  in this experiment. We estimate those value very roughly. The accuracy of  $\rho$  is limited by the pressure measurement using the ionization gauge normally calibrated for nitrogen gas. Its accurate sensitivity for argon gas is not known. Also, some pressure difference between the ionization gauge and the ionization volume exists due to the flow of argon gas. The systematic error due to differences of the sensitivity and the pressure is evaluated to be +23 % of the value of  $\epsilon_{mcp}$ .

The multi-charged Ar ions is expected to be several % of Ar ions produced by 5.5-MeV alpha particles. We estimate two systematic errors due to multi-charged Ar ions. The total ionization cross section used as  $\sigma$  to estimate  $\epsilon_{mcp}$  provides the total number of electrons in ionization processes. The total number of ions should be smaller than that of electrons because of multiple ionizations. Using the multiple-to-single ionization ratios of bare projectile with 2.31 MeV/amu for Ar measured by Haugen et al.<sup>(13)</sup>, the systematic error due to use of the total ionization cross section is evaluated to be +24 % of  $\epsilon_{mcp}$ . On the other hand, the counting loss of multi-charged ions exist, because their flight times are shorter than those of Ar<sup>+</sup> ions. The systematic error due to the counting loss of multi-charged ions was evaluated to be -10 % of  $\epsilon_{mcp}$ .

Consequently,  $\epsilon_{mcp}$  and the errors are obtained to be  $0.59 \pm 0.09$   $^{+0.24}_{-0.06}$  for Ar ions which include several % of multi-charged ions and have the incident energies ranging from 3 to 4.7 keV.

### 3.7 Counting loss due to the dead time and backgrounds

According to Fraser's estimation, a time constant, at which gain of a channel recovers by conduction current after electron multiplication in the channel, is about 0.15 s in rear plates of two-stage MCPs<sup>(10)</sup>. We assume  $10 \times 0.15$  s as the dead time of channel in pulse counting mode of the MCP for rough estimation. An average counting rate per channel was about  $2 \times 10^{-6}$  typically, which is mainly due to backgrounds. From Eq.(9) in the Appendix, the probability of the counting loss is obtained to be  $3 \times 10^{-6}$  and is negligible in this experiments.

The counting rate of backgrounds was measured to be  $1.5 \text{ s}^{-1}$  without the alpha-particle beam. It is considered that they are mainly due to field emission of the MCP and natural radioactivity (<sup>40</sup>K) in glass disk of MCPs itself<sup>(14, 15)</sup>. The background counting rate with the alpha-particle beam, however, was measured to be  $5 \text{ s}^{-1}$  typically. The ions and photons due to alpha particle impact on surfaces of the metal electrodes and the chamber wall seem to be the main source of such additional backgrounds.

The collimated alpha-particle beam is needed for the following; the reduction of alpha particles impacting on materials surrounding the ionization volume, the improvement of flight-time resolution to separate single-charged ions from multi-charged ions and determination of more accurate incident-energy.

## 4 Conclusion and future plans

1. The single-ion-counting method using the alpha-particle-impact ionization in Ar gas was demonstrated at the counting rate of the order of  $10^{-2} \text{ s}^{-1}$ .
2. The intrinsic detection efficiency of the MCP was obtained to be  $0.59 \pm 0.09$   $^{+0.24}_{-0.06}$  for Ar ions which include several % of multi-charged ions and have the incident energies ranging 3 to 4.7 keV. This value is close to the open area ratio of the MCP of 65 %.

In the next experiment, we are planning as follows:

- In order to measure pressures of target gas, the spinning rotor gauge will be introduced with the closed chamber system. It does not make outgassing, background ions and gas flow. The atomic density can be monitored continuously during the measurement. Also, it can be obtained absolutely from the well known viscosity of gaseous atom.

- A well-collimated beam of alpha particle is used. It is required for the good mass resolution to separate multi-charged ions, and the reduction of background ions.
- The absolute detection efficiency are measured for Xe ions in the impact energy of several keV, whose mass is almost same as that of Ba ions.

## Appendix

The statistical characteristics of random events with the low probability of occurrence can be presented by the Poisson process,

$$P(N, \tau) = \frac{(n\tau)^N e^{-n\tau}}{N!}, \quad (7)$$

where  $N$  is the number of events within a given period of time  $\tau$  and  $n$  the average rate of events. Since  $P(0, \tau)$  is the probability of *no* event during the time  $\tau$ , the probability of occurrence of one event or more within  $\tau$  is

$$P(N > 0, \tau) = 1 - P(0, \tau) = 1 - e^{-n\tau}. \quad (8)$$

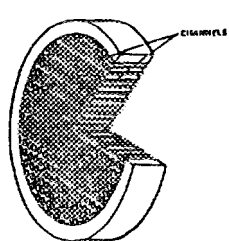
When  $n\tau \ll 1$ ,

$$P(N > 0, \tau) = n\tau. \quad (9)$$

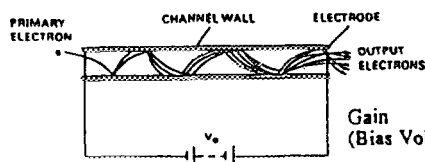
## References

- (1) M. Miyajima, S. Sasaki and H. Tawara, KEK Proceedings, **91-5**, (1991) 19.
- (2) M. Miyajima, S. Sasaki and H. Tawara, Hyperfine Interactions, **74**, (1992) 159.
- (3) M. Miyajima, S. Sasaki and H. Tawara, IEEE Trans. **NS41**, (1994) 835.
- (4) J. -C. Vuilleumier et al., Phys. Rev. **D48**, (1993) 1009.
- (5) R. S. Gao et al., Rev. Sci. Instrum., **55**, (1984) 1756.
- (6) K. Tobita et al., Jap. J. Appl. Phys, **55**, (1984) 1756.
- (7) A. Müller et al., Rev. Sci. Instrum., **57**, (1986) 349.
- (8) B. Brehm et al., Meas. Sci. Technol., **6**, (1998) 953.
- (9) C. Firmani and E. Ruiz, Rev. Sci. Instrum., **53**, (1982) 570.
- (10) G. W. Fraser et al., Nucl. Instrum. and Meth., **A306**, (1991) 247.

- (11) M. E. Rudd et al., *Rev. Mod. Phys.* **57**, (1985) 965.
- (12) K. Oba, C. Okuyama and H. Kume, Hamamatsu Photonics, Electron Tube Division, Technical Manual, RES-0795, (1990).
- (13) H. K. Haugen et al., *Phys. Rev.*, **A26**, (1982) 1962.
- (14) R. F. Malina et al, *IEEE Trans.* **NS31**, (1984) 404.
- (15) O. H. Siegmund and R. H. Malina, *IEEE Trans.* **NS31**, (1984) 776.



**Microchannel Plate (Galileo MCP-18B)**  
 Plate Outside Diameter 2.44 cm  
 Active Area Diameter 1.94 cm  
 Channel Diameter 10  $\mu\text{m}$   
 Center-to-Center 12  $\mu\text{m}$   
 Thickness 400  $\mu\text{m}$   
 L/D Ratio 40:1  
 Bias Angle 5 degree  
 Open Area Ratio 65 %



Gain  $7 - 8 \times 10^3$  per plate  
 (Bias Voltage 1000 V/plate)

Fig. 1 The characteristics of the MCP.

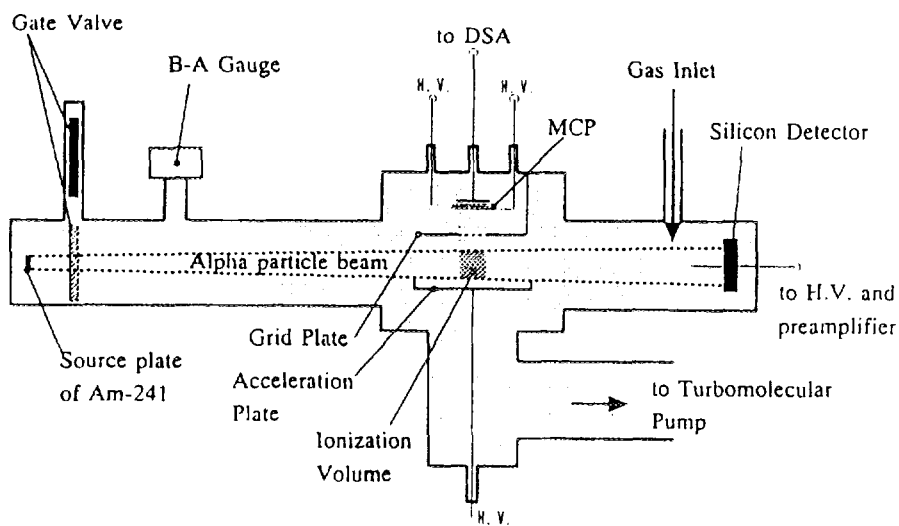


Fig. 2 The schematic view of experimental apparatus for single-ion-counting.

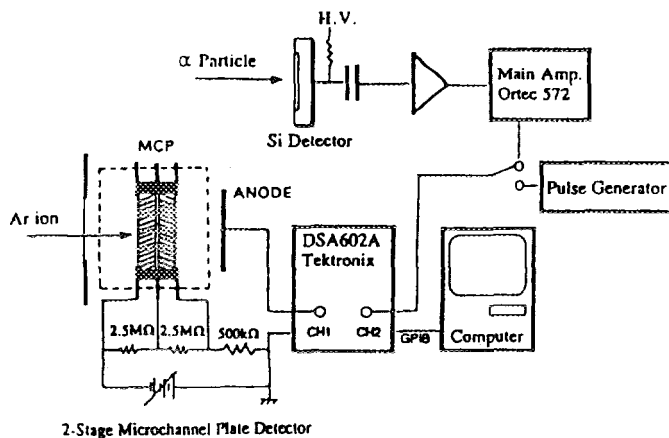


Fig.3 The schematic diagram of the detector system.

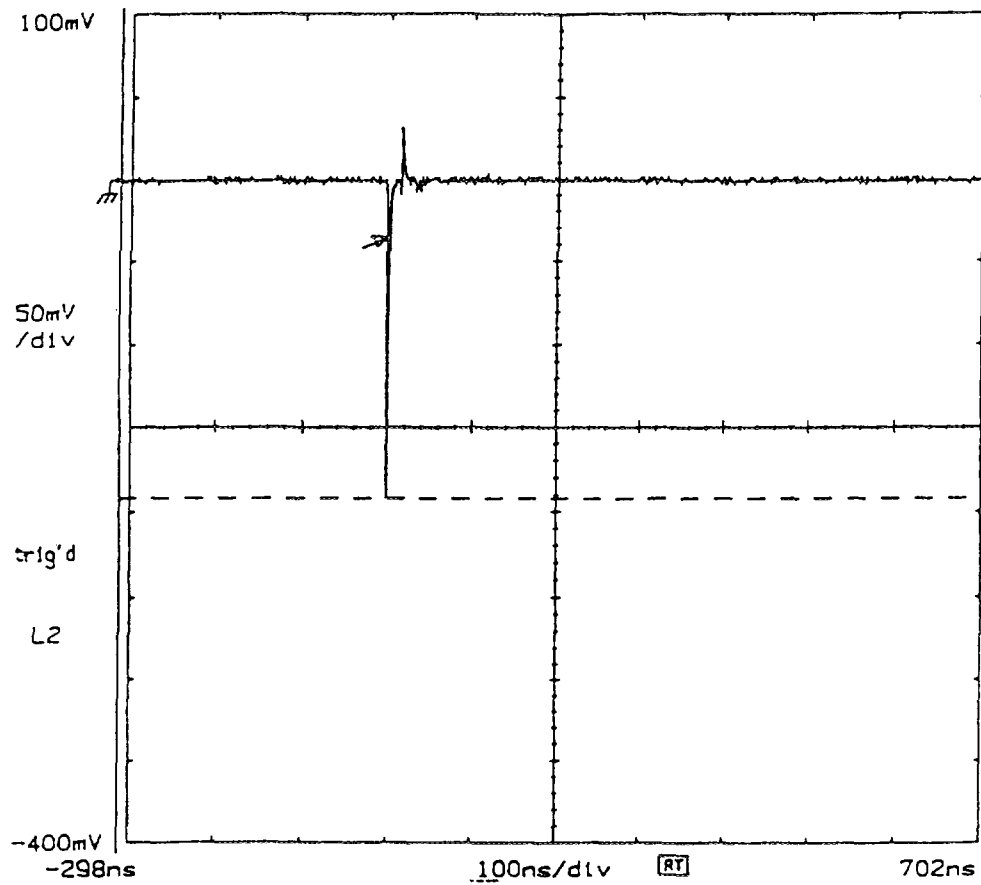


Fig.4 The single response of the MCP for a single-Ar-ion impact recorded on a display of the DSA.

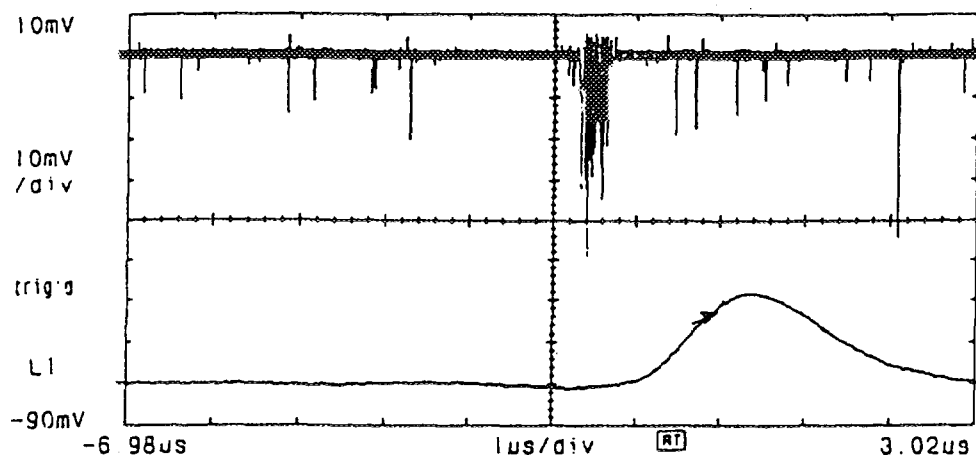


Fig.5 The pulses of the MCP (the top) triggered by the alpha-particle signals recorded on a display of the DSA.

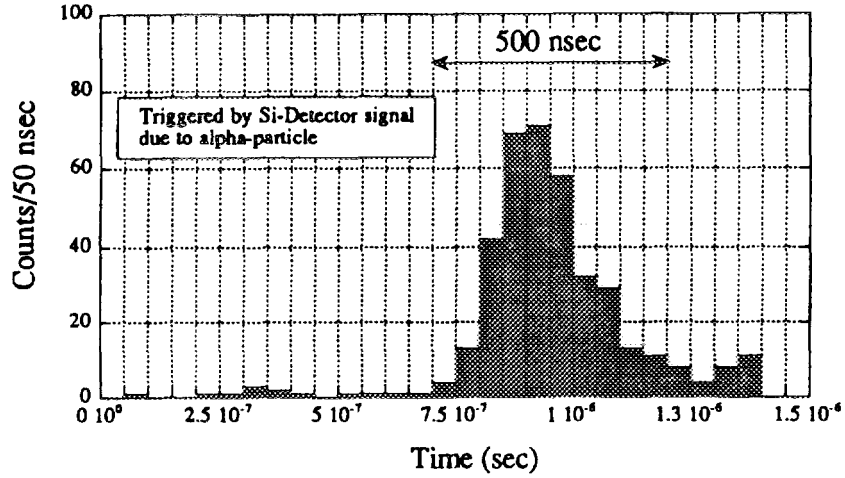


Fig.6 The time spectrum of Ar-ion signals coincident with alpha-particle signals

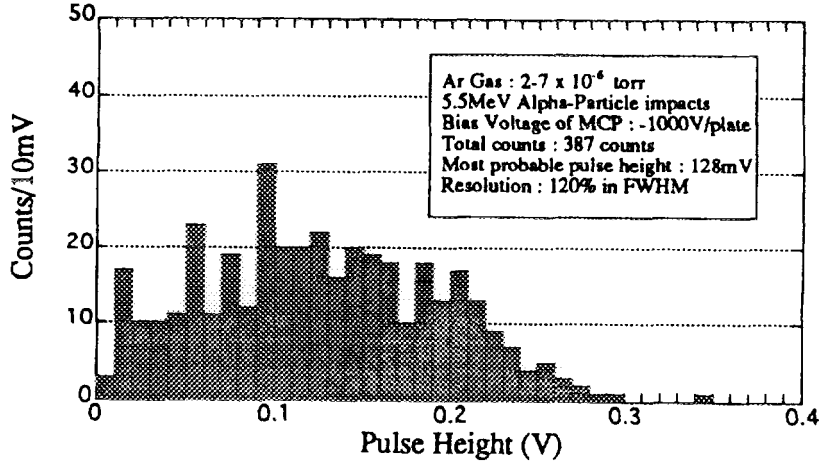


Fig.7 The pulse height distribution of Ar-ion signals in the time region of 500 ns on the time spectrum.

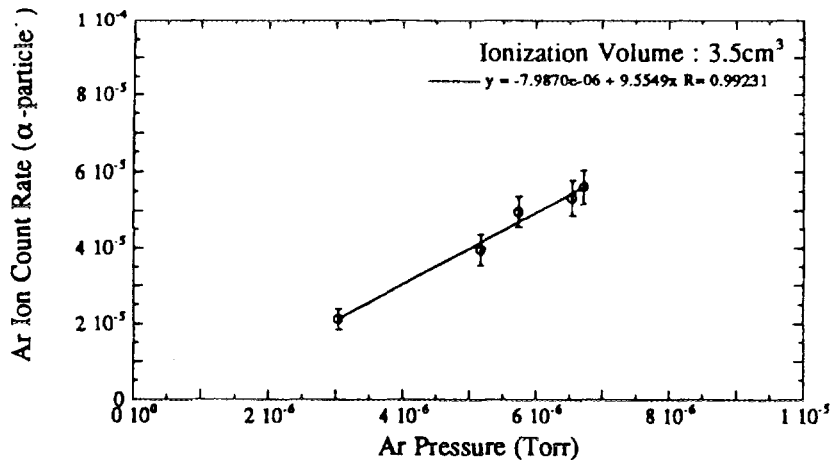


Fig.8 The counts of Ar-ion signals per alpha particle as a function of argon-gas pressure.

# SUPERHEATED LIQUID DROP DETECTOR

## RESPONSE TO LOW LET RADIATION

Teruko Sawamura, Tatsuya Joji, Shuichi Tsuda and Masakuni Narita  
Department of Nuclear Engineering, Faculty of Engineering,  
Hokkaido University

### 1. INTRODUCTION

Superheated liquid drop detectors utilizing radiation-induced bubble formation in superheated liquid have been used for neutron and recently also for gamma-ray detection. The detectors are composed of drops of a sensitive liquid with low-boiling point and supporting material, where the liquid drops are dispersed. During storage, the detectors are externally pressurized to be insensitive to radiation. By removing the pressure, the liquid becomes superheated and sensitive to the radiation.

Radiation-induced charged particles, recoiled ions in the case of neutron exposure, transfer their kinetic energy to the liquid along trajectories which result in very high local temperature regions, which have been called 'thermal spikes' by Seitz<sup>1)</sup>. After a short transient time, the liquid involved in the region evaporates and a gas-liquid interface is formed. The minute vapor-regions expand by evaporation of the surrounding liquid till all the liquid of the drop becomes vapor. Thus visible bubbles are formed.

The neutron flux or dose is estimated by counting these bubbles by the naked eye, optical image analyzer, or acoustic methods. Neutron detection sensitivity has been calculated by considering interactions between neutrons and constituent atoms of sensitive liquids and bubble formation criteria for emitted ions from the interactions<sup>2),3),4)</sup>. In the calculation, protons emitted from the sensitive liquid or the supporting material are ignored, because those are considered not to meet the criteria. However, recently the superheated liquid drop detector has been suggested to be sensitive to protons or gamma-rays in some experiments<sup>5),6)</sup> but details of the process of sensing such as with radiation has not been discussed.

In this paper, we study the conditions of bubble formation especially for

low LET radiation such as of protons and gamma rays.

## 2.CONDITIONS OF BUBBLE FORMATION

According to Seitz<sup>1)</sup>, the thermal spike produced by radiation vaporizes the liquid, the so called nucleation, but not all the vaporization (=nucleation) develops into visible bubbles. The process from minute vapor embryo to bubble is considered to be the following: if the pressure in the embryo,  $P_{in}$ , is equal to the sum of the pressure,  $P_t$ , of the surrounding liquid and the inward force from surface tension,  $\gamma$ , in an equilibrium state, the radius of the embryo( here the embryo is assumed spherical) remains constant. Then the radius,  $R_c$ , satisfies the equation,

$$P_{in} = P_t + \frac{2\gamma}{R_c} . \quad (1)$$

The radius  $R_c$  is called the critical radius. If the radius  $R$  of the embryo is larger than  $R_c$ , then  $P_{in} \geq P_t + \frac{2\gamma}{R}$  and the vapor sphere develops with additional vapor

from the surrounding liquid. When  $R \leq R_c$ , the vapor embryo collapses.

The energy required to produce an embryo with the critical radius,  $R_c$ , is called the critical energy. We discussed the critical energy elsewhere<sup>7)</sup>. According to Seitz's theory of bubble chambers<sup>1)</sup>,

$$E_c = \frac{4\pi}{3} R_c^3 H_{fg} + 4\pi R_c^2 \gamma(T) + \frac{4\pi}{3} R_c^3 P_t , \quad (2)$$

$H_{fg}$ : the heat of vaporization per unit volume.

Apfel's expression for  $E_c$  is given as<sup>8)</sup>,

$$E_c = 4\pi R_c^2 \gamma(T) + \frac{4\pi}{3} R_c^3 \{P_t - P_s(T)\} , \quad (3)$$

$P_s(T)$ : equilibrium vapor pressure at  $T$ .

Bugg and recently Harper derived  $E_c$ <sup>4),9)</sup> as,

$$E_c = \frac{4\pi}{3} R_c^3 H_{fg} + 4\pi R_c^2 \left\{ \gamma(T) - T \frac{\partial \gamma}{\partial T} \right\} + \frac{4\pi}{3} R_c^3 P_t . \quad (4)$$

There are few experimental data for the critical energy  $E_c$ . In this paper we adopted equation (4) by referring to Apfel's<sup>8)</sup> and Harper's<sup>4)</sup> experiments<sup>10)</sup>.

For nucleation eventually to be followed by bubble formation, the energy

deposition,  $E$ , must be larger than  $E_c$ . This is the first condition for bubble formation.

The second condition is related to the spatial distribution of energy deposition. The detailed process before the equilibrium state is established in the liquid exposed to radiation is unknown and therefore, so is the size of the energy-deposited region available to produce an embryo with radius  $R$ . We assume that the size can be expressed by a distance,  $\ell$ , along a charged particle trajectory and that the energy,  $(dE/dx) \times \ell$  is effectively consumed by the embryo production. Here,  $(dE/dx)$  is the effective energy deposition per unit distance, which is approximately represented by the stopping power of the liquid for the particle emitted by the interaction of the radiation with the liquid atom. For the bubble formation, the radiation-induced particle has to deposit the energy  $E = (dE/dx) \times \ell \geq E_c$ .

The two conditions, then are:

$$E \geq E_c \quad (c1)$$

and

$$\left(\frac{dE}{dx}\right) \geq \frac{E_c}{\ell} \quad (c2)$$

, where the term of the right hand side of equation (c2) exhibits the lower limits of the stopping power for the charged particles possible to form a visible bubble.

Instead of  $\ell$  we introduce a parameter 'a' and 'b' as a measure of the available region, in the same manner as Harper<sup>(4,11)</sup>;

$$\ell = aR_c, \quad \ell = bR_{tc} \quad (3)$$

, here  $R_{tc}$  is an equivalent radius of the liquid sphere, derived from the equality,

$$\frac{4\pi}{3} \rho_g R_c^3 = \frac{4\pi}{3} \rho_l R_{tc}^3 \quad (\rho_g, \rho_l; \text{densities of the vapor and liquid}).$$

With this parameter the lower limits of the stopping power becomes:

$$E_c/(aR_c) \quad \text{or} \quad E_c/(bR_{tc}).$$

### 3.FREON-12 AND OCTAFLUOROPROPANE AS SENSITIVE LIQUIDS

Freon-12 and other liquids have been reported to be sensitive to protons or gamma-rays. From condition (c2), lighter particles or lower LET radiation could be

detected with liquids having low  $E_c$ . The low boiling point results in the lower  $E_c$ , which is shown just below. In this section we consider Freon-12 as the most sensitive liquid among the liquids that have been studied, and octafluoropropane(OFP) which may be more sensitive than Freon-12. In table.1 shows material parameters, and  $R_c$ ,  $E_c$  and  $E_c/R_c$  obtained by the parameters at  $T = 20$  °C for both liquids<sup>10)</sup>. The boiling point of OFP is  $\sim 7$  °C lower than that of Freon-12. The effect of this difference appears in values of  $R_c$ ,  $E_c$ , and  $E_c/R_c$ : the  $R_c$  of OFP is 1/3 of  $R_c$  of Freon-12 and the  $E_c$  of OFP is 1/15 of that of Freon-12. The temperature dependence of  $R_c$  and  $E_c$  was calculated with (1) and (2)~(4), and are shown in Fig.1 and 2.

Another parameter included in the conditions of bubble formation is the stopping power of the liquids for ions. It was calculated by the TRIM-code<sup>12)</sup>. The stopping power of ions emitted from interactions of neutrons with nuclei constituting Freon-12 are shown in Fig.3. The figure shows that the second condition (c2) is much more critical for a proton than for other ions. This is clearly depicted in Fig.4, for the stopping power for the lightest ion, carbon, and a proton, and the bubble formation conditions, (c1) and (c2) with  $a=1$ . The stopping power of OFP is also shown in the figure.

If a particle produced by radiation has the energy and stopping power in the hatched area(right of line (1) and above line (2) ) of the figure, it can grow to a visible bubble. In this figure the cross point of the line (2) and the stopping power curve determines the lower limit of energy for the bubble formation. Thus the lower limit of energy of carbon in Freon-12 or OFP is nearly 300 keV. The proton cannot form a visible bubble. The figure also indicates that  $E_c/\ell$  in (c2) must be lower than 0.53 Mevcm<sup>2</sup>/mg for a proton to form a visible bubble. The curves of  $(E_c, E_c/\ell)$  and the stopping power determines the lower limit of energy of an ion to form a visible bubble.

In fig. 5, the black and white circles are points  $(E_c, E_c/\ell)$  of Freon-12 and OFP respectively at  $T=5, 10, 15, 20, 25, 30, 35$ , and 40 °C. The curves are calculated with several values of  $a$ . The values decrease with increases in temperature. These curves and the stopping power for a proton are simultaneously shown in Fig.6. For a given temperature and  $a$ , a lower and an upper limit of energy for the bubble formation can be derived with this figure.

Gamma-rays emit electrons by interactions with atoms of the sensitive liquid and the supporting material where the liquid drops are dispersed. The primary electrons from the photoelectric effect, Compton scattering and pair creation, produce secondary and slowed-down electrons, which could form visible bubbles. In fig. 7 the electron stopping power is shown together with the

$(E_c, E_c/\ell)$ -curves<sup>13)</sup>. The energy range for the electrons to form visible bubbles is obtained in the manner as that for protons described above. In this case, Freon-12 could not detect electrons, and therefore would be insensitive to gamma rays. The OFP would be sensitive to electrons having  $(E_c, E_c/\ell)$ -points below the stopping power curve.

The parameter  $a$  or  $b$  is kept undetermined in this section. At present, we only have Harper's experimental value for this parameter,  $b=4.3(a \approx 1.2)$  for Freon-12 exposed to <sup>252</sup>Cf-neutrons<sup>11)</sup>. The value of  $a$  will be discussed in the next section.

#### 4. DISCUSSION AND CONCLUSION

d'Errico et al. reported that the superheated liquid drop detector(SDD vial, pen dosimeter, Apfe Enterprise co., sensitive liquid is Freon-12) was sensitive for 5.5 MeV protons at 25 °C and also stated that protons from the reaction <sup>35</sup>Cl(n,p)<sup>35</sup>S(Q=615 keV) contributed to bubble formation together with <sup>35</sup>S ions in thermal neutron irradiation. They explained that the number of bubbles first increased at 25-30 °C and became constant at 30-40 °C<sup>5)</sup>. The proton energy from <sup>35</sup>Cl(n,p)<sup>35</sup>S is nearly equal to 615 keV, and in Freon-12 the protons are slowed down and the energy may distribute from zero to 615 keV. For the visible bubble formation by all of these protons at 30-40 °C, the value of  $a$  must be about 5 and then  $E_c/(aR_c) \approx 0.2$  MeVcm<sup>2</sup>/mg from figure 7.

Applying  $a=5$  for OFP, we have  $E_c/(aR_c) \approx 0.1$  MeVcm<sup>2</sup>/mg at 20 °C. With this( $a=5$ ,  $E_c/(aR_c) \approx 0.1$  MeVcm<sup>2</sup>/mg at 20 °C), we may consider the energy region of electrons that form visible bubbles. From figure 7, only 1 keV electrons could form visible bubbles. If the temperature increases to 25 °C, the energy range extends to 0.5-2 keV. In gamma-ray irradiation, the bubble formation should be produced by these electrons in the sensitive liquid, some of which may be produced in the liquid and some of which may be produced in the supporting material and move into the liquid.

Koizumi measured the relative sensitivity of gamma rays to neutrons of the superheated liquid drop detector(BDG, use for gamma ray, BTI co.)<sup>14)</sup>. From the above discussion, it is likely that a detector which is sensitive to gamma rays is also sensitive to neutrons. Harper et al. found that hexafluoropropen(C<sub>3</sub>F<sub>6</sub>, boiling point=-29.4 °C) was sensitive to gamma rays<sup>6)</sup>. The boiling point of this liquid seems too high for bubble formation by the electron to be explained with our discussion.

To verify the considerations above, we should calculate detector sensitivities for protons and gamma rays and compare the calculations with corresponding measurements, which would establish the values of  $\ell$ ,  $a$ , or  $b$ , the size of the effective energy deposition, its characteristics and its validity.

### Acknowledgment

We wish to thank Mr. K.. Koizumi(PNC) for his valuable discussions.

### References

- (1)Seitz F.:Phys Fluids,1,2(1958)
- (2)Lo Y. & Apfel R.E.:Phys. Rev. A38,5260(1988)
- (3)Wang C.K.C.:Health Phys. 62, 215(1992)
- (4)Harper M.J. & Nelson M.E.:Rad. Prot. Dos., 47,535(1993).
- (5)d'Errico F. & Alberts W.G.:Rad. Orot. Dos., 54, 357(1994)
- (6)Harper M.J., Baker B.W. & Nelson M.E.:Health Phys., 68,670(1995)
- (7) T.Sawamura, T. Joji and H. Yamazaki:Proc. 9th Workshop Rad. Detector and Their Uses.,139(1995)
- (8)Apfel R.E.,Roy S.C. & Lo Y.C.:Phys. Rev., A31,3194(1985)
- (9)Bugg D.V.:Prog. Nucl. Phys. edit.by O.R. Frish (Pergamon Press,1958), vol7, chap.1
- (10)T.Sawamura and H. Yamazaki:Bulletin of the Faculty of Engineering, Hokkaido Univ.173,31(1995)(in Japanese)
- (11)Harper M.J.:Nuci. Sci. Eng.,114,118(1993)
- (12) Ziegler J.F. & Manoyan J.M.: Nucl. Inst. Meth. in Phys. Res.,B35,215, (1988)
- (13)Holt P.D.:p.42-48 in Charged Particle Tracks in Solids and Liquids(Proc. 2nd L. H. Gray Conf.,1969,Published by The Institute of Physics and The Physical Society Conference Series No.8)
- (14)K.Koizumi:Private communication(1995)

Table 1. Material parameters and calculated values  
for Freon-12 and octafluoropentane..

	Freon-12 $CC_{12}F_2$	octafluoropentane $C_3F_8$
molecular weight	120.9	188.02
boiling point at 1 atm	-29.8	-36.7
temperature $T$ (°C)=20		
vapor density $\rho_g$ (Kg/m <sup>3</sup> )	32.0	71.0
liquid density $\rho_l$ (Kg/m <sup>3</sup> )	1326	1370
vapor pressure $P_s$ (bar)	5.72	7.66
surface tension $\gamma$ (N/m)	$9.11 \times 10^{-3}$	$4.31 \times 10^{-3}$
heat of the vaporization $H_{fg}$ (J/mol)	19800	19500
critical radius $R_c$ (cm)	$3.87 \times 10^{-6}$	$1.30 \times 10^{-6}$
critical energy $E_c$ (keV) (2)	13.3	0.873
critical energy $E_c$ (keV) (3)	0.356	0.019
critical energy $E_c$ (keV) (4)	9.16	0.482
$E_c / R_c$ (MeVcm <sup>2</sup> /mg), $E_c$ (2)	2.60	0.492

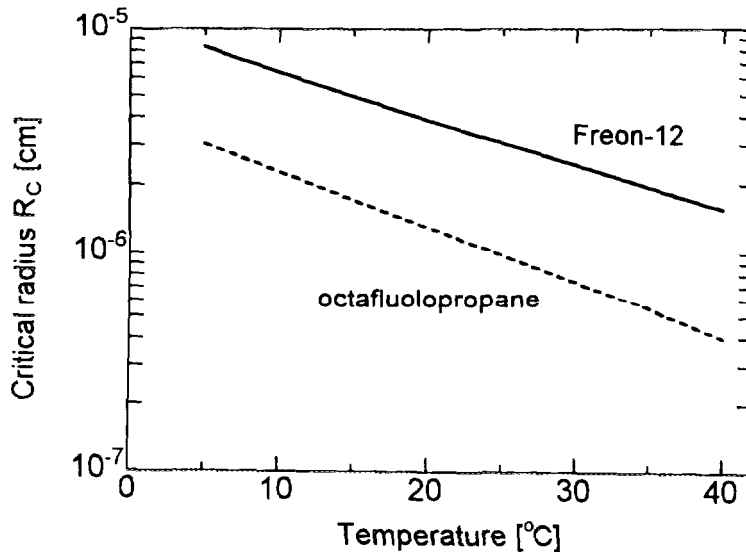


Fig.1 Critical radius  $R_c$  vs. Temperature  $T$ .

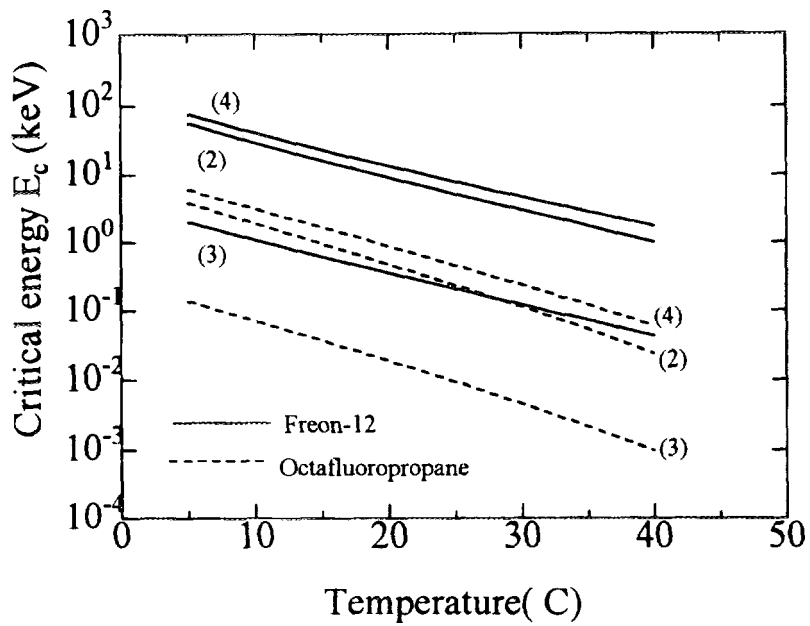


Fig.2 Critical energy  $E_c$  derived by eq.(2), (3) and (4) vs. Temperature  $T$ .

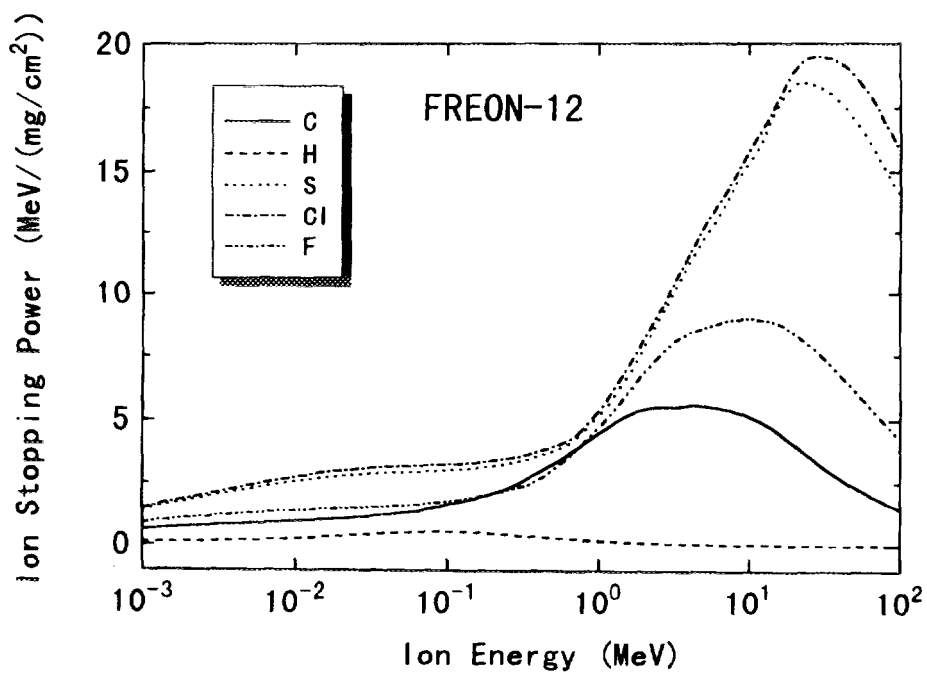


Fig.3 Stopping Power of freon-12 for ions

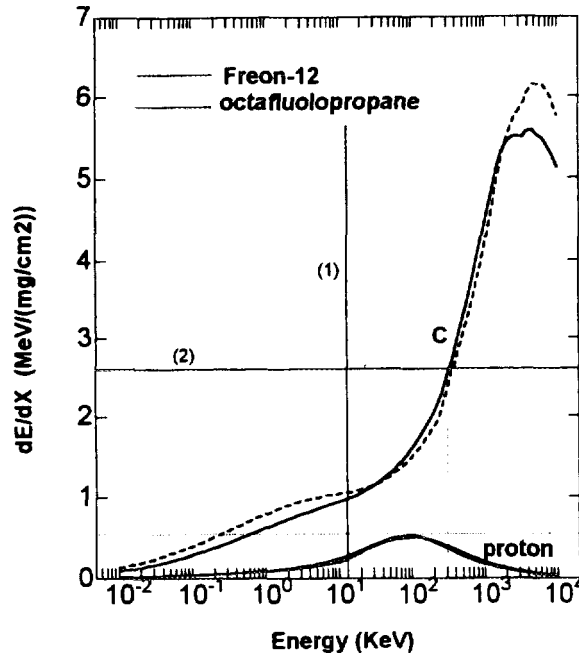


Fig.4 Stopping power of Freon-12 and PFO for  $^{12}\text{C}$  and proton

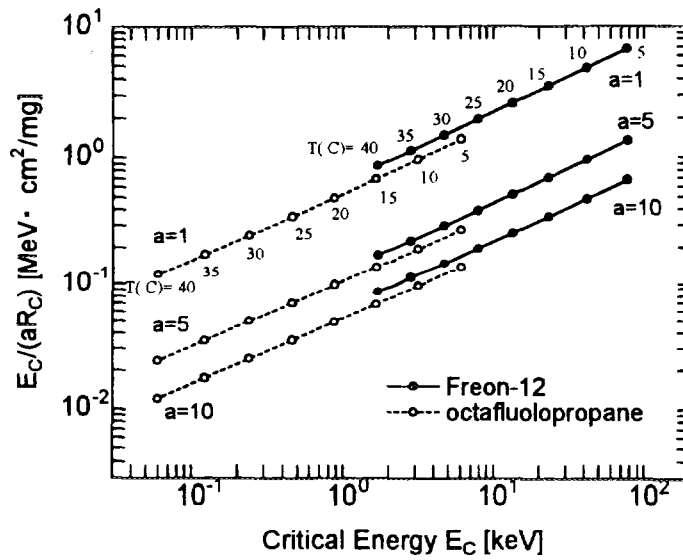


Fig.5  $E_c/(aR_c)$  vs.  $E_c$ .

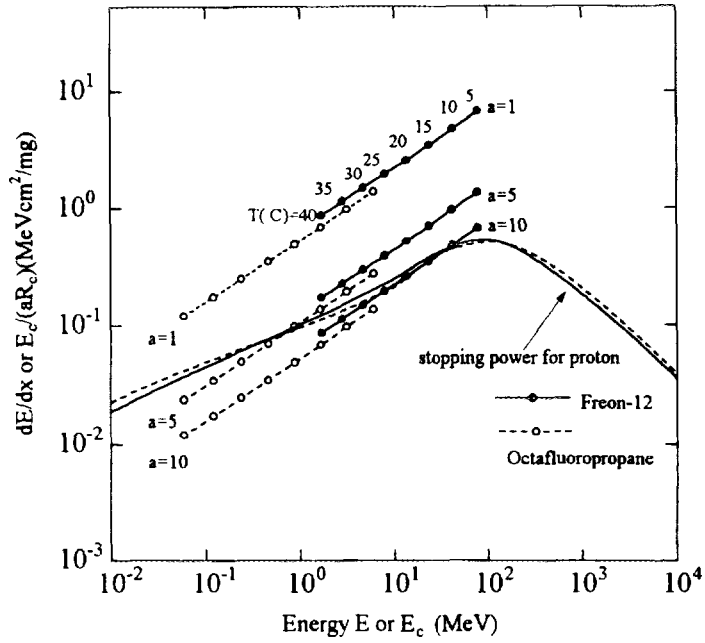


Fig.6 ( $dE/dx$ ) for proton &  $E_c/(aR_c)$  as a function of energy

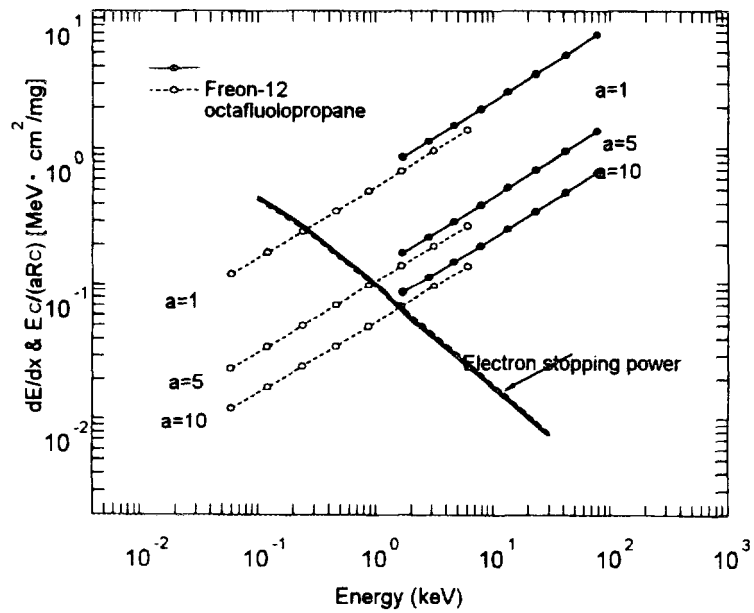


Fig.7 ( $dE/dx$ ) for electron &  $E_c/(aR_c)$  as a function of energy

# Triton, Deuteron and Proton Responses of the CR-39 Track Detector

Tomoya YAMAUCHI, Hiroyoshi MATSUMOTO and Keiji ODA

Department of Nuclear System Engineering,  
Kobe University of Mercantile Marine

## 1. INTRODUCTION

In recent years, several types of copolymer of the CR-39 plastic with higher sensitivity have been developed as new track detectors<sup>(1,2)</sup>. Etchable tracks of proton were recorded even at an incident energy of 20 MeV in some of these detectors<sup>(3)</sup>. Hence, there is an increasing interest in applying these new track detectors not only to space dosimetry but also for neutron dosimetry using recoiled proton and deuteron, or generated triton<sup>(4)</sup>. More precise measurements of emitted particles in some fusion experiments will be possible using these detectors<sup>(5)</sup>.

For these applications of the track detector, precise response data of hydrogen isotopes are required. Few calibration studies, however, have been made for triton and deuteron<sup>(6-8)</sup>. Furthermore, even for proton, calibration data at near the track end-point have never obtained completely, because the fact that the response should vary rapidly along particle trajectory at low incident energy is not well taken into account for the response analysis. Then we must develop the suitable method for the response calibration of track detector to hydrogen isotopes with energies of a few MeV.

In the present study, we assessed the response of the CR-39 detector to proton, deuteron and triton from their etch-pit growth curves obtained by multi-step etching technique<sup>(9,10)</sup> and the difference among their track registration properties was discussed. In order to avoid incorrect evaluation due to the missing track effect<sup>(6,11)</sup>, particle irradiation was performed at various incident energies. The response function,  $S(R)$ , etch rate ratio,  $S$ , as a function of the residual range,  $R$ , was experimentally evaluated for all hydrogen isotopes by this method. In the next, we obtained another form of response functions of  $S(E)$ ,  $S(\beta)$  and  $S(LET_{200})$ , which were presented as functions of the particle energy,  $E$ , the particle velocity,  $\beta(=v/c)$ , and the linear energy transfer in the case where the cut-off energy is 200 eV,  $LET_{200}$ , respectively. These information will be useful also

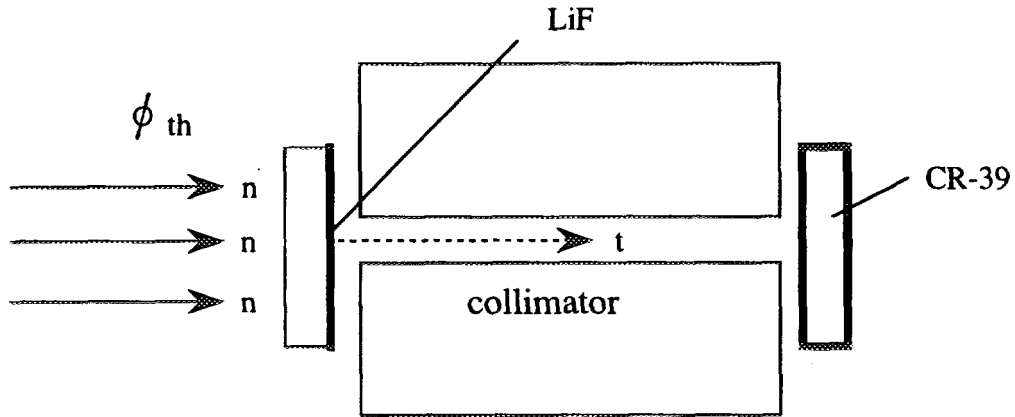


Fig. 1. Schematic view of neutron-to-triton convertor.

in understanding the fundamentals of the latent track formation mechanism in the plastic track detectors.

## 2. EXPERIMENTALS

### 2.1. Irradiation of Hydrogen Isotopes

Proton and deuteron irradiation was made at normal incidence on the CR-39 samples (BARYOTRAK, Fukubi-Kagaku, Japan) using a tandem Van de Graaff accelerator in Kobe University of Mercantile Marine. Selected incident energies were 0.4, 0.7 and 1.0 MeV for proton and 0.8 and 1.7 MeV for deuteron. Pulsed beams were used to attain the suitable etch-pit density of about  $10^3$  pits/cm<sup>2</sup>.

Because tritium is radioactive ( $\beta^-$  emitter), it is not permitted to accelerate it as an ion beam in this system by the limitation of radiation protection. Then we tried to perform the triton irradiation using  ${}^6\text{Li}(n,t){}^4\text{He}$  reaction in the thermal neutron field at Heavy Water Facility in Kyoto University Research Reactor. Figure 1 shows the schematic view of neutron-to-triton convertor used in this work.  ${}^6\text{Li}$  enriched LiF thin-film with a thickness of about  $0.2\ \mu\text{m}$  is coated on Si substrate. Generated triton were collimated and hit on the CR-39 plastic with an incident energy of 2.7 MeV in vacuum condition. To obtain the lower energy triton, the polyethylene films with a thickness of about  $20\ \mu\text{m}$  were mounted on the samples surface, which stopped the incidence of alpha-particles, and the surroundings was substituted to  $\text{CO}_2$  gases from the air in order to suppress the contaminous proton incidence by  ${}^{14}\text{N}(n,p){}^{14}\text{C}$  reaction. Triton with an energy of about 1.2 MeV was obtained in this condition<sup>(8)</sup>.

## 2.2. Multi-step Etching Technique

Irradiated samples were chemically etched in a stirred 6N-KOH solution at 70 °C. About 10 etch-pits were selected on every samples to course their growth with etching. The etching procedure was stopped every 10 minutes and dimensions of the etch-pits were measured on a TV monitor showing an optical-microscopic picture. These process was repeated until the etch-pits were fully over-etched. The thickness of layer removed was monitored by the track radius of fission fragments from a  $^{252}\text{Cf}$  source on the same surface of the sample. The bulk etch rate was found to be about 2.4  $\mu\text{m}/\text{h}$  and it was constant within experimental error. This multi-step etching process gives us a variation of etch-pit radius with the thickness of layer removed, called a growth curve.

Figure 2 shows typical etched surface of the CR-39 samples irradiated by 2.7 MeV triton at indicating etching steps. Two type of etch-pits are observed. Triton etch-pits are small ones at the center of the pictures and other two large etch-pits at the left-side are those of 2.1 MeV alpha-particles simultaneously generated with triton through neutron reaction with  $^6\text{Li}$ . It is easy to distinguish the etch-pits of triton from those of alpha-particles, as shown in these photographs. It was impossible, however, to discriminate etch-pits of triton from those of proton or deuteron.

## 3. RESPONSE FUNCTION OBTAINED FROM GROWTH CURVE

### 3.1. Response against Residual Range

Through the multi-step etching process, we obtained the growth curves of hydrogen isotopes with various incident energies. Typical growth curves of triton are shown in Fig.3. The triton ranges,  $R_0$ , with incident energies of 1.2 and 2.7 MeV were assessed from the shape of growth curves in spherical phase and found to be 15.2 and 48.1  $\mu\text{m}$ , respectively<sup>(9,10)</sup>. Ranges of proton and deuteron were also assessed in the same manner and they are found to be in agreement with the theoretical values<sup>(12)</sup>.

The response was reconstructed from the shape of growth curve in the both of the conical and the transition phase, based on the following fundamental relation,

$$S(R) = \frac{1 + g^2}{1 - g^2}, \quad (1)$$

$$R = R_0 - \left[ G - r \frac{1 - g^2}{2g} \right], \quad (2)$$

where  $G$  is the thickness of layer removed,  $r$  is the etch-pit radius at  $G$ , and  $g$  is the growth rate of  $r(g = dr/dG)$ . In analyzing the growth curves, the best-fit polynomial

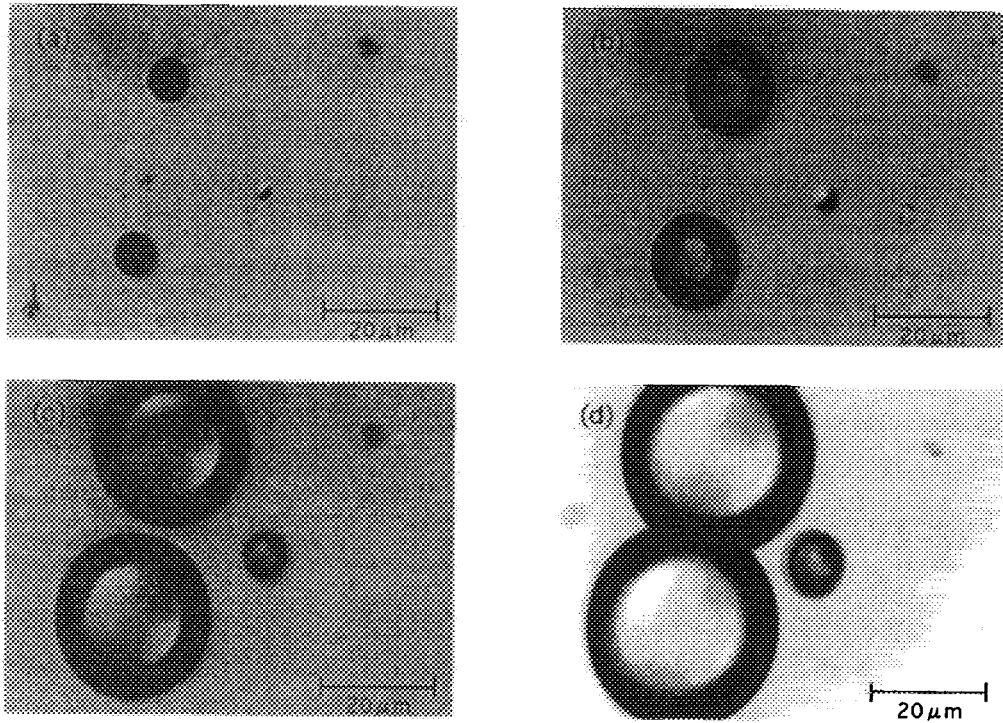


Fig. 2. Photographs of the etched CR-39 surface irradiated using  ${}^6\text{Li}(n,t){}^4\text{He}$  reaction in vacuum. G: thickness of layer removed. (a)  $G=5.0\mu\text{m}$ , (b)  $G=10.0\mu\text{m}$ , (c)  $G=20.0\mu\text{m}$ , (d)  $G=30.0\mu\text{m}$ .

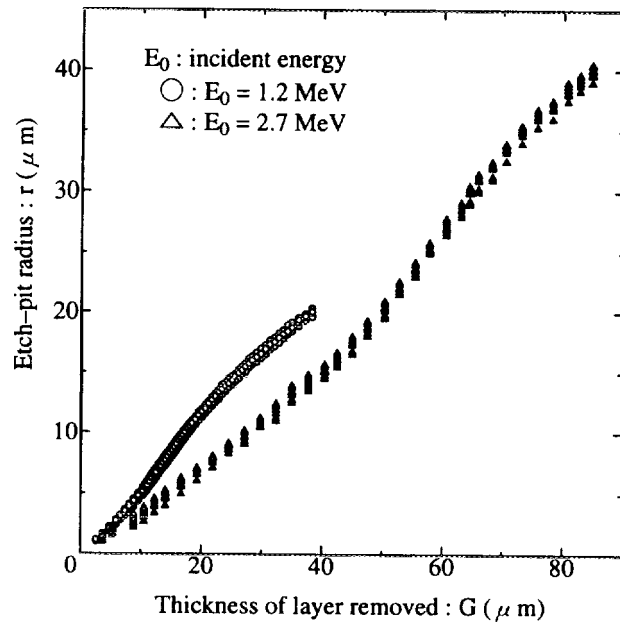


Fig. 3. Growth curves of triton etch-pits with incident energies of 1.2 and 2.7 MeV.

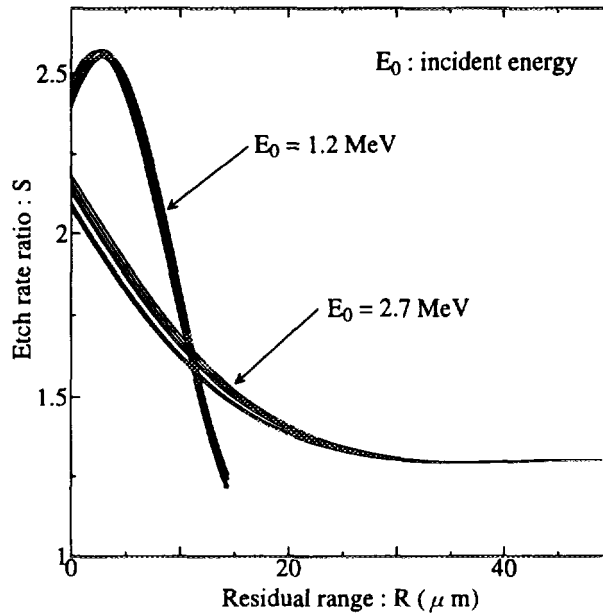


Fig. 4. Response curves of triton.

was obtained firstly. Then the growth rate was calculated by differentiating it and the response was calculated as a function of the residual range according to eqs.(1) and (2).

Figure 4 shows the response curves of triton calculated from growth curves shown in Fig.3. Many curves were derived from the choice of the etch-pit and the used fitting function. As shown in this figure, The curves for the same incident energy are close one another. There is, however, a serious disagreement between the two groups of curves with different incident energy. The curves for 1.2 MeV have a peak of response at a residual range of about  $3 \mu\text{m}$ , but the curves for 2.7 MeV have no peaks and have etch rate ratio at such short residual ranges. This disagreement has already shown to be caused by the missing track effect<sup>(6)</sup>. Because of this effect, the response at the short residual ranges never reflects on the shape of growth curve at above a certain incident energy<sup>(6,11)</sup>. Namely, for 2.7 MeV triton, response near the track end-point, in principle, cannot be evaluated from the growth curves. Then we regard the curves for 1.2 MeV show the real response at residual ranges less than  $11 \mu\text{m}$ , which is the intersection of the two groups of curves. On the other hand, above the intersection, the response for 1.2 MeV are lower than those for 2.7 MeV. This is considered to be caused by a surface effects of the presence of the induction layer. Consequently, curves for 2.7 MeV are regarded to be closer to the real one at residual ranges above the intersection.

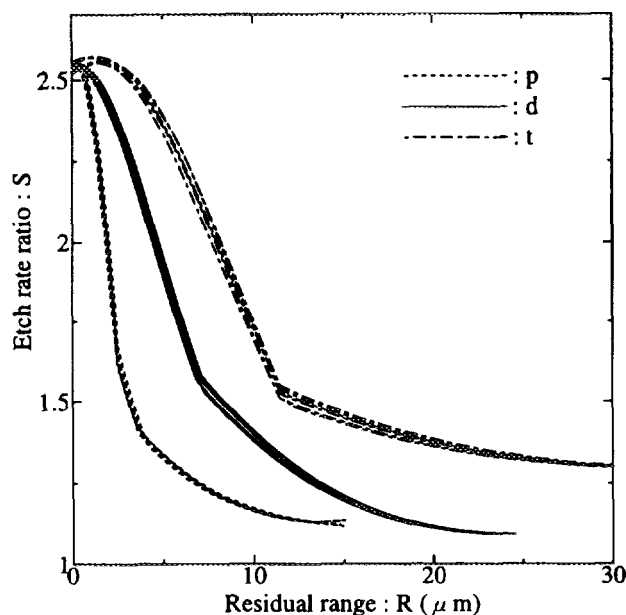


Fig. 5. Response function of the CR-39 detector to energetic hydrogen isotopes against residual range.

Similar response analysis were also made for the CR-39 samples irradiated by proton and deuteron. Figure 5 shows the obtained response of the CR-39 detector for the all hydrogen isotopes as a function of residual range. Two or three bends on each curves arose from the connections of response curves with different incident energy above mentioned. These is a significant difference in the shape of response curves among the isotopes, especially in the width of the response peaks near the track end-points corresponding to the Bragg's peaks. The width of the peak increases in the order of proton, deuteron and triton. This is compatible with theoretical assessment on the response distribution along the particle trajectory. The space resolution of the track registration characteristic of the CR-39 detector was found to be enough to detect the difference of the damage distribution along trajectory between hydrogen isotopes. This indicates the potential application of the CR-39 detector for the separate measurement of the energetic hydrogen isotopes.

### 3.2. Response Functions in the Other Forms

On the basis of the relation between the incident energy and the range<sup>(12)</sup>, we obtained the another forms of response curves represented against the particle energy,  $E$ , and particle velocity,  $\beta(= v/c)$ . Response curves against particle energy are shown in Fig.6.

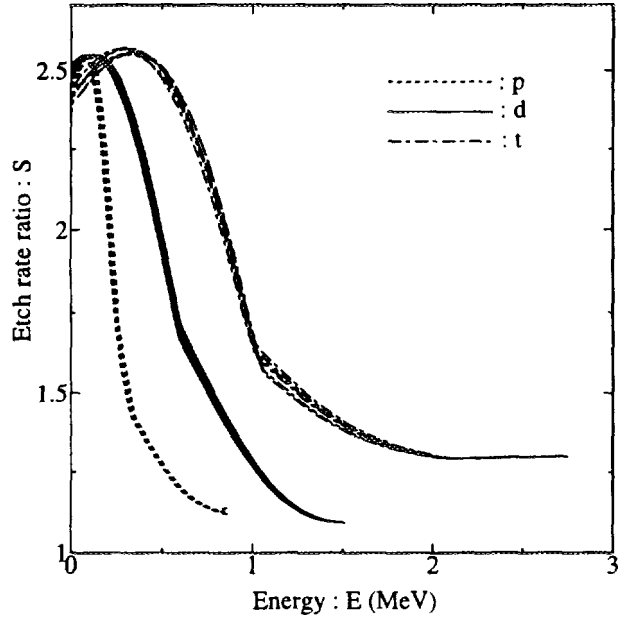


Fig. 6. Response function of the CR-39 detector to energetic hydrogen isotopes against particle energy.

As shown in this figure, difference of response curves between hydrogen isotopes are also observed in this form. On the contrary to this, as shown in Fig.7, the response curves of the isotopes represented against particle velocity  $\beta (= v/c)$  are close to one another. This implies that the difference appeared in the response curves indicating against residual range and particle energy, shown in Fig.5 and Fig.6, are mainly caused by the difference in mass of the hydrogen isotopes.

Figure 8 shows the response curves against  $LET_{200}$  for hydrogen isotopes and alpha-particle. Response curves for hydrogen isotopes are found to be close each other also in this form. This indicates that  $LET_{200}$  has good correlation with the response for hydrogen isotopes. Nevertheless, the response for alpha-particle is larger than those for hydrogen isotopes at above the  $LET_{200}$  of  $70 \text{ keV}/\mu\text{m}$ . For triton, this region of  $LET_{200}$  corresponds to the residual ranges less than  $8 \mu\text{m}$ , in where the response has the peak value. It seems to indicate the existence of particular mechanism on the latent track formation near the track end-point of hydrogen isotopes. Further investigations are need on the difference of the response between hydrogens and alpha-particle.

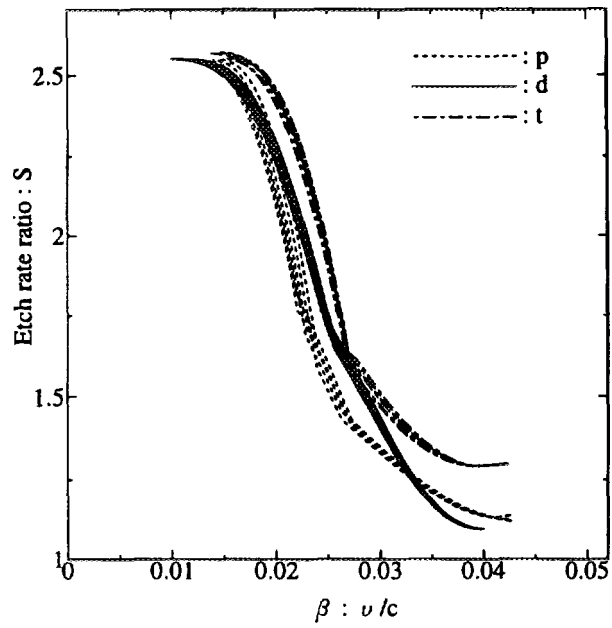


Fig. 7. Response function of the CR-39 detector to energetic hydrogen isotopes against particle velocity.

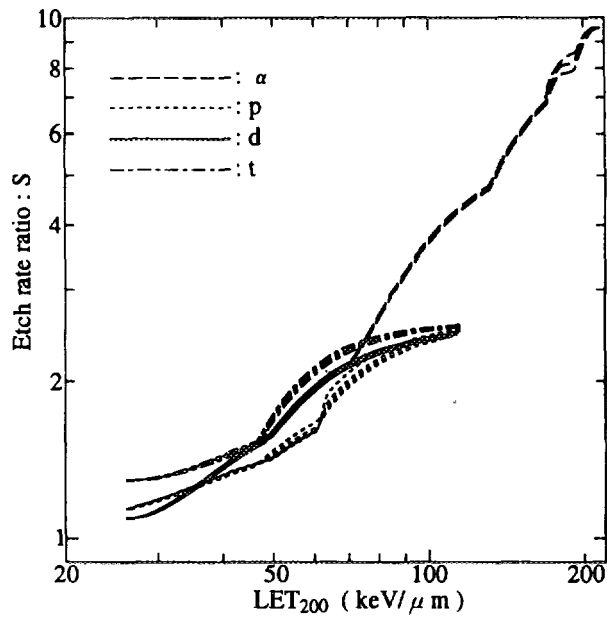


Fig. 8. Response function of the CR-39 detector to hydrogen isotopes and alpha-particle against  $LET_{200}$ .

#### 4. CONCLUSIONS

Comprehensive investigations were made for the response of CR-39 track detector to proton, deuteron and triton at energies of a few MeV. The response were assessed from their etch-pit growth curves obtained by multi-step etching technique. In order to avoid the incorrect evaluation due to the missing track effect, particle irradiation was performed at various incident energies. The obtained responses were summarized as the response function,  $S(R)$ , which were plots of the etch rate ratio,  $S$ , against the residual range,  $R$ . A clear difference was observed in the shape of the response function of among hydrogen isotopes. This implied the potential of discriminative measurement of energetic hydrogen isotopes using CR-39 track detector. Response functions in other forms were also obtained indicating as functions of particle energy,  $E$ , particle velocity,  $\beta(=v/c)$ , and linear energy transfer,  $LET_{200}$ . Difference of response was also observed in the function of  $S(E)$ , but not in  $S(\beta)$ . This indicates that the difference in the form of  $S(R)$  and  $S(E)$  were caused by the difference in mass of the isotopes. In the form of  $S(LET_{200})$ , response of hydrogen isotopes were also close one another, but they had significantly lower values of etch rate ratio than that of alpha-particle at the short residual ranges. These information will be useful also in understanding the fundamentals of the latent track formation mechanism.

#### REFERENCES

- (1) M. Fujii *et al.* (1993). Nucl.Tracks Radiat.Meas.,22,pp.199-204.
- (2) K. Ogura *et al.* (1995). Radiation Measurements,25,pp.159-162.
- (3) K. Ogura (1995). 12th Symposium on SSNTD, Waseda University.
- (4) K. Oda *et al.* (1991). Nucl.Inst.Meth.,B16,pp.302-308.
- (5) H. Azechi *et al.* (1986). Appl.Phys.Lett., 49,pp.555-557.
- (6) T. Yamauchi *et al.* (1995). Radiation Measurements,24,pp.101-104.
- (7) M. Sadowski *et al.* (1995). Radiation Measurements,25,pp.175-176.
- (8) T. Yamauchi *et al.* (1996). Proc. 30th Symposium in KURR.pp.229-238.(in Japanese)
- (9) G. Somogy (1980). Nucl.Instrum.Meth., 173,pp.21-42.
- (10) K. Oda *et al.* (1992) Nucl.Tracks Radiat.Meas.,20,pp.505-510.
- (11) T. Yamauchi *et al.* (1995) KEK Proc. 95-1,pp.97-106.
- (12) E.V. Benton and R.P.Henke (1969) Nucl.Inst.Meth.,67,pp.87-92.

# CHARGE SENSITIVE AMPLIFIER

The state of Arts

Kunishiro Mori

Clear Pulse Co., Chuo 6-26-8, Otaku, Tokyo, 143 Japan

## 1. INTRODUCTION

In general, roles of electronic system for measuring energy spectrum of radiation are to extract signals produced by radiation from a detector, to amplify those and to achieve the better signal to noise(S/N) ratio of those through a filter circuit with an appropriate band-width. where it is essential not to deteriorate signal amplitudes. In the radiation detectors, signals are essentially charges produced by radiation, then it is naturally the best way to use a charge sensitive amplifier (CSA) system to extract those signals. The CSA is thought to be the best amplifier suitable to almost all the radiation detectors, neglecting economical points of view.

The CSA has the history of 30 years since it had been introduced for radiation measurements. An operational amplifier was introduced to Japan for the first time in 1960<sup>th</sup>. Since that time, the operational amplifiers have been rapidly applied to electronic instruments in various fields from DC amplifiers and high-frequency amplifiers to audio-products. On the other hand, the CSA has been only applied to special fields like radiation detection because the concept of "charges" is not so universal against the concepts of "voltage" and "current". The CSA, however, is low noise and high speed amplifiers and might be applicable not only to radiation measurements, but also piezoelectric devices and also bolometers.

In this article, I briefly describe about noise in the CSA in section 2. The basic circuit on the CSA are introduced in section 3. In section 4, the concept of "equivalent noise charges" (ENC) is introduced and a method for measurements of the ENC is shown. In section 5, I explain about the importance of the "open-loop gain" in the CSA to achieve better performance of it and how to realize in a practical CSA. I also touch to characteristics on a counting rate of the CSA in section 6 and to various circuit used in the CSA in section 7. The CSAs which are commercially available at present and the special purpose CSAs are introduced in section 8.

## 2. Noise

There are two types of noise in the CSA, with which we encounter in amplifying signals produced by radiation. One is the noise which originate in nature from fluctuation of carriers in electronic devices and parts. The other noise result from external sources such as switching noise from SCRs and/or switching regulators, micro-phonics, and mechanical vibrations. The latter is sometimes superposed on signals through various routes and deteriorates results in measurements. The generation of those noise should be naturally suppressed at the sources, but we always confront with picking up those in any electronic amplifying system. Normally, it is so difficult to avoid picking up those noise in the CSA and is no exaggeration to say that we have to make bests suppress those case by case. The noise which originate from fluctuation of carries in devices is described briefly, because it affects on designing amplifiers.

### 2-1. Thermal noise

The thermal noise originate from irregular motion of thermally excited carriers in conductors. The irregular motion of carriers arises small current pulses in the conductors. Those current induce electromotive force between the both ends of the conductor because of its resistance. This kind of noise is called as white noise, since the frequency distribution is constant all over the frequency. The thermal noise is expressed with a source of the electromotive force  $E_t$  connected with the resistor  $R_L$  in series by an equivalent circuit as shown in Fig. 1. The mean square voltage of the thermal noise is expressed by a following equation.

$$E_t^2 = 4kTR_L \Delta f. \quad (1)$$

where  $k$  is the Boltzmann constant ( $1.38 \times 10^{-23}$  J/K),  $T$  the absolute temperature, and  $\Delta f$  the unit frequency. From the Eq.(1), the mean square voltage of the thermal noise infinitely increases according to the resistance,  $R_L$ . However, in a practical circuit, capacitance exists in parallel to the resistor  $R_L$  as shown in Fig.2, and limits the noise. The noise at a low frequency region gives rise to large effects on the output voltage of noise  $E_{no}$  and those at a high frequency region have less effects because of the capacitance  $C$ . The  $E_{no}$  increases as the  $R_L$  increases, but that decreases at a high frequency region, since the cutoff frequency decreases.

### 2-2. Input current noise

Fluctuation of leakage current at the gate of junction-type field effect transistors (JFET) and also of semiconductor radiation detectors gives rise to the input current noise at the input

resistance  $R_i$ . The mean square noise is written as follows:

$$V_e^2 = 2qIR_i^2\Delta f, \quad (2)$$

where the  $q$  is unit electronic charge ( $1.6 \times 10^{-19}$  C) and  $I$  the current. In this equation, the  $V_e$  also increases as the  $R_i$  increases as of the thermal noise. However, the effects are also same as those in the thermal noise because of the existence of capacitance parallel to the  $R_i$ . In order to decrease this kind of noise at the CSA, it is necessary to select a JFET with low leakage gate current.

### 2-3. Shot noise

Shot noise originates from fluctuation of current, such as the drain current of JFETs, the collector current of transistors, and etc.. The mean square noise current is given by the following equation,

$$i_s^2 = 2qI\Delta f. \quad (3)$$

The mean square noise current can be converted to the mean square noise voltage by an equation,

$$V_s^2 = 2qIGm^{-2}\Delta f, \quad (4)$$

where the  $Gm$  is transconductance of the transistor expressed by the emitter resistance,  $r_e$ , as follows:

$$Gm = 1 / r_e = qI / kT. \quad (5)$$

Then, the mean square noise voltage is rewritten again as follows:

$$V_s^2 = 2kT\Delta f / Gm = 4kT\Delta f / 2Gm = 4kTR_{eq}\Delta f. \quad (6)$$

Namely, it is equivalent to the thermal noise in a resistor  $R_{eq}$  inserted into the circuit.

On the other hand, there does not exist the shot noise in an uniform conductor like the FET, because the shot noise arises from the current flowing through a potential barrier such as pn-junction in transistors and a surface barrier of the cathode in vacuum tubes. However, there exists a kind of the thermal noise, which originates from modulation of a conduction channel width in FETs and is written in the same manner as the shot noise.

$$V_s^2 = 4kTR_{eq}\Delta f, \quad (7)$$

where the  $R_{eq}$  is equal to  $0.7 / Gm$ . From the Eq.(3), the noise current of the shot noise is proportional to square root of its band-width and then the noise power spectrum is constant. This is also a kind of the white noise. In order to decrease effects due to the shot noise to the CSA, there may be no way except finding suitable semiconductor devices from a view point of the transconductance.

### 2-4. Low frequency noise (1/f noise)

The low frequency noise has a power spectrum inversely proportional to the product of frequency and power  $\alpha$ . Normally, the  $\alpha$  is equal to unity and is therefore called 1/f noise. The 1/f noise is commonly observed in almost all devices. It is sometimes called as pink noise, flicker noise or semiconductor noise. The  $\alpha$  is normally unity as mentioned above, but depends on devices. In the case of  $\alpha = 2$ , the noise is called as red noise. The excess noise, as described later, is also the same kind of this noise. In the JFET, the 1/f noise is small and this is a reason why it is used to the CSA. On the other hand, the MOSFET has a large 1/f noise. Then, it is not normally used to the CSA.

### **2-5. Excess noise**

The excess noise is originally a kind of the 1/f noise. Here, It is specially described here, because we are sometimes conflict with this noise in practical circuit. This noise originates from devices superposed on the thermal noise. The name, excess noise, stems from that reason. The noise originates from a resistor into which current flows. Especially resistors made of carbon black, which is not an uniform conductor, become the noise sources. The noise is thought to be originated from discharges between small grains of carbon. The same originates from phenomena on the surface of the semiconductors. This type of is negligible in metal film resistors and also wired resistors. It is possible to make effects from the excess noise smaller by selecting sorts of semiconductor devices, the feed-back resistors and the load resistors for biasing in the CSA.

### **2-6. Noise due to dielectric loss of capacitors**

The dielectric loss of capacitors is one of the noise sources in low noise amplifiers. The noise originates as parallel noise charges as described later (see the third term of the right side in Eq.(3) in section 4). The coupling condenser  $C_c$  and insulating material around the input of FET should be material with low dielectric loss. For example, capacitors made of low dielectric loss material such as polystyrene, Teflon or polypropylene as the coupling capacitors can be expected to lead to good results. Mica or mylor capacitors are unexpectedly a large noise source, and are not recommended to use for the CSA.

### **2-7. External noise**

In order to operate the CSA at the best performance, it is of importance to use the CSA

under well-understood environments from a view point of the external noise. For example, It happens frequently that the coaxial cables, which connect between the CSA and a detector or a test pulser, pick up the external noise because of its insufficient net shield. Furthermore, the earth points themselves are sometimes noisy around the measurement system. In these cases, good results may be sometimes achieved by connecting the earth point near the CSA input to an earth copper board which is spread out for shielding the electronic system. It is also an important factor to shield the noise which is generated by power supplies with switching regulators, personal computers and CRTs which may exist around the experimental apparatus. It may be a mostly effective way to avoid picking up the noise by separating the AC line for the measurement system from the lines for those, and furthermore to put a noise cut transformer and a filter circuit for the DC power line. In the case that a pulse height analyzer (PHA) is used, it is recommended to wound a coaxial cable several times on a amorphous ring in order to connect a shaping amplifier output to the PHA input, because it is also a noise source.

### 3. Principle of the charge sensitive amplifier

The basic circuit of the CSA is composed of an operational amplifier as shown in Fig.3 (a). In this circuit, the output voltage increases stepwise as any charge signal inputs, and finally saturates because it reaches out of range of the amplifier. Then, it is necessary to discharge accumulated charges on the feed back capacitor  $C_f$  by a switch or to feed a same amount of charges with the opposite sign into the input in order to recover the operation of the CSA. However, the number of parts in the CSA is essentially minimum and the signal to noise ratio become excellent in this case. The circuit in which a feedback register  $R_f$  puts in parallel to the  $C_f$  is shown in Fig.3 (b). In this circuit, the output voltage decreases exponentially from its peak value  $E_{out}$  with a decay time constant of  $\tau (C_f \times R_f)$  sec and the S/N ratio slightly increases as the thermal noise arise in the  $R_f$ .

The coupling method of the CSA to a detector is shown in Fig.4, (a) and (b). The DC coupling is used as shown in Fig.4,(a), when leakage current at the detector is quite low. However, the AC coupling is normally used to connect the detector through a  $C_e$  in order to cut the detector biasing voltage and to feed only charges to the input of the CSA. The CSA, which is built up by an operational amplifier with a JFET at the input stage, has disadvantage at the S/N ratio compared with a single ended type circuit with an FET as shown in Fig.5, nevertheless it of course works properly. The noise in the CSA with the operational amplifier is a square root of 2 times larger than one of the single ended type CSA even if the same JFET is used because the operational

amplifier has two differential inputs, namely is equivalent to have two FETs at the input. Then, the single ended type circuit has advantage at the S/N ratio. The single ended type CSA is possible to build only by three transistors as shown in Fig.5. This circuit is so simple and is operated fairly well. The JFET  $J_1$  is coupled to a PNP transistor  $Q_1$  by the so called cascode connection and those function just like an transistor. Therefore, characteristics of the  $Q_1$  is also of importance such as those of the  $J_1$ . Noise figure, transition frequency ( $f_T$ ) and capacitance ( $C_{ob}$ ) of the  $Q_1$  are good parameters for its selection. Since the  $Q_1$  is operated as the common base, the drain voltage of the  $J_1$  is fixed at 0.6 to 0.7 volt higher than one of the base of the  $Q_1$ . It is therefore possible to avoid the decrease of the gain at a high frequency region due to Miller effect, which is depend on the capacitance between the gate and the drain of the  $J_1$  by fixing the drain voltage. A summed current of the drain current due to signals and the current in the load resistor  $R_2$  flows through the  $R_1$ . It is natural to make the drain current larger in order to increase transconductance ( $G_m$ ) of the JFET. In a case that the drain current is much larger than current in  $R_2$ , the drain current can be determined as follows:

$$\text{The drain current} = (V_A - V_1 + 0.7) / R_1, \quad (8)$$

where the  $V_A$  is the voltage of the positive power supply as shown in the Fig.5. Using this relation, it is possible to tune the drain current of the  $J_1$  at any value. Generally, the transconductance  $G_m$  increases as the drain current increases. However, the self-heating of the JFET results in the increase of the gate current and eventually increases the noise. It is necessary to determine the optimum drain current by measurements. The gain of the circuit A is written as follows:

$$A = G_m \times R_2. \quad (9)$$

It is possible to increase the gain A by increasing resistance  $R_2$ , but its frequency response is deteriorated by the capacitance existed between the collector of  $Q_1$  and the base of  $Q_2$ . The voltage of the base of  $Q_1$  is a parameter to determine maximum amplitude of positive going voltage. If the saturation amplitude with the positive polarity is necessary to be larger, it is possible to do that by increasing the base voltage of the  $Q_1$ . However, this results in an increment of the drain voltage of  $J_1$ . Generally, the gate current of the JFET increases according to the increase of the drain voltage. Then, this leads to increase the noises of the JFET. Furthermore, the  $G_m$  decreases if the drain voltage is reduced under the pinch-off voltage of the JFET. It is an important point not to make the drain voltage too higher if the CSA is required to operate at low noise because the noises increases due to the close correlation between the drain voltage and the gate current at the JFET mention above.

#### 4. Noise of the charge sensitive amplifier

The equivalent noise charges (ENC) of the CSA is expressed as follows:

$$\overline{ENC^2} = \overline{ENC_s^2} + \overline{ENC_p^2} + \overline{ENC_{1/f}^2} \quad (10)$$

$$\begin{aligned} &= \frac{1}{2} \overline{e_n^2} C_{in}^2 \int_{-\infty}^{\infty} \left\{ [w'(t)]^2 + \left[ \frac{1}{\tau_{in}^2} w(t) \right]^2 \right\} dt \\ &\quad + \frac{1}{2} \overline{i_n^2} \int_{-\infty}^{\infty} [w(t)]^2 dt \\ &\quad + \frac{1}{2} A_f C_{in}^2 \end{aligned} \quad (11)$$

$$= \frac{1}{2} \overline{e_n^2} C_{in}^2 F_1 + \frac{1}{2} \overline{i_n^2} F_2 + \frac{1}{2} A_f C_{in}^2. \quad (12)$$

$$\overline{e_n^2} = 4 k T R_s = 4 k T \frac{0.7}{g_m}. \quad (13)$$

$$\overline{i_n^2} = 4 k T \frac{1}{R_p} + 2 q_s I_o. \quad (14)$$

$$A_f C_{in}^2 \sim 4 k T (D \cdot C_d). \quad (15)$$

where  $ENC_s$  means the series noise,  $ENC_p$  the parallel noise, and  $ENC_{1/f}$  the  $1/f$  noise,  $W$  and  $W'$  the weighting function and its time derivative,  $\tau_{in}$  the time constant which is determined with the input capacitance  $C_{in}$  and the feed-back resistance  $R_f$ ,  $e_n$  the noise voltage which originates from an equivalent series noise resistance ( $1/G_m$  in the FET),  $i_n$  the noise current due to an equivalent parallel noise resistor (thermal noise) and the input current (shot noise),  $A_f$  the mean square voltage, which is determined from the spectral density of the  $1/f$  noise,  $i_o$  the leakage current of the gate current of the FET,  $R_p$  the resultant resistance of resistors connected to the input,  $D$  the constant of the dielectric loss of capacitors connected into the input, and  $C_d$  the input capacitance.

In Eq.(10), the first term on the right side is expressed with an equivalent series noise resistance and relates to the input capacitance and the  $G_m$  of the JFET. This noise can be reduced by increasing the  $G_m$  of the JFET. The second term is dependent on a resistor connected to the input and the leakage current of both the JFET and the detector. The third term is equivalent noise charges which are depend on the  $1/f$  noise and on the dielectric loss of the input capacitance. The  $1/f$  noise is negligible in the JFET, but is not always negligible in the MOSFET and the vacuum tube. These equations stand for the case that the response of a shaping circuit to an input of the

step function shows the triangular wave form with a peaking time of  $t_p$ . In this case, the  $F_1$  and the  $F_2$  in eq.(11) are equal to  $2/t_p$  and  $2t_p/3$ , respectively. However, the noise width due to a shaping circuit with a single differentiation and four integration is only several % worse than that due to the triangular shaping. Normally, the  $t_p$  can be regarded to be a product of the time constant CR and the integration times. From these equations, the noise of the CSA is understood to depend on the characteristics of the JFET, and the resistance and the capacitance connected to the input of the JFET including those of the detector, the cable and their dielectric loss, and the leakage current of the detector.

A basic assembly of circuit for measuring noises in the CSA is shown in Fig.6. The ENC is calculated from the  $V_{SCA}$  and the  $V_p$  measured by the assembly of Fig.6 in the following manner,

$$ENC = \frac{V_{SCA} \times C_T \times V_T \times 2.35 \times K}{V_F \times 1.6 \times 10^{-19}} \quad (16)$$

$$K_{Si} = 3.6$$

$$K_{CdTe} = 4.5$$

$$K_{Ge} = 2.95$$

$$V_{SCA} = \sqrt{(V_N)^2 - (V_M)^2}$$

$V_N$  : noise voltage measured with a true root mean square voltmeter

$V_F$  : peak value of signal observed by the oscilloscope

$V_T$  : pulse height of the test pulse

$C_T$  : capacitance for the charge injection

where the K is a constant which depends on the detector material. In order to evaluate the noise of the CSA with the circuit assembly in Fig.6, the  $V_p$  and the  $V_{SCA}$  are measured with the oscilloscope and the true root mean square voltmeter by changing the capacitance of the variable capacitor. If the values of the  $V_T$  and the  $C_T$  are already known respectively, the ENC is easily calculated from the above equation. The  $V_M$  is the noise of the shaping amplifier and is measured by the root mean square voltmeter without the CSA. The figure 2.35 in the Eq.(16) is a constant which is used to convert the root mean square width to the full width at half maximum (FWHM). The noise can be measured in the number of electrons in the case of K=1. The ENC in energy (energy equivalent noise charges) for the Si, CdTe or Ge detector is calculated by using each value for K described above.

## 5. Open-loop gain of the charge sensitive amplifier

In order to make measurements with low noise amplifiers, it is essential for the CSA to effectively collect charges induced in the detector by radiation. In the case of the AC coupling between the CSA and the detector, where its equivalent circuit is shown in Fig.7, the induced charges in the detector distribute on the detector capacitance  $C_{det}$ , the stray capacitance  $C_{stray}$  which includes the capacitance of the cable for connection, and the composite capacitance of a coupling capacitor  $C_c$  and  $A \times C_f$ , where  $A$  is the open-loop gain of the CSA and  $C_f$  the feedback capacitance. Neglecting the  $C_{stray}$  and using the  $C_c$ , only the small fraction of charges produced in the detector cannot be fed into the input of the CSA, if  $A \times C_f \gg C_{det}$  is not hold. This is a case that the S/N ratio is deteriorated. Namely, the S/N ratio becomes better if the open-loop gain ( $A$ ) is larger. From this reason it is essential to make the open-loop gain as large as possible in order to properly operate the CSA, which is inherently low noise. The situation is also the same as the case in the DC coupling.

There exist generally three methods to make the open-loop gain larger. Those are:

1. to use a constant current source,
2. to use a boot strap circuit, or
3. to use a current feed-back circuit.

An example of circuit, which is built with a method using a constant current source (1), is shown in Fig.8. Here, the load resistor  $R_2$  of the  $Q_1$  in Fig.5 is replaced with a constant current source. The  $R_2$  in Fig.5 is composed of the  $Q_2$ ,  $R_2$  and  $V_2$  in Fig.8. In this case, the effect of the constant current source looks like as if a load resistor exists and results in the larger open-loop gain. In the example, it is possible to use a constant current diode instead of a transistor.

An example that a boot strap circuit (2) is used in the CSA is shown in the Fig.9. In this circuit, an NPN transistor is used for  $Q_1$  different from the circuit described above. It is also possible to use a PNP transistor for  $Q_1$ . Here, the voltage variation on the load resistor  $R_1$  of  $Q_1$  is fed into the other side of  $R_1$  through two emitter followers of  $Q_2$  and  $Q_3$  removing the DC variation. As a result, the voltage variation on the both sides of  $R_1$  diminishes and then the current in  $R_1$  does not change. Namely, the  $R_1$  works as a constant current source and is equivalent to a larger resistor.

In the method of the current feed-back (3), the current which is equal to the change of the drain current of the JFET is inversely injected into the drain as shown in Fig.10. As the result, the current in  $Q_1$  becomes larger and the open-loop gain also increases. The amplified output is taken from the emitter of the  $Q_2$ . Actually, the emitter is pulled down with a resistor to a negative voltage supply in a practical circuit. In Fig.10, an NPN transistor is used for  $Q_1$ , but it is easy to replace it

with a PNP transistor. In these three methods, the noise increases in the case of a small input capacitance so as the number of parts, which are normally noise sources, increases. However, these methods are means to increase the open-loop gain of the CSA and then are possible to improve the noise characteristics as a result. The CSAs, which are commercially available, make use of one of three methods and achieve their large open-loop gain.

## 6. Characteristics on counting rate

The CSA normally outputs signals which exponentially decay with a time constant of  $\tau$  sec. Accordingly, the successive outputs are superimposed on the slope of a preceding output. This is so-called a phenomenon of "pile-up". A typical wave forms of pile-up are shown in Fig. 11. If the rate of signal inputs increases, there exists a chance in which a peak voltage of any signal reaches to the level of the saturation voltage in the CSA, even though each signal amplitude is small. The upper limit of the signal rates, to which the CSA can be operated under a small number of saturated signals, can be estimated with a following equation.

$$n_m = \frac{2}{\tau} \left[ \frac{V_m - E_\gamma G_c}{2.5 E_\gamma G_c} \right]^2$$

$n_m$  = the maximum counting rate in cps,

$\tau$  = the decay time constant of the CSA in sec,

$V_m$  = the maximum output voltage of the CSA in volt.

$E_\gamma$  = the energy deposition of an incident radiation in MeV.

$G_c$  = the conversion coefficient of deposition energy to voltage.

As a typical example, let's consider a Si detector. The counting rate at which the output signals of about 6% saturate is 90 kcps (kilo counts per second) for alpha-particles of 5 MeV, assuming  $\tau$  is 1 msec,  $V_m$  4 V, and  $G_c$  45 mV (Cf = 1 pF) for calculation. In the cases of the  $E_\gamma$  of 0.5 MeV and of 50 MeV, it is 10 Mcps and 193 cps, respectively. It can be thought from the results of the above calculation that signals from the CSA never saturate in the spectroscopy of gamma-rays from a checking source of  $^{137}\text{Cs}$  or  $^{60}\text{Co}$  which is normally used for detector calibration. However, it may be limited at the successive shaping amplifiers. In the special cases that measurements are made with using accelerator's beam, with particles of a large energy deposition per particles in the detector or in the strong field of radiation, the  $C_f$  and the  $R_f$  should be adjusted to the appropriate values.

## 7. Various circuit available for the CSA

### 7-1. Clipping circuit for avoiding pile-up and buffer amplifiers

As one of the valuable circuit to the CSA, there is a cable driving circuit with a voltage gain. It is advantageous to put a voltage amplifier, which is able to drive coaxial cables, with a CSA in a pre-amplifier rather than to realize the pre-amplifier by the CSA itself. Firstly, there sometimes happens that the external noise induced in the output cable are fed into the input of the CSA through the feedback capacitor  $C_f$  if the pre-amplifier itself is the CSA. This is avoidable with a buffer amplifier with a voltage gain built-in just after the CSA. Secondly, it is possible to simplify the CSA so as not to need a driving power, because the high input impedance of the buffer amplifier can be realized. Thirdly, it is also possible to improve the S/N ratio by amplifying signals before transmitting those against for external noises induced in the transmission cable. Lastly, it is the most important point that the decay time of signals can be shortened by making a clipping circuit for avoiding pile-up of the signals between the CSA and the buffer amplifier. Let us consider a case in which a voltage sensitive amplifier with the AC coupling is simply connected to the CSA. Assuming that the voltage amplifier saturates at 8 volt and has the voltage gain of 10, the output signals from the amplifier mostly saturate and its counting rate corresponds to 1/5 of a value mentioned above, if this is assumed to happen in the CSA. In order to avoid the situation, it is to build an appropriate clipping circuit between the CSA and the buffer amplifier so as to make the decay time of signal shorter to some extent that its decay time constant does not affect to the shaping time constants in the main amplifier. The typical example of signal wave forms from the CSA output is shown in the upper figure in Fig. 12 and those passed through a clipping circuit with an appropriate time constant is also shown in the lower figure in Fig. 12. Generally, the time constant of the clipping circuit is selected to be a value from 50  $\mu$ sec to 100  $\mu$ sec, if the shaping time constant  $\leq 3$   $\mu$ sec in the main amplifier. The clipping circuit is effective to avoid the pile-up of signals as shown in Fig. 12. The signal wave-form which passes through the clipping circuit is observed with a long undershoot across zero level as shown in Fig. 13. This undershoot arises from clipping the wave-form with a decay time of the CSA. Namely, the signal wave form from the clipping circuit shows a shape arise from the double clipping of a step function, the first one in the CSA for avoiding the pile-up and the second one in the clipping circuit. The overshoot lasts during a period corresponding to the decay time constant and affects to the shaping in the main amplifier. Therefore, the pulse height spectrum measured by an amplifier with the long overshoot deteriorates according to an increase of the counting rate. This is due to fluctuation of the DC level at the main amplifier output during the period of the overshoot. In order to compensate and

recover the overshoot to the zero level as fast as possible, a so-called pole zero cancellation (PZC) circuit is available. An example of a typical signal wave form observed by using both the clipping and the PZC circuit is also shown in Fig. 13. Such a circuit is practically realizable to obtain the wave form without the overshoot and also to achieve the short decay time of signal by using the clipping circuit together with the PZC circuit. The PZC circuit can be in principle built by adding a resistor  $R_2$  to a clipping circuit composed of a capacitor  $C_c$  and a resistor  $R_1$  as shown in Fig. 14. In this case, the clipping time constant is determined with the product of  $C_c$  and  $R_1$ , and the time constant determined with  $C_c$  and  $R_2$  has to be equal to the decay time of signal ( $\tau_{CSA}$ ) at the CSA. In actual cases, the output from the CSA has some offset voltage and then the DC component of signal should be cut by adding a capacitor with a large capacitance to the  $R_2$  in series. The PZC can be adjusted by changing the value of  $R_2$ , while observing the response of a step function from a test pulser or actual wave forms produced in a detector by radiation. This procedure is only needed when the decay time constant of the CSA has been changed, and is not needed when the detector has been replaced. It should be remarked that the PZC should not be adjusted by using a mercury pulser which generates pulses with a long decay time, since it sometimes causes over compensation. The over compensation is also a source of fluctuation. Normally, the PZC circuit is also built in the main amplifier. It is for compensation to the clipping time constant in the pre-amplifier and is not for compensation to the decay time constant of the CSA. There exist methods to adjust both the PZCs for the decay time constant of the CSA and the clipping time constant in the pre-amplifier. However those are not mentioned here because those are beyond the scope of this paper.

## 7-2. Active filter circuit for power supplies

In single ended amplifiers not like operational amplifiers with differential inputs, the external noise from power supplies sometimes affect directly to the input of the amplifiers. Such noise should be removed by adding filter circuit with a wide bandwidth in the power supplies. At present, organic-solid-aluminum condenser (OS condenser) with a large capacitance and with excellent high frequency characteristics are commercially available and are suitable for this purpose. However, there sometimes happen the cases that it is hard to use large capacitors in size. For example, it is sometimes hard to find room for the large capacitors in a system, in which the many CSAs are densely arrayed, in order to construct a large detector array. In those cases, so-called ripple-killer circuit, which is used in the compact audio-circuit, is also effective in the pre-amplifier. This circuit diagram is shown in Fig.15. This filter circuit is very simple and is equivalent to a filter of which the effect is  $h_{fe}$  times larger than a CR filter composed of resistors

inserted to the base of the transistor and the  $C_1$  in a low frequency region. It can be also extended to a high frequency region by using a high frequency transistor. However, it is essentially necessary to again add a CR filter circuit at the output, in order to avoid the shot noise, the input current noise and the  $1/f$  noise due to the high frequency transistor. The transistor operates as an emitter follower since it is used as a type of the collector common. Then, a voltage source is required between the collector and the emitter to operate as a follower and yet it is also a heat source in the case the CSA is a hybrid circuit.

## 8. Commercially available CSA

It might be ideal that users themselves design and build electronic circuit suitable for their purposes in measurements or order those with their own specification to a company. However, the users are not always familiar to the electronic circuit. It may be possible to solve such users problems by use of several hybrid CSAs which have presently been commercially available. The components like the feed-back resistor and/or the feed-back capacitor are easily replaceable in those hybrid CSAs. Normally, their performance are evaluated without the coupling capacitor  $C_c$  and the load resistor  $R_L$ . In order to properly use those, it will be taken into accounts that the load resistor and the coupling capacitor slightly increase noises in the CSA, although the load resistor is essentially needed for biasing and the coupling capacitor, too.

Here, I will show the test results in performance of a hybrid CSA, CS-513-2 (Clear Pulse, Co.) as an example. It has been used as a pre-amplifier including the  $C_c$  and  $R_L$ . It is a compact size version of CS-507 (Clear Pulse, Co.). The CS-507 had been developed more than 10 years ago and several thousands pieces had already been produced. In a package of the new version, a capacitor for test pulse injection is removed and the drain current of the FET is fixed. In the catalog of the CS-513-2, the ENC equivalent to a Si detector is described to be 1.3 keV in FWHM at an input capacitance of 0 pF, and the increasing rate of noise against the input capacitance is 20 eV/pF, where the feed-back resistance of 1 G $\Omega$  and the feed-back capacitance of 1 pF are used in the CSA and the shaping is made with a time constant of 2  $\mu$ sec in the main amplifier.

As the first example, the ENCs, which were measured as a function of the input capacitance for five different load resistors, are shown in Fig. 16, where the shaping of  $(CR)^1$ - $(RC)^4$  was made with a time constant of 2  $\mu$ sec in the main amplifier and the ENC is expressed with the width equivalent to a Si detector in FWHM. The peaking time was about 7  $\mu$ sec. An poly-propylene condenser of 6.8 nF was used as the  $C_c$ . The second example is the ENCs which were measured as a function of the input capacitance with the four different shaping time constants as shown in

Fig.17, where the load resistor of  $1\text{ G}\Omega$  and the coupling condenser of  $6.8\text{ nF}$  were used. The peaking time was 3.5, 7, 10 and  $17\text{ }\mu\text{sec}$  according to the shaping time constant of 1, 2, 3 and  $5\text{ }\mu\text{sec}$ , respectively. The ENC measured with the shaping time constant of  $5\text{ }\mu\text{sec}$  is the largest among those for other time constants in a region below the input capacitance of  $50\text{ pF}$ . It was due to that the clipping time constant of  $50\text{ }\mu\text{sec}$  for avoiding pipe-up in the preamplifier could not be negligible for the shaping time constant of  $5\text{ }\mu\text{sec}$  in the main amplifier. If the clipping time constant is made more than  $100\text{ }\mu\text{sec}$ , all the data are lowered by  $0.2\text{ keV}$  in Fig.16. At the last, the rise time of the output signal from the CSA was measured against the input capacitance with different polarities as shown in Fig.18. The rise time is slowly increasing as the input capacitance increases and is almost equal at the both polarities. Since the parameters, which were variable in the CSA, the  $C_f$  of  $1\text{ pF}$  and the  $R_f$  of  $1\text{ G}\Omega$  had been selected for the CS-507 more than 10 years ago. Those parameters have been accepted like one of standards in this field at present. In order to select those parameters in the CS-507, we had paid a big attention about its flexibility in use and how to suppress its oscillation. We had also another requirement that it should be of a low power consumption because one of the usage was for balloon flight experiments. Naturally, there exist some differences on designing between products oriented to special aims and universal usages. Furthermore, it is not possible to replace circuit elements in the case of the hybrid circuit and it is also required to produce massively those from an economical point of view. However, it was the most important point that the hybrid circuit should be stable in any operation with the various values of the  $C_f$  and the  $R_f$ , which were smaller than the values described above. In the CS-507, it was possible to add a resistor and a capacitor parallel to the  $R_f$  and the  $C_f$  to change its apparent sensitivity to charges and also to make the decay time shorter. It had been proved for the CS-507 to work stable by the  $C_f$  of  $1000\text{ pF}$  and the  $R_f$  of  $1\text{ M}\Omega$  without any phase compensation outside the hybrid circuit. It may be interesting to introduce examples of CSAs for special purposes, here.

The first example is a CSA for a detector with a large capacitance. In order to improve noise characteristics for such a detector, there exists no any appropriate methods except decreasing the increasing rate of noise on the input capacitance by increasing the  $G_m$  of the FET. That is of course realizable by making use of an FET with the large  $G_m$  or by effectively increasing the resultant  $G_m$  of several FETs with the almost same characteristics connected in parallel. The ENCs of a CSA, which was designed for a detector with more than  $100\text{ pF}$  and built by four FETs with the same characteristics connected in parallel, were measured as a function of the input capacitance for five different shaping time constants as shown in Fig.19. The rise times of the same CSA were also measured as a function of the input capacitance as shown in a lower figure in Fig.20. The each FET used here has a noise width of  $0.4\text{ keV (Si)}$  itself. The performance was excellent at the input capacitance below  $100\text{ pF}$ . In the case of the shaping with a time

constant of 2  $\mu\text{sec}$ , the increasing rate of noise was 4 eV/pF from the measured results of the ENC's (0.8 keV for 0 pF and 1.2 keV for 100 pF) as shown in Fig.19. The measurements were made by an universal main amplifier with the shaping of  $(CR)^1 \times (RC)^4$ . The rise times were measured at the output of the buffer amplifier. Those were limited with the response of the buffer amplifier below the input capacitance about 70 pF.

The second example is also for a special type of the CSA which was designed for a detector with a large capacitance. In this CSA, the FETs were separated from the circuit and were fixed adjacent to the detector. The FETs were connected with a coaxial cable of 80 cm to the circuit. The CSA was designed to use at a low temperature, but the measurements were made at a room temperature. Furthermore, it was intended to shorten the rise time by lowering the gain of the buffer amplifier. The  $R_f$  is 10  $G\Omega$  and the  $C_f$  of 2 pF were put at the same place of the FETs. The ENC's and the rise times are shown as a function of the input capacitance in Fig.21 and Fig.22, respectively.

The last example is a CSA with the fast rise time of the order of nsec. It is possible to make the rise time of the CSA faster to some extent by changing the  $C_f$  to a larger value, namely making a closed-loop gain smaller. In order to build the CSA with the rise time of the order of nsec. much consideration should be paid to select circuit elements, its arrangement, the resultant stray capacitance and etc.. The Si JFET are not suitable for this purpose and the GaAs FET or the bipolar transistor is normally used. A block diagram of the CSA with a bipolar transistor is shown in Fig 23 as an example . This CSA has been designed for reading signals from a sense wire of a multi-wire proportional chamber and has been already hybridized. The rise time was less than 1 nsec at the input capacitance of 0 pF and a few nsec at 10 pF. The rise time can be improved by making the  $C_f$  larger, while sacrificing the rise time at 0 pF. In order to design this kind of the CSA, it is better not to make number of amplification stages more than three in the feed-back loop, since it becomes difficult to achieve phase compensation in the feed-back loop of the CSA in order to avoid the self-oscillation. At present its, noise characteristics can not be evaluated, because there are not commercially found any electronic system for measurements like the PHA and also a true root mean square volt-meter in this frequency region. Furthermore, it was necessary to develop a very fast mercury pulse, since there does not commercially exist even a mercury pulser with a ultra-fast rise time and without any ringing.

## 9. Conclusions

In this article, I have described an outline of the charge sensitive amplifier and its related

circuit. I have also described how to build the CSA suitable to various purposes and how to operate to achieve those. The CSA is principally an excellent amplifier not only for radiation measurement but also for any sensors from which signals are charges. However, it seems that any new basic findings or techniques do not exist in this field recently. We are continuing to make efforts to develop various hybrid circuit using devices and parts commercially available. We are also developing a CSA with a rise time less than 1 nsec by using a GaAs FET in order to apply to analog communication at a region of 1 GHz by using lasers.

In this paper, I did not cite any references, since the CSA has a history more than 30 years and excellent text books and papers related to it are thought to be easily found anywhere.

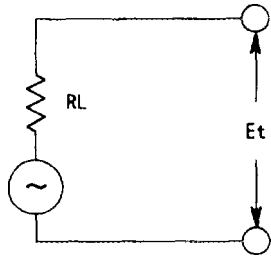


Fig. 1. Equivalent circuit of thermal noise.

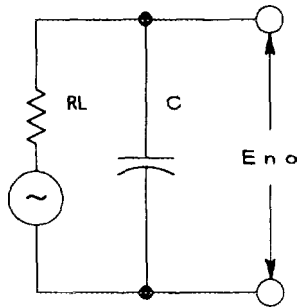


Fig. 2. Equivalent circuit of the thermal noise with a parallel capacitance.

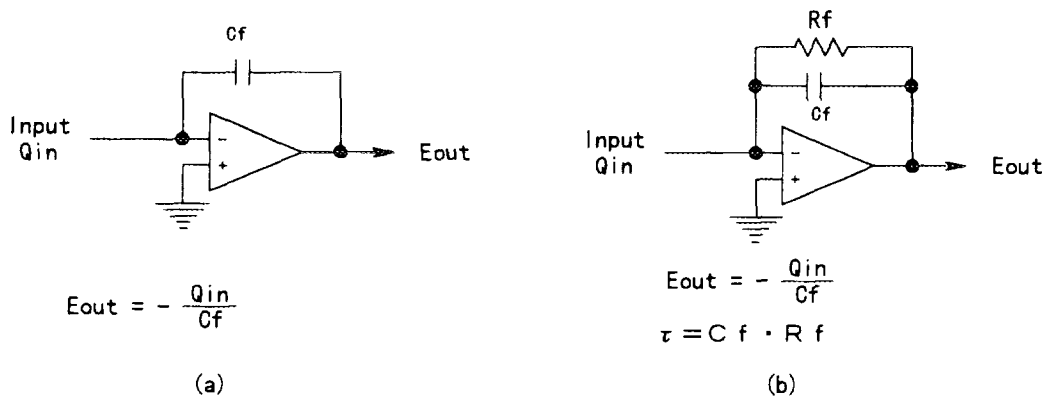


Fig. 3. Basic circuit diagram of charge sensitive amplifiers.

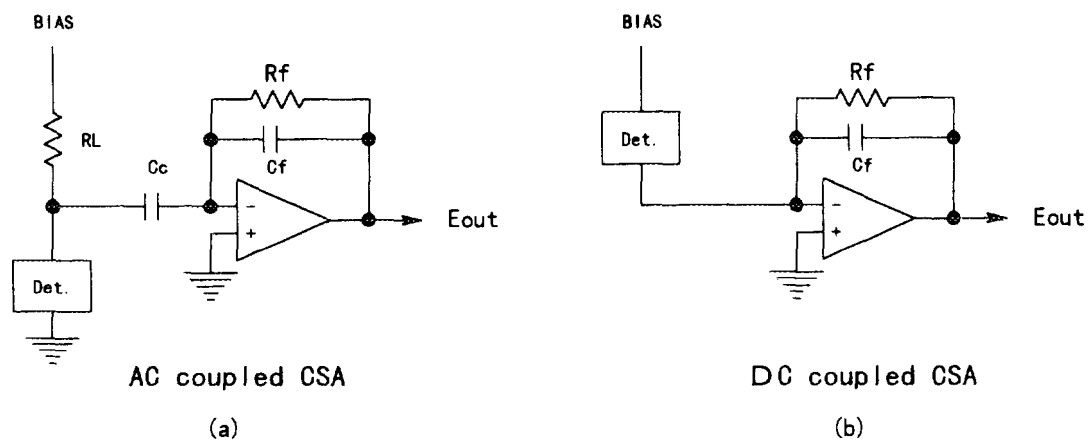


Fig.4. Two methods for coupling the CSA to a detector.

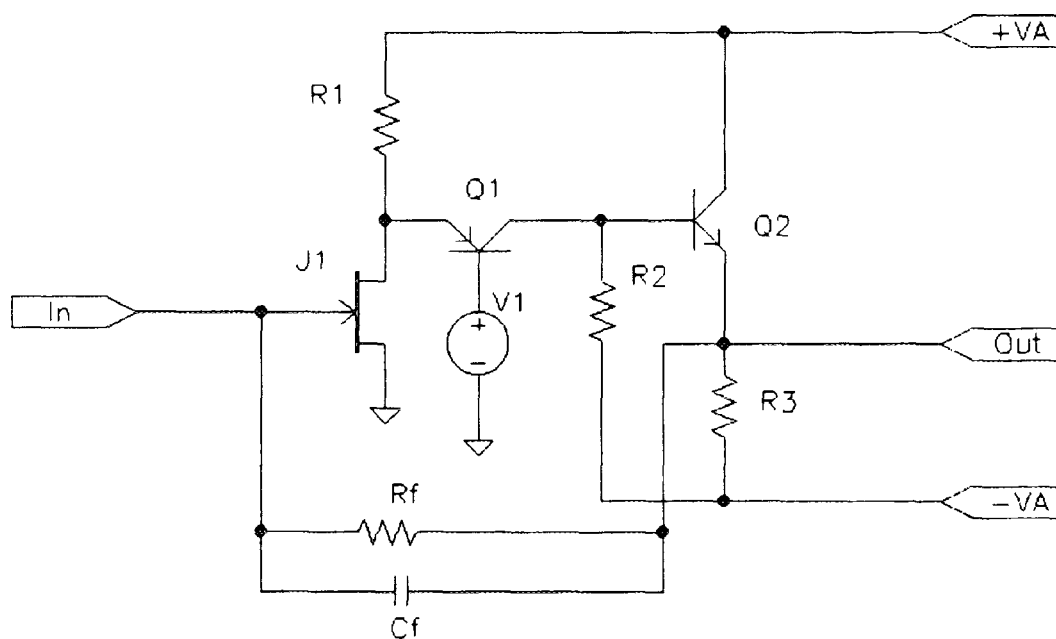


Fig.5. Circuit diagram of a single ended type of the CSA.

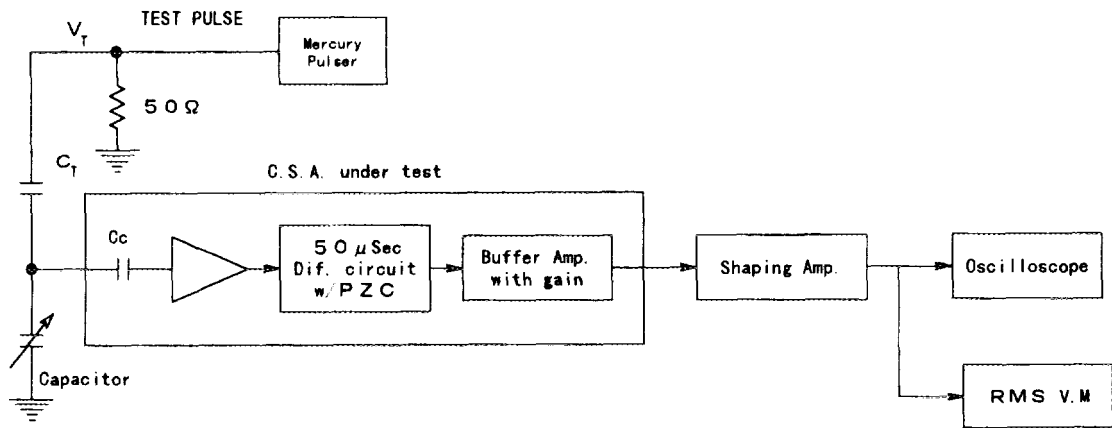


Fig.6. System for measuring noise of the CSA.

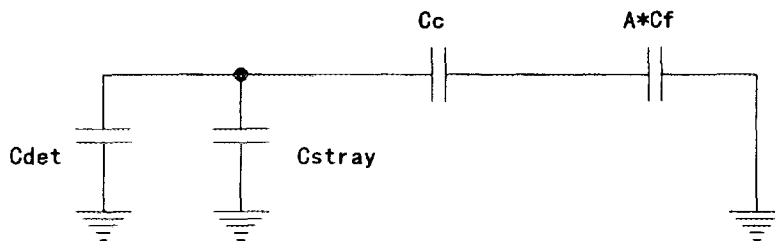


Fig.7. Equivalent circuit of the CSA coupled with a detector.

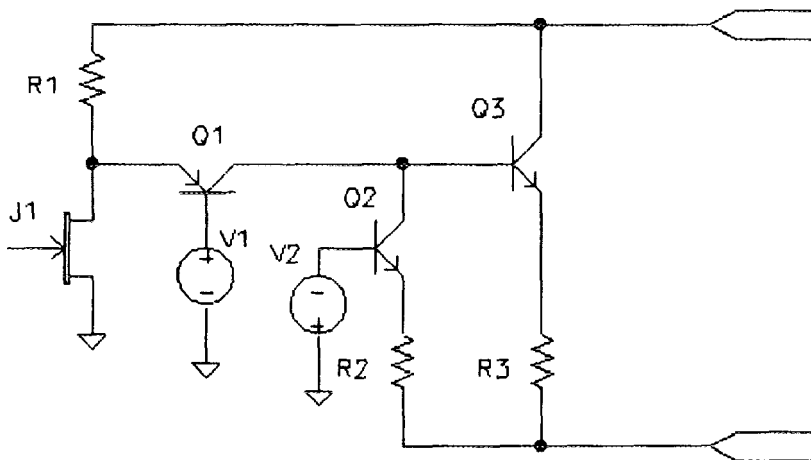


Fig.8. Circuit diagram of the CSA with a constant current source.

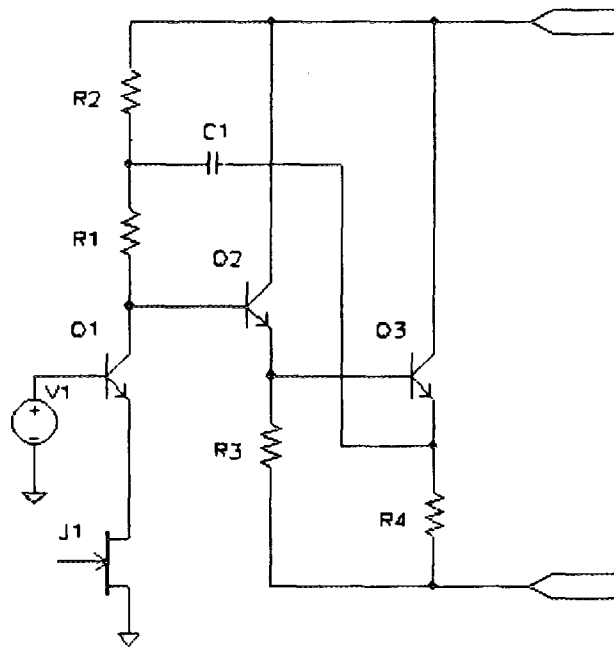


Fig.9. Circuit diagram of the CSA with a boot strap circuit.

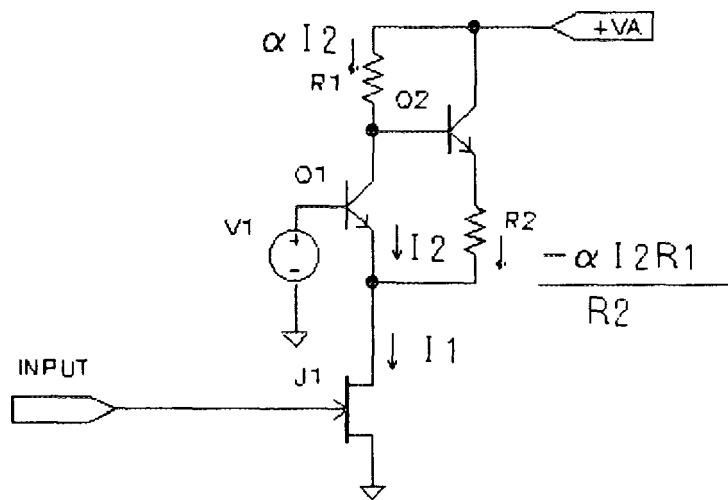


Fig.10. Circuit diagram of the CSA with a current feed-back circuit.

Pile-up of output signal

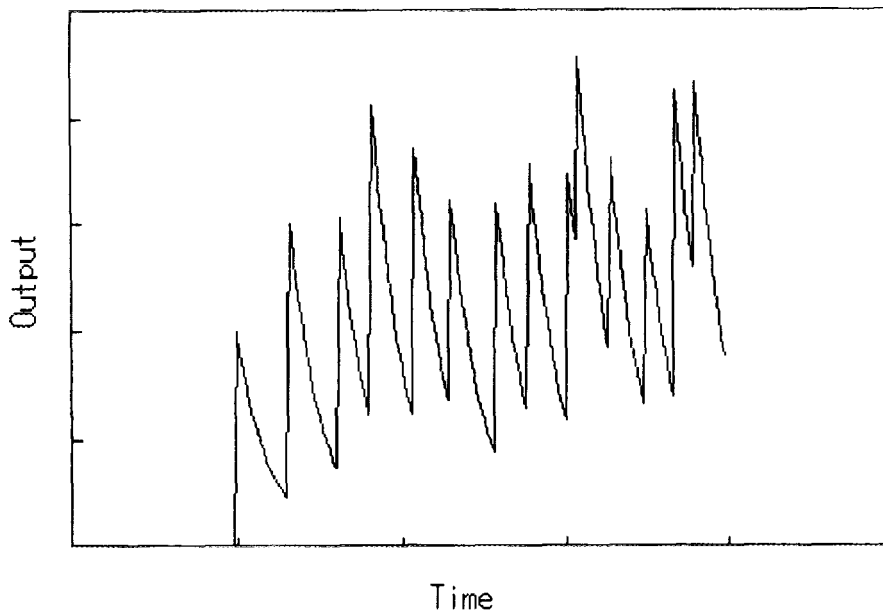


Fig.11. An example of "pile-up" wave- forms of the output signal from the CSA.

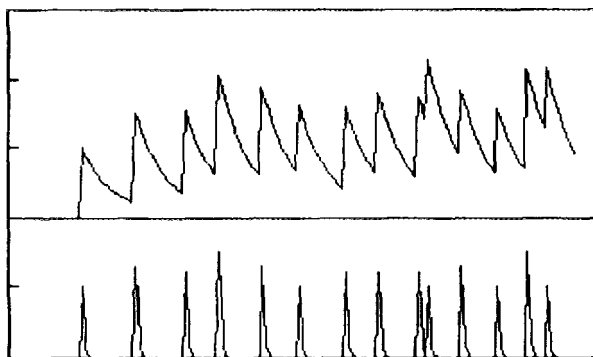


Fig.12. Examples of wave-forms due to pile-up (upper) and those due to clipping (lower).

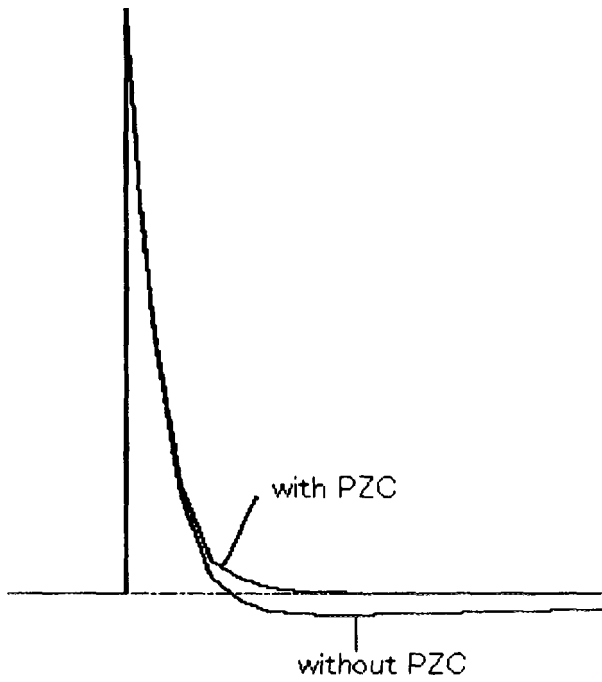


Fig. 13. Wave-forms of signal passed through a clipping circuit without PZC and with PZC circuit.

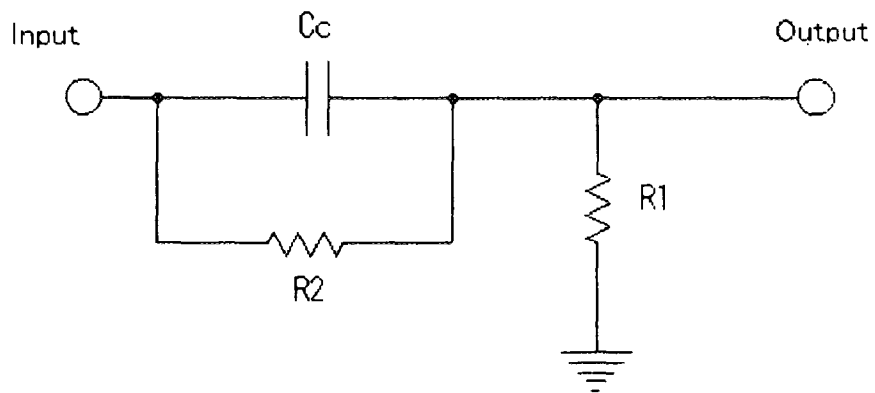
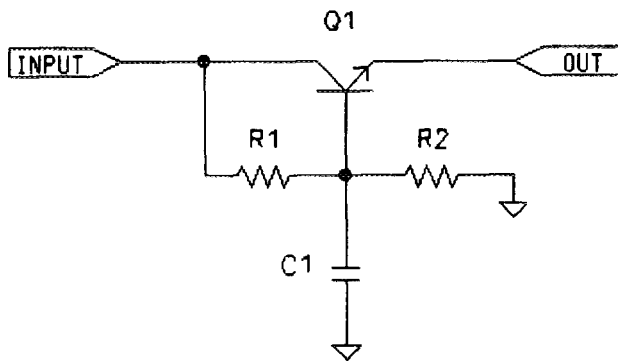


Fig. 14. Diagram of a clipping circuit with the PZC.



$$Z_b = \frac{1}{1/R_c + \omega C1}$$

$$Z_{OUT} = \frac{1}{h_{fe}} \frac{1}{1/R_c + \omega C1}$$

$$R_c = R1 // R2$$

Fig. 15. Diagram of a ripple killer circuit.

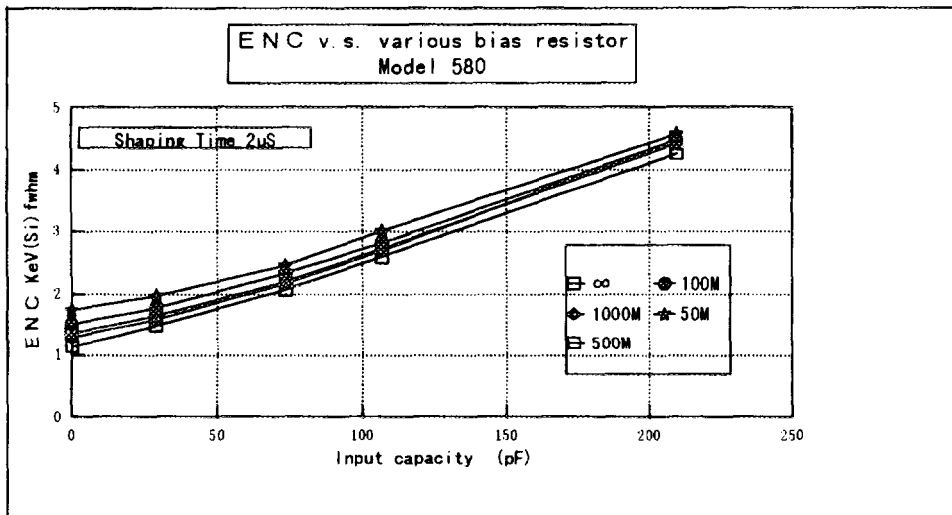


Fig. 16. Equivalent noise charges (ENC) measured as a function of the input capacitance for five different loads resistors.

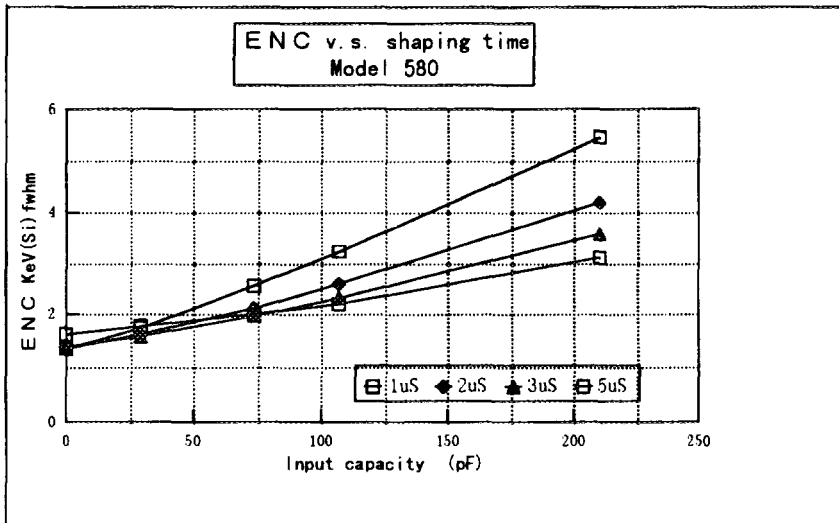


Fig.17. Equivalent noise charges (ENC) measured as a function of the input capacitance with four different clipping time constants in the main amplifier.

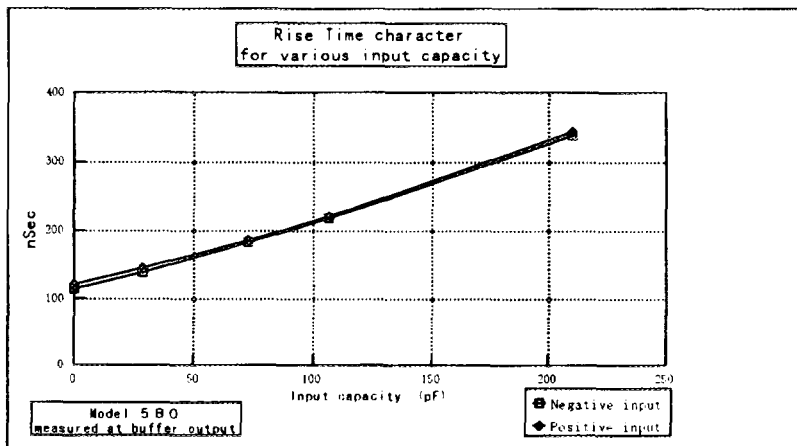


Fig.18. Rise time of the CSA measured as a function of the input capacitance.

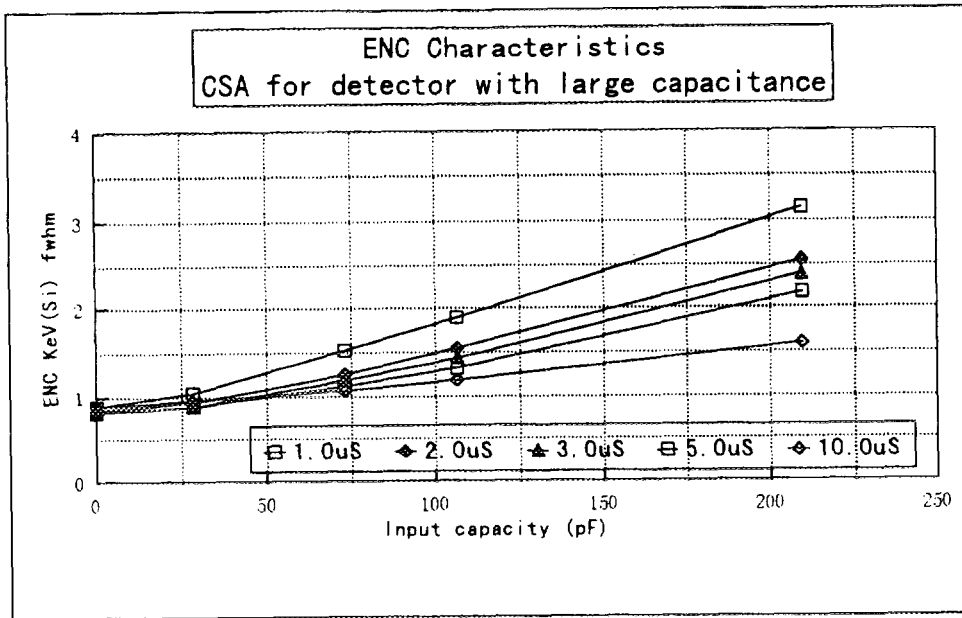


Fig.19. Equivalent noise charges (ENC) measured with the CSA for a large input capacitance.

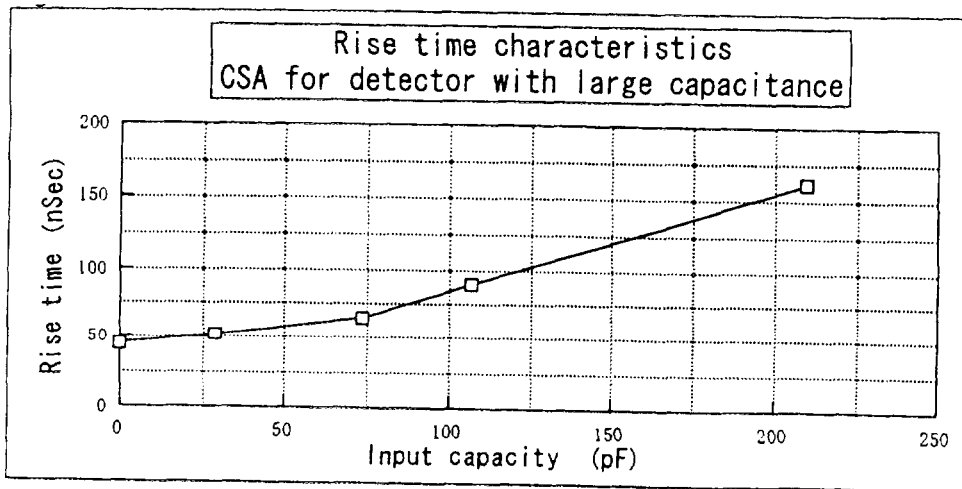


Fig.20. Rise times measured with the CSA for a large input capacitance as a function of the input capacitance.

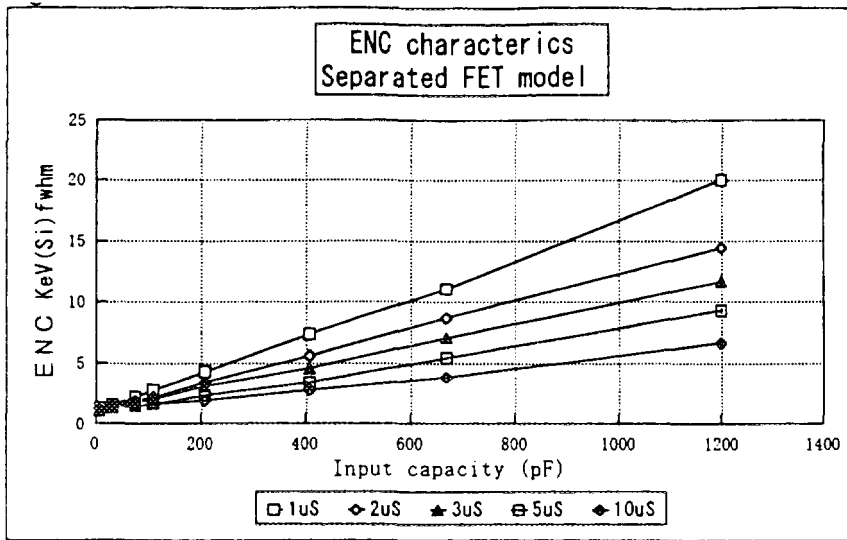


Fig.21. Equivalent noise charges (ENC) measured with a CSA with separated FETs.

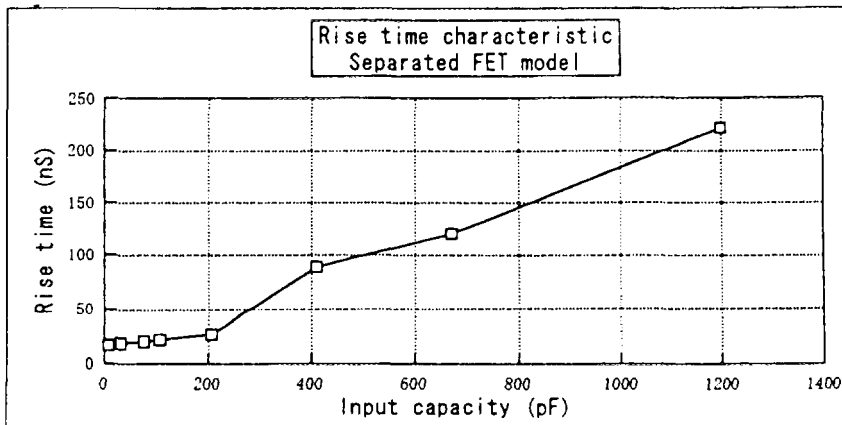


Fig.22. Rise times of the CSA with separated FETs as a function of the input capacitance

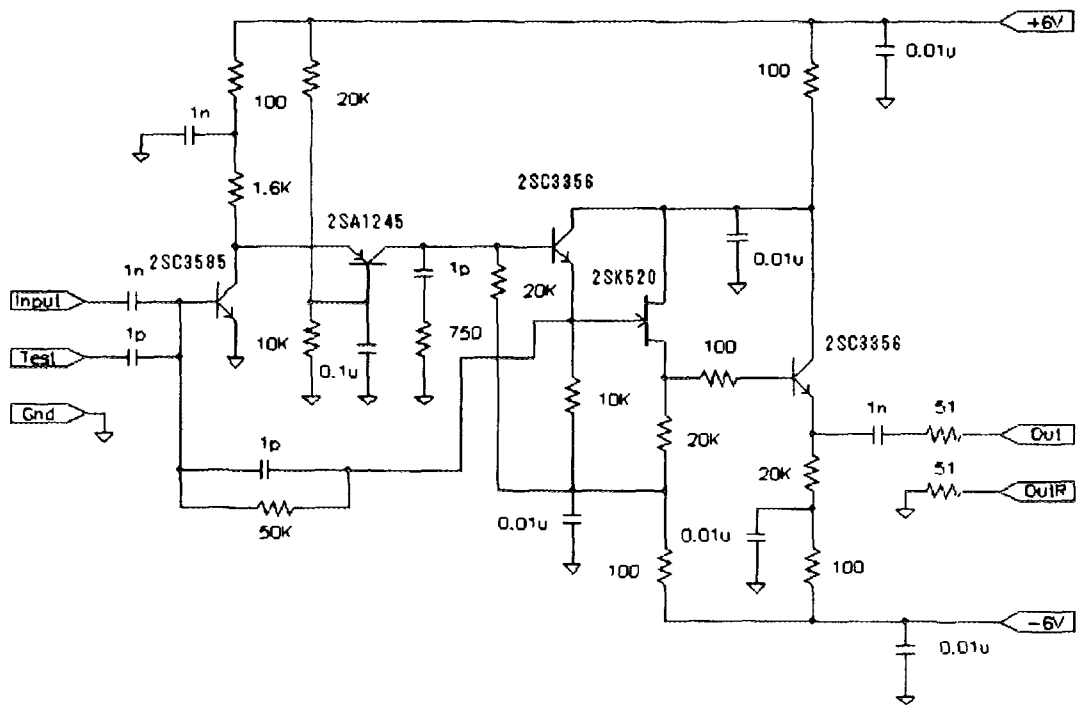


Fig.23. Circuit diagram of a fast CSA with a bipolar transistor instead of an FET.

# SIGNAL PROCESSORS FOR POSITION-SENSITIVE DETECTORS

Ken-ichi Hasegawa

College of Engineering, Hosei University

## 1. INTRODUCTION

Position-sensitive detectors (PSD) are widely used in various fields: condensed matter studies, material engineering, medical radiology, particle physics, astrophysics and industrial applications. X-ray diffraction analysis is one of the field where PSDs are the most important instruments. In this field, many types of PSDs are employed: position-sensitive proportional counters (PSPC), multi-wire proportional chambers (MWPC), imaging plates, image intensifiers combined CCD cameras and semiconductor array devices. We report two readout systems used for PSDs. One is a charge-division type which has high stability. The other is an encoder with multiple delay line readout circuits, which is useful for fast counting. The multiple delay line encoding system can be applicable to high countrate 1D and 2D gas proportional detectors.

## 2. CHARGE-DIVISION CIRCUIT FOR PSPC

We constructed several PSPCs for X-ray residual stress measurements and high energy-resolution PIXE experiments<sup>(2)</sup>. One of these detectors is a charge-division type PSPC using a carbon fiber as the anode wire<sup>(1)</sup>. The carbon fiber has a stable resistance of  $4 \text{ k}\Omega/\text{cm}$ .

Fig.1 shows the block diagram of the charge-division PSPC. The pulse charge  $Q$  induced by an incident X-ray at a position  $P$  on the anode is divided into the charge  $Q_a$  and  $Q_b$ . The ratio of  $Q_a/Q_b$  are proportional to  $(R_b + Z_b)/(R_a + Z_a)$ , where  $R_a$  and  $R_b$  are the resistances between the both ends of the anode and  $P$ , and  $Z_a$  and  $Z_b$  are the input impedances of the charge-sensitive amplifiers connected to the anode ends,  $A$  and  $B$ , respectively. The charges of  $Q_a$  and  $Q_b$  are converted into voltage pulses of  $V_a$  and  $V_b$  with charge-sensitive amplifiers, respectively. Summing up of the pulses of  $V_a$  and  $V_b$  are carried out with a summing amplifier in one of the shaping amplifiers. Signal processing of  $V_a/(V_a+V_b)$  is carried out with a divider. This ratio,  $V_a/(V_a+V_b)$ , has a linear relation to  $(L-X)/L$ , where  $L$  and  $X$  are the anode total length and the distance from  $X$  to the end  $A$ , respectively.

In order to obtain a stable operation of the signal processor, a digital divider has been designed<sup>(3)</sup>. The signals of  $V_a$  and  $V_a+V_b$  are converted with two 12 bit ADCs to digital data, respectively. We use 10 bits as the data bits. If we use a 10 bits digital divider, several output

channels have large digitizing errors. A flat response can not be obtained.

The digitizing errors in the digital divider are reduced by adding extension bits to data bits<sup>(4)</sup>. We use 6 additional bits as the extension bits. The 16 bit division is carried out for each combination of ADC outputs. The number of the extension bits depends on the pulse-height spectrum. In our applications the number of the position channels is 512 that corresponds to 9 bits. As we set the lower limit of the pulse-height to 256ch, the pulses with pulse-height lower than 256ch are rejected. If a pulse-height distribution with a lower part is to be analyzed, the analyzing channel must be increased. A log amplifier and associated logics can be employed to increase the number of the channels<sup>(5)</sup>.

The sensitivity distribution of the PSPC measured by 5.9 keV X-ray irradiation is shown in fig.2. This measured sensitivity decreases slightly at near both ends because of the decrease of the irradiation X-ray flux. The anode wire is 10 cm long, which has a resistance of 40 k $\Omega$ . Since the capacitance of the feedback capacitors of the charge-sensitive amplifiers is 1pF, the input impedances are not much lower than the anode resistance. The analyzing range is from 130 ch to 400 ch. This range can be extend by using of feedback capacitors with larger capacitance than 1pF. The time constants of the shaping amplifiers are 0.5  $\mu$ s. The sensitivity is so uniform that no sensitivity correction of spectra is required.

Our PIXE experiments use a monochromator combined with the PSPC. This system has a high energy-resolution. A PIXE spectrum of crystalline Si is shown in fig.3 as one of the measured examples. The energy resolution estimated from the FWHM of the satellite peak  $KL^0$  is 4.9eV.

The conversion time of our processor is 3.5  $\mu$ s, which is set by signal processing time of the analog part. Recent computers with fast memories can directly deal with PSPC signals. The digital division can be carried out in such a computer. The processing time depends on the characteristics of the computer and its associated electronics. A VME bus with a digital divider is also reported<sup>(6)</sup>.

### 3.MULTIPLE DELAY LINE ENCODER

#### 3.1 Conventional delay line encoder

The block diagram of a PSPC with conventional delay line encoder is shown in fig.4. The taps of the delay line are connected with the cathode strips of the PSPC. The delay line converts the pulse height distribution of the induced charges on the cathode strips into two pulses propagating towards the extremities. The arrival of the pulse at one end is detected by a constant fraction discriminator after amplification. This pulse is used for starting of the time-to-digital converter (TDC). Similarly, the pulse at the other end is used as a stop pulse. The output pulse of the summing amplifier has the energy information. Unwanted pulses in measurements can be rejected by

the energy window. Such a PSPC system is commercially available.

### 3.2 Fast MWPC

Many synchrotron radiation experiments require high-count-rate area detectors. We attempted to develop a MWPC with high-count-rate capability for these experiments<sup>(1)</sup>. Fig.5 shows the configuration of the MWPC with two types of position encoders: a priority encoder and a delay line type encoder. Each combination of both encoder outputs determines one of 92 x 96 channels. The priority encoder determines the Y coordinate of an avalanche from the anode signal, while a local readout technique is employed to find the X coordinate from cathode signal. For fast readout, we have developed a new encoding system employing many delay line encoders. Each encoder covers a small area of the detector with a short conversion time.

### 3.3 Circuits

In order to determine the X coordinate of an event, we have to find the center of the charge distribution induced to the cathodes. In the detector, this is done by 15 independent delay line encoders. Each encoder accepts signals from eight cathode strips, and determines the local X coordinate. The block diagram of the delay line encoder is shown in fig.6. Eight preamplifier outputs are fed to a delay line with a 20 ns delay time between adjacent taps. The start pulse is derived from the prompt cathode signal given by a summing amplifier with parallel input resistors. A single-channel analyzer (SCA) with a computer controlled lower level inspects the output of this amplifier: when the pulse amplitude does not fall into a predetermined range, the conversion operation in the TDC is canceled. Each preamplifier consists of a charge-sensitive amplifier and a shaping amplifier with time constant of 100ns. The processing time of the delay line encoder is about 300 ns, of which 200 ns is the total delay time of the delay line used, and 100 ns is the recovery time of the preamplifiers.

The 15 delay lines employed in the whole system have delay-times distributed around the nominal value of 200 ns. In order to compensate for the variations, a variable frequency oscillator shown in fig.7 has been incorporated in each TDC. The oscillator utilizes a transistor and a coaxial cable as the delay line. The cable length and the transmission time of the transistor determine the period of the output clock pulses. This transmission time depends on the transistor bias current, which is controlled by a computer through a DAC. This circuit can supply 100 MHz clock pulses as shown in Fig.7. The control range is 20%. The clock frequency can be adjusted, so that the pixel size in the X direction corresponds to 2 mm on the detection surface. To encode the X coordinate into 12 codes, the mean clock frequency of the variable oscillator in each encoder was adjusted to 75 MHz by setting the length of the coaxial cable. This frequency is low enough to drive the ECL logics and binary counters stably. The computer controlled delay circuit is also used to compensate for unavoidable delay-time variation in the amplifiers and the constant fraction timing circuits.

Fig.9 shows the configuration of the delay line encoders. Eight encoders cover all the 64 cathodes, of which the 56 central cathodes are doubly covered: the signal from a cathode strip is led simultaneously to the front and back encoders through the associated charge-sensitive amplifier, except for four strips at either extremity, which provide signals only to front encoders. An encoder produces 12 different local channel addresses of which the eight central addresses are used to increment the memory. Owing to the overlapped configuration of encoders, events occurring in the two channels at either boundary of each encoder are counted twice. This configuration prevents to lose any pulse at the boundary regions. Software makes corrections for the data in the common channels as well as for the spatial response of the detector, after the data are read into the computer.

### *3.4 Automatic adjustment*

One of the most important characteristics of position-sensitive detectors is the uniform sensitivity. In order to obtain good uniformity, we devised the computer correction method of the encoders. The adjustments of the characteristics of all the encoders are achieved in the following manner. First, variable delays and oscillator frequencies on the TDCs are set at initial values. Then, test pulses of 10 KHz are given in turn to the eight inputs of a delay line encoder to generate a data set in the memory. A regression line is calculated which relates the cathode positions to the addressed memory channels. An iteration program varies the variable delay time and the oscillator frequency so that the difference between the calculated line and the ideal line is minimized. In this way the conversion characteristics of all the encoders are adjusted in turn.

### *3.5 Applications*

This MWPC can collect data at rate up to 1 Mcps. The spatial resolution is 2 mm. Many experiments require area detectors with a higher resolution. Our detector is only a prototype. After construction of this detector, no budget has been supplied to build a new detector, so we could not try to develop an area detector with a finer pitch. However, the multiple delay line encoder described here has no limitation regarding the number of channels, so it can be used for a PSD with a large channel number. Micro-strip position-sensitive proportional counters under development have also high counting ability. A fast FIFO memory combined with this encoder can be used as a readout system of such a fast detector.

## **References**

- (1) K.Hasegawa, K.Mochiki, M.Koike, Y.Satow, H.Hashizume and Y.Iitaka, Nucl. Instr. and Methods in Phys. Res., **A252** (1986)158.
- (2) H.Hamanaka, K. Hasegawa and Y.Yamamoto: International Journal of PIXE, **2**, 3 (1992)263.
- (3) S. Kobashi et al.:Advances in X-RAY ANALYSIS, **24** (1980) 103.

- (4) M. Koike and K.Hasegawa: Nucl. Instr. and Meth., **A272** (1988) 840.  
 (5) M. Koike et al.: Nucl. Instr. and Meth., **A 567** (1990) 567.  
 (6) A. Uratani, K. Yoshimura, Y. Takenaka and C.Mori: Nucl. Instr. and Meth. **A353** (1994) 246.

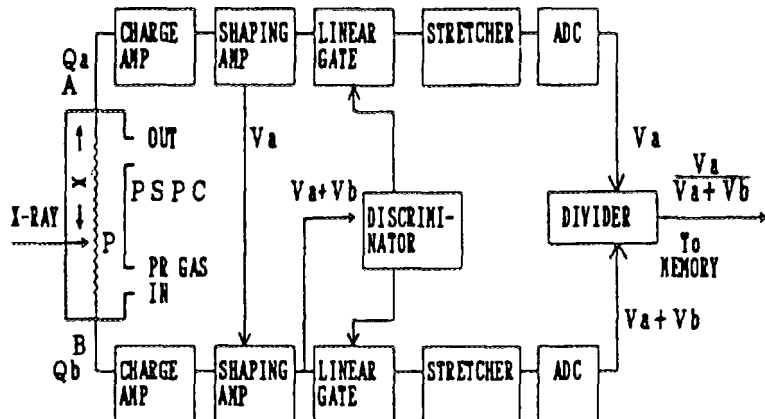


Fig. 1. Block diagram of charge-division signal processor

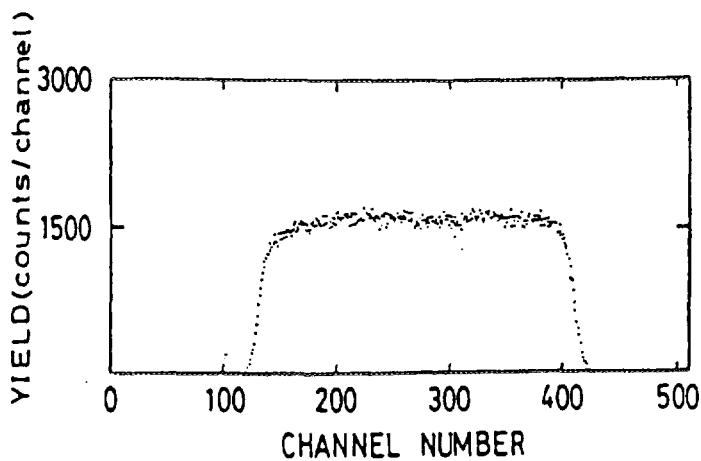


Fig. 2. Sensitivity distribution of PSPC.

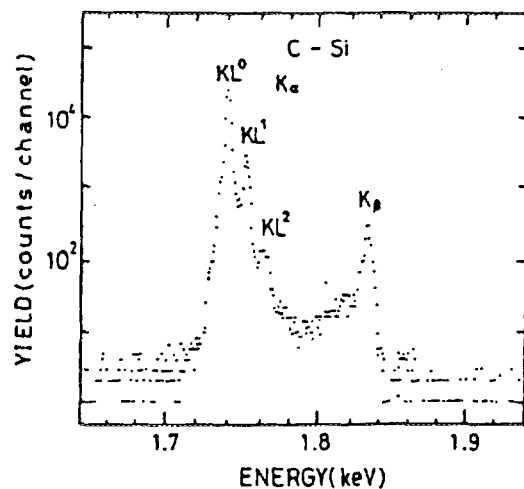


Fig. 3. PIXE spectrum of crystalline Si.

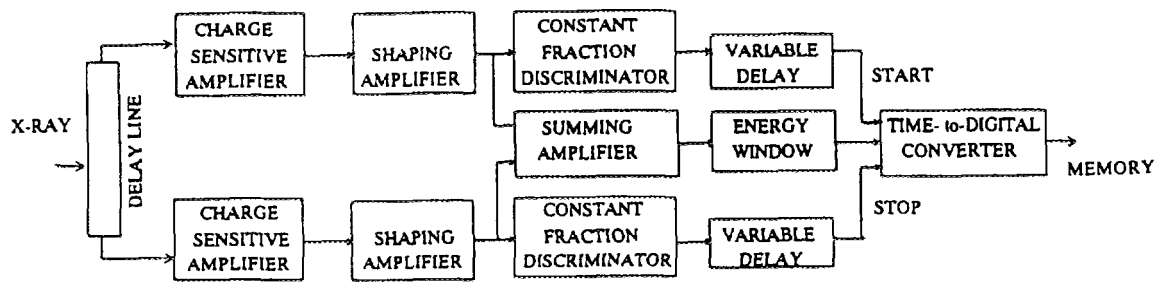


Fig. 4. Block diagram of conventional delay line encoder

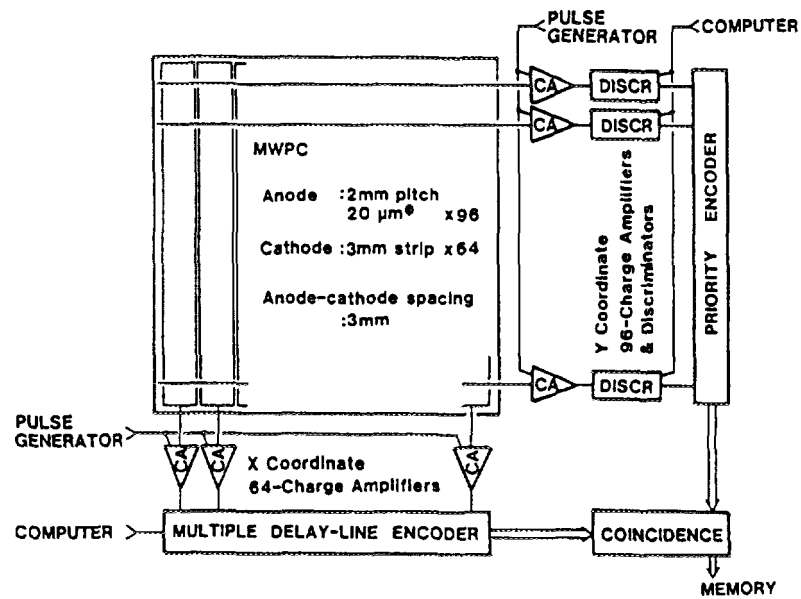


Fig. 5. MWPC and position encoders.

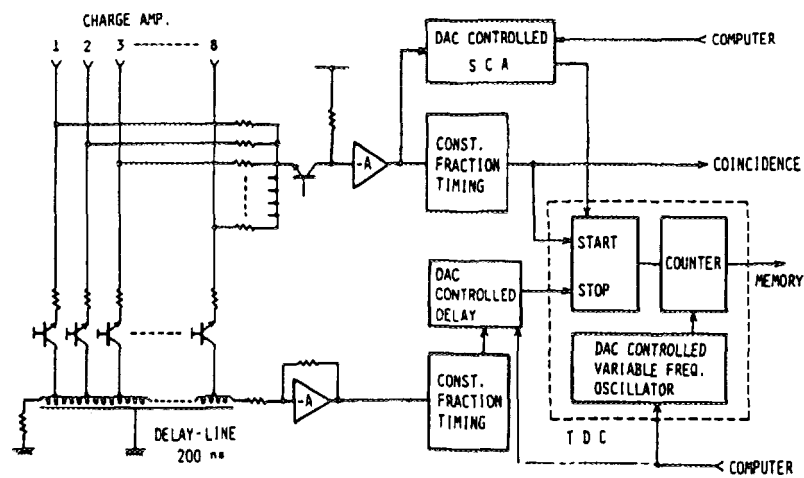


Fig. 6. Block diagram of the delay line encoder

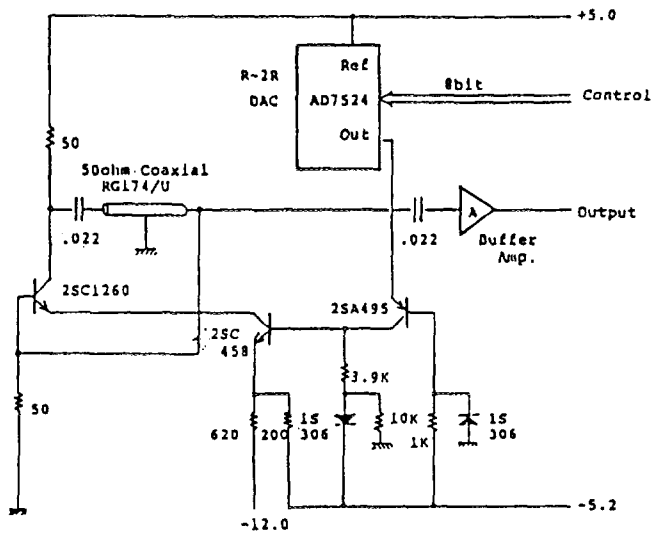


Fig. 7. DAC controlled variable frequency oscillator.

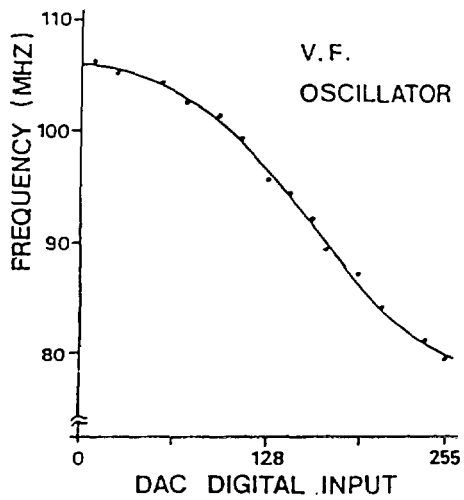


Fig. 8. DAC control characteristics.

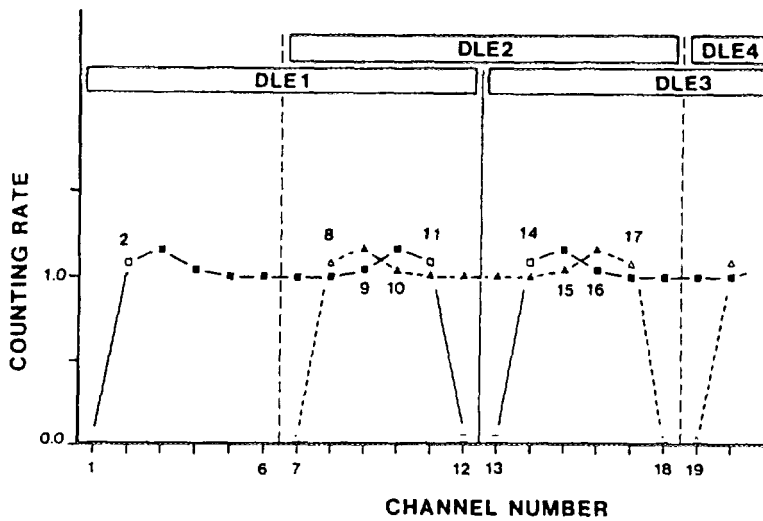


Fig. 9. Configuration of the delay line encoders.

# Time- and Depth-Resolved Measurement of Ion Tracks in Condensed Matter

Kazuie Kimura, RIKEN

## A. Unusual temperature-dependent decay of self-trapped excitons formed at high density in ion irradiated BaF<sub>2</sub>

Recently, luminescence of photoexcited BaF<sub>2</sub> and several alkali halide crystals have attracted interest not only as new scintillators for high energy physics but also as crystals presenting new exciton luminescence called Auger electron free luminescence (AEFL). We have studied dynamics of exciton luminescence induced by irradiation with several kinds of ions of low energies of about 2.0 MeV/nucleon with development of techniques for fast luminescence decay measurements (SISP) of 100 ps resolution. Excitation-density dependent shortening of the lifetime of AEFL was found and the results were reported already.<sup>1)</sup> In this report, the effects of ion irradiation and of temperature on STE's are described. Drastic lifetime shortening was observed for the self-trapped exciton (STE) of ion-irradiated BaF<sub>2</sub>.<sup>2)</sup> Figure 1 shows decay curves of STE luminescence of photo-, electron-, and He-ion-irradiated BaF<sub>2</sub>. Heavier ions caused increased shortening of the STE lifetime. Under the present condition of the high density excitation, which is intensified with increasing the mass of the projectile, the STE decays according to the STE-STE exchange in Instantaneous luminescence intensity  $I(t)$  can be expressed by following equation addition to the spontaneous process. The

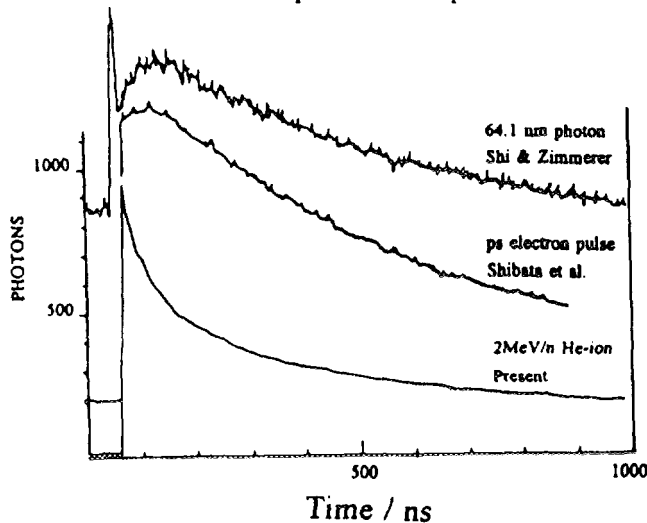


Fig. 1 A comparison of the decay of STE in BaF<sub>2</sub> induced by different sources.

competition rate equations could be solved analytically.

$$I(t) = k / [(a + N(0))^{-1} \exp(kt) - a]$$

where  $N(0)$ ,  $k$ , and  $a$  stand for the number density of STE at time 0, the rate constant of spontaneous luminescence of STE, and a constant dependent on the radii of the track and STE and on the critical exchange interaction, respectively. This equation could simulate the result fairly well ( Fig. 2).

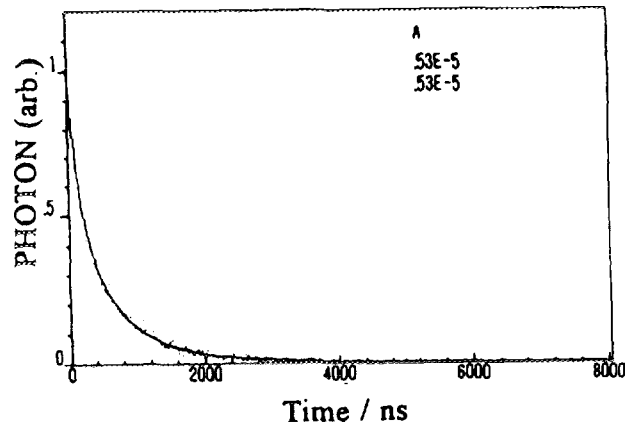


Fig. 2 Fitting of Eq. 1 to the decay curve for He-ion BaF<sub>2</sub>

Decreasing temperatures shortened the decay time from several ns to about 400 ps with no prominent change in its intensity.<sup>3)</sup> This temperature effect was contrary to that for photoirradiation by synchrotron radiation which results in a lengthening of the decay time from about 1  $\mu$ s at room temperature to about 10  $\mu$ s at 50 K.<sup>4)</sup> Both effects of temperatures and masses projectile ions are shown in Fig. 3 comprehensively. The results may be explained by following model mentioned briefly. The slow rises seen in case of photoirradiation shown in Fig. 1 suggests that STE's can be regenerated through the recombination of holes (H-centers) and electrons (F-centers). The temperature decreases should result in slowing down in these recombinations. By contrast, in case of the ion irradiation, the F-

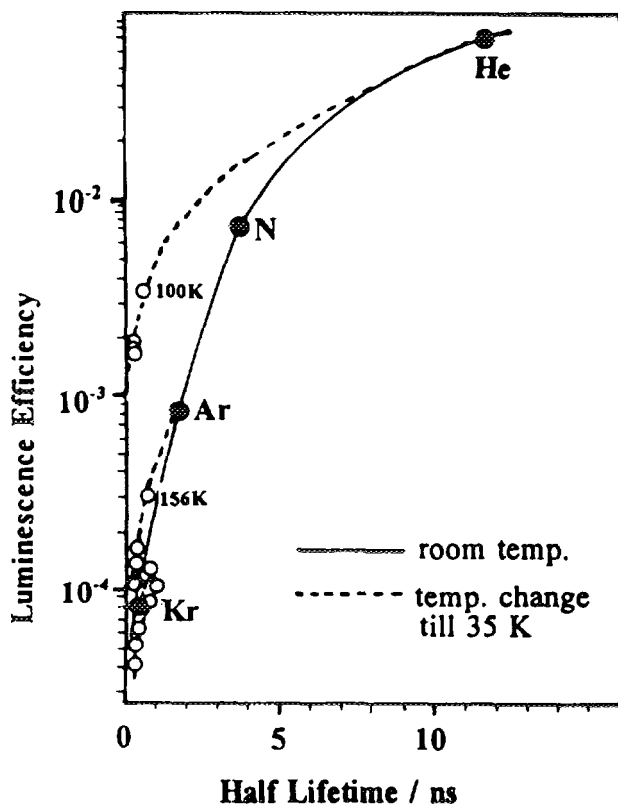


Fig. 3 Temperature and the mass of projectile dependencies of the luminescence efficiency and the half-life.

and H-centers are formed at such a high density that each cannot localize separately and that they can recombine always. Decreasing temperatures suppress the expansion of the volume covered by F- and H-centers so that the density of STE increases.

#### A. Track-depth resolved dynamics of excited states in ion irradiated rare gases

The radiation effects induced by ion irradiation have been mainly on the primary collisions in physics while product analysis have been major methods in chemistry and biology. As for the relevance between the two approaches, we can find very few studies. This study aims to elucidate the physico-chemical stages of ion irradiation by focusing on dynamics of excited states along the ion track. This may be achieved by measuring the Bragg curve of the luminescence from the track in the condensed phase; for this, we developed a digital camera for the ion track, a track scope, composed of an imaging fiber mounted in a cryostat and a position sensitive photon counter. This allows us to obtain depth dependent luminescence spectra, efficiency, and decay. The depth can be converted into several parameters including derivatives of ion energy, stopping power, velocity, and relative excitation density. In our previous study of helium, we found that the lowest triplet excimer plays the main role: Along the Bragg curve, the regeneration of upper level excimers through

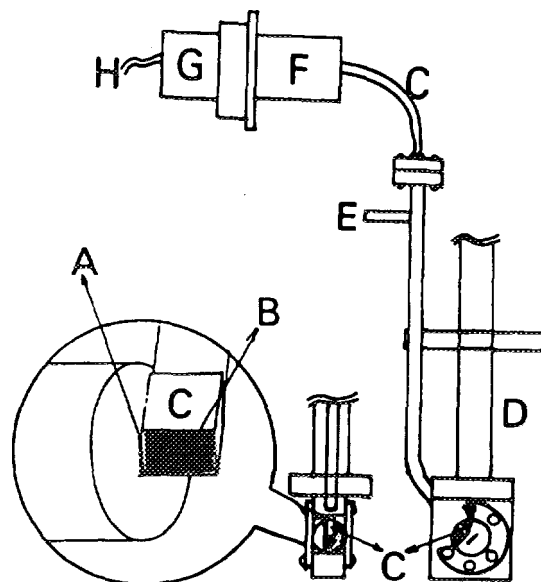


Fig. 4 A track scope. A: a beam slit by 0.1x2 mm; B: a capillary plate; C: a quartz imaging-fiber of a 2x2 mm cross section; D: a cold part of the trackscope; E: connection to a pump and gas bombs; F: a lens system; G: an intensified CCD camera; H: connection to a computer system.

the reaction of two triplet excimers increases (enhancement of luminescence), and near the Bragg peak, the reactions of the three excimers occur to result in the quenching. An extra Bragg peak caused by the Fano-type mechanisms appeared near the termination of the track. Now the study are extended to other rare gases. With increasing atomic number, rare gases evolve in electronic properties such as excited states, the electronic conduction level in the condensed phase ( $V_0$ ), and the electron mobility. These effects on the physico-chemical stage will be studied. We developed a modified track scope essentially composed of the same parts to the previous one but can pressurize gases up to 40 atm near the critical temperature, resulting in nearly condensed gases. The track length could therefore be adjusted by altering the pressure. This track scope is illustrated in Fig. 1. A capillary plate was used to transmit only the luminescence perpendicular to the track. Figure 2 shows the specific luminescence  $dL/dx$  vs. the track depth in Ar-ion irradiated dense argon-gas. The luminescence is vacuum ultra violet light originating from argon excimers. The  $dL/dx$  is damped earlier than the stopping power, a result quite different from the result in case

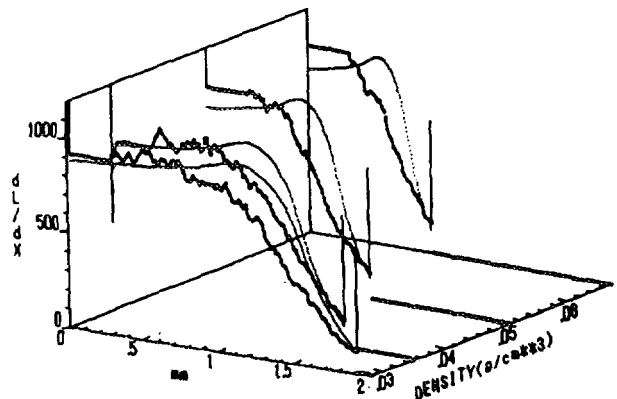


Fig. 5 The specific luminescence intensity  $dL/dx$  vs. the track depth of Ar-ion irradiated Ar gas.

track. Similar results were observed for other rare gas samples. The results counter to what scintillator theory and experiments have indicated. This may be explained by the charge exchange and direct excitation processes which were also important in the appearance of the 2nd Bragg peak in the helium sample.

**Reference**

- 1) K. Kimura and J. Wada; Phys. Rev. **B48**, 15535(1993).
- 2) K. Kimura; Nucl. Instr. Meth. **B90**, 100(1993); K. Kimura and H. Kumagai; Rad. Eff. Def. Solids. **126**, 45(1993).
- 3) K. Kimura; to be published on Nucl. Instr. Meth. **B** (1996) and J. Elec. Spec. Re. Phenomena(1996).
- 4) C. Shi, T.Kloiber and G. Zimmerer; Physica Scripta, 41, 1022(1990).
- 5) Private communication.
- 6) K. Kimura, Phys. Rev. **A47**, 327(1933)

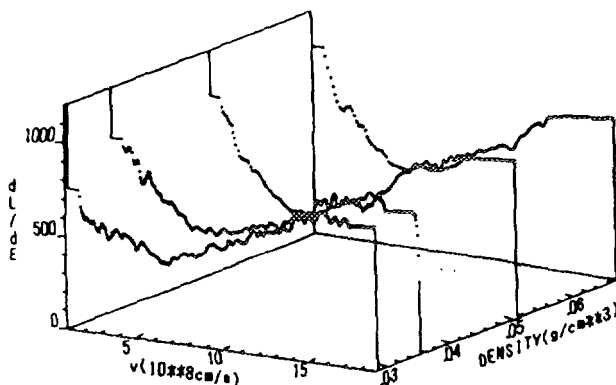


Fig. 6 The luminescence efficiency as a function of the ion velocity obtained by the conversion of data from Fig. 5.

of the helium sample. The high-density excitation can enhance the luminescence in helium while it is quenching in this case. Figure 3 shows the luminescence efficiency ( $dL/dE$ ) as a function of the velocity of ions;  $dL/dE$  rises toward the termination of the

A weak  $^{57}\text{Co}$  source ( $\sim 1$  kBq) electroplated on an aluminum foil was mounted on the flat wall of the counter. In order to examine of the operation of the counter, energy spectra of emitted electrons from the source were recorded below 22 K, at 22-53 K, at 46-200 K, at 47-200 K, above 55 K, above 60 K and above 15 K by filling helium, neon, the He+N<sub>2</sub> gas mixture, the He+CO mixture, the He+Ar mixture and hydrogen, respectively, into the counter. In cases of helium and neon, the operation of the counter was also examined at room temperature.

### 3. Gas Multiplication

After an atom of the counter gas is ionized by an incident electron, a long time more than 100  $\mu\text{s}$  is necessary for the resultant positive ion to go to the cathode. On the other hand, the shaping time of the electronic system is much shorter than 100  $\mu\text{s}$ , usually about 1  $\mu\text{s}$ . Accordingly, owing to clipping of a signal pulse, the pulse height is lower than that expected from the number of ion pairs formed in the counter. Mathieson and Charles derived an expression for estimating this effect<sup>(9)</sup>,

$$\frac{V_{R0}}{V_R} = \frac{0.087 + 0.797 \log(T/t_0)}{2 \ln(b/a)}, \quad (1)$$

where  $T$  is the shaping time,  $V_R$  the expected pulse height,  $V_{R0}$  the observed pulse height,  $V$  the anode voltage,  $a$  and  $b$  the anode and cathode radii, respectively. Here, the observed pulse height is evaluated from the peak position in the energy spectrum which is caused from superimposed contributions of 5.6-keV K-LL Auger electrons and 7.3-keV K-conversion electrons. The time  $t_0$  in Eq. (1) is given by

$$t_0 = \frac{a^2 p \ln(b/a)}{2\mu V}, \quad (2)$$

where  $\mu$  is the mobility of a positive ion and  $p$  is the pressure of the counter gas at room temperature. The gas-multiplication factor  $M$  is calculated from the equation

$$V_R = \frac{GAE_i}{CW} e, \quad (3)$$

where  $W$  is the W-value of the counter gas,  $C$  the electric capacitance of the charge sensitive preamplifier,  $G$  the gain of the amplifier,  $E_i$  the energy of an incident electron and  $e$  the elementary electric charge. In the present case, the energy of an incident electron is estimated by taking the average of the contributions of K-LL Auger and K-conversion electrons.

An electron is multiplied in a proportional counter through electron collisions with gas molecules to form an electron avalanche. The gas-multiplication is promoted by photo-electrons due to photons emitted from excited atoms. In this case, the measured gas-multiplication factor  $M$  is given by<sup>(10)</sup>

$$M = A + \gamma_p A^2 + \gamma_p^2 A^3 + \dots = \frac{A}{1 - \gamma_p A} \quad (\gamma_p A < 1), \quad (4)$$

where  $\gamma_p$  is the number of electrons emitted through the photo-effect per ion pair formed in the counter and  $A$  is the gas-multiplication factor expected when the contribution of photoelectrons is negligibly small.

# Gas-Multiplication Factor of a Proportional Counter Operated at Low Temperature Described with the Diethorn, Rose-Korff and Townsend Expressions

Kazuko Fukumura, Akio Nakanishi and Takayuki Kobayashi  
Department of Physics, Shiga University of Medical Science,  
Seta, Otsu, Shiga 520-21, Japan

## 1. Introduction

The conversion electron Mössbauer spectroscopy (CEMS) is exceedingly useful for investigating the properties of a thin layer of materials which are formed on the surface of a thick substrate. A proportional counter in which a sample material is mounted is most popularly used for detecting low-energy electrons in CEMS. In order to study temperature dependence of the properties of the sample material, therefore, it is expected to operate the proportional counter at low temperature.

Detection of low-energy electrons with a proportional counter was first performed at room temperature by Swanson and Spijkerman in 1970<sup>(1)</sup>. Isozumi and Takafuchi could operate a counter above 77 K, in 1975, by filling pure helium and a mixed gas of helium and a quenching gas in a similar way as at room temperature<sup>(2)</sup>. In 1987, Isozumi *et al.* could successfully detect low-energy electrons from <sup>57</sup>Co at 5 K with a proportional counter filled with pure helium<sup>(3)</sup>. Since 1991 the operation of a proportional counter at higher temperature between 13 and 295 K have been studied by the present authors<sup>(4-6)</sup>.

The operating mechanism of a proportional counter at room temperature is well known, but it has been investigated insufficiently at low temperature. The present authors has tried to study the mechanism at low temperature by comparing the parameter  $\Delta V$  estimated by the Diethorn method<sup>(7)</sup>, which is the mean energy required to produce an ion pair between two successive ionization events, with the W-value<sup>(8)</sup>. When the influence of photoelectrons on the gas-multiplication factor is great, the parameter  $\Delta V$  was estimated by taking away this influence in the conventional way as described later by Eq. (3). In the present work, the gas-multiplication factor is expressed with the Rose-Korff and Townsend methods as well as with the Diethorn method. A proportional counter with helium or neon works only at low temperature. This is discussed in terms of the number of electrons emitted when an ion is neutralized at the cathode of the counter.

## 2. Experiment

The experimental system is the same as that described elsewhere<sup>(4)</sup>. The proportional counter is drum-shaped and has a sensitive area with size of 20 mm in diameter and 16 mm in height. The anode is a Au-coated tungsten wire of 30- $\mu$ m diameter. The counter was filled with pure helium, neon or hydrogen, or mixed gases of He+1.3%Ar, He+5%N<sub>2</sub>, He+10%CO or He+2%CH<sub>4</sub> of 1 bar at room temperature. Helium and neon were purified with a trap of molecular sieves cooled at 77 K.

The gas-multiplication factor  $A$  is expressed theoretically in many ways. In this work, the expressions by Diethorn, Rose and Korff, and Townsend are discussed. The Diethorn expression is given by

$$\frac{\ln A}{V} = \frac{\ln 2}{\Delta V \cdot \ln(b/a)} \left\{ \ln V - \ln[Kpa \ln(b/a)] \right\}, \quad (5)$$

where  $\Delta V$  gives the mean energy described in volt that an electron acquires between two successive ionizing events and  $K$  is the minimum value of  $E/p$  above which the gas multiplication takes place when  $E$  is defined as the electric field<sup>7)</sup>. The multiplication factor derived first by Rose and Korff<sup>(11)</sup> and modified later by Kocharov and Korolev<sup>(12)</sup> is

$$\frac{\ln A}{\sqrt{V}} = \frac{2}{\epsilon_0 \ln(b/a)} \sqrt{V} - C_1 \sqrt{\frac{pa}{\ln(b/a)}}, \quad (6)$$

where  $\epsilon_0$  is the mean energy required to produce a secondary electron by an primary electron through the ionization process and  $C_1$  is a constant in relation to the ionization cross section. The Townsend expression formulated by Williams and Sara<sup>(13)</sup> is

$$\ln\left(\frac{\ln A}{V}\right) = -\frac{V_i pa \ln(b/a)}{D} \cdot \frac{1}{V} - \ln(V_i \ln(b/a)), \quad (7)$$

where  $V_i$  is the ionization energy of an atom of the counter gas and  $D$  is a constant.

The expressions (5)-(7) are available when  $10^2 \leq E/p \leq 10^3$ ,  $E/p \leq 10^4$  and  $E/p < 300$  ( $V \cdot \text{cm}^{-1} \cdot \text{Torr}^{-1}$ ), respectively<sup>(14)</sup>. In the present experimental situations, the gas-multiplication factor  $A$  can be described with every expressions (5)-(7) because  $E/p < 260$  ( $V \cdot \text{cm}^{-1} \cdot \text{Torr}^{-1}$ )<sup>(15)</sup>.

## 4. Results and Discussion

### 4.1 Gas-Multiplication at Low Temperature

In Fig. 1, the measured values of  $\ln M/V$  are plotted as a function of  $\ln V$  with the black symbols in the Diethorn way given by Eq. (5). In cases of the measurements with pure helium and neon, and with the mixture He-CO, the plotted values are nearly on the straight lines. But the gas-multiplication factor increases much faster with the anode voltage in cases of the measurements with the mixed gases He-Ar, He-CH<sub>4</sub> and He-N<sub>2</sub> and with pure hydrogen. In these cases, the measured values were analyzed with the least-square simultaneous fitting to both Eqs. (4) and (5), the results of which are shown by the white symbols together with the obtained value of  $\gamma_p$ . The measured values of the multiplication factor with pure helium and neon are shown in Fig. 2 in three ways given by Eqs. (5)-(7). All the values are nearly on the straight lines in three expressions. The obtained results for hydrogen are shown in Fig. 3 in a similar way to Fig. 2. The influence of photoelectrons to the multiplication factor is remarkable and the observed values are not on a straight line as shown with the black symbols. The values modified with Eqs. (4)-(7) in a similar way to the case in Fig. 2 are on the straight lines as shown with the white symbols in the figure. The observed multiplication factor with the gas mixtures of He-Ar, He-CH<sub>4</sub>, He-N<sub>2</sub> and He-CO can be analyzed in a similar way.

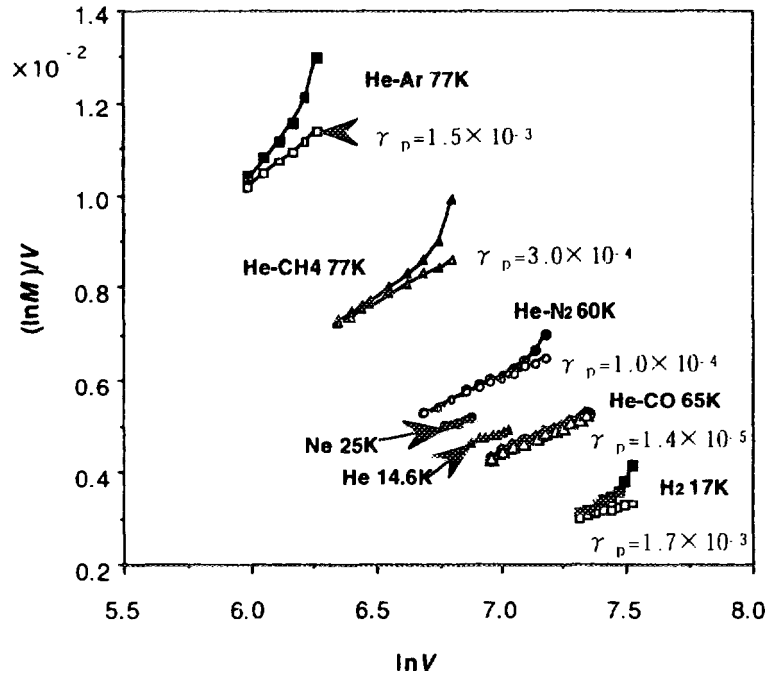


Fig.1 Gas-multiplication factor for expressed in the Diethorn way. The observed and modified, in the way given in the text, factors are shown with the black and white symbols, respectively.

The parameters obtained with Eqs. (4)-(7) are given in Table 1. The values of  $\gamma_p$  obtained from the expressions (5)-(7) agree well each other. The value of the parameter  $\epsilon_0$  in the Rose-Korff expression (6) is expected to be as large as the W-value<sup>(14)</sup>. This is realized when the counter gas is helium or neon, but in case of hydrogen the obtained  $\epsilon_0$  is larger than the W-value. The parameter  $\epsilon_0$  for the Penning gas-mixtures He-Ar and He-CH<sub>4</sub> is smaller than the W-value, while that for the other mixtures He-N<sub>2</sub> and He-CO is somewhat larger. The energy  $V_i$  of helium and neon estimated from Eq. (7) is quite similar to the ionization energy, while that of hydrogen is more than two times larger compared with the ionization energy. It is difficult to compare the parameter  $V_i$  in a mixed gas with the ionization energy, because there is no clear definition of the ionization energy of a mixed gas. In the present work, therefore, the parameter  $V_i$  is compared with the ionization energy of the minor gas molecule, i.e. CH<sub>4</sub> in case of the mixture He-CH<sub>4</sub>. The measured value of  $V_i$  of He-Ar is smaller than that of the ionization energy of Ar and *vice versa* in the other gas mixtures.

There is only few other measurements of  $V_i$  in a proportional counter filled with the pure gases and gas mixtures used in the present experiment, because these gases and gas mixtures are not popular as a filling gas of a proportional counter operated at room temperature. In the present work, therefore, the parameter  $V_i$  was compared with the corresponding ionization energy. This parameter can also be obtained from the experiments of a gas discharge. The first Townsend coefficient  $\alpha$ , which is the number of ion pairs per cm produced in a Townsend avalanche, is given by<sup>(13)</sup>

Table 1. Parameters obtained with three expressions of Diethorn, Rose and Korff, and Townsend. The W-value  $W$  and ionization energy  $I$  are also given.

	Diethorn			Rose-Korff			Townsend			$W$ (eV)	$I$ (eV)
	$\gamma_p$	$\Delta V$ (V)	$\Delta V/W$	$\gamma_p$	$\epsilon_0$ (V)	$\epsilon_0/W$	$\gamma_p$	$V_i$ (V)	$V_i/I$		
He (14.6 K)		68	1.6		40	1.0		24	1.0	41.3	24.6
Ne (25 K)		55	1.6		35	1.0		21	1.0	35.4	21.6
H <sub>2</sub> (17 K)	$1.7 \times 10^{-3}$	77	2.1	$1.8 \times 10^{-3}$	55	1.5	$1.8 \times 10^{-3}$	33	2.1	36.5	15.4
He-Ar (77 K)	$1.5 \times 10^{-3}$	26	0.9	$1.6 \times 10^{-3}$	17	0.6	$1.6 \times 10^{-3}$	10	0.6	28.6	15.8 (Ar)
He-CH <sub>4</sub> (77 K)	$3.0 \times 10^{-4}$	39	1.3	$3.3 \times 10^{-4}$	24	0.8	$3.5 \times 10^{-4}$	14	1.1	30.3	12.6 (CH <sub>4</sub> )
He-N <sub>2</sub> (60 K)	$1.0 \times 10^{-4}$	44	1.4	$1.2 \times 10^{-4}$	30	1.0	$1.2 \times 10^{-4}$	18	1.2	31.5	15.6 (N <sub>2</sub> )
He-CO (65 K)		46	1.5		33	1.1		20	1.4	31	14.0 (CO)
										(30-35)	

Table 2. Parameters obtained from the experiments of a gas discharge.

	$V_i$ (V)	$I$ (eV)	$V_i/I$
He <sup>(1)</sup>	11	24.6	0.4
Ne <sup>(1)</sup>	25	21.6	1.2
Ar <sup>(1)</sup>	13	15.8	0.8
H <sub>2</sub> <sup>(1)</sup>	26	15.4	1.7
H <sub>2</sub> <sup>(2)</sup>	27.2	15.4	1.8
Ar+10%CH <sub>4</sub> <sup>(3)</sup>	16	12.6 (CH <sub>4</sub> )	1.3

(1) Ref. 16, (2) Ref. 17 and (3) Ref. 13.

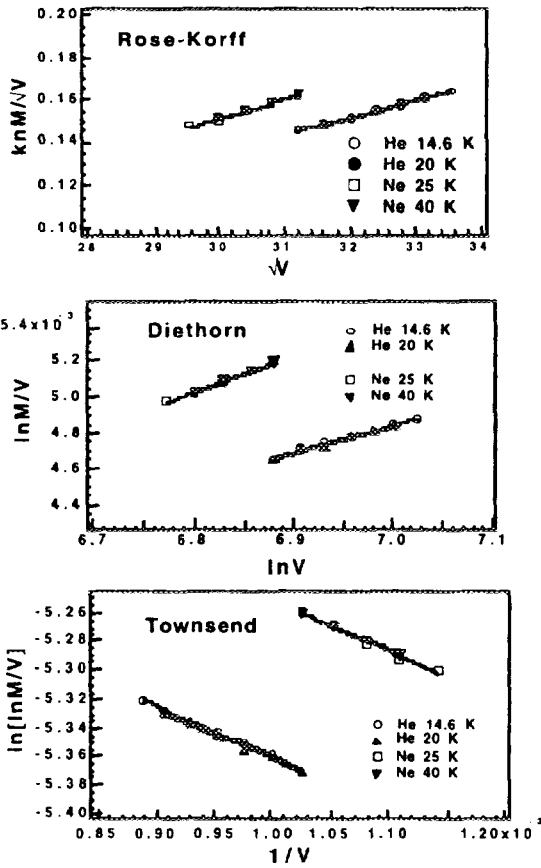


Fig. 2 Gas-multiplication factor for helium and neon described in three ways in the text.

$$\frac{\alpha}{p} = A_1 \exp\left(-\frac{B_1 p}{E}\right), \quad (8)$$

where  $A_1$  and  $B_1$  are the constants and the parameter  $V_1$  is described with these constants,  $V_1 = A_1/B_1$ . The experimental results so far obtained with this method are summarized in Table 2. The value  $V_1$  of neon (25 V<sup>(16)</sup>) is comparable with the result obtained in the present work (21 V). However,  $V_1$  of helium (11V) is extremely small, i.e., approximately half of the ionization energy, which may be the influence of impurity gases. In case of hydrogen,  $V_1$  is 26<sup>(16)</sup> or 27.2<sup>(17)</sup> V which agrees well the present result 33 V. The value 16 V of the gas mixture Ar-CH<sub>4</sub> obtained by Williams and Sara<sup>(13)</sup> is similar to the present result 14 V of the He-CH<sub>4</sub> mixture, but it is not evident that a comparison between them is reasonable or not because the major component of the mixture is different in two measurements, i.e., argon and helium.

#### 4.2 Influence of Electrons Emitted at Neutralization

As can be seen in Fig. 2, the gas-multiplication factor of helium and neon at low temperature is described well with any expressions (5)-(7), which means that the influence of photoelectrons to the multiplication factor is negligibly small. At room

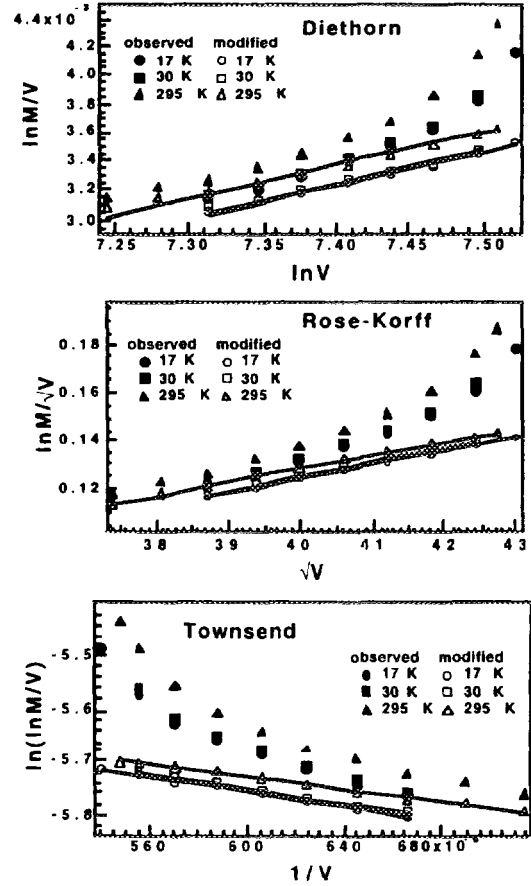


Fig. 3 Gas-multiplication factor for hydrogen described in three ways in the text. The black and white symbols represent the observed and modified factors, respectively.

temperature, the multiplication factor changes with time after filling the pure gas into the counter. The multiplication factor observed just after filling the gas is given in Fig. 4 in the Diethorn expression (5). The parameter  $\Delta V$  estimated at room temperature, 32 V, is small in comparison with that at low temperature shown in Table 1. Taken into consideration that the  $W$ -value of helium decreases extremely with very few impurity, this small  $\Delta V$  suggests that impurity molecules in helium and neon play a determinant role in operation of the proportional counter at room temperature and make the value of  $\gamma_p$  in Eq. (4) large,  $1.2 \times 10^{-3}$  for helium and  $1.5 \times 10^{-3}$  for neon, because almost no photon from an excited impurity molecule is absorbed by the other molecules of very few impurity. The proportional counter works at low temperature, below 22 K for helium, and at room temperature. At any other temperature, spurious pulses appear at a anode voltage of several hundred volts and the counter discharges at a higher voltage: no signal pulse becomes higher than noise level due to the low energy of electrons emitted from  $^{57}\text{Co}$  and the small gas-multiplication factor. The anode voltage at which the counter discharges

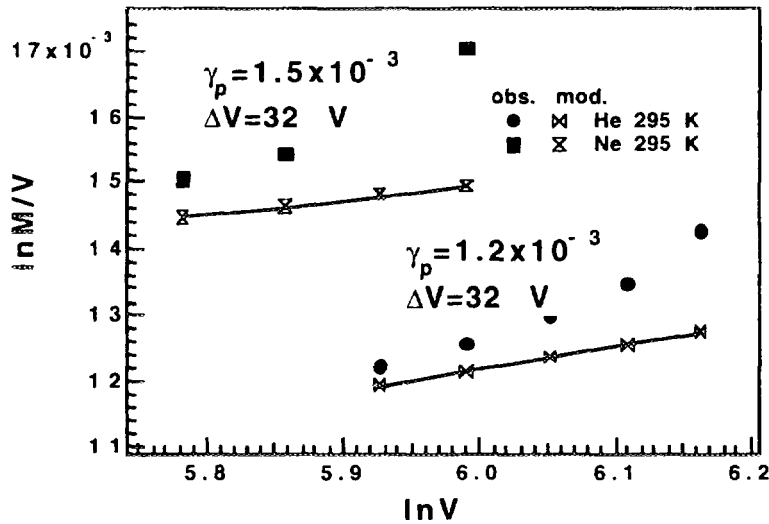


Fig. 4 Gas-multiplication factor for helium and neon observed just after filling the gas into the counter.

or spurious pulses appear is given as a function of temperature in Fig. 5. In the figure, the results obtained by Isozumi *et al.*<sup>(18,19)</sup> are also shown. The value of  $E/p$  corresponding to the anode voltage is marked on the right vertical axis.

A self-maintaining discharge of the counter takes place when the following Townsend condition is satisfied<sup>(20)</sup>;

$$\gamma \cdot A = 1, \quad (9)$$

where  $\gamma$  is the number of electrons liberated per ionization and is described in three terms

$$\gamma = \gamma_i + \gamma_p + \gamma_m. \quad (10)$$

Here,  $\gamma_p$  has been already defined at Eq. (4) and  $\gamma_i$  and  $\gamma_m$  are the number of electrons emitted when an ion is neutralized at the cathode and those emitted when a metastable atom transfers to the ground state at the cathode, respectively. It is not necessary to think about  $\gamma_m$  because the lifetime of a metastable state is very short in the experimental

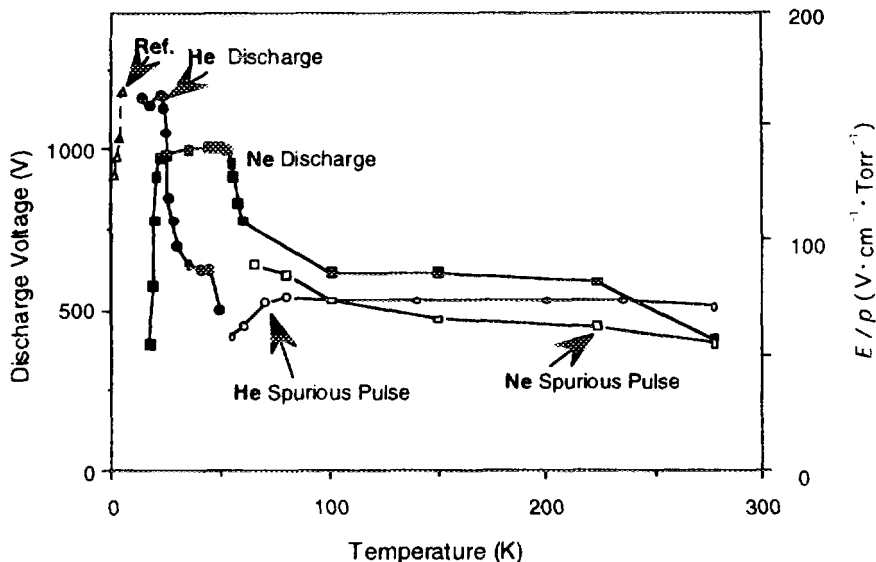


Fig. 5 Anode voltage at which the counter discharges or spurious pulses appear.

situations of the present work. The gas-multiplication factor  $A$  just before a self-maintaining discharge is approximately 330 for helium at low temperature and does not change with gas density, from which  $\gamma$  is estimated to be  $3 \times 10^{-3}$ . If this value of  $\gamma$  is mainly contributed by  $\gamma_p$ , the gas-multiplication factor increases much faster with the anode voltage than that shown in Fig. 1 because a photoelectron comes back to the zone near the anode wire within  $1 \mu\text{s}$  after a gas molecule is excited and causes the electron avalanche to grow up faster. The discharge of the counter at low temperature, therefore, is not due to photoelectrons but due to electrons formed at neutralization of an ion. These considerations lead that  $\gamma_i = 3 \times 10^{-3}$ . This value of  $\gamma_i$  agrees well with that estimated by comparing the pulse height of a signal and spurious pulses by Isozumi *et al.*<sup>(21)</sup>; i.e.,  $\gamma_i = 2.5 \times 10^{-3}$ . Spurious pulses follow a signal pulse at an interval of about  $100 \mu\text{s}$  and have no contribution to the gas-multiplication factor, because the signal pulse is clipped in about  $1 \mu\text{s}$ . It is, therefore, reasonable to assume that it is not  $\gamma_p$  but  $\gamma_i$  that is responsible to the discharge of the counter. The gas-multiplication factor of helium and neon at low temperature is described with the expressions (5)-(7) as seen in Fig. 2 and, therefore,  $\gamma_p$  is expected to be negligibly small at low temperature. The parameter  $\Delta V$  of helium at 20 K and of neon at 40 K are the same as that of helium at 14.6 K and that of neon at 25 K, respectively. Supposing that, at higher temperature too,  $\gamma_p$  is small and  $\Delta V$  has no temperature dependence, the maximum gas-multiplication factor  $A$  can be estimated, with the Diethorn expression (5), from the anode voltage at which the counter discharges or the spurious pulses appear as shown in Fig. 5. The value of  $\gamma_i$  is calculated from the maximum multiplication factor by using the Townsend condition (9), which is shown in Fig. 6 as a function of temperature. The figure tells us the value  $\gamma_i$  at low temperature is approximately  $3.0 \times 10^{-3}$  for helium and  $5.3 \times 10^{-3}$  for neon. It increases drastically above 20 K in case of helium and above 53 K in case of neon, and approaches a value close to 0.17 being the value of  $\gamma_i$  at room temperature<sup>(22)</sup>. From the above discussions, it may safely be said that a proportional counter filled with helium or

neon works stably because of a small value of  $\gamma_i$  at low temperature. The value of  $\gamma_i$  increases with temperature and the counter starts to discharge at a small gas-multiplication factor. At higher temperature, therefore, the counter does not work for all practical purposes.

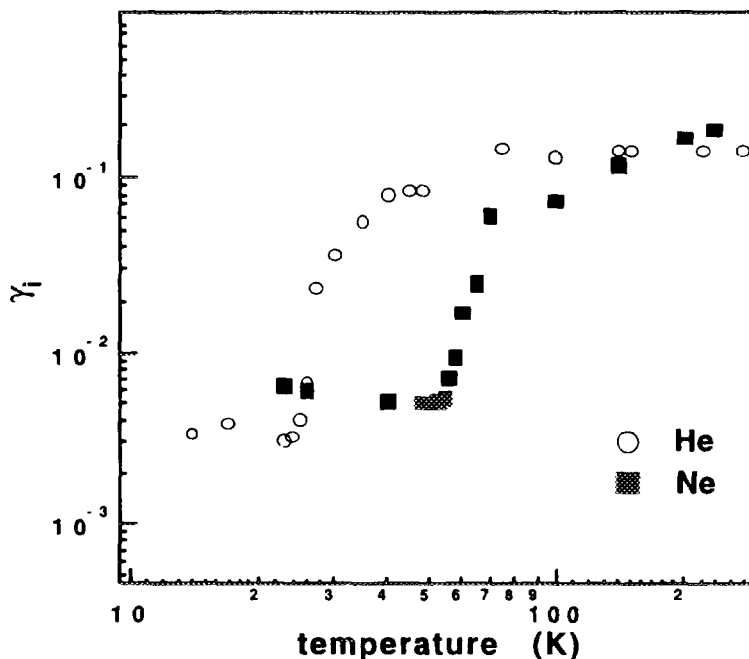


Fig. 6 Number of electrons emitted at neutralization of an ion  $\gamma_i$  given as a function of temperature.

In the present work, the following conclusions are derived. The gas-multiplication factor of a proportional counter filled with helium, neon or the He+10%CO mixture is described well with the expressions (5)-(7) of Diethorn, Rose and Korff, and Townsend. When the counter gas is hydrogen, He+1.3%Ar, He+2%CH<sub>4</sub> or He+5%N<sub>2</sub>, the influence of photoelectrons is remarkable, but the above three expressions are also available if this influence is excluded from the observed multiplication factor. The number of photoelectrons per ion pair  $\gamma_p$  estimated so as to fit simultaneously to Eq. (4) and to the expressions (5)-(7) is very similar to each other. By estimating several parameters with the above three expressions, it becomes possible to discuss in detail about the operational mechanism of a proportional counter. When the counter is filled with helium or neon, the number of electrons emitted at neutralization of an ion  $\gamma_i$  plays a determinant role in stability of the counter operation.

## References

- (1) K. R. Swanson and J. J. Spijkerman, *J. Appl. Phys.*, **41** (1970) 3155.
- (2) Y. Isozumi and M. Takafuchi, *Bull. Inst. Chem. Res. Kyoto Univ.*, **53** (1975) 147.
- (3) Y. Isozumi, S. Kishimoto, R. Katano and H. Takekoshi, *Rev. Sci. Instrum.*, **58** (1987) 293.
- (4) K. Fukumura, R. Katano, T. Kobayashi, A. Nakanishi and Y. Isozumi, *Nucl. Instrum. Methods*, **A301** (1991) 482.
- (5) K. Fukumura, A. Nakanishi, T. Kobayashi, R. Katano and Y. Isozumi, *Nucl. Instrum. Methods*, **B61** (1991) 127.
- (6) K. Fukumura, A. Nakanishi and T. Kobayashi, *Nucl. Instrum. Methods*, **B86** (1994) 387.
- (7) W. Diethorn, NYO-6628 (1956).
- (8) K. Fukumura, A. Nakanishi and T. Kobayashi, *KEK Proceedings*, **95-1** (1995) 121.
- (9) E. Mathieson and M. W. Charles, *Nucl. Instrum. Methods*, **72** (1969) 155.
- (10) B. Rossi and H. H. Staub, *Ionization Chambers and Counters*, (McGraw-Hill, New York, 1949).
- (11) M. E. Rose and S. A. Korff, *Phys. Rev.*, **59** (1941) 850.
- (12) G. E. Kocharov and G. A. Korolev, *Bull. Acad. Sci., USSR, Phys. Ser.*, **27** (1963) 308.
- (13) A. Williams and R. I. Sara, *Int. J. Appl. Radiation Isotopes*, **13** (1962) 229.
- (14) H. J. Specht and P. Ambruster, *Nukleonik*, **7** (1965) 8.
- (15) W. Bambynek, *Nucl. Instrum. Methods*, **112** (1973) 103.
- (16) P. R. Evance, *Spark, Streamer, Proportional and Drift Chambers*, (The Richelieu Press, London, 1974).
- (17) D. J. Rose, *Phys. Rev.*, **104** (1956) 273.
- (18) S. Kishimoto, Y. Isozumi, R. Katano and H. Takekoshi, *Nucl. Instrum. Methods*, **A262** (1987) 413.
- (19) Y. Isozumi, S. Ito, T. Fujii and R. Katano, *Rev. Sci. Instrum.*, **60** (1989) 3262.
- (20) M. J. Druyvesteyn and F. M. Penning, *Rev. Mod. Phys.*, **12** (1940) 87.
- (21) Y. Isozumi, R. Katano, S. Ito and S. Kishimoto, *Nucl. Instrum. Methods*, **A355** (1995) 443.
- (22) W. W. McDaniel, *Collision Phenomena in Ionized Gases*, (John Wiley & Sons, 1964).

# Design of an Efficient Pulsing System for a Slow-Positron Beam

Nagayasu Oshima  
Department of Accelerator science,  
The Graduate University for Advanced Studies  
1-1, Oho, Tsukuba-shi, Ibaraki, 305 Japan

Takenori Suzuki  
Radiation Safety Control Center,  
National Laboratory for High Energy Physics  
1-1, Oho, Tsukuba-shi, Ibaraki, 305 Japan

Ikuzo Kanazawa  
Department of Physics, Tokyo Gakugei University  
4-1-1, Nukuikitamachi, Koganei-shi, Tokyo, 184 Japan

Yasuo Ito  
Research Center for Nuclear Science and Technology,  
The University of Tokyo  
Tokai, Ibaraki, 319-11 Japan

## 1 Introduction

Positron-annihilation lifetime spectroscopy (PALS) has been applied for a long time in order to conduct materials research, since the positron-lifetime spectra reflect the state especially concerned with defects and electron states. In order to obtain a start signal in a positron-lifetime measurement, the  $\beta^+$  decay radioisotope  $^{22}\text{Na}$  is suitable for a positron source, since it emits a 1.27-MeV  $\gamma$  quantum together simultaneously with positron. PALS uses the 1.27-MeV  $\gamma$  quantum for a start signal and a 0.51-MeV positron annihilation  $\gamma$  quantum for a stop signal. However, positrons from  $^{22}\text{Na}$  are not convenient due to the wide energy distribution for a precise spot investigation, such as the surface of materials, the interface of multilayers and the depth dependence of specimens, etc.

For such extended applications, a variable-energy positron beam is a useful technique. However, the 1.27-MeV  $\gamma$  quantum is no longer available in the technique as the start

signal to give information about positron injection into matter. Thus, some contrivance must be added to a positron-beam system. Up to the present, two methods are known to make up for the lack of the start signal. One way to know when positrons strike a target is the detection of secondary electrons, which are emitted from the surface after positron impact<sup>(1)</sup>. In this method there are some limitations for a positron-lifetime measurement: the time-of flight of the secondary electrons to the detector results in an insufficient time resolution, and the secondary electrons are not always emitted, which reduces the detection efficiency<sup>(1)</sup>.

The other method to obtain a start signal is to manipulate the positron beam so that the positrons can only arrive at preselected times<sup>(2)</sup>. In this case, the trigger signal to the pulsing system is available as the start signal for PALS. A pulsed slow-positron beam system using a pulsed parabolic-potential bias,<sup>(3)</sup> which produced a trigger signal, was constructed by W.S. Crane and A.P. Mills, Jr. in 1985; and a time resolution less than 500ps was achieved. However, the 500ps resolution is not sufficient to study PALS. The time resolution of the detection system should be about 250ps for PALS; in other words, the time width of a slow-positron pulse should be about 180ps.

For the last several years, pulsed slow positron system with sufficient time resolution has been developed using an RF bunching<sup>(4,5,6)</sup> and applied to PALS of some condensed matter<sup>(7,8,9)</sup> by Munchen Univ. and Electrotechnical Laboratory in Japan. Their bunched-positron beam has a 150ps time width, but the RF method is not cheap to construct at the laboratory level, and moreover the pulsed slow positrons with the RF have a limitation in their minimum energy, about 500 eV.

In this paper, a new design of a pulsed slow positron system for PALS measurement is reported. By using this new system, it will be possible to obtain a short-pulsed slow-positron beam with high efficiency ( $\geq 50\%$ ) and a relatively low minimum energy ( $\sim 200$  eV). This system is also easy to construct on the laboratory scale.

## 2 Design of the pulsing system

Basically, this method originates from the pulsing system which was applied for a positronium study by Mills et al.<sup>(2,10)</sup>, where 10ns time-width positron pulses were formed, which is the time resolution only useful when long lifetimes of o-Ps in gases and vacuum is the matter of concern.

Our design of the pulsed slow-positron beam line and the lifetime measurement system

are shown in Fig.1. Fast positrons from a radioisotope enter a moderator placed behind the positron source, and a fraction of the positrons stopped in the moderator reaches the surface with thermal energy. Consequently, positrons can be reemitted as slow positrons due to the negative work function of the moderator for the positrons. These slow positrons are collected and accelerated by an electric field which is formed between the moderator and a mesh electrode.

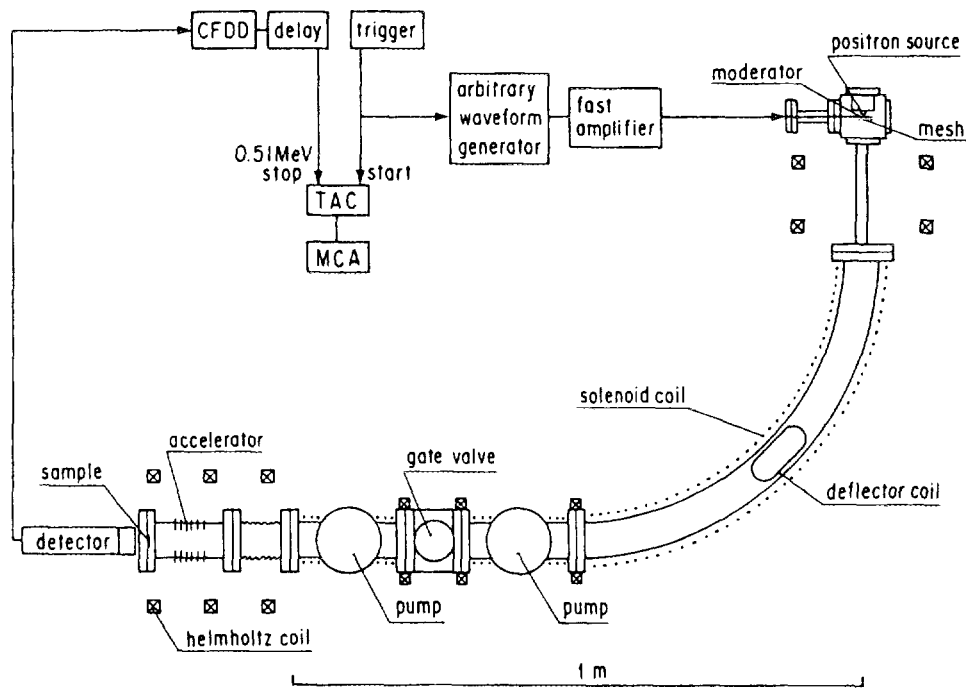


Figure 1: A design of a pulsing system for slow-positron beam

In this system there is one solenoid coil and eight Helmholtz coils to lead positrons from the moderator to the sample. To adjust the implantation energy of the pulsed positrons, an accelerator ring is placed before the sample which can form a static electric field in the direction of the beam axis. The use of an arbitrary waveform generator and a post amplifier (shown in Fig.1) is the fundamental part of the pulsing system by which positrons are sent to the sample at a defined regular interval.

### 3 Analytical examination of the pulsing system

We assume that a positron leaves the moderator with energy  $E_0$ [eV] at  $t=0$  and then arrives at the sample at  $t=T_0$ .  $T_0$  is given as follows(1):

$$T_0 = \frac{1}{\sqrt{2s}} \left\{ \frac{L_1}{\sqrt{E_0}} + \frac{2L_2(\sqrt{E_0 + V_a} - \sqrt{E_0})}{V_a} \right\}, \quad (1)$$

where  $E_0$ [V] is the moderator bias,  $s(=\frac{e}{m_e})$ [C/kg] the specific charge of positron,  $L_1$ [m] the distance from the moderator to the accelerator ring,  $L_2$ [m] the length of the accelerator, and  $V_a$ [V] the acceleration bias of the accelerator ring. To inject positrons into the sample at  $T_0$  within one pulsing interval, the positrons which are reemitted from the moderator should have an appropriate energy  $V(t)$ [eV], where  $V(t)$ [V] is the solution of

$$T_0 - t = \frac{1}{\sqrt{2s}} \left\{ \frac{L_1}{\sqrt{V(t)}} + \frac{2L_2(\sqrt{V(t) + V_a} - \sqrt{V(t)})}{V_a} \right\}. \quad (2)$$

Positrons which leave the moderator at time  $t$  arrives at the sample at time  $T_0$  in each interval of pulsing if the moderator bias( $V(t)$ ) is supplied exactly.  $V(t)$  should be cycled at less than about 30MHz, since a pulsing interval longer than about 30 ns is preferred to measure the positron lifetime.

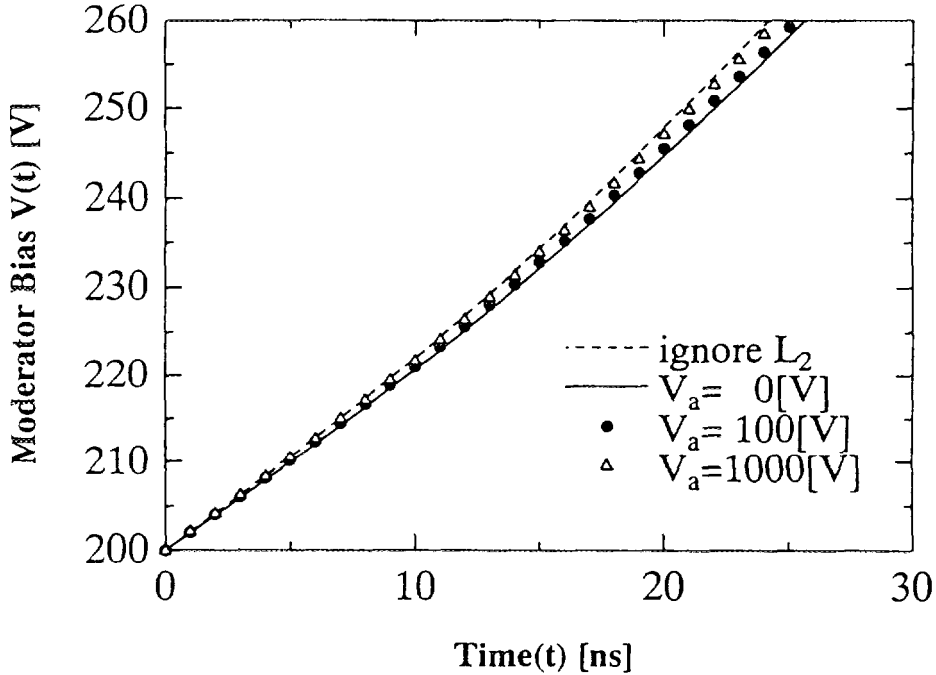


Figure 2: The waveform of the moderator bias ( $V(t)$ ) for the geometry in Fig.1

After pulsing, the positron-energy distribution would spread somewhat due to the acceleration  $V(t)$ . To bunch particles under conservative forces, any system must obey Liouville's theorem, which keeps the constant volume of phase space occupied by an en-

semble of particles. This principle demands that the energy is spread if the time width is decreased.

The moderator bias( $V(t)$ ), which is a function of  $t$ , is shown in Fig.2; making proper assumptions of the parameters of the system shown in Fig.1 as  $L_1=1.65[\text{m}]$ ,  $L_2=0.1[\text{m}]$  and  $E_0=200[\text{eV}]$ , we calculated the moderator bias for four cases. The solid line was calculated with  $V_a=0[\text{V}]$ , which means no acceleration by the accelerator ring. The broken line corresponds to the case where  $L_2$  was neglected( $L_2=0$ ), which is an approximation when  $V_a$  has a sufficiently high value. Consequently,  $V(t)$  for other cases exists between the solid line and the broken line. For instance,  $V_a=100[\text{V}]$  for a circle and  $V_a=1000[\text{V}]$  for a triangle, respectively. The approximate  $V(t)$  with  $L_2=0$  reduces to the following simple form:

$$V(t) = \frac{L_1^2}{2s(T_0 - t)^2} \quad (3)$$

and

$$T_0 = \frac{L_1}{\sqrt{2sE_0}}. \quad (4)$$

The simple equations (3) and (4) easily give the waveform of  $V(t)$  before solving equations (1) and (2).

However, to produce a short positron pulse which is available for PALS using this system, there are two special requirements. One requirement is to use a special bias supply that can generate a suitable fast changing bias( $V(t)$ ). We have estimated that it is possible to make an electronics circuit to supply a moderator bias of up to  $E_0+60\text{v}$  with a fast arbitrary waveform generator(AG5100, YOKOGAWA) and a fast post amplifier(T142-4029A, THAMWAY). The other requirement is the narrow energy distribution of slow positrons, because if positrons have an uncertain velocity while traveling from the moderator, the arrival time to the sample would also be uncertain, namely the time width of the pulse would spread.

The plotted calculated data in Fig.3, which include a consideration of the positron energy uncertainty before pulsing and is useful to roughly estimate the pulsing efficiency. These data were calculated on the condition that  $E_0(0\sim 200[\text{V}])$ ,  $L_1(0\sim 200[\text{cm}])$ ,  $L_2=0[\text{cm}]$  and  $V(t)(E_0\sim E_0+60[\text{V}])$  using equations (3) and (4), and the slow-positron energy distribution was assumed to be Gaussian. The horizontal axis of Fig.3 gives the uncertainty in the positron energy expressed by the FWHM(eV) of the Gaussian distribution. The vertical

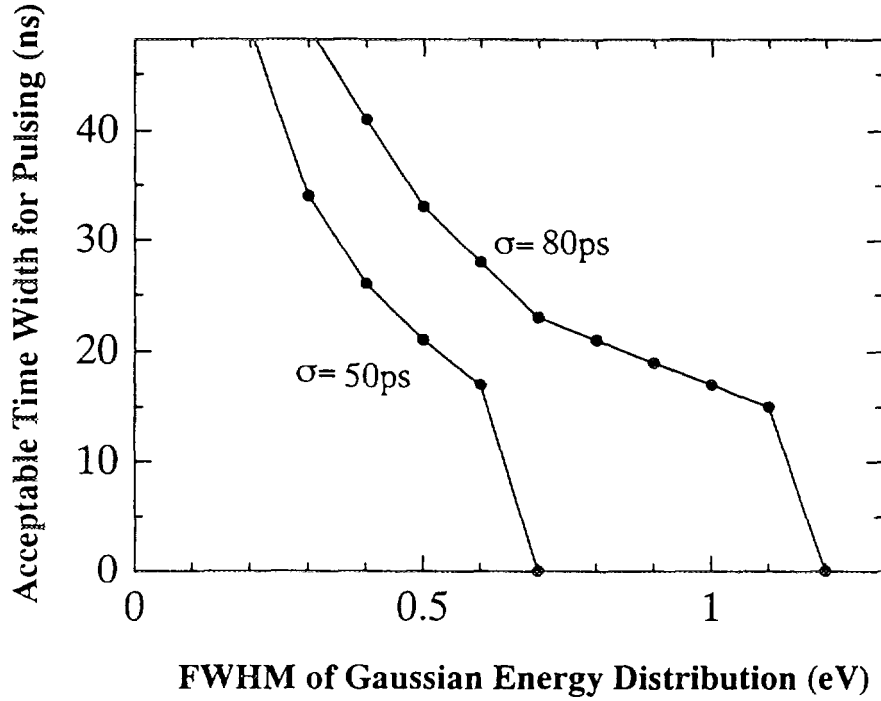


Figure 3: The relationship between the maximum time window for pulsing and the slow-positron energy uncertainty

axis is the maximum time window that can be bunched to pulsed positrons within  $\sigma$ (ps) lag time from  $T_0$ . Here, it should be noticed that  $\sigma$  is not the time resolution of the start-signal detection. We have estimated that the real time resolution for the start-signal detection is more than twice  $\sigma$ . Therefore, the pulsing system should be designed aiming for  $\sigma \leq 80$ ps. The solid line in Fig.3 ( $\sigma=80$ ps) gives useful information that if the energy uncertainty of positrons which are reemitted from the moderator are 1eV at FWHM, the  $V(t)$  moderator bias can be supplied to the time window  $t=17$ ns to make a positron pulse within a 80ps time lag from  $T_0$ . If the positron-energy distribution is 1eV at FWHM, the efficiency for the pulsing, which is to be produced at 30ns intervals, is 57%(=17ns/30ns) at the maximum.

The waveform generator of the moderator bias( $V(t)$ ) is not fast enough. It cannot generate waveform especially when  $V(t)$  suddenly decrease to  $E_0$  for a repeat. However, if a sufficiently narrow positron energy distribution is obtained, say about 0.5eV, high efficiency of pulsing would become possible.

## 4 Conclusion

In this paper, a new design concept for a pulsed slow-positron system has been reported, and the possibility of the system for pulsing has been analytically demonstrated. Especially, a high efficiency of positron pulsing can be achieved. To construct this system, a fast electronics circuit to generate the moderator bias( $V(t)$ ) and slow positrons having narrow energy distribution of less than 1.0eV are required. The former can be attained by use of the modern fast electronics and the latter requirements easily fulfilled using a conventional moderator<sup>(2,3,5)</sup>.

We have already started to construct the electronics and attained narrow energy distribution of the reemitted positron energy; 0.58eV at FWHM with a Ni moderator. Therefore, the designed system has a strong possibility to be produced at a laboratory scale.

## References

- [1] K.G.Lynn, W.E.Friese and P.J.Schultz, Phys. Rev. Lett. 52 (1984)
- [2] A.P.Mills,Jr., Appl. Phys. 22 (1980)273.
- [3] W.S.Crane and A.P.Mills,Jr., Rev. Sci. Instrum. 56 (1985) 1723.
- [4] D.Schödlbauer, P.Sperr, G.Kögel and W.Triftshäuser, Nucl. Instrum. Methods. B34 (1988) 258.
- [5] P.Willutzki, J.Stormer, G.Kögel, P.Sperr, D.T.Britton, R.Steindl and W.Triftshäuser, Meas. Sci. Technol. 5 (1994) 548.
- [6] R.Suzuki, Y.Kobayashi, T.Mikado, H.Ohgaki, M.Chiwaki, T.Yamazaki and T.Tomomasu, Jpn. J. Appl. Phys. 30 (1991) 532.
- [7] G.Kögel, D.Schödlbauer, W.triftshäuer, J.Winter, Phys. Rev. Lett. 60 (1988) 1150.
- [8] D.T.Britton, P.Willutzki, W.Triftsha'user, E.Hammerl, W.Hansch, and I.Eisele, Appl. Phys. A58 (1994) 389.
- [9] R.Suzuki, T.Mikado, M.Chiwaki, H.Ohgaki and T.Yamazaki, Appl. Surf. Sci. 85 (1995) 87.
- [10] A.P.Mills,Jr., and L.Pfeiffer, Phys. Rev. Lett. 43 (1979) 1961.

# DEVELOPMENT OF A DISTRIBUTED RADIATION DETECTION SYSTEM USING OPTICAL FIBERS

Fredrik Jensen, Goro Inouchi, Eiji Takada,  
Hiroyuki Takahashi, Tetsuo Iguchi, Masaharu Nakazawa  
Department of Quantum engineering and Systems Science,  
University of Tokyo  
7-3-1 Hongo, Bunkyo-ku, Tokyo, JAPAN

Tsunemi Kakuta  
Japan Atomic Energy Research Institute  
Advanced Science Research Center,  
Research Group for Quantum Radiation Measurement  
2-4 Shirakata-Shirane, Tokai-mura, Naka-gun  
Ibaraki-ken 319-11, JAPAN

## 1. INTRODUCTION

A system capable of radiation sensing over a distance of several kilometers have been realized using optical fibers and Optical Time Domain Reflectometry (OTDR). In connection with this we have also studied the fundamental properties of some optical fibers subjected to both gamma and neutron radiation.

Optical methods such as OTDR allow for measurement of induced attenuation in optical fibers of several kilometers length. The principle of OTDR is shown in fig.(1). It relies on the backscattering of light that has been launched in an optical fiber from a pulsed source<sup>(1)</sup>. The light is Rayleigh scattered from refractive index fluctuations in the core of the fiber and the backscatter is subsequently detected. The OTDR can sense changes in the total attenuation coefficient and it is well known that radiation can induce attenuation in optical fibers<sup>(2)</sup>. It therefore becomes possible to detect radiation with optical fibers. The radiation shows up as an increase in the slope of the curve given by the backscattered intensity as a function of distance (see fig.(1)). The slope is thus proportional to the induced loss which in turn is related to the absorbed dose. Thus we get both the radiation level and the radiation distribution in space simultaneously. An example of an experimental OTDR trace is shown in fig.(2). Two pieces of fiber were irradiated at the same exposure rate of 100kR/hr at a temperature of 15°C.

The irradiated pieces were 2m and 10m long respectively. It was found that for the present system the minimum fiber response length was about 10m. This depends on the laser used, i.e. the pulse length and intensity, as well as the read out electronics of the system.

The response of the optical fiber to radiation depends on dose rate and radiation type but also temperature. Further the power and wavelength of the injected light is of great importance. Of particular concern is dose rate and temperature dependence. Factors inherent in the fiber affecting the radiation induced attenuation include the fabrication process, presence of intrinsic defects and dopants as well as fiber type (multimode, single mode etc.). For sensing applications it is for these reasons imperative to determine the dependency of the radiation induced response on the above parameters. Different fibres may be suitable in different sensing applications depending on total dose, dose rate and temperature.

The sensitivity of optical fibers depend strongly on dopants and probing wavelength. This feature can be seen in fig.(3). In general a shorter wavelength means higher sensitivity. The highest sensitivity of the fibers shown is for PbO-doped fibers. However, as suitable sensing fiber lengths for the investigated OTDR system is typically several hundred meters up to several kilometers Ge-doped fibers are the most readily available. We have thus investigated the response of the OTDR system with Ge-doped fibers.

## 2. RADIATION EFFECTS ON THE OPTICAL PROPERTIES OF OPTICAL FIBERS

The interaction between radiation and the fiber glass produces changes in the electronic structure of the material in the core and cladding. Free electrons and holes created by radiation are captured on preexisting defects to create so-called color centers that absorb light. In addition structural defects may be created by radiation and these radiation induced defects may then capture electrons and holes just as in the case of the preexisting defects. The situation may be additionally complicated by interactions between different types of color centers which may change the absorption spectrum of the fibers.

Thus what we will measure in absorption-based radiation sensing with optical fibers is the increase in color center density, which shows up as an increase in absorption of the fibers. An idealized absorption spectrum is displayed in fig.(4) for Ge-doped glass. Three major color centers contribute in this simplified picture to the absorption spectrum<sup>(3)</sup>: the oxygen

hole center (OHC) at 517nm, the Ge(1)-center at 281nm and finally Ge(2) at 213nm. We can observe that over the major portion of the visible spectrum the absorption of Ge-doped glass is given by two color centers in this simplified picture.

### 3. SIMPLE PHENOMENOLOGICAL MODEL

To predict the absorbed dose from attenuation measurements we need to find a working relation between the radiation induced loss and the absorbed dose in the fiber. As mentioned in the initial section the induced loss can depend on several parameters and this is in fact the case for Ge-doped fibers. This complicates the use of Ge-doped fibers for radiation measurements as the actual induced loss will depend on temperature, dose rate and also injected light power. However the latter parameter can be controlled in the experiments by on-line monitoring. Left is thus temperature and dose rate. It should be noted at this point that fiber materials exist in which the radiation induced loss is much less dependent on temperature and dose rate and the effect is in fact negligible for certain fiber types<sup>(4)</sup>, such as P-doped fibers.

A model have thus been developed which can account for changes in temperature and dose rate. The model is based on the creation and decay of two color centers and can describe the growth and recovery of the induced loss of Ge-doped fibers at the OTDR system wavelength of 850nm. The parameters of the model can be obtained by a least square fit to experimental data. The functional form of the model is that of saturating exponentials in the growth phase and decaying exponentials in the recovery phase:

$$A(t, T, \dot{D}) = \dot{D} \cdot L \cdot \sum_{i=1}^2 F_i(t, T)$$

where

$$F_i(t, T) = R_i(T) \cdot t_{R_i}(T) \cdot \{1 - \exp[-t/t_{R_i}(T)]\} \quad t < t_e$$

$$F_i(t, T) = F_i(t_e, T) \cdot \exp[-(t - t_e)/t_{R_i}(T)] \quad t > t_e$$

$A$ = Induced Loss (dB/km)	$i$ = Color center index
$\dot{D}$ = Dose Rate	$R_i$ = Population Rate
$T$ = Temperature	$t_{R_i}$ = Relaxation Time
$L$ = Length of Sensing Fiber	$t_e$ = End of Irradiation

To test the validity of this model the model parameters were determined from experimental growth and decay curves at various temperatures and dose rates. The time dependency of the two color centers in the model is shown in fig.(5) and fig.(6) respectively. A fit to experimental data by giving the experimentally determined temperature as only parameter is shown in fig.(7). Finally in fig.(8) we show irradiation data at different dose rates with model fits at corresponding dose rates. There is some discrepancy between the data and the model, especially at the higher dose rate. However in the experiment we irradiated slightly longer pieces of fiber at the higher dose rates. A correction for this might improve the overlap of the model with the data at higher dose rates. At this point it has not yet been possible to include photo bleaching effects in the model. Further the long-time recovery behavior is not fully accounted for. Perhaps this flaw may be remedied by including an additional long-lived loss component in the model. A more detailed study is also necessary to assign the model "color centers" to physical ones, however for the present purpose of modeling temperature and dose rate effects to predict dose values, the model seems to be adequate.

#### 4. CONCLUSION

We have confirmed the importance of temperature and dose rate for the response of Ge-doped fibers to radiation. A phenomenological model have been found to account for temperature and dose rate effects. From this model it is possible to make dose predictions from attenuation measurements when the temperature and dose rate are known.

Ge-doped fibers have been found to have a relatively low sensitivity to both neutron and gamma radiation. In addition, as noted, temperature and dose rate dependencies complicate the analysis. However we point out that these problems may all be solved if we use fibers, such as P-doped fibers, which contain color centers of long lifetime. This would remove both the temperature and dose rate dependencies that complicate the use of Ge-doped fibers, in addition the radiation sensitivity is increased.

Finally OTDR has been investigated as a possible read-out method for distributed radiation measurements. Features such as spatial resolution and fiber response length depend on the particular system used. For our system the minimum pulse length was 3ns, giving a spatial resolution in the meter range and a response length to radiation of about 10m if accurate dose values were to be obtained. We found OTDR to be a suitable method for

radiation induced attenuation measurements in optical fibers, especially for long fiber lengths and long time scales where questions of lightsource stability becomes important for other systems. Ge-doped fibers were found to be complicated to use for distributed dosimetry with OTDR. However with a more sensitive fiber the system can be used also to this end.

### References

- (1) J.P.Dakin (ed.), The Distributed Fiber Optic Sensing Handbook (Springer Verlag, Berlin 1990)
- (2) E.J. Friebele, K.J. Long, C.G. Askins, M.E. Gingerich, M.J. Marrone, D.L. Griscom, Radiation Effects in Optical materials, SPIE, 541, (1985) p.70
- (3) E.J.Friebele, D.L.Griscom, Color Centers in Glass Optical Fibers, Mat.Res.Soc.Symp.Proc., 61 (1986) p.318
- (4) H.Henschel, O.Köhn, H.U.Schmidt, Optical fibers as radiation dosimeters, NIM B69 (1992) p.307

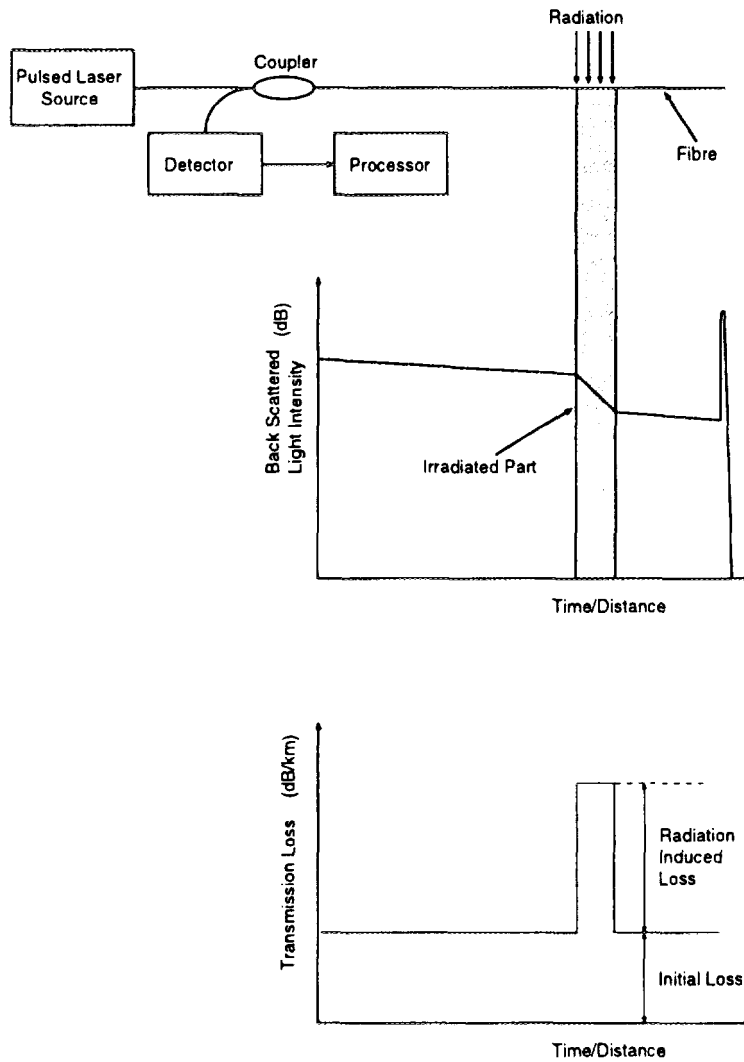


Figure 1: The principle of OTDR measurements

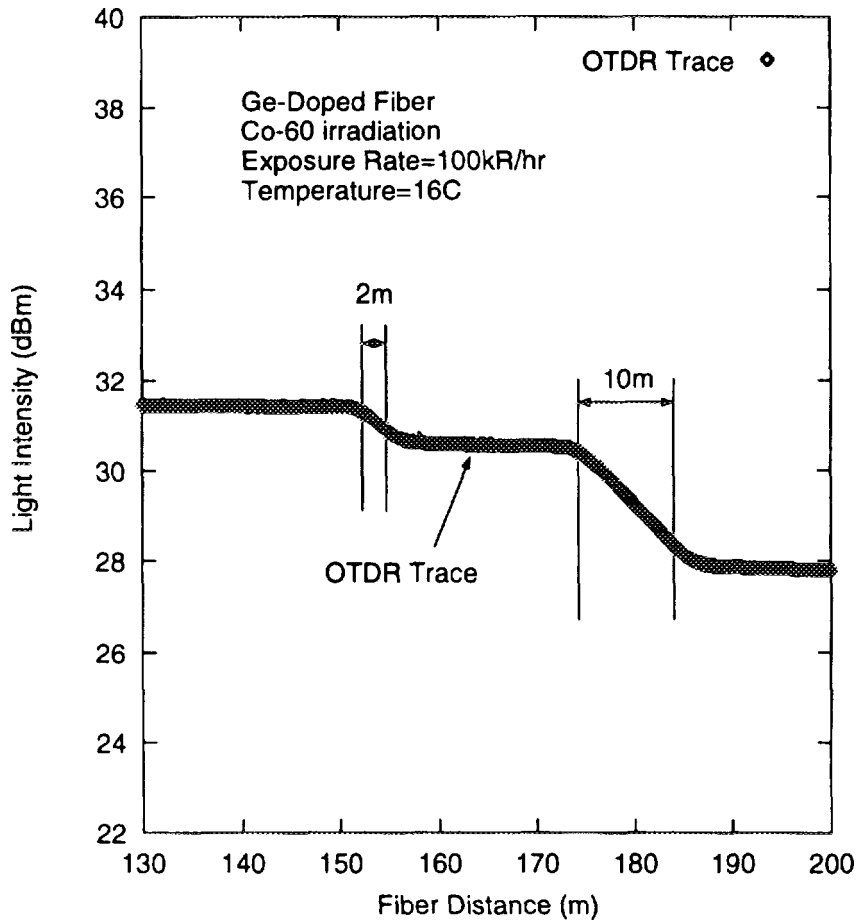


Figure 2: Radiation induced loss in Ge-doped GI fiber as measured by OTDR. A 2m and 10m piece were irradiated respectively.

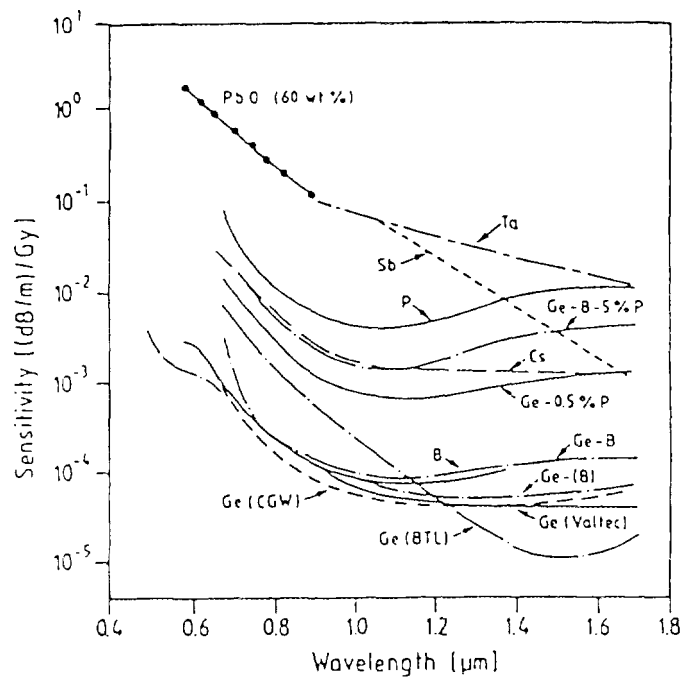


Figure 3: Sensitivity of optical fibers to radiation

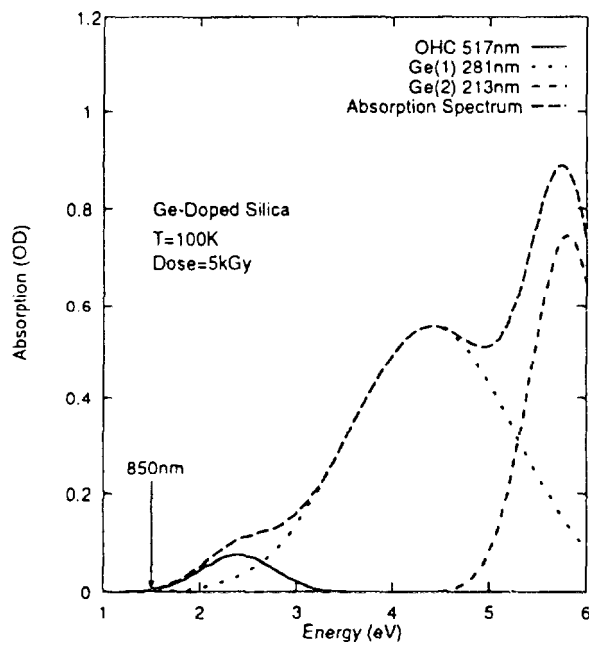


Figure 4: Color centers in Ge-doped glass (Idealized spectrum).

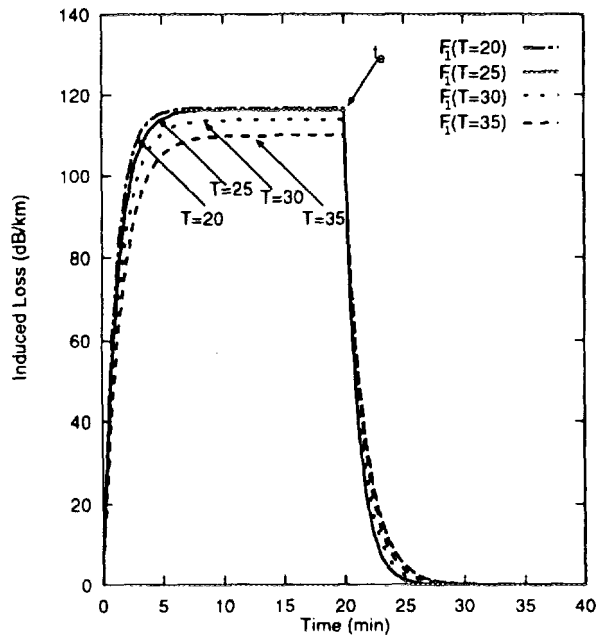


Figure 5: Time dependency of color center density  $i = 1$

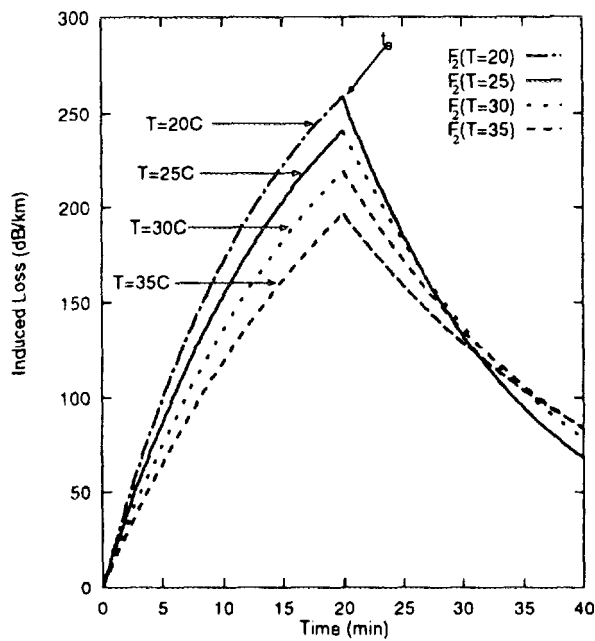


Figure 6: Time dependency of color center density  $i = 2$

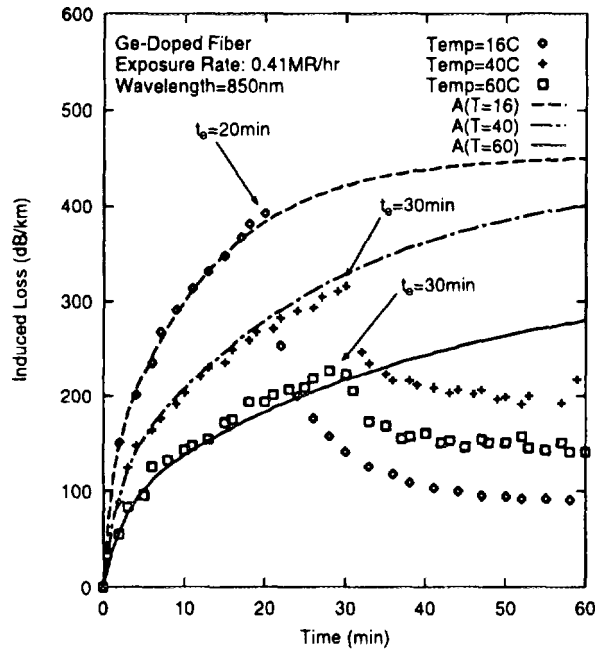


Figure 7: Model prediction with temperature as parameter. Exposure rate: 410kR/hr

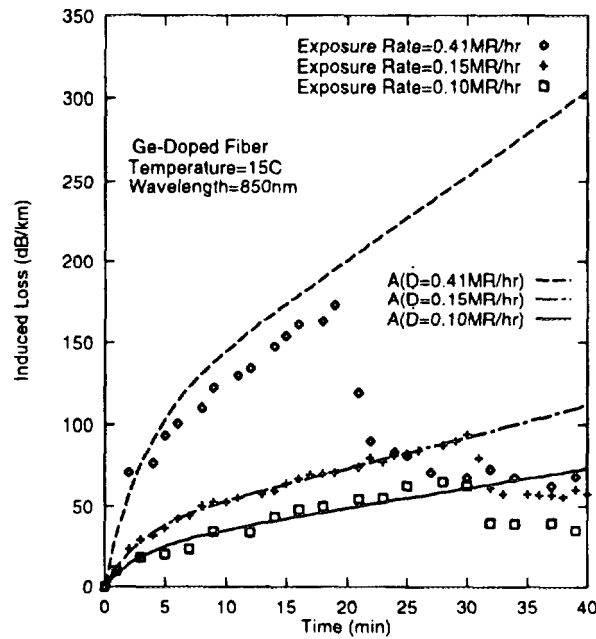


Figure 8: Model prediction with dose rate as parameter. Ambient Temperature: 15C (no fiber lead part correction)

# Development of optimal charge sensitive preamplifier for Superconducting Tunnel Junction

M.Ukibe, M.Nakazawa

Department of Quantum Engineering and Systems Science, Faculty of Engineering,  
The University of Tokyo, Hongo, Bunkyo-ku, Tokyo, 113, Japan

M.Kisimoto, M.Katagiri

Advanced Research Center Japan Atomic Energy Research Institute, Tokai-mura, Naka-  
gun, Ibaraki, Japan, 319-11

M.Kurakado

Advanced & Technology Research Laboratories.,  
Nippon Steel Corporation, 1618 Ida, Nakahara-ku, Kawasaki 211, Japan

## 1. INTRODUCTION

In the field of X-ray spectroscopy, it is necessary to develop a radiation detector with good energy resolution. Now, a semiconductor radiation detector has the best energy resolution in all kind of detectors. Since present performance of semiconductor detector is almost theoretical limit due to inherent characteristic of the semiconductor, it is very difficult to improve that further. Therefore, a radiation detector using superconducting tunnel junction (STJ) has been investigated very actively by many groups of the world<sup>1-10</sup>. Because the energy resolution of the STJ may be 40 times better than that of a Si detector, we have developed a superconducting tunnel junction type X-ray detector for various experiments practically. In the practical experiments, the STJ is needed to have a large detection efficiency and good energy resolution. However, the STJ has a large capacitance as the detection area of the STJ becomes large. Therefore, it is necessary to optimize a charge sensitive preamplifier for the STJ in order to reduce the electronic noise of the detector and improve the energy resolution.

## 2. Optimization of PREAMPLIFIER

In case of using a JFET charge sensitive preamplifier for STJ detectors, the equivalent noise charge (ENC) is defined as followings<sup>11-13</sup>

$$ENC = [4k_b T_f \alpha A_m C_d (C_{gs}/g_m) / \tau_{sp} + 1/3(2eI_d + 4k_b T_d / R_d) \tau_{sp} + 2A_{1/f} C_{gs} A_m C_d + A_{gr} C_d^2]^{1/2} \quad (1)$$

In the eq.(1),

$A_m = ((C_d/C_{gs})^{1/2} + (C_{gs}/C_d)^{1/2})^2$  : matching coefficient of  $C_{gs}$  and  $C_d$   
 $I_d$  : leakage current of STJ detector  
 $k_b$  : Boltzman constant  
 $T_d, T_f$  : temperature of detector and JFET  
 $R_d$  : dynamic resistance of STJ detector  
 $C_{gs}, C_d$  : gate-source capacitance of JFET and capacitance of STJ detector  
 $g_m$  : transconductance of JFET  
 $\tau_{sp}$  : shaping time  
 $\alpha$  : form factor<sup>11)</sup>  
 $A_{1/f}, A_{gr}$  : 1/f noise coefficient and generation-recombination coefficient

The first term is the series noise and depends on the capacitance of STJ detector and the inversed transconductance ( $1/g_m$ ). The second term is called parallel noise and depends on the leakage current of STJ detector and the inversed dynamic resistance of STJ ( $1/R_d$ ). The third term is due to 1/f type noise. The fourth term is due to the generation-recombination noise caused by traps in a gate depletion layer of the JFET. In the our measurement system, the third term and the fourth term can be negligible because the 1/f noise is very small for Si JFETs and the small generation recombination noise can be estimated.

According to eq.(1), we optimized the cooled JFETs preamplifier for the  $178\mu\text{m} \times 178\mu\text{m}$  Nb/Al-AlOx/Al/Nb STJ having a junction capacitance of 1900pF and low leakage current. As for the first and second term of eq.(1), it is revealed that the ENC decreases as JFETs is cooled down from room temperature and the transconductance  $g_m$  of JFET increases. Also, the  $g_m$  of JFET increases at the low temperature near 140K. Therefore, parallel connection of JFETs and cooling of the JFETs are usually performed to increase the  $g_m$ <sup>12)</sup>.

### 3.EXPERIMENT

According to the first and second term of the eq.(1), we estimated the suitable number of JFETs for the parallel connection. The number of JFET is four with consideration of electronic condition, i.e., power dissipation. Consequently, We have made up a charge sensitive amplifier with cooled 4-JFETs with consideration of power dissipation and space for set in. Five kinds of JFET, that is, or namely SNJ450LD3

which is used in Canberra-2003T preamplifier, 2SK147, 2SK162, 2SK363 and 2SK190 were used to investigate the noise characteristics of the preamplifier.

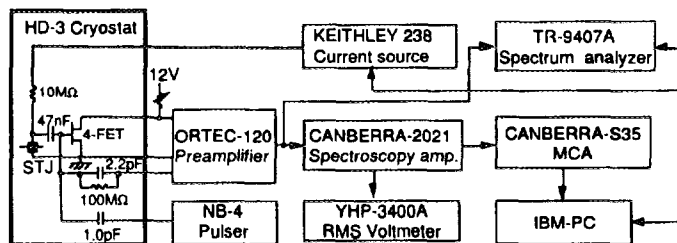


Figure.1 shows the block diagram of Fig.1 Block diagram of electronics for measurement with STJ

electronics for measurement. The four JFETs were mounted to the teflon plate at a 77K cooling stage in a conventional  $^3\text{He}$  cryostat and were operated at about 130K. The ORTEC 120-4 was used as the preamplifier. The root mean square voltages of output of spectroscopy amplifier are measured by using a RMS voltmeter(YHP-3400A). From the results, ENC of the preamplifier with five kinds of JFETs are obtained. Figure.2 shows the obtained ENC characteristics as a function of shaping time  $\tau_{sp}$ .

The minimum ENC, 3100 rms electrons, was obtained at the shaping time of  $2\mu\text{sec}$  by SNJ450LD3 and 2SK190. The ENC characteristics of 2SK190 is almost flat at the shaping time from 2 to  $12\mu\text{sec}$ . In addition, power dissipation of 2SK190(15mW) is the least of all. The ENC characteristic of 2SK147 which has been sometimes referred is two or three times larger than that of 2SK190.

FWHM energy resolutions for 5.9keV X-ray and pulser were measured as a function of shaping time  $\tau_{sp}$  in the case of SNJ450LD3 and 2SK190. The results are shown in Fig.3. And the shaping time dependance of ENC was compared with that of pulser FWHM for SNJ450LD3 and 2SK190. Figure.4 shows that results. The both are almost the same. For the purpose of investigating the reason of the excellent noise characteristics for 2SK190, spectral densities of preamplifier noise as a function of frequency in 0.1-100kHz range was measured for five kinds of JFET, respectively, by using a spectrum analyzer(TR-9407A). The results are shown in Fig.5. The spectral densities for 2SK190 is lower than that for the others JFETs in all range and especially good in the range below 2kHz. Consequently, it is revealed that the best JFET for the preamplifier is 2SK190 which has low noise characteristics in low frequency range.

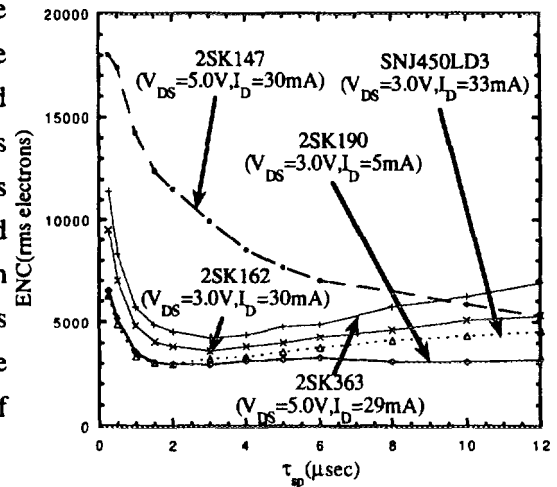


Fig.2 ENC dependence of  $\tau_{sp}$  for different JFETs at  $C_D=1900\text{pF}$

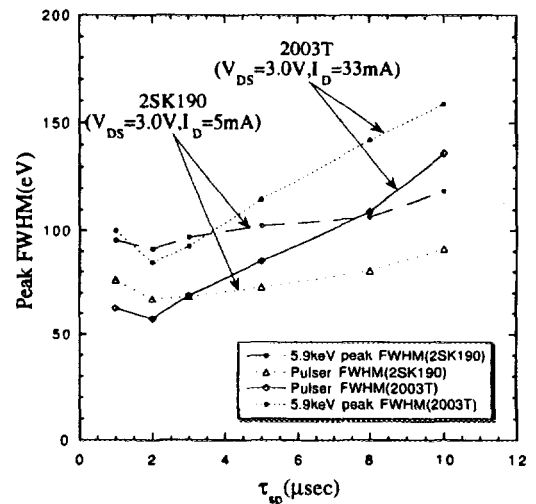


Fig.3 Shaping time dependence of the measured resolutions of 5.9keV peak and pulser

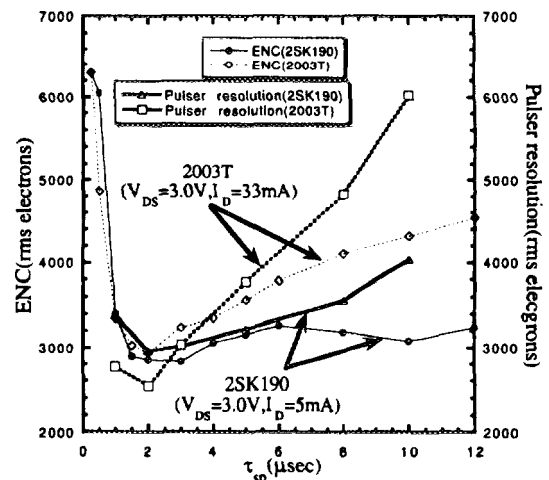


Fig.4 Correlation of  $\tau_{sp}$  dependence between ENC and Pulser resolution

A X-ray spectrum of  $^{55}\text{Fe}$  was measured by the preamplifier using four 2SK190s. The X-ray spectrum is shown in Fig.6. The best energy resolution, 73eV for 5.9keV and 61eV for pulser are obtained.

#### 4. Conclusion

It is confirmed that the cooled 2SK190 has excellent noise characteristics for the preamplifier of large area STJs. The best energy resolution of the fabricated  $178\mu\text{m} \times 178\mu\text{m}$  Nb/Al-AlO<sub>x</sub>/Al/Nb STJ was 73eV for 5.9keV X-ray and 61eV for pulser when the STJ was operated at the bias current of 6.8nA with the preamplifier using 2SK190s as the 4-JFETs.

#### References

- (1) M.Kurakado and T.Takahashi, *ouyoubuturi* **63** (1994) p374
- (2) K.Ishibashi et al., *IEEE Tran.Mag.*, **25** (1989) p1354
- (3) A.Matsmura et al., *NIM A* **329** (1993) p227
- (4) P.K.Gosh, *Intriduction to Photoelectron Spectroscopy, Chemical Analysis Vol. 67* (John Wiley & Sons ,NewYork,1983) Chp.7
- (5) M.Thompson and M.D.Barker, *Auger Electron Spectroscopy, Chemical Analysis Vol. 74* (John Wiley & Sons ,NewYork,1985) Chp.2
- (6) R.W.Fink, R.C.Jopson, H.Mark and C.D.Swift, *Rev.Mod.Phys.*, **38**(1966)513
- (7) M.O.Krause, *J.Phys.Chem.Ref.Data.*, **8** (1979)307
- (8) E.J.McGuire, *Phys.Rev A* **.3.** (1971)587
- (9) D.L.Walters and C.P.Bhalla, *Phys.Rev A* **.4.**(1971)2164
- (10) M.O.krause, *Phys.Rev A* **.22** .(1980)1958
- (11) V.Radeka, *IEEE Trans. Nucl. Sci.* NS-21(1974)51
- (12) F.S.Goulding, *Nucl. Instr. and Meth.* 142(1977)213
- (13) E.Grams, K.G.Lynn, et al., *Nucl. Instr. and Meth.* A311(1992)529

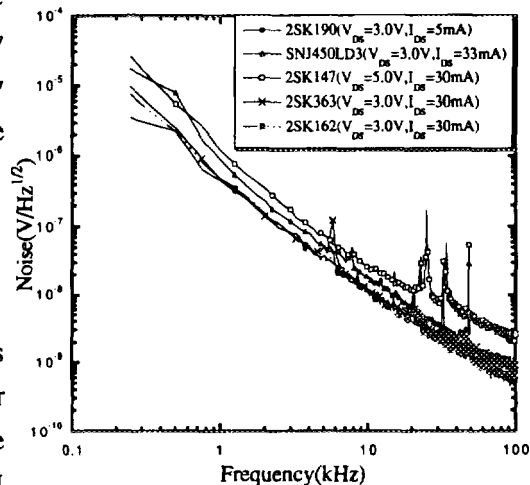


Fig.5 Spectral densities of the noise as a function of frequency in 0.1kHz-100kHz range for different JFETs

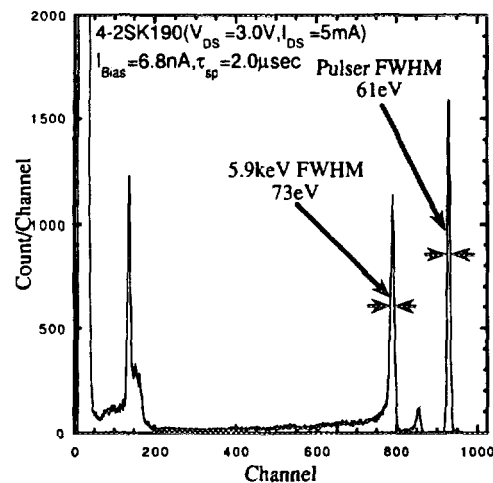


Fig.6  $^{55}\text{Fe}$  X-ray spectrum obtained by the 4-2SK190 preamplifier

# SYSTEM OF PATTERN ANALYSIS OF PIXE SPECTRA

K. Murozono, S. Iwasaki, J. Inoue, K. Ishii, M. Kitamura

*Department of Quantum Science and Energy Engineering, Tohoku University,  
Sendai 980-77, Japan*

K. Sera

*Cyclotron Research Center, Iwate Medical University, Takizawa 020-01, Japan*

S. Futatsugawa

*Nishina Memorial Cyclotron Center, Japan Radioisotope Association, Takizawa 020-01, Japan*

## 1. INTRODUCTION

The application of Particle-Induced X-ray Emission (PIXE) as an elemental analysis technique is still limited to academic studies. We aim at industrial realization of PIXE with mass processing of aerosol samples for environmental monitoring or biomedical samples for health check or diagnosis, etc. For this purpose, it is an important issue to eliminate complexity in PIXE spectrum analysis. Previously we have proposed a new method called *pattern analysis method*.<sup>(1)</sup> In this approach, a PIXE spectrum is considered as a linear superposition of some fundamental patterns named reference spectra, i.e., spectra of elements in a sample whose intensities are normalized and a continuous spectrum of bremsstrahlung and gamma-ray. This treatment reduces difficulty in the decomposition of overlapping peaks. If we can determine reliable reference spectra beforehand, a simple multiplication of the Moore-Penrose (MP) pseudoinverse of a matrix composed of those reference spectra by a PIXE spectrum gives directly the relative concentrations of the elements. Thus the analysis can be conducted quickly and automatically. The present method has been validated in a few cases, such as SUS316 stainless steel sample and standard solution INTB1.<sup>(2)</sup>

Based on the previous studies regarding the pattern analysis method, a tentative software system has been developed. To test the feasibility of the method, the system was implemented in a personal computer for MCA data collection and applied to some spectra from serum, hair, liver, etc., which are common samples in PIXE. These samples are candidates in the industrial PIXE, which would lead to next generation PIXE.<sup>(3)</sup>

## 2. PATTERN ANALYSIS SYSTEM

The analysis system consists of several modules which are used for model calculation of the reference spectra, for the MP pseudoinverse matrix calculation, for conduction of the actual

analysis, etc. Necessary data bases of X-ray emission have been created from recent literature values, i.e., proton ionization cross sections<sup>(4)</sup>, K and L X-ray relative emission rates<sup>(5)</sup>, and their energies<sup>(6)</sup>. Data of the measurement conditions, i.e., detector resolution and efficiency, and the X-ray transmission rates of absorbers are determined experimentally using other programs.<sup>(7)</sup> The system has been developed tentatively in a MATLAB environment<sup>(8)</sup> because of its simplicity in matrix computation, visualization, and program development.

In the pattern analysis method, it is a major assumption that reliable reference spectra of all elements in a sample can be obtained beforehand. In this study, we adopted a model calculation to obtain reference spectra. In this model-based approach, K X-ray peaks for the elements with atomic number  $Z=11$  to 60 and L X-ray peaks for  $Z=31$  to 92 are simulated as follows. First, their relative intensities are computed using data base values. Second, these intensities are adjusted to an actual measurement condition by multiplying the detector efficiency and the transmission rate of an absorber. Finally, each X-ray line is folded by a Gaussian profile function with width corresponding to the detector resolution. Therefore, the system can compute reference spectra of all elements from sodium to uranium.

After the reference spectra are determined, a matrix is composed whose column vectors are those reference spectra. Then the MP pseudoinverse of the matrix is computed with a MATLAB function based on the singular-value decomposition algorithm. Since the actual analysis is only to multiply the pseudoinverse matrix by a PIXE spectrum, the results can be obtained immediately without complicated tasks. Furthermore, once the pseudoinverse matrix is computed, the same matrix can be used for a series of PIXE spectra from the same kind of samples measured in the same condition. Thus the system is especially suitable for industrial uses of PIXE where a lot of similar spectra should be analyzed in a short time.

### 3. TEST OF THE SYSTEM

To test the feasibility of the present system, some PIXE spectra have been measured at Nishina Memorial Cyclotron Center (NMCC) of Japan Radioisotope Association in Takizawa, Iwate prefecture, and analyzed using the system. In NMCC, PIXE is conducted using a vacuum chamber equipped with two Si(Li) detectors. The detectors are located at angles of  $90^\circ$  and  $135^\circ$ , which are used for the higher energy X-ray with a changeable absorber and for the lower energy X-ray without absorber respectively. The spectra measured with the  $90^\circ$  detector were analyzed in our test. The samples of serum, liver, hair, etc. were prepared on polypropylene backing films. The samples have been bombarded by several 10 nA of 2.9-MeV protons; integrated charge was around 100  $\mu\text{C}$ .

In the following sections, some questions related to the practical implementation of the system are described.

### 3.1 Continuum Component

In the present method, the continuous spectrum of bremsstrahlung and gamma-ray is treated as a pattern. In thin samples on a backing film, we had adopted previously<sup>(1)</sup> a PIXE spectrum from a backing film as a pattern of the continuum. However, noticeable discrepancies were observed between the continuum of PIXE spectra from some samples and backing spectra through the test. This is attributed to the atomic bremsstrahlung<sup>(9)</sup> from elements in the samples. Therefore, we adopt an approximation of the continuum pattern derived by fitting a curve to the continuum in a sample spectrum tentatively. The curve is a combination of 3 components: a polynomial function and two exponential ones. The polynomial function is fitted to the lower energy side of bremsstrahlung, while the two exponentials are fitted to the higher energy side of bremsstrahlung and to gamma-ray. The result of this approach is shown in the next section.

### 3.2 Pre-selection of Candidate Elements

If we calculate the MP inverse matrix from the total set of reference spectra of all possible elements, the system may accept any kind of sample. This naive approach encountered a difficulty: some spectra showed finite concentrations for elements which were unlikely included in the samples, and sometimes negative values as well. This is interpreted as an ill-conditioned feature of the least-squares criterion of MP inverse matrices and unavoidable discrepancies between reference spectra based on the model calculation and actual spectra. To eliminate this difficulty, it was necessary to select elements initially using *a priori* knowledge of content elements in the samples. The selection can be made also by pre-processing a spectrum before analyzing a large number of similar samples. This pre-selection of elements is mathematically equivalent to limiting the solution space in order to stabilize or regularize the ill-conditioned situation.

An example of the PIXE spectrum from a serum sample is shown in Fig. 1 by a dotted line, the result of the present method is given by a solid line and the fit to the continuum by a dashed line. The analysis was conducted with the reference spectra of Cl, K, Ca, Fe, Ni, Cu, Zn, Se, Br, In and Pb, which were pre-selected using both *a priori* information on the sample and the results of peak identification, as well as the continuum derived as mentioned in the previous section. The indium was added to the sample as an internal standard. The quality of fitting is reasonable except for the indium K line peaks, which indicates the validity of the pre-selection.

### 3.3 Use of Funny Filter

Several test analyses revealed the existence of another type of difficulty, i.e., the disagreement of indium K line peaks such as seen in Fig. 1. This can be explained by the strong interference between K lines of potassium and calcium and L lines of indium. In fact, similar result has been observed in the analysis of the PIXE spectrum from INTB1 standard sample for peaks of silver and cadmium.<sup>(2)</sup> In contrast, the strong interference between  $K_{\beta}$  of element Z and  $K_{\alpha}$  of element Z+1, which occurs commonly in Z=20 to 30, has not caused any serious problems in the

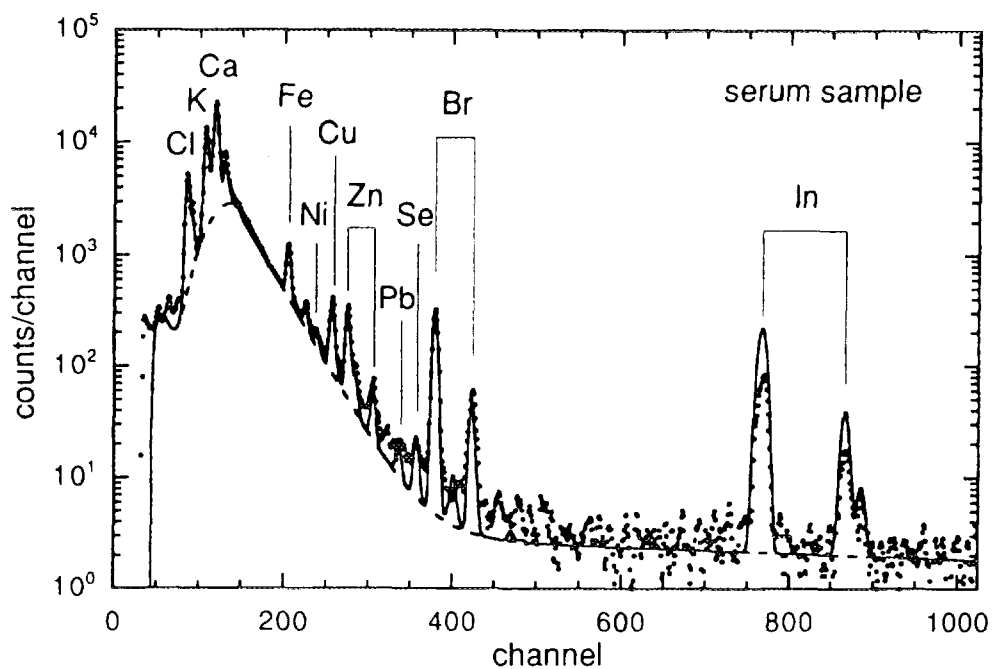


**Fig. 1** The PIXE spectrum from a serum sample. The raw data is shown by a dotted line, the result of analysis using the previous system by a solid line and the fit to the continuum by a dashed line. The analysis was conducted with the elemental reference spectra of pre-selected 11 elements: Cl, K, Ca, Fe, Ni, Cu, Zn, Se, Br, In and Pb. The reference spectra of the continuum was derived as mentioned in section 3.1.

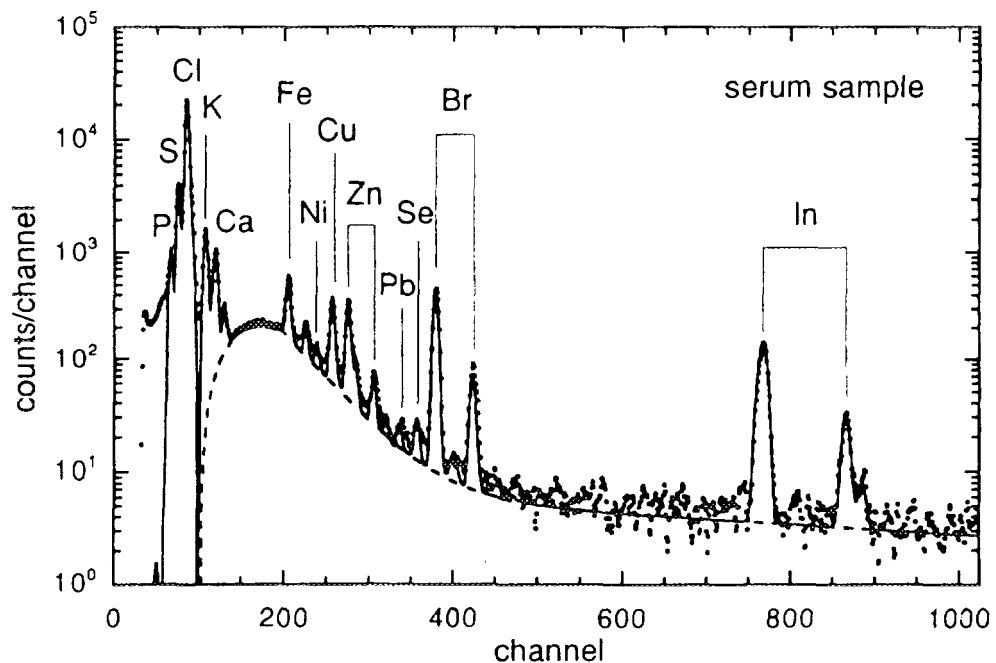


**Fig. 2** The PIXE spectrum from a serum sample measured with the funny filter. The dotted, solid and dashed lines correspond to the same curves used in Fig. 1. The analysis was conducted with the reference spectra of pre-selected 13 elements: P, S, Cl, K, Ca, Fe, Ni, Cu, Zn, Se, Br, In and Pb. The reference spectra of the continuum was derived as mentioned in section 3.1.

pattern analysis method, as discussed in the previous paper <sup>(1)</sup> for the SUS316 case. Since both K and L lines are major components of reference spectra of light and heavy elements respectively, the independence of the spectra of those elements becomes very poor compared with the SUS316 case. Thus, in such a case, K line peaks of heavier element could not be decomposed correctly.

In the present study, we found that this difficulty can be reduced in measurements by using a special absorber called *funny filter*,<sup>(10)</sup> i.e., a pin-holed thick absorber. While the thickness of the filter is enough to absorb the lower energy X-rays, the pinhole can adjust the intensities of those X-rays. On the other hand, higher energy X-rays can penetrate the filter without absorption. Thus the efficiency of the detection system flattens in the wide energy range, and intensities of K and L lines of heavy elements become comparable. This increases orthogonality between reference spectra of light and heavy elements; as a result, the ill-conditioned situation is avoided. Figure 2 shows an example of the analysis for the PIXE spectrum measured with a funny filter. The sample is the same serum as in Fig.1. The result of the analysis is in good agreement with the raw spectrum data including the K lines of indium.

#### 4. SUMMARY

We have developed an analysis system based on the pattern analysis method. By testing the system, several difficulties of the present method have been identified. We found the following solutions for them: pre-selection of candidate elements in a sample and the use of a proper absorber. The pre-selection of the candidate elements will not be a serious drawback in the industrial PIXE, because it will be easy to pre-process the spectra for a few samples in the beginning of the mass processing of samples of the same kind. On the other hand, reduction of the efficiency due to the use of funny filter is significant only in the lower energy region, where we usually do not suffer from insufficient yields of lighter elements in common samples. The selection of the most suitable filter requires PIXE user to be deeply experienced. In particular, it is not easy to choose the best filter to suppress the yield of peak of an abundant element as the absorption edge filter. It will be important task to find a set of suitable combination of representative samples and corresponding filters.

Furthermore, the peak profile model should be improved from the simple Gaussian approximation to more realistic ones with exponential tail, flat component below the peak and escape peaks, etc. It is also necessary to develop a theoretical approach for the background shape of the bremsstrahlung.

## References

- (1) S. Iwasaki, H. Fukuda, K. Yoshizaki, M. Kitamura and K. Ishii, *IJPIXE*, **4** (1994) 131.
- (2) H. Fukuda, S. Iwasaki, K. Yoshizaki, M. Kitamura, K. Ishii, K. Sera and S. Futatsugawa, *KEK proceedings 95-1* (1995) 324.
- (3) S. Iwasaki, K. Ishii, K. Yoshizaki, H. Fukuda, K. Murozono, J. Inoue, M. Kitamura, H. Yokota, Y. Iwata and H. Orihara, *IJPIXE* (in press).
- (4) D. D. Cohen and M. Harrigan, *At. Data Nucl. Data Tables*, **33** (1985) 255.
- (5) J. H. Scofield, *At. Data Nucl. Data Tables*, **14** (1974) 121.
- (6) E. Storm and H. Israel, *Nucl. Data Tables*, **A7** (1970) 565.
- (7) K. Sera and S. Futatsugawa, *Nucl. Instr. and Meth.* (in press).
- (8) The MathWorks, Inc., Natic, MA 01760, USA.
- (9) S. A. E. Johansson and J. L. Campbell, "PIXE: A Novel Technique for Elemental Analysis", (Wiley, Chichester, 1988) p. 36.
- (10) K. Sera and S. Futatsugawa, *IJPIXE* (in press).

# Digital Signal Processing for CdTe detectors using VXibus Data Collection Systems

Daiji Fukuda, Hiroyuki Takahashi, Tomohiko Kurahashi, Tetsuo Iguchi and Masaharu Nakazawa

Department of Quantum Engineering and Systems Science The University of Tokyo 7-3-1  
Hongo, Bunkyo-ku, Tokyo 113, JAPAN

**Abstract** — Recently fast signal digitizing technique has been developed, and signal waveforms with very short time periods can be obtained. In this paper, we analyzed each measured pulse which was digitized by an apparatus of this kind, and tried to improve an energy resolution of a CdTe semiconductor detector. The result of the energy resolution for  $^{137}\text{Cs}$  662keV photopeak was 13keV. Also, we developed a fast data collection system based on VXibus standard, and the counting rate on this system was obtained about 50 counts per second.

## 1 INTRODUCTION

CdTe detectors have many attractive properties for  $\gamma$ -ray spectroscopy, as compared with other semiconductor detectors such as Ge or Si. For example, this detector can be operated at room temperature because of wide band gap, has high detection efficiency because of big atomic numbers, and so on. However considerable charge collection loss has been observed due to a difference between the electron and hole mobilities. Therefore observed pulse heights are different from each other depending on the charge production position even if the same energy is deposited in the detector. The process of charge collection loss, as shown in Figure 1, is recorded in a rising part of the observed pulse, so it is possible to know its original deposited charge if this part is analyzed in detail.

In this paper, we described this charge collection loss in the detector as a model and tried to improve energy resolution of the detector, comparing observed pulses with model pulse functions. At the same time, we tried to develop fast data collection systems based on VXibus standard(VMEbus Extensions for Instrumentation).

## 2 DIGITAL SIGNAL PROCESSING METHOD

A signal pulse from a planar CdTe detector can be described as the following equation,

$$Q(x, t) = \frac{Q_0}{\lambda_e d} [v_e \{1 - \exp(-\lambda_e t)\}] + \frac{Q_0}{\lambda_h d} [v_h \{1 - \exp(-\lambda_h t)\}] \quad (1)$$

where  $x$  is the charge carrier position at time  $t$ ,  $Q(x, t)$  is the collected charge at time  $t$ ,  $Q_0$  is the deposited charge,  $\lambda_e$  and  $\lambda_h$  are the electron and hole trapping coefficients, respectively,  $v_e$  and  $v_h$  are the electron and the hole velocities. The first term in the right side of eq.(1) shows an electron component which will become constant after electron collection time  $t_e = x_0/v_e$ , where  $x_0$  is the initial charge carrier generating position. The second term shows a hole component which similarly will become constant after hole collection time  $t_h = (d - x_0)/v_h$ , where  $d$  is the length between an anode and a cathode. For simplicity, the charge detrapping effect is currently ignored in our analysis.

Although an observed pulse waveform and also a pulse height will vary with a signal generating position in the detector, we can get the original charge by fitting eq.(1) to a measured pulse waveform. However, this fitting function is too complicated to solve directly. Thus we adopted the pattern matching method. Figure 2 schematically shows this method. First, we generated 600 reference waveform patterns by changing  $x_0$  in eq.(1). Then, we compared the measured waveform with reference waveform patterns and find the most probable reference waveform by the residual value  $r$ ,

$$r = \sum_t \{P[t] - Q_0 M_i[t]\}^2 \quad (2)$$

where  $t$  is discrete time,  $P[t]$  denotes signal amplitude at discrete time  $t$ ,  $Q_0$  corresponds to the original deposited charge in the detector,  $M_i[t]$  is reference signal amplitude and  $i$  is the model number which denotes the charge generated position as  $x_0 = d/600 \times i$ . For the most probable reference waveform,  $Q_0$  is given by following equation,

$$Q_0 = \frac{\sum P[t] M_i[t]}{\sum \{M_i[t]\}^2} \quad (3)$$

The merit of this pattern matching method is that nonlinear problems which exist in such as eq.(1) are converted into a linear least squares method, so there is no fear that the solution of the equation cannot converge.

In actual calculation of pattern matching, we used reference waveform patterns which are given by a convolution of eq.(1) with a differential response function, considering preamplifier properties.

### 3 EXPERIMENT

Figure 3 shows a experimental setup using a  $^{137}\text{Cs}$   $\gamma$  source. The upper side of this figure 3 shows conventional data collection systems using GPIB. The pulse waveforms from the detector and the preamplifier are digitized at a digital storage oscilloscope and these discrete waveforms are transported to workstation through GPIB cable. The down side of figure 3 shows a data collection system using VXIbus and the waveforms digitized at ADC module are transported to a system controller at high speed through VXIbus. Lynx OS which is a kind of UNIX works on this system controller, thus it is possible not only to do the pattern matching here, but also to calculate it on the other machines by transporting the digitized waveforms through a network. For example, the counting rates on both systems are shown in table 1. Using VXIbus systems, we had thirty two times as good value as that of conventional GPIB systems. However, we had no time enough to make a full experimental setup of VXIbus system, so the GPIB system was used to get the waveforms of a CdTe detector.

The size of a planar CdTe detector was  $2\text{mm}\times 4\text{mm}\times 2\text{mm}$  and 100V bias voltage was applied to this detector. We used an ORTEC/142A as the preamplifier and this output pluses were digitized by a Tektronix TDS640 DSO with a sampling frequency of 500MHz.

We applied the above pattern matching method to each measured pulse waveform, and figure 4 shows its result. The x axis means the model number  $i$  which represents the charge generated position in the detector, and the y axis means the initial generated charge  $Q_0$  which is given by eq.(3). The number of analyzed waveforms is eight thousand and during this correction process no pulse was lost. Figure 5 shows a pulse height spectrum after pattern matching method. For comparison, a pulse height spectrum taken by a conventional analog shaping system with a shaping time of  $0.5\mu\text{s}$  is also shown in this figure. A 662keV photo peak and a structure of Compton scattering are clearly shown after processing. An observed energy resolution of a photo peak was 13keV(FWHM).

### 4 CONCLUSION

The output pulse of a CdTe detector was modeled and the energy resolution of the detector had remarkably improved by using pattern matching method. The result of the energy resolution after this processing was 13keV(FWHM) for 662keV photo peak without any collection loss.

Also, a fast data collection system based on VXibus was developed and the counting rate had a good improvement compared with conventional GPIB systems. This method can be applied to a detector having any electrode configuration if signal pulses are modeled.

## References

- [1] M.G.Scannavibi, et al.,Nucl. Instr. and Meth., A353 (1994) 80-84.
- [2] P.N.Luke, Proc. of 1994 IEEE Nucl. Symp., Norfolk.
- [3] W.Akutagawa and K.Zanio, J.A.P, vol. 40 num. 9 (1969) 3838-3854.
- [4] I.Lazarus and P.J.Coleman-Smith, Proc. of 1994 IEEE Nucl. Symp., Norfolk.
- [5] H.Takahashi, et al.,IEEE Trans. on Nucl. Sci., NS-41, No.4 (1994) 1246-1249.

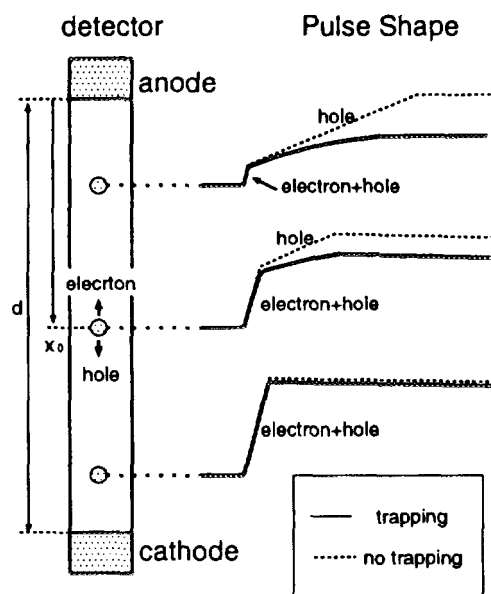


**Figure 1:** Process of charge collection loss depending on charge generating position

	GPIB	VXibus
points per waveform	2000	2048
cps	1.556	49.76

**Table 1:** Result of counting rate experiment using GPIB and VXibus systems

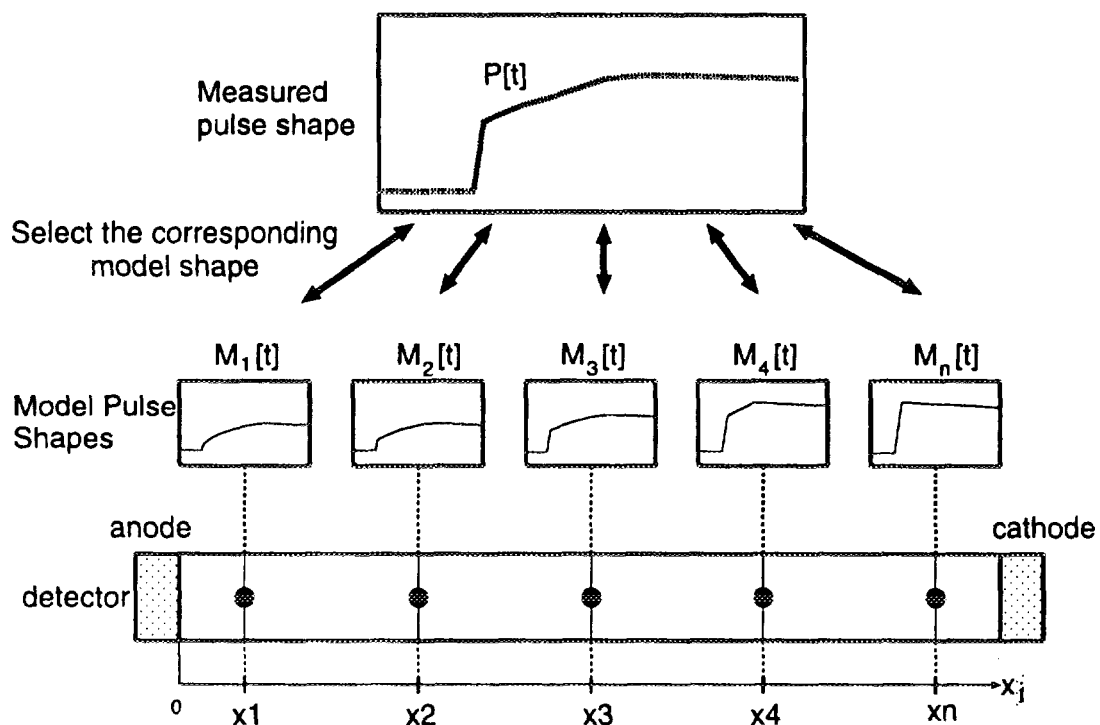


Figure 2: Pattern matching method for estimating the signal generating position.

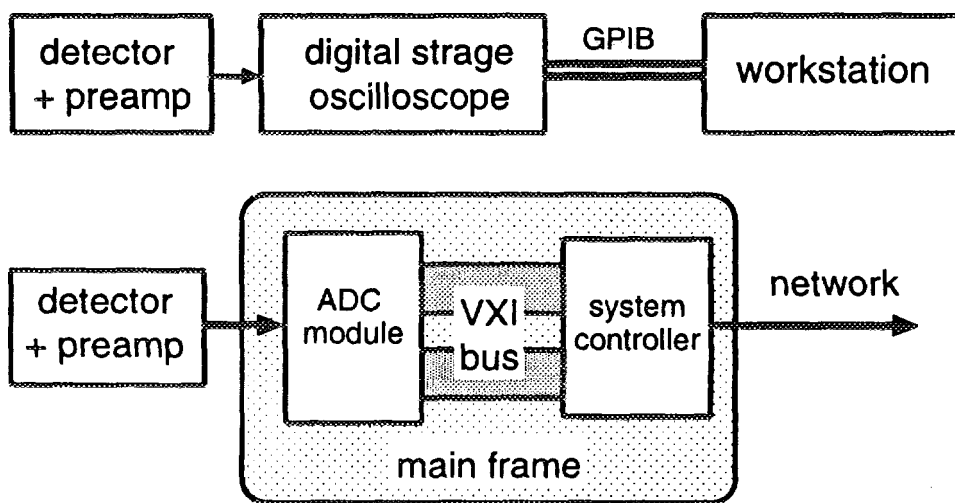
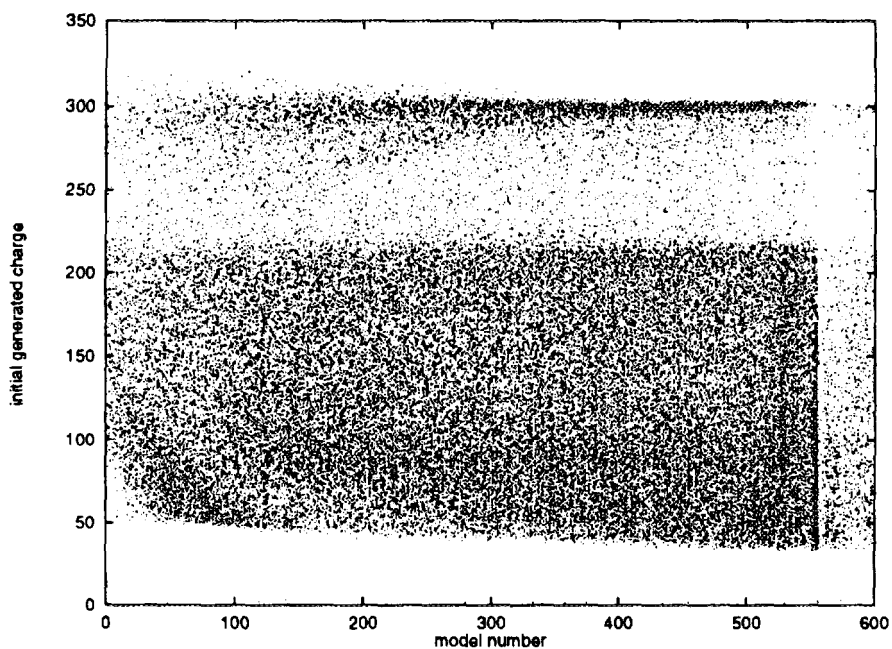
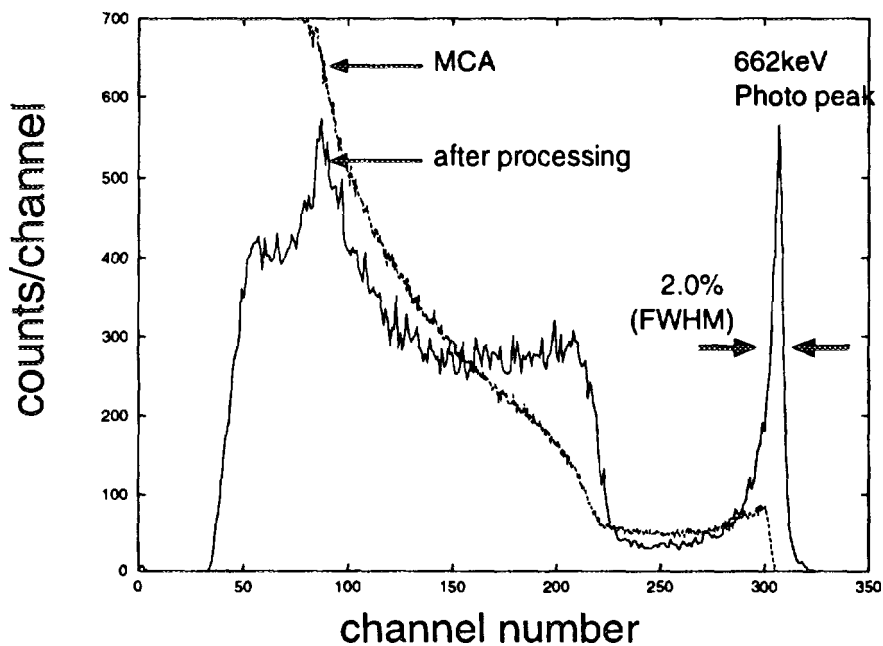


Figure 3: Block diagram of data collection systems based on GPIB and VXIbus.



**Figure 4:** Result of pattern matching method. This shows the relation between the model number and the pulse height.



**Figure 5:** Pulse height spectrum after correction process. Pulse height spectrum taken by normal analog shaping system is also shown.

# ESTIMATE OF PULSE-SEQUENCE DATA ACQUISITION SYSTEM FOR MULTI-DIMENSIONAL MEASUREMENT

Yasunori KITAMURA, Takeji SAKAE, Akihiro NOHTOMI, Masaru MATOBA  
*Department of Nuclear Engineering, Kyushu University, Fukuoka 812, Japan*

Yuzuru MATSUMOTO  
*Kyushu Teikyo Junior College, Fukuoka 836, Japan*

## Abstract

A pulse-sequence data acquisition system has been newly designed and estimated for the measurement of one- or multi-dimensional pulse train coming from radiation detectors. In this system, in order to realize the pulse-sequence data acquisition, the arrival time of each pulse is recorded to a memory of a personal computer (PC). For the multi-dimensional data acquisition with several input channels, each arrival-time data is tagged with a 'flag' which indicates the input channel of arriving pulse. Counting losses due to the existence of processing time of the PC are expected to be reduced by using a First-In-First-Out (FIFO) memory unit. In order to verify this system, a computer simulation was performed. Various sets of random pulse trains with different mean pulse rate (1-600 kcps) were generated by using Monte Carlo simulation technique. Those pulse trains were dealt with another code which simulates the newly-designed data acquisition system including a FIFO memory unit; the memory size was assumed to be 0-100 words. And the recorded pulse trains on the PC with the various FIFO memory sizes have been observed. From the result of the simulation, it appears that the system with 3 words FIFO memory unit works successfully up to the pulse rate of 10 kcps without any severe counting losses.

## 1. INTRODUCTION

In general, unprocessed data can be obtained by using time-sequence data acquisition methods. The methods have some advantages, and it is a good example that the data can be adopted to various purposes by processing it into the suitable forms according to their demands. In the field of radiation detection and measurement, it seems that the pulse-sequence data acquisition of the radiation detecting pulse train is interesting. The reason is that it is considered that this method is effective to time domain correlation experiments for studying the various processes of radiation.

One of the applicable example is reactor noise analysis. In the reactor noise analysis, dynamic reactor parameters such as subcriticality or neutron life time are evaluated by analyzing the fluctuation of the neutron population or flux in a nuclear reactor operated in static state. Only one neutron detector which is settled in an appropriate position of operated nuclear reactor is used, then dynamic reactor parameters can be evaluated without disturbing the operation of the reactor by using this technique. And by processing the data of reactor noise in a short time, real-time subcriticality monitor can be developed[1].

One of the traditional pulse-sequence data acquisition technique is data recording using magnetic tapes. The data recorded on the magnetic tapes have to be handled in off-line way, then the practicality of real-time analysis is spoiled.

In order to solve this problem, pulse-sequence data acquisition system using a personal computer (PC) were developed for radiation detecting pulse train[2]. In this system, the pulse-sequence data acquisition is realized by recording digitized time data of each pulse coming from radiation detectors. And the time data is written onto PC's memory with an interrupt service of the CPU. Therefore, the pulse-sequence data recorded on PC's memory are ready for real-time analysis. From the consequence of the test experiments using this system, it appeared that many pulses which arrived within the time intervals of the interrupt service were lost. To solve this problem and achieve the multi-dimensional measurement for time domain cross-correlation experiments, improved pulse-sequence data acquisition system has been designed newly. In this report, outline and estimate of this system using Monte Carlo simulation technique is mentioned.

## 2. PULSE-SEQUENCE DATA ACQUISITION SYSTEM

In the pulse-sequence data acquisition system, 1 MHz oscillator and 32 bit scaler whose value is read and wrote from CPU though the I/O port of the PC were used. In this system, the scaler counts the oscillator, then it is considered that the scaler has time data with the resolution of  $1 \mu\text{s}$ . Each pulse requests the interrupt service of the CPU when the pulse arrived at live time of the CPU. And as the interrupt service routine, the

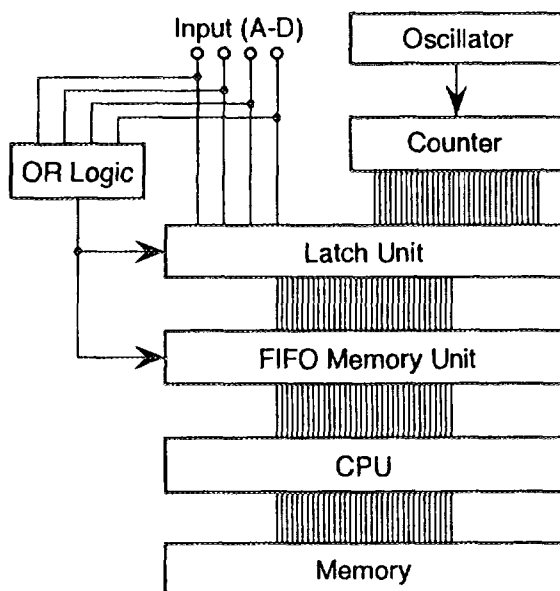


Figure 1: Outline of the Improved Pulse-Sequence Data Acquisition System

time data held in the scaler can be read out and written onto memory of the PC when the pulse arrives[2]. From the consequence of this system's test experiments with  $\gamma$ -ray sources, it appeared that the system using EPSON PC-386LSR (i386CPU, 20 MHz) were fairly successful and had some problems to be solved. That is, many pulses arrived within the processing time intervals of the interrupt service were neglected. Then the system were able to be regarded to be nonparalysable with the dead time  $20 \mu\text{s}$ ; it was evaluated from the minimum time interval of the neighboring pulses in the recorded pulse-sequence data.

Then the improved pulse-sequence data acquisition system has been designed

newly. Figure 1 shows the outline of the improved system. In the improved system, the status levels of all input channels are latched simultaneously in addition to the time data which is held in the scaler. Then identifying data of input channels is included in each latched data. And First-In-First-Out (FIFO) memory unit is installed in the improved system to reduce the counting losses which occurs because of the existence of the CPU's processing time.

### 3. SIMULATION

In this study, estimate of the improved pulse-sequence data acquisition system has been verified. To achieve this purpose, calculation code simulating the improved system with various sizes of FIFO memory unit (0–100 words) has been developed. In this calculation code, the frequency of the oscillator and the processing time interval of the CPU have been assumed to be 1 MHz and 20  $\mu$ s respectively.

As random pulse trains, Poisson pulse trains with various mean pulse rates (1–600 kcps) have been generated by using Monte Carlo simulation technique[3]. Suppose  $n$  as counting number in a time interval  $\Delta t$ . Then in case of Poisson distribution,  $P(n)$  which is probability of  $n$ 's generating is written as follows:

$$P(n) = \frac{\lambda^n}{n!} e^{-\lambda} \quad (n = 0, 1, 2, \dots; \lambda > 0), \quad (1)$$

$$\sum_{n=0}^{\infty} P(n) = 1, \quad (2)$$

where  $\lambda$  is average number of counting number  $n$  in  $\Delta t$ . By using random number  $\xi$  which is generated in [0, 1] uniformly,  $n$  is determined from a following inequality:

$$\sum_{i=0}^{n-1} P(i) < \xi \leq \sum_{i=0}^n P(i). \quad (3)$$

In this study,  $\Delta t$  is determined to be 1  $\mu$ s and  $n$  is assumed to be only {0, 1}. Therefore, Equations (1) (2) and (3) can be written as follows:

$$P(n) = \begin{cases} P(0) = e^{-\lambda} \\ P(1) \approx \sum_{n=0}^1 P(n) - P(0) = 1 - e^{-\lambda}, \end{cases} \quad (4)$$

$$P(0) < \xi \leq P(0) + P(1) = 1, \quad (5)$$

then  $n$  can be written as follows:

$$n = \begin{cases} 1 & (\text{when } \xi > P(0)) \\ 0 & (\text{when } \xi \leq P(0)). \end{cases} \quad (6)$$

When  $n$  is 1, it means that the detection occur in  $\Delta t$ . And when  $n$  is 0, it means that the the no detection occur in  $\Delta t$ . Therefore, to repeat this process, Poisson pulse train of the time resolution 1  $\mu$ s can be obtained. In order to estimate the improved system, Poisson pulse trains of various mean pulse rates have been generated. And the recorded pulse trains obtained on PC's memory have been observed in case of various FIFO memory sizes. Figure 2 is a time interval distribution of neighboring pulses obtained in this way.

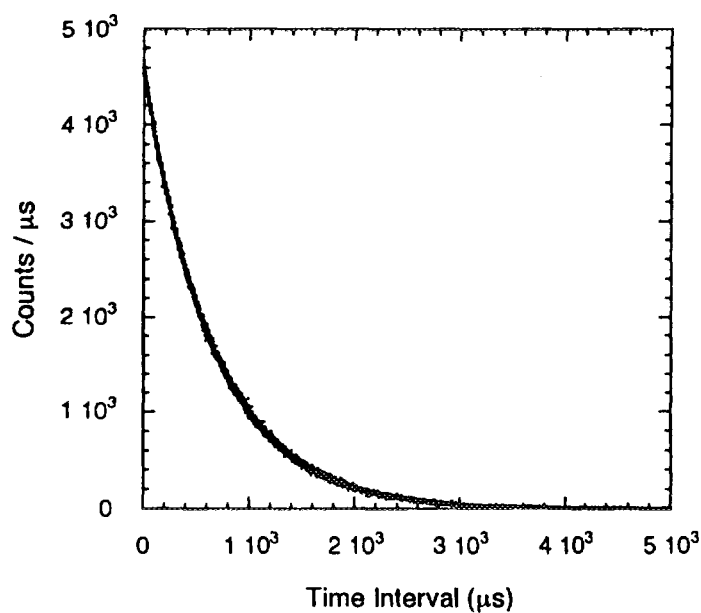


Figure 2: Time Interval Distribution of Poisson Pulse Train

## 4. RESULTS AND DISCUSSION

### 4.1 ONE-DIMENSIONAL MEASUREMENT

In order to evaluate the improved pulse-sequence data acquisition system, the efficiency has been examined. Figure 3 shows the efficiency in case of one-dimensional measurement. As 50 kcps is reciprocal number of 20  $\mu$ s, it is considered that 50 kcps is

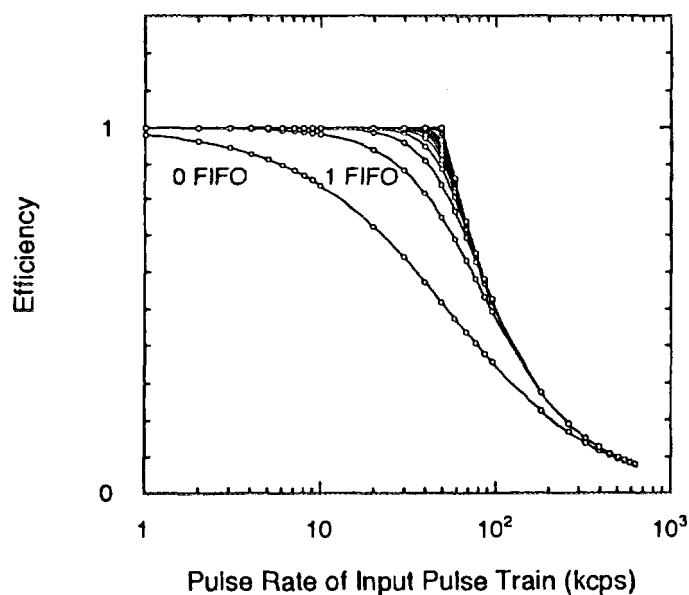


Figure 3: Efficiency of the Improved System (One-Dimensional Measurement)

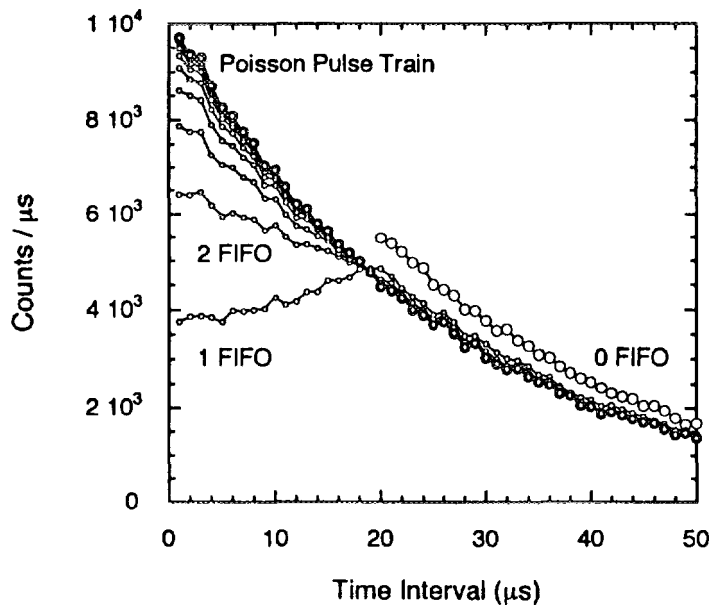


Figure 4: Time Interval Distribution (39.3kcps, One-Dimensional Measurement)

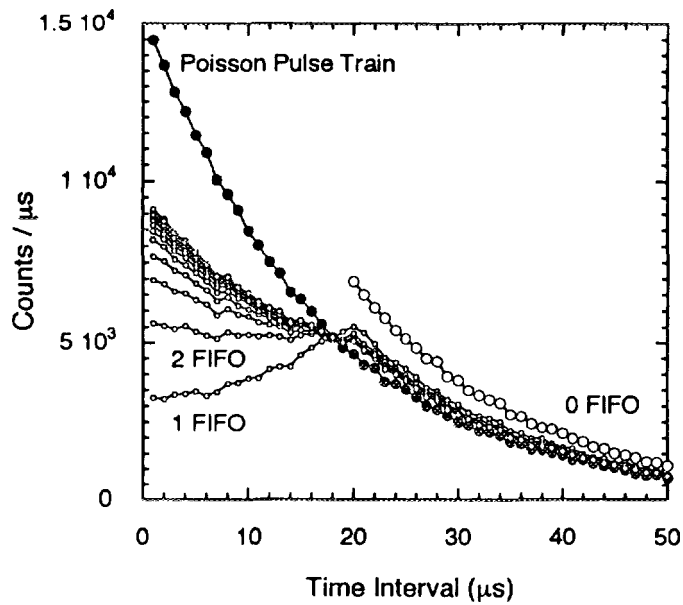


Figure 5: Time Interval Distribution (58.2kcps, One-Dimensional Measurement)

the limit of the CPU's ability. When FIFO memory unit is not installed, the system can be regarded as the nonparalysable type, then half of the pulses coming from a detector are lost for 50 kcps[4]. When FIFO memory unit is installed, the system can work up to the limit of the CPU's ability without any counting losses. That is, when the pulse rate of Poisson pulse train is less than 50 kcps, it appears that the efficiency reaches 1 as the FIFO memory size is increased. And when pulse rate is higher than 50 kcps, it appears that efficiency saturates though the FIFO memory size is increased.

In order to verify qualitative deterioration of the pulse trains, time interval dis-

tributions have been observed. Figures 4 and 5 are the examples of the time interval distributions when 39.3 kcps and 58.2 kcps respectively. In Figure 4, it is observed that the pulses which come in longer interval than  $20 \mu\text{s}$  decrease as the FIFO memory is increased. And it is observed that the pulses which come in shorter interval than the CPU's processing time  $20 \mu\text{s}$  are recovered as the FIFO memory size is increased. In Figure 5, it is also observed that the pulses which come in longer interval than  $20 \mu\text{s}$  decrease as the FIFO memory size is increased. And it is observed that pulses which come in shorter interval than  $20 \mu\text{s}$  saturate though FIFO memory size is increased.

## 4.2 MULTI-DIMENSIONAL MEASUREMENT

Figure 6 shows the efficiency of four-dimensional measurement for the example of multi-dimensional measurement. In case of four-dimensional measurement, as the four pulse trains have almost same pulse rates respectively, the the limit of the system's ability corresponds to the quarter of 50 kcps. Except for this point, the same tendency is observed

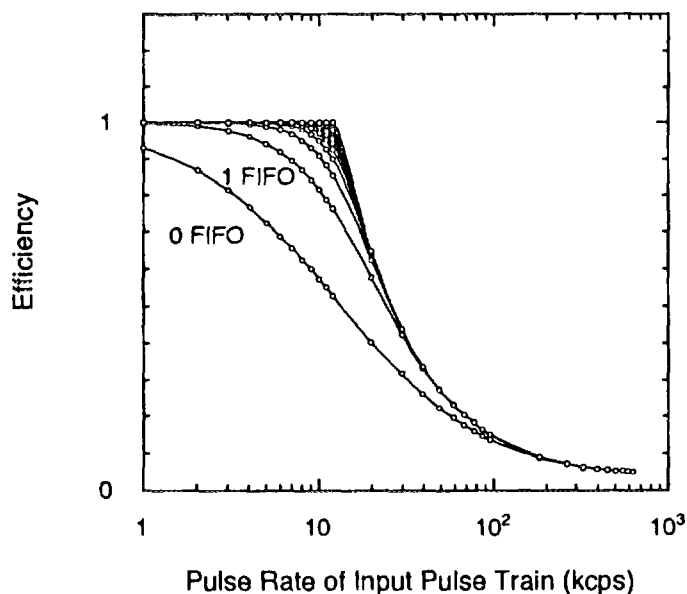


Figure 6: Efficiency of the Improved System (Four-Dimensional Measurement)

compared with the case of one-dimensional measurement.

Figure 7 and 8 are the examples of the time interval distributions when 11.0 kcps and 39.2 kcps respectively. In multi-dimensional measurement, it is observed that pulses which come in shorter and longer interval than the CPU's processing time  $20 \mu\text{s}$  are recovered as the FIFO memory size is increased. And especially in Figure 8, a periodical property of time interval which does not exist in one-dimensional measurement is observed.

It is considered that it occurs because of the conflict with other pulse trains and can be explained as mentioned below. Suppose the system which is not installed the FIFO memory unit because of simple discussion. Moreover, suppose two-dimensional measurement experiments of A-pulse-train and B-pulse-train is done with this system (Figure 9). When a pulse of A-pulse-train is counted at  $t$  at live time of the system, the system turns dead and any pulses are neglected until  $t + \tau$  (where  $\tau$  is the processing time of the CPU). And the system turns live again at  $t + \tau$ , then the conflict occurs. That is, if the next counting is from A or simultaneous counting of both, the dead time

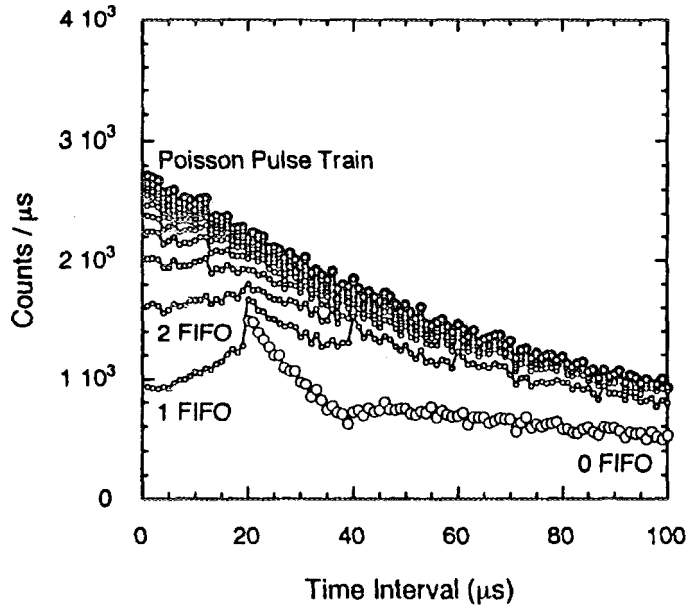


Figure 7: Time Interval Distribution (11.0kcps, Four-Dimensional Measurement)

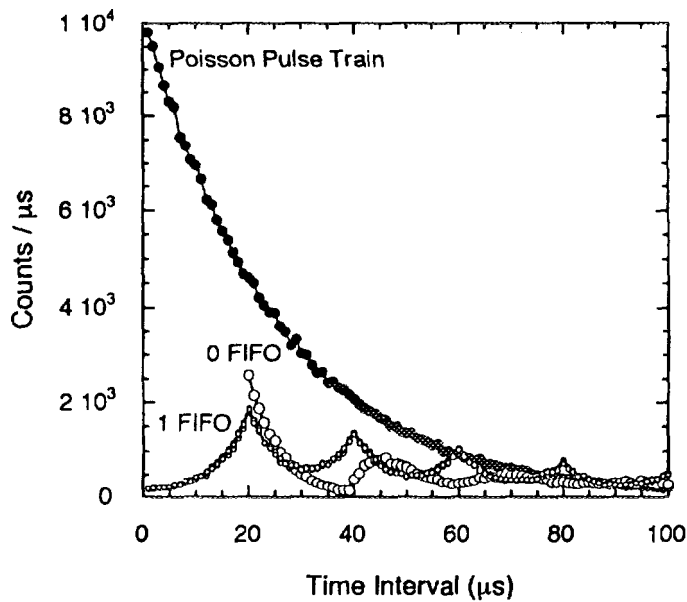


Figure 8: Time Interval Distribution (39.2kcps, Four-Dimensional Measurement)

at that moment is regarded as  $\tau$  from the A's viewpoint. If the next counting is from B at  $t + \tau + \Delta t_1$  (where  $\Delta t_1$  is conflict time from  $t + \tau$  to the next pulse's arrival), the system turns dead again until  $t + 2\tau + \Delta t_1$ . And then, if the next counting is from A or simultaneous counting, the dead time is regarded as  $2\tau + \Delta t_1$  at that moment from the A's viewpoint. In the similar way, the dead time from A's viewpoint can become  $\{\tau, 2\tau + \Delta t_1, 3\tau + \Delta t_1 + \Delta t_2, 4\tau + \Delta t_1 + \Delta t_2 + \Delta t_3, \dots\}$ . Therefore, A's time interval distribution becomes summation of the time interval distributions of the systems with various dead time. When the pulse rates of both pulse train is not so low,  $\{\Delta t_1, \Delta t_2, \Delta t_3, \dots\}$  become

almost 0 respectively. Then in case of the high pulse rates, the periodical property of time interval appears clearly.

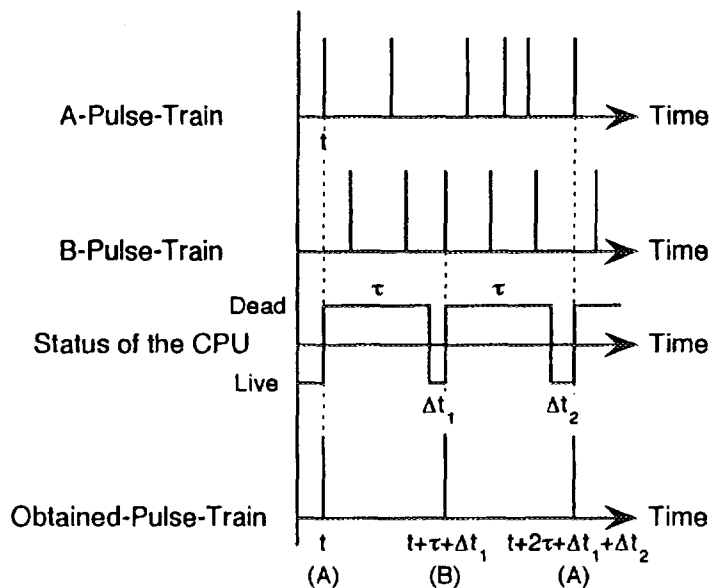


Figure 9: Outline of the Conflict of Pulse Trains

## 5. CONCLUSION

The pulse-sequence data acquisition system for multi-dimensional measurement were newly designed and estimated by using Monte Carlo simulation technique. And by installing FIFO memory unit, it was verified that counting losses due to the existence of processing time of the PC reduced effectively. From the result of the simulation, it appeared that the system with 3 words FIFO memory unit works successfully up to the pulse rate of 10 kcps without any severe counting losses.

## References

- [1] T.Misawa, Nucl.Sci.Eng.(USA, 1990).104,p.53.
- [2] Y.Kitamura, Proceedings of the Sixth Workshop on Topics in Nuclear Radiation Detection.(Hiroshima University, 1995)p.168.
- [3] T.Tsuda, Monte Carlo Technique and Simulation, 3rd ed. (Baifukan, Tokyo, 1995).
- [4] G.F.Knoll, Radiation Detection and Measurement(*In Japanese*), 2nd ed. (Nikkan Kogyo Press, Tokyo, 1991).

# CHARACTERIZATION OF NEUTRON DETECTOR COMBINED WITH NE213 AND CaF<sub>2</sub>(Eu)

Mashashi Takada and Takashi Nakamura  
Cyclotron and Radioisotope Center, Tohoku University

Tokushi Sibata  
Institute for Nuclear Study, University of Tokyo

## INTRODUCTION

With increasing manned space flights, it becomes important to estimate the exposure of crew to the cosmic rays. There have been measured the cosmic-ray charged particles with Si-SSD detectors and the LET spectrometers, but the measurement of cosmic-ray neutrons is very scarce<sup>1</sup>, although the neutrons produced in the space mission have a certain amount of contribution. Differently from the neutron detection on the ground level, it is difficult in the space environment. It is because the neutron measurement requires to discriminate between the neutron events due to charged particles caused from neutron reaction and the charged particle events due to incident charged particles under an intense charged-particles, mainly protons, field in space.

To distinguish the neutron events from the external charged particle events, we have designed the phoswich detector which is able to discriminate neutrons from charged particles in this study. If the detector wall is sensitive to the charged particle and signals from the wall can be identified, we can discriminate these events. This is because the charged particles entering the detector are sensed by the wall, but neutrons are not detected unless the charged particles from neutron reactions hit the detector wall.

In this work, the property of the n- $\gamma$  discrimination and the response functions of the developed phoswich detector were measured with gamma rays from radioactive sources and neutrons from a Be+Cu target bombarded by protons from the RIKEN ring cyclotron at the Institute of Physical and Chemical Research. The measured response functions were compared with Monte Carlo calculations. We also tested to measure a small amount of neutrons under the intense charged-particles mixed field which was

realized in the RIKEN ring cyclotron for the space application.

## DETECTOR DESIGN AND OPERATION

### DETECTOR

The phoswich detector consists of two different scintillators which are optically coupled with a single photomultiplier. In this case output pulses from the inner and the outer detectors have to be identified each other. The one possible way to discriminate pulses from two detectors is achieved by using different scintillators having different light decay time. Since the decay time of liquid scintillator is a few nsec, the light time of the wall counter must be as much as 1μsec.

We designed a new neutron detector consisting of an inner neutron detector covered with a sensitive wall to charged particles. Here in this study, we selected the NE213 liquid organic scintillator as an inner detector, because it has the best characteristics of pulse shape discrimination between neutrons and gamma rays. In order to avoid the light shield between the inner and the outer detectors, we have to select the outer wall detector which is chemically stable to the organic liquid. We finally chose the  $\text{CaF}_2(\text{Eu})$  crystal among of many inorganic crystals as a wall counter to combine with the inner NE213 scintillator.

The cross sectional view of the detector is shown in fig.1. It consists of a 40.8mm diam. by 45.8mm long NE213 organic liquid scintillator surrounded by a 5mm thick  $\text{CaF}_2(\text{Eu})$  inorganic scintillator except the one front surface. The decay times of main light output components from NE213 and  $\text{CaF}_2(\text{Eu})$  are 3.7 and 940 to 1000nsec, respectively. The length of NE213 corresponds to a range of 68MeV proton and of 7.5MeV electron. A photomultiplier was coupled to the bottom surface of  $\text{CaF}_2(\text{Eu})$  through a pyrex optical glass and a pyrex light guide.

### OPERATIONAL PRINCIPLE

If neutrons and photons of no charge enter the detector, they do not lose its energy in the  $\text{CaF}_2(\text{Eu})$  scintillator unless the charged particles produced from neutron and photon reactions hit the  $\text{CaF}_2(\text{Eu})$  scintillator. If charged particles enter the detector, charged particles lose its energy in the  $\text{CaF}_2(\text{Eu})$  scintillator. Fig.2 shows the signals which

are produced by the interaction of a neutron and a charged particle with the detector in three cases that can occur in this detector. Fig.2-(A) shows the case that a neutron or a photon of no charge is incident to the counter and a produced charged particle does not hit the  $\text{CaF}_2(\text{Eu})$  scintillator. In this case, the scintillation is produced by the only NE213 and the signal from the photomultiplier has the only fast component (the decay time of a few nsec) as shown in the right side of Fig.2-(A). Fig.2-(B) indicates the case that a neutron or a photon of no charge is incident to the counter and a produced charged particle hits the  $\text{CaF}_2(\text{Eu})$  scintillator. In this case, the scintillations are produced by both the NE213 and  $\text{CaF}_2(\text{Eu})$  scintillators and the signal from the photomultiplier has two components (the decay times of a few nsec fast component and about  $1\mu\text{sec}$  slow component) as shown in the right side of Fig.2-(B). Fig.2-(C) depicts the case that a charged particle enters into the counter. In this case, the signal from the photomultiplier has the same as in Fig.2-(B).

We can therefore identify the events which the charged particles react with the  $\text{CaF}_2(\text{Eu})$  crystal wall by looking at the slow component of the scintillation light. The fast and slow components of the signal can be analyzed by using a charge integration type ADC. The charge integration of the signal is carried out during the time period specified by a gate pulse. The fast component can be analyzed by a narrow gate pulse (fast gate in Fig.2) adjusted at the peak of the signal. The slow component is analyzed by a wider gate (slow gate in Fig.2) set at the long tail of the signal.

Fig.3 shows three gate pulses to the signal which we used in this study. The gate for the fast component is shown as TOTAL and the gate for the slow component is shown as CaF. The DECAY gate is used for the n- $\gamma$  discrimination.

The pulse heights obtained by three gates are denoted as  $L_{\text{total}}$ ,  $L_{\text{decay}}$  and  $L_{\text{CaF}}$ . A two dimensional plot of  $L_{\text{total}}$  and  $L_{\text{decay}}$  is shown in Fig.4. This data was taken by using an  $^{241}\text{Am}$ -Be source. The areas A and B correspond to the gamma-ray events and the neutron events, respectively. The n- $\gamma$  discrimination property is very important for the organic liquid scintillator. Although the property of n- $\gamma$  discrimination for this phoswich detector is slightly poorer than the ordinary NE213 detector, this phoswich detector has still enough n- $\gamma$  discrimination property. A two dimensional distribution of  $L_{\text{total}}$  and  $L_{\text{CaF}}$  is shown in Fig.5. This data was taken from the measurement of neutrons produced by the  $^7\text{Li}(p,n)$  reaction of proton energy  $E_p=80\text{MeV}$ . In Fig.5 two areas labelled A and B can be seen. The area of thin locus labelled A corresponds to the events which the charged particle produced from neutron reactions interacted only in the NE213 whereas the area B refers to the events which they passed through both the NE213 and  $\text{CaF}_2(\text{Eu})$  scintillators. Thus we can pick up

the events in area A that neutrons enter the detector excluding the events that the charged particle produced from neutron reactions interacted in the  $\text{CaF}_2(\text{Eu})$  scintillator.

## RESPONSE FUNCTIONS FOR GAMMA RAYS

The measurements of the response functions for gamma rays were carried out using the standard gamma-ray sources of  $^{137}\text{Cs}$ ,  $^{22}\text{Na}$ , and  $^{60}\text{Co}$ , and a  $^{241}\text{Am-Be}$  source. The energy of the Compton edge of each gamma ray was used for the energy calibration since the Compton scattering is the dominant process in the NE213 organic liquid scintillator for photon energies up to several MeV. In the case of the  $^{241}\text{Am-Be}$  source, the gamma-ray events were selected by means of the n- $\gamma$  discrimination. Additional measurements with a properly adjusted shadow block of a 15cm thick lead enabled us to subtract photons scattered in air, from the walls, from the detector support and from the remaining environment as well as any random background photons (mainly originating from concrete walls). The background events with shadow block were measured for the same period as the gamma-ray measurement. The response functions were obtained by subtracting the background. The response function for 4.43MeV gamma rays measured with a  $^{241}\text{Am-Be}$  source is shown in Fig.6. The light output L is expressed in MeVee unit which denotes the light yield produced by an electron of 1MeV in NE213.

The detector response functions for gamma rays were also calculated using the electron photon shower Monte Carlo code EGS-4 <sup>2</sup>. For response function calculation, the events that the electron deposits its energy in the  $\text{CaF}_2(\text{Eu})$  crystal were excluded from the pulse height, and the events that the energy is deposited only in NE213 was considered to contribute to the pulse height.

The response function calculated by the EGS4 for 4.43MeV  $^{241}\text{Am-Be}$  gamma rays is shown in Fig.6. The finite energy resolution of the detector was taken into account by smoothing the EGS-4 calculations with a Gaussian distribution. The experimental spectra were normalized to the spectra calculated with EGS-4 in the region of Compton edge indicated by an arrow in Fig.6.

The calculated spectra can reproduce well the experimental pulse heights near the Compton edge, but deviate largely at lower part of the pulse height spectra. The disagreement at the lower part might be due to the fact that the energy of photon source is not mono-energy because of scattering from a container of source, and that the

background subtraction with shadow block is not sufficient.

## RESPONSE FUNCTIONS FOR NEUTRONS

The experiments to measure response functions for neutrons were carried out at the RIKEN Ring Cyclotron, Institute of Physical and Chemical Research. The neutron beams were produced by the bombardment of 80 and 90 MeV protons on a target which consists of 2.0cm thick Be backed by 2.0cm thick Cu so as to stop incident protons. This phoswich detector was positioned at a distance of 13m downstream from the target at 0 degree with respect to the proton beam axis. The neutron beam impinged on the front surface of the cylindrical detector. The time interval between the light output signal from the detector and the RF signal associated with the proton pulse was measured using a CAMAC TDC to get the time of flight information of neutrons.

The response functions for neutrons were obtained by setting a gate on neutron events of the n- $\gamma$  discrimination and a gate for the TDC spectrum corresponding to a given energy. The events that did not interact with the  $\text{CaF}_2(\text{Eu})$  wall were selected. The energy scale of the pulse height was calibrated using the standard gamma-ray sources, as described before. The response functions obtained for  $E_n=60\text{-}64\text{MeV}$  by using 80MeV and 90MeV protons are shown in Fig7, and agree well each other.

The response functions used in our experiment were calculated for neutrons up to 80MeV, using the Monte Carlo code, SCINFUL<sup>3</sup>. The treatment for the charged particles which escape out from the detector was changed. We took only the events which deposited the total energy of the charged particle produced from a neutron in the detector. The photomultiplier, the thin aluminum cladding and the  $\text{CaF}_2(\text{Eu})$  crystal were not included in the detector structure in the calculation. The neutrons impinged on the detector along the symmetry axis of the detector. In order to take into account the finite pulse height resolution of the detector, the calculated response was folded with a Gaussian distribution with  $\sigma=20\%$ . The spectrum calculated with the SCINFUL code for neutrons of energy interval 60-64MeV is also shown in Fig7 for comparison. The pulse height is given in unit of electron equivalent energy (MeVee). The experimental spectra were normalized to the calculated spectrum at the region indicated by the arrows in Fig7. The calculated response function, except at very lower pulse heights. This may be because the cross section data for the  $^{12}\text{C}(n,x\alpha)$ ,  $^{12}\text{C}(n,xt)$  and  $^{12}\text{C}(n,x^3\text{He})$  reactions have poor accuracy.

## NEUTRON MEASUREMENT UNDER THE INTENSE CHARGED PARTICLE MIXED FIELD

A test experiment was carried out at the same beam line for the neutron response function measurements at the RIKEN Ring Cyclotron. A mixed field of neutrons and protons was produced by bombarding 100MeV protons on a 10mm thick Li target. The phoswich detector was placed at 8m downstream from the Li target at 0 degree to the proton beam axis. The maximum proton energy was degraded to about 65MeV owing to the energy loss by the vacuum shield (3cm thick acrylic plate) of target chamber. The detector was set so that the proton beam impinged on the lateral side of the detector as shown in Fig.8. In the experimental setup, all protons impinging into the detector interact with the  $\text{CaF}_2(\text{Eu})$  crystal, thus protons detected by the phoswich detector always generate output signals from the  $\text{CaF}_2(\text{Eu})$  crystal. Neutrons produced by the Li target can interact with the NE213 scintillator without producing signals from the  $\text{CaF}_2(\text{Eu})$  crystal. We therefore can select the only neutron signals from the signals produced in the mixed field of protons and neutrons.

The obtained two-dimensional plot of  $L_{\text{total}}$  and  $L_{\text{CaF}}$  is shown in Fig.9. The protons whose ranges are smaller than the  $\text{CaF}_2(\text{Eu})$  crystal thickness produce signals only in the  $\text{CaF}_2(\text{Eu})$  crystal, not in the NE213 scintillator. These events correspond to the symbol 'A' in Fig.9. The protons whose ranges are longer than the  $\text{CaF}_2(\text{Eu})$  crystal thickness produce signals in both the  $\text{CaF}_2(\text{Eu})$  crystal and the NE213 scintillator. In this case, the energy loss in the  $\text{CaF}_2(\text{Eu})$  crystal decreases with increase of the proton energy and the energy deposit to the NE213 scintillator increases with the proton energy as far as protons stop inside the NE213 scintillator. These events are shown as the symbol 'B' in Fig.9. The neutron events which do not interact with the  $\text{CaF}_2(\text{Eu})$  crystal are shown as the symbol 'C' in Fig.9.

The spectra of all events projected on the  $L_{\text{total}}$  axis is shown in Fig.10. The solid circles indicate the proton spectrum. The discontinuity between the region 'A' and 'B' in Fig.10 is due to the fact that the  $dL/dE_p$  for the  $\text{CaF}_2(\text{Eu})$  crystal is smaller than that for the NE213 scintillator. The open circles in Fig.10 were obtained by selecting the region 'C' in Fig.9, which corresponds to a neutron spectrum. Fig.10 clearly indicates that the neutrons are successfully selected by the phoswich detector under the intense charged-particle mixed

field including a large number of protons and a small number of neutrons.

In the following experiment of more intense charged particle flux, we found that a part of proton events were mixed into neutron events, owing to the imperfect discrimination between proton and neutron events. This may be induced by some abnormal action of the circuit. We will make experiment again by investigating this problem.

## CONCLUSION

It was found that the n- $\gamma$  discrimination property of the phoswich detector of NE213 and  $\text{CaF}_2(\text{Eu})$  was slightly poorer than the ordinary NE213 detector, but it was still possible to measure the neutrons with this detector by discriminating gamma rays. The response functions for gamma rays and neutrons which were measured experimentally with this detector were almost the same as those of the ordinary NE213 detector, and agreed well with the calculated response functions. This shows that by inserting the  $\text{CaF}_2(\text{Eu})$  crystal wall the characteristics of this detector did not change so much, and moreover the energy resolution of the Compton edge was improved. For about five years, this phoswich detector consisting of the organic liquid combined with the inorganic crystal has been chemically stable, and has kept the same property.

This phoswich detector can distinguish the charged particle events with the accompanying signals from the  $\text{CaF}_2(\text{Eu})$  crystal, which enables us to detect neutrons under the intense charged particle mixed field. But under more intense charged particle flux it failed to discriminate the neutron events from the charged particle events perfectly.

We are also planning to develop a new detector which will be able to identify neutrons under more intense charged particle mixed field. The new detector is the phoswich detector of NE213 combined with NE115 or Pilot-U.

## ACKNOWLEDGMENTS

We wish to thank Dr. Y. Uwamino, Mr. N. Nakanishi, Mr. S. Fujita, Mr. S. Nakajima of the Institute of Physical and Chemical Research and Mr. T. Kurosawa of the Cyclotron and Radioisotope Center of Tohoku University for their assistances during the experiments. We also thank the cyclotron staffs of the Institute of Physical and Chemical Research for their

cyclotron operation.

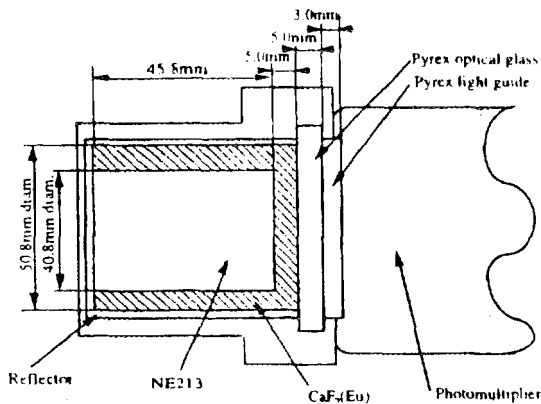


**Fig 1.** Diagram of the phoswich detector which we designed. This detector consists of NE213 surrounded by a 5mm thick  $\text{CaF}_2(\text{Eu})$  crystal except one surface.

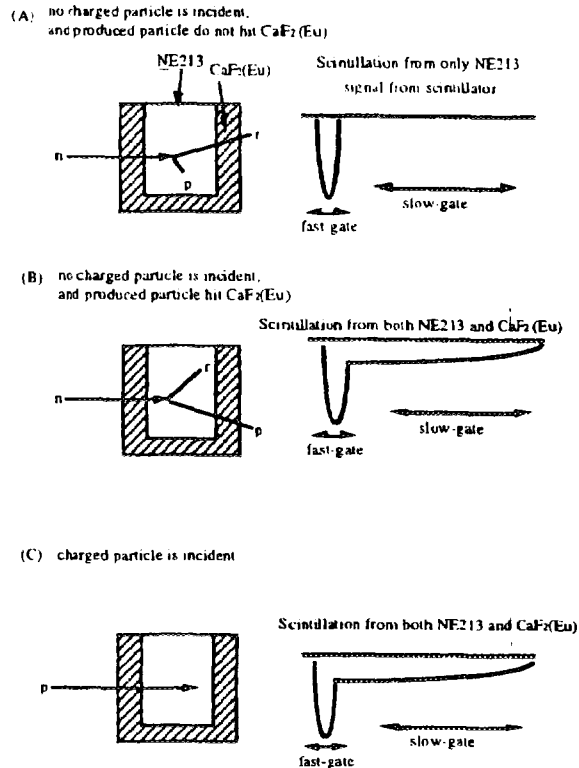


**Fig 2.** Signals produced by the scintillator in three cases which can occur in this detector.

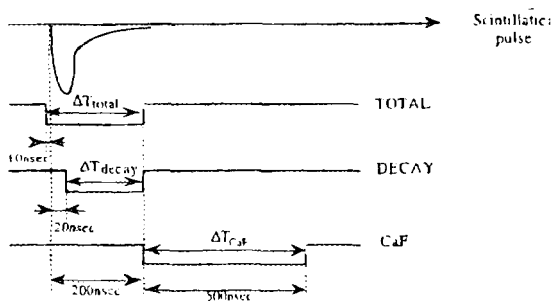


**Fig 3.** Time relations between the pulses from the photomultiplier anode and the gate inputs to three ADCs.

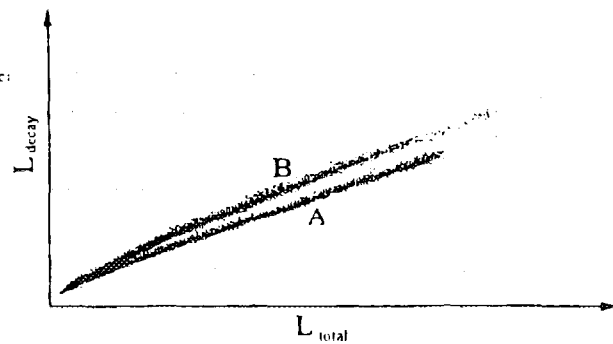


**Fig 4.** A two-dimensional plot of  $L_{\text{decay}}$  versus  $L_{\text{total}}$  measured with  $^{241}\text{Am-Be}$  source by selecting the events without  $\text{CaF}_2$  signals.

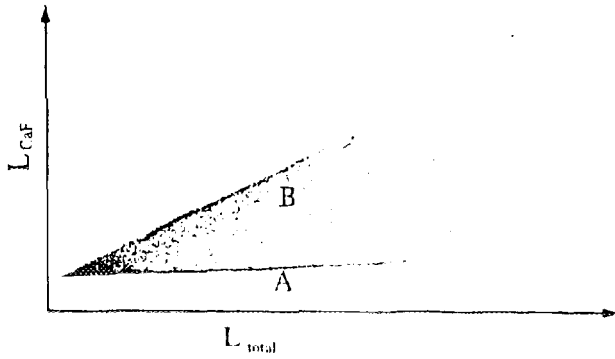


Fig 5. A two-dimensional plot of  $L_{CaF}$  versus  $L_{total}$  measured with neutrons produced by the  ${}^7\text{Li}(p,n)$  reaction of proton energy  $E_p=80\text{MeV}$ .

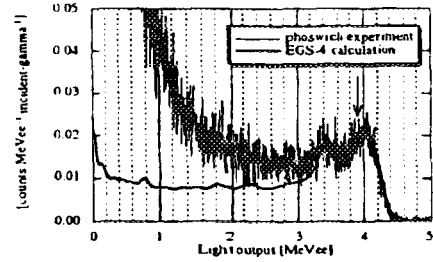


Fig 6. Response function measured for 4.43MeV photons from an  ${}^{241}\text{Am}$ -Be source, compared with the EGS-4 calculation.

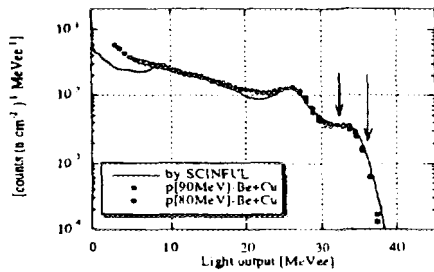


Fig 7. Response function for incident neutrons with energies between 40-42MeV. The experimental results are compared with the SCINFUL calculation.

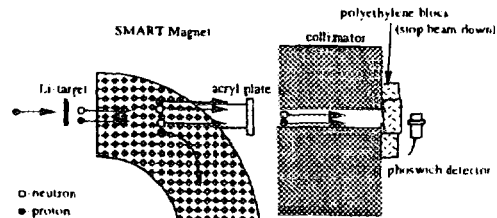


Fig 8. Schematic view of the experimental set up for the experiment in the mixed field of proton and neutron.

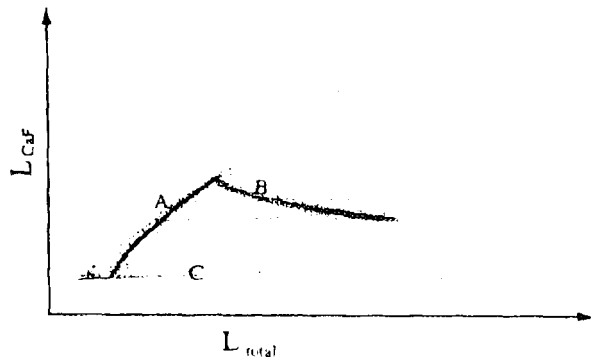


Fig 9. A two-dimensional histogram of the CaF component  $L_{CaF}$  versus the TOTAL component  $L_{total}$  measured in the mixed field of neutron and proton. The regions of symbol 'A' and 'B' indicate the case where the protons entered the detector.

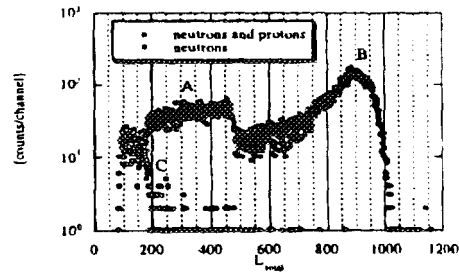


Fig 10. Pulse height of the TOTAL component measured in the proton mixed neutron field. The solid circles show the proton spectra, the open circles the neutron spectra.

#### REFERENCE

1. J.A.Lockwood, C.Chen, L.A.Friling and R.N.St.Onge, *J.Geophys. Res.* **81**, 177, (1976)
2. W.R.Nelson, H.Hirayama and D.W.O.Rogers, SLAC report no.265, Stanford 1985.
3. J.K.Dickens, Oak Ridge National Laboratory Report ORNL 6463 (1988).

# SIMULATION OF THE PEAK EFFICIENCY FOR A STACKED NaI(Tl) SPECTROMETER

H.Yoshida, H.Murohka, K.Anami, A.Nohtomi, Y.Uozumi, T.Sakae, M.Matoba

Department of Nuclear Engineering, Kyushu University

N.Koori

Fuculty of Integrated Arts and Sciences, the University of Tokushima

T.Maki

School of Nursing and Technology, University of Occupational and Environmental Health

## Abstract

A stacked NaI(Tl) spectrometer has been developed to measure proton spectra in wide energy range. In the measurement of charged particles with intermediate energy, the detecting efficiency of the spectrometer decreases considerably due to nuclear reactions or out-scatterings in the detector material. A Monte Carlo simulation code has been developed to estimate the peak efficiency (peak-to-total ratio) of the spectrometer. The calculated efficiency for intermediate energy is in good agreement with the experimental one.

## 1. INTRODUCTION

The nuclear data in intermediate energy region are useful for many applications that include the effects of space radiation on astronauts and their equipment, shielding design for accelerator, spallation neutron sources, medical isotopes production and so on. However, the data aren't enough in this region. Thus, it is desired to measure continuum and whole spectra of charged particle emission reaction to obtain the most reliable data sets. To evaluate reliable data sets, systematic studies of nuclear reactions are carried out in this energy region. Especially, a few data sets of  $(p, p')$  reaction are obtained below 200 MeV. It is interesting to measure continuum spectra of  $(p, p')$  reactions and to investigate the reaction mechanism in the higher energy region. Therefore, A stacked NaI(Tl) spectrometer<sup>[1]</sup> which consists of two Si semiconductor detectors and five NaI(Tl) scintillators has been developed to measure proton spectra of wide energy range up to 400 MeV.

In the measurement of charged particles with intermediate energy, the detecting efficiency of the spectrometer decreases considerably due to nuclear reactions or out-scatterings in the detector material. It is important to obtain the peak efficiency of the

spectrometer in intermediate energy region. Therefore, a Monte Carlo simulation code<sup>[2]</sup> has been developed to estimate the peak efficiency (peak-to-total ratio) of the spectrometer. In the calculation, it is important to use the reliable data of nuclear interactions. So a set of empirical formula for the data are applied. In this paper, calculated results of peak efficiency and response function are compared to experimental results that performed at the ring-cyclotron facility of the Research Center for Nuclear Physics (RCNP), Osaka university.

## 2. EXPERIMENTS

A schematic diagram of the stacked NaI(Tl) spectrometer is shown in Fig.1. It consists of four NaI(Tl) scintillators of 2 inches cubic and a cylindrical one of 8 cm in diameter by 18 cm long. Two Si semiconductor detectors which have thickness of 150 and 300  $\mu\text{m}$  are placed in front of the scintillators. Their active area of 450  $\text{mm}^2$  determines the active area of the spectrometer. For cubic scintillators, photomultiplier tubes (Hamamatsu R329,R329-02) are attached to the opposite faces (top and bottom) respectively with the optical compound (Oken 6262A), and for a cylindrical scintillator, a photomultiplier tube (Hamamatsu R1308) is attached.

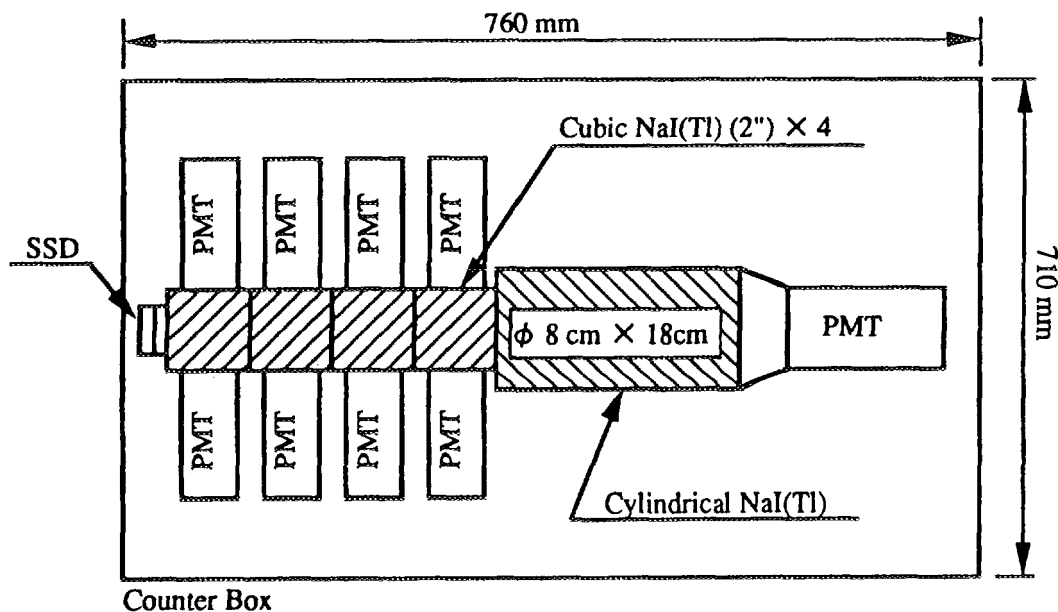


Fig.1 Schematic diagram of the stacked NaI(Tl) spectrometer.

Tests of the spectrometer were performed using 300 and 350 MeV proton beam from the ring cyclotron at the RCNP. The proton beam bombarded a  $\text{CH}_2$  target of 1.2 mm thick set in a scattering chamber for a polarimeter. The experimental arrangement is shown in Fig.2. Approximately monochromatic energy protons were obtained from elastic

$pp$  scatterings. To reject particles from proton-carbon inelastic scatterings, the  $pp$  events were selected by recoil proton measurement using a coincidence spectrometer. For 350 MeV proton beam, the spectrometer was located at  $\theta_{Lab} = 30^\circ$  and  $45^\circ$ , which corresponded to  $E_p = 250$  and 160 MeV, respectively. And for 300 MeV proton beam, it was located at  $\theta_{Lab} = 30^\circ, 50^\circ$  and  $60^\circ$ , which corresponded to  $E_p = 214, 110$  and 62 MeV, respectively.

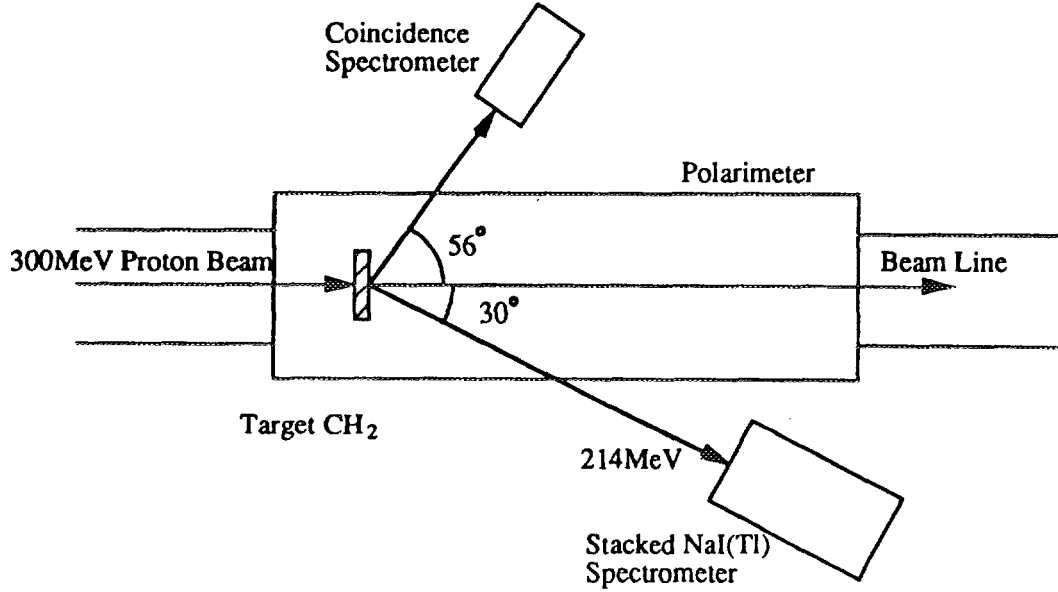


Fig.2 Experimental arrangement.

### 3. MONTE CARLO CODE

A Monte Carlo simulation code has been developed to estimate the peak efficiency (paak-to-total ratio) of the stacked NaI(Tl) spectrometer. In this code, nuclear reaction, elastic scattering and multiple coulomb scattering are considered as interaction between incident protons and nuclei in the detector material (NaI). In clculating the efficiency, an incident proton was assumed to be lost by a nuclear reaction. The total raction cross-section  $\sigma_R^{[3]}$  is given empirically by

$$\sigma_R = 0.045A^{0.7} f(A) g(E_p) \quad (\text{barn}), \quad (1)$$

with

$$f(A) = 1 + 0.016 \sin(5.3 - 2.63 \ln A),$$

$$g(E_p) = 1 - 0.62 \exp(-E_p/200) \sin(10.9E_p^{-0.28}),$$

where  $E_p$  is the proton energy and  $A$  is the mass number of the material.

In the case of very large detectors, the peak efficiency is determined by the reaction loss. On the other hand, in the case of relatively small detectors, the out-scattering will be caused by elastic and multiple coulomb scattering. The elastic scattering cross-section  $d\sigma_{E_p}/d\Omega$ <sup>[3]</sup> is given by

$$\frac{d\sigma_{E_p}}{d\Omega} = \left[ kR^2 \frac{J_1(x)}{x} \right]^2 \exp \left[ -cx \left( 1 + \frac{x}{40} \right) \right] \quad (cm^2/sr), \quad (2)$$

with

$$\begin{aligned} R &= \left[ 0.14A^{1/3} + 0.122(A+1)/A \right] \times 10^{-12} \quad (cm), \\ x &= 2kR \sin(\theta/2), \\ c &= 0.2(208/A)^{1/3}, \\ k &= \frac{pv}{h} = 2.197E_p^{1/2} \times 10^{12} \quad (cm^{-1}). \end{aligned}$$

This equation didn't reproduce the cross-section of the experimental value for <sup>40</sup>Ca<sup>[4, 5]</sup>. Therefore, the equation was modified to be

$$\frac{d\sigma_{E_p}}{d\Omega} = W \left[ \frac{R}{2 \sin(\theta/2)} \right]^2 \exp \left[ -cx \left( 1 + \frac{x}{40} \right) \right] \quad (cm^2/sr), \quad (3)$$

with

$$W = 144.4E_p^{-1.337},$$

where  $W$  is the normalization factor as a function of  $E_p$ . The calculated cross-sections using eq.(2) and (3) are shown in Fig.3, together with experimental cross-sections. The  $W$  is obtained from the experimental value for <sup>40</sup>Ca. However, eq.(3) can reproduce the experimental value for other nuclei<sup>[6]</sup>. Since particles at intermediate energy region have long range, the number of particles scattered out of the detector is sensitive to very small inclination of trajectory due to multiple coulomb scattering. The inclination is calculated by the Kuhn's fast algorithm<sup>[7]</sup> based on the Molière's formula<sup>[8]</sup>. the Kuhn's fast algorithm is described followings.

The probability  $dP(\theta)$  of scattering into an angle between  $\theta$  and  $\theta + d\theta$  after traveling a distance  $\Delta s$  (cm) through some material is given by

$$\begin{aligned} dP(\theta) &= (1 - 0.827/B) \exp \left[ - \left( \frac{\theta}{\theta_{1/e}} \right)^2 \right] \frac{d\theta^2}{\theta_{1/e}^2} \\ &\quad + \Theta(\theta - \sqrt{2}\theta_{1/e}) \frac{\chi_c^2}{4} d \left( - \frac{1}{\sin^2(\theta/2)} \right), \end{aligned} \quad (4)$$

with

$$\begin{aligned} \chi_c^2 &= 0.1569 \frac{z^2 Z^2 \rho \Delta s}{p^2 v^2 A}, \\ B - \ln B &= b = \ln \left[ \frac{6700z^2 Z^{4/3} \rho \Delta s / A}{\beta^2 + 1.77 \times 10^{-4} z^2 Z^2} \right], \\ \theta_{1/e} &= \chi_c \sqrt{B - 1.25}. \end{aligned}$$

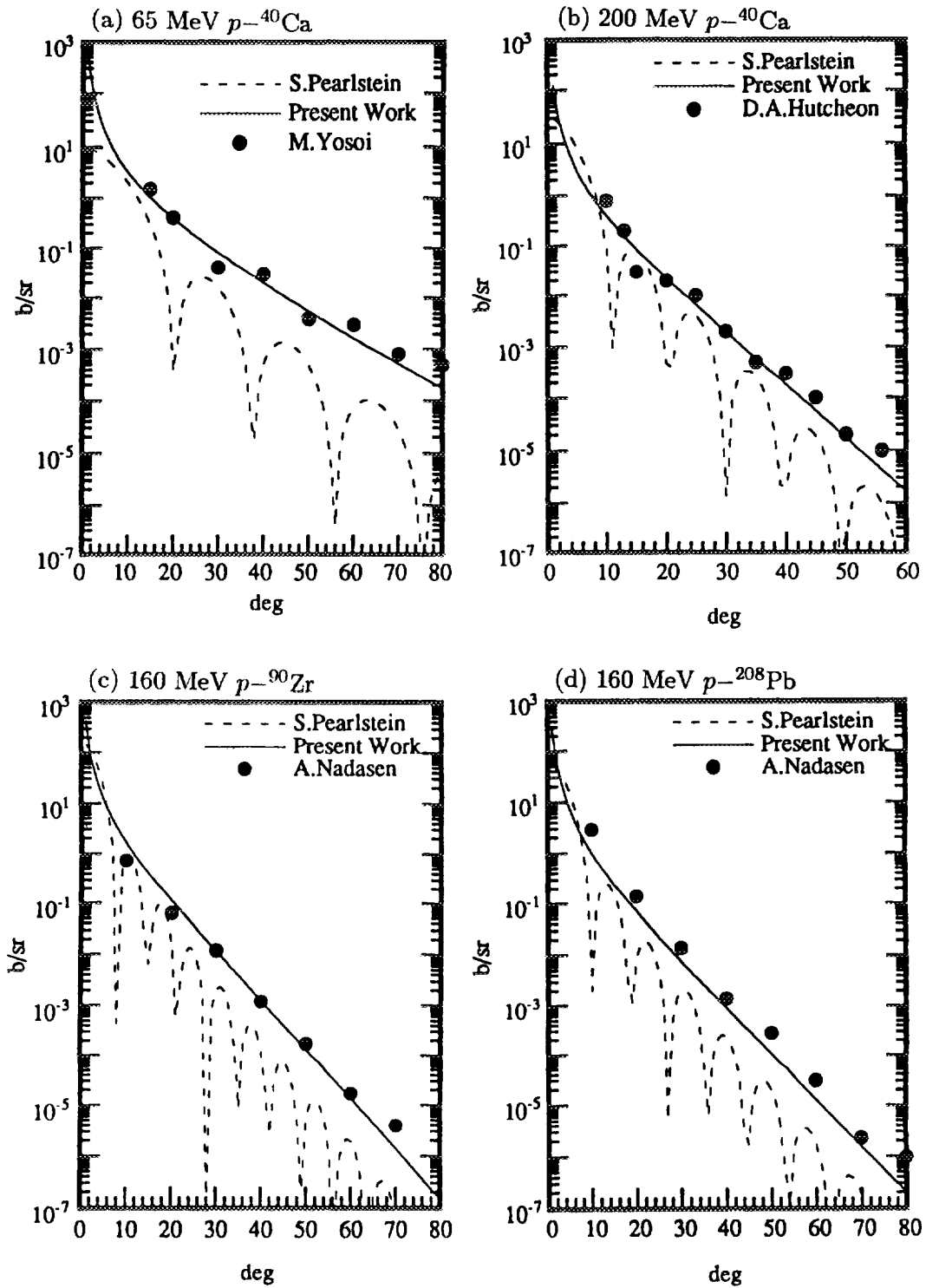


Fig.3 Elastic scattering cross-section. (a) 65 MeV  $p-^{40}Ca$ <sup>[4]</sup>, (b) 200 MeV  $p-^{40}Ca$ <sup>[5]</sup>, (c) 160 MeV  $p-^{90}Zr$ <sup>[6]</sup> and (d) 160 MeV  $p-^{208}Pb$ <sup>[6]</sup>.

Integrating eq.(4) yields the probability of scattering into an angle between 0 and  $\theta$ , and the total probability of scattering into an angle between 0 and  $\pi$  is slightly less than 1 and is given by

$$P(\pi) = 1 - 0.827 \frac{1}{B} + \frac{\chi_c^2}{4} \left( \frac{1}{\sin^2(\theta_{1/e}/\sqrt{2})} - 1 \right). \quad (5)$$

With this in mind, each multiple scattering angle is determined from random number  $R$ . If  $P(\pi) \geq R \geq 1 - 0.827/B$ ,  $R$  is transformed to  $R' = R - 1 + 0.827/B$  and  $\theta$  is given by

$$\theta = 2 \arcsin \left( \frac{\chi_c \sin(\theta_{1/e}/\sqrt{2})}{\sqrt{\chi_c^2 - 4R' \sin^2(\theta_{1/e}/\sqrt{2})}} \right). \quad (6)$$

Otherwise, for  $R < 1 - 0.827/B$ ,  $\theta$  is given by

$$\theta = \theta_{1/e} \left[ \ln \left( \frac{1 - 0.827/B}{1 - 0.827/B - R} \right) \right]^{1/2} \quad (7)$$

The peak efficiency of the stacked NaI(Tl) spectrometer has been calculated with the above conditions.

#### 4. RESULTS AND DISCUSSION

In Fig.4, response functions of the stacked NaI(Tl) spectrometer are shown. The solid line is calculated using the Monte Carlo code, and dots are experimental results in counts per 2 MeV. In the calculation, the number of the incident protons is set to be equal to the experiment. As shown in Fig.4, the shapes of the response functions obtained from

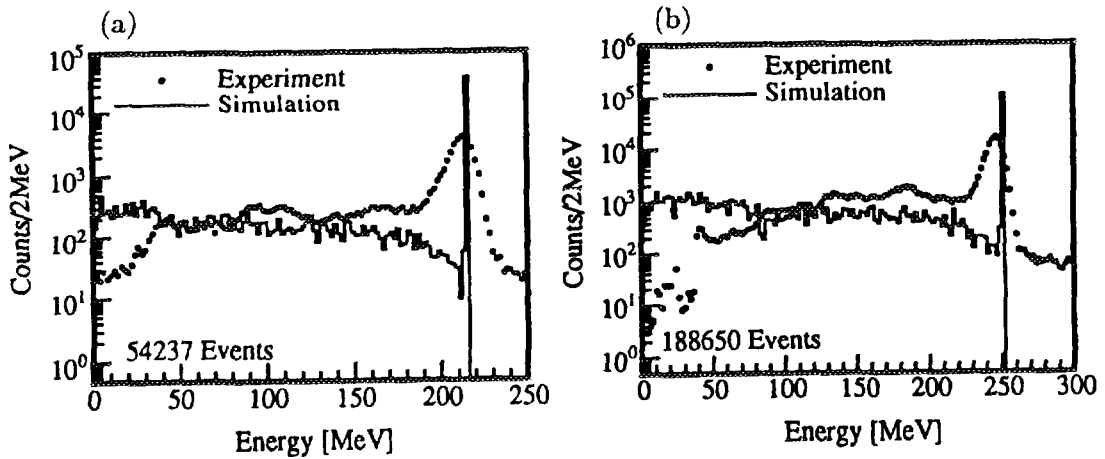


Fig.4 Response function of the stacked NaI(Tl) spectrometer.  
(a)  $E_p = 214$  MeV and (b)  $E_p = 250$  MeV.

the calculation are different from experimental results. The difference of shapes in the tail part is caused by the assumption that the incident proton is lost by nuclear reaction in calculation. Width of the peak part is caused by the kinematical width of incident energy and the response of NaI(Tl) and other equipments.

The code developed in this work can generate the energy spectra of each NaI(Tl) scintillator. In Fig.5, the energy spectra of each NaI(Tl) scintillator are shown. The solid line and dots are the same meaning as Fig.4.

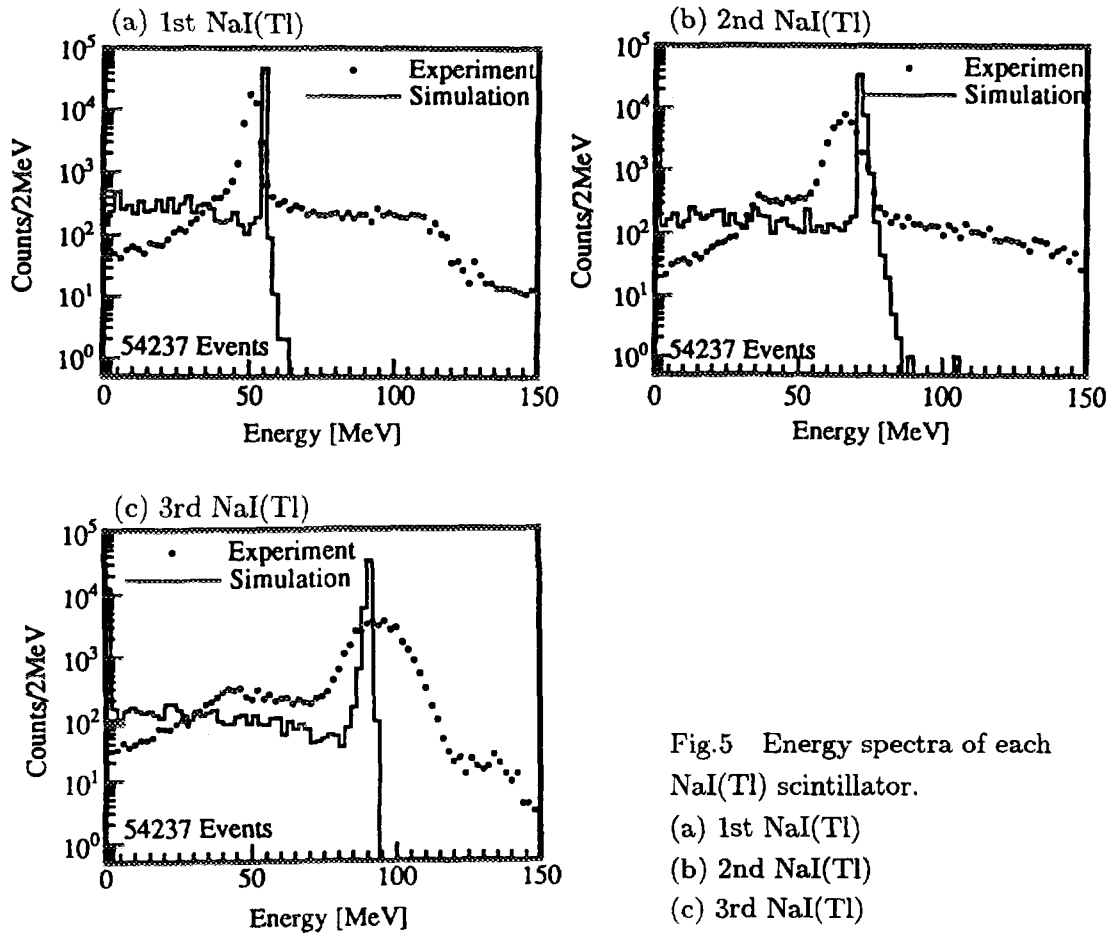


Fig.5 Energy spectra of each NaI(Tl) scintillator.  
 (a) 1st NaI(Tl)  
 (b) 2nd NaI(Tl)  
 (c) 3rd NaI(Tl)

The peak efficiency of the stacked NaI(Tl) spectrometer and each NaI(Tl) scintillators are shown in Table.1. The efficiency of the spectrometer is labeled "Total". The efficiency obtained from the present calculation is in good agreement with the experimental value.

In Fig.6, the peak efficiency of the stacked NaI(Tl) spectrometer is shown. The solid line is obtained from the calculation, and closed circles are the experimental results. The calculated efficiency is in good agreement with the experimental one. Since the spectrometer consists of cubic and cylindrical scintillators, the slope of calculated efficiency changes at about 270 MeV.

Table.1 Peak efficiency.

Energy		Experiment	Simulation
62MeV	Total	95.6%	95.8%
110MeV	Total	92.0%	89.5%
160MeV	1st NaI(Tl)	86.6%	88.1%
	2nd NaI(Tl)	79.1%	80.5%
214MeV	Total	81.3%	81.1%
	1st NaI(Tl)	89.4%	87.5%
	2nd NaI(Tl)	77.1%	77.3%
	3rd NaI(Tl)	68.1%	69.6%
250MeV	Total	69.0%	69.6%
	1st NaI(Tl)	85.1%	86.1%
	2nd NaI(Tl)	76.6%	76.3%
	3rd NaI(Tl)	65.6%	63.9%
	4th NaI(Tl)	55.2%	58.0%
	Total	57.5%	59.0%

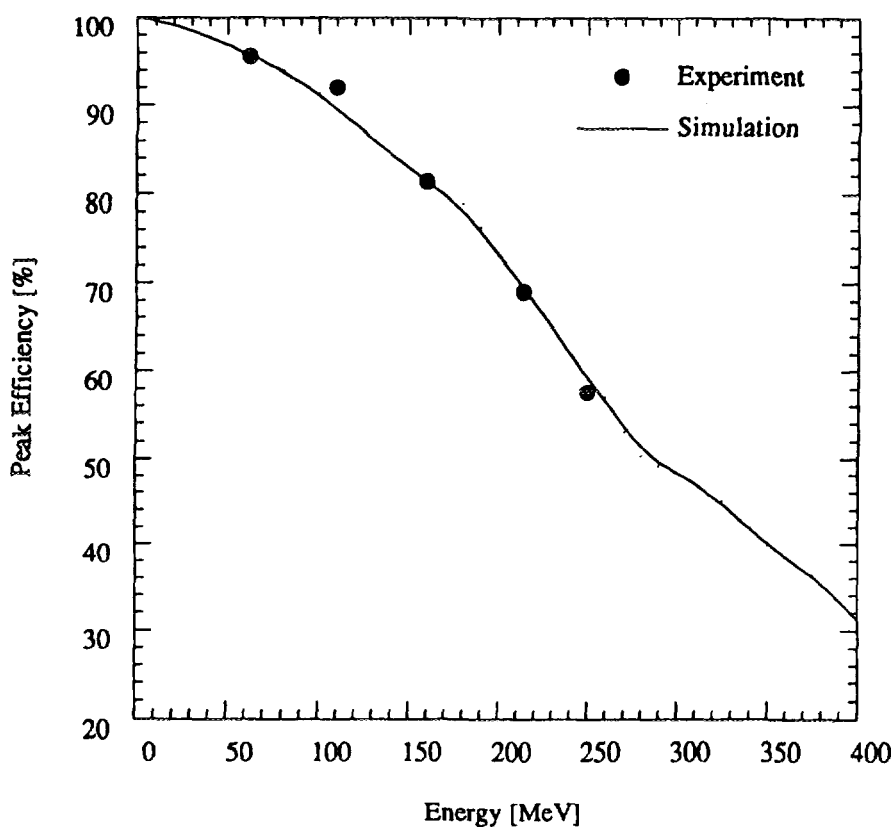


Fig.6 Peak efficiency of the stacked NaI(Tl) spectrometer.

## 5. CONCLUSION

A Monte Carlo simulation code for the stacked NaI(Tl) spectrometer has been developed. In order to reproduce the experimental data by using the code, a set of cross-section data for elastic scattering was obtained by modification of empirical equation.

The shapes of the response functions obtained from the calculation are different from experimental results. On the other hand, the calculated peak efficiency is in good agreement with the experimental one. Therefore, the code is applicable for the analysis of continuum spectra in intermediate energy region.

## References

- [1] M.Yamashita: Master thesis, Kyushu Univ. (1994)
- [2] H.Yoshida: Master thesis, Kyushu Univ. (1996)
- [3] S.Pearlstein: J.Astrophys. 346(1989)1049
- [4] M.Yosoi, H.Sakaguchi, M.Nakamura, M.Ieiri, H.Togawa, S.Hirata, T.Nakano, H.M.Shimizu, M.Iwaki, O.Kamigaito, T.Noro, H.Ikegami and S.Kobayashi: RCNP Annual Report, (1977)6
- [5] D.A.Hutcheon, W.C.Olsen, H.S.Sherif, R.Dymarz, J.M.Cameron, J.Johnsson, P.Kitching, P.R.Liljestrang, W.J.McDonald, C.A.Miller, G.C.Neilson, D.M.Sheppard, D.K.McDaniels, J.R.Tinsley, P.Schwandt, L.W.Swenson and C.E.Stronach:Nucl.Phys. A483(1988)429
- [6] A.Nadasen, P.Schwandt, P.P.Singh, W.W.Jacobs, A.D.Bacher, P.T Debevec, M.D.Kaitchuck and J.T.Meek: Phys.Rev.C 23(1981)1023
- [7] S.E.Kuhn and G.E.Dodge: Nucl.Instr.& Meth. A322(1992)88
- [8] G.Molière: Z.Natureforsch. 3a(1948)78

# Use of Si-PIN Photodiode X-ray Detector for PIXE

J. Inoue, S. Iwasaki, K. Murozono, K. Ishii, and M. Kitamura

*Department of Nuclear Engineering, Tohoku University  
Aramaki-Aza-Aoba, Aobaku, Sendai 980-77, Japan*

## 1. INTRODUCTION

Si-PIN photodiode type detector is one of the X-ray detectors which have shown significant improvement in resolution recently <sup>(1)</sup>. It was reported that most advanced detector had a specification value of FWHM of 250 eV at 5.9 keV<sup>\*</sup>. This value is worse only by 100 eV than the typical value of conventional Si(Li) detectors. The remarkable advantage of the detector is high operability with the Peltier cooling system and low voltage bias. The detector with a preamplifier and cooler is housed in a box whose size is 9.5x4.4x2.9<sup>t</sup> in cm. Disadvantage of this detector is still in the small sensitive volume, especially thickness of the detector; this might cause insufficient efficiency of the detector for observation of the higher energy X-rays. In this paper, basic characteristics of this type of detector and feasibility to the PIXE has been investigated.

## 2. BASIC CHARACTERISTICS OF Si-PIN PHOTODIODE DETECTOR

First, basic characteristics of the detector has been studied using some radioactive X-ray sources. List of the used X-ray sources are shown in Table 1 with the related nuclear data. Energy resolution of the detector has been derived as the FWHM values of Gaussian peaks fitted to the source spectra in the energy range from 4 keV to 26 keV. The relation between the resolution and X-ray energy was derived by the least-squares method by assuming that FWHM of the peak was expressed by the quadratic sum of energy dependent and independent terms. The result is given by a shifted curve from that of the conventional Si(Li) detector by about 100 eV as shown in Fig. 1. At 5.9 keV, the observed data are rather consistent with the nominal value of the specifications given by the manufacturer. Intrinsic efficiency of the detector was also derived from the experimental data. In Fig. 2, the data are compared with the calculated curves both for a typical Si(Li) detector and the Si-PIN photodiode detector in slab geometry with the thicknesses of 5000 and 500  $\mu\text{m}$ , respectively. The observed data for the Si-PIN photodiode detector scatter, but show a trend of the efficiency similar to the calculated one. The calculate curve is almost the same with that of the conventional detector below 10 keV, while the efficiency value is decreasing considerably with increase the X-ray energy above 15 keV; this energy corresponds to the energy of characteristic K- X-rays of elements around  $Z=40$ ; the efficiency value becomes almost one-tenth of that of conventional type Si(Li) detector or less.

<sup>\*</sup>) taken from the specifications of XR100T in catalogue of Amptek, Inc., 6 DeAngelo Drive, Bedford, MA 01730, USA.

**Table 1:** The list of standard sources with the related nuclear data (2).

Nuclide	Decay Mode	Trans.	Energy(keV)	Emission Probability
Fe-55	EC	Mn K $\alpha$	5.89	0.249
		Mn K $\beta$	6.49	0.034
Sr-85	EC	Rb K $\alpha$	13.34-13.40	0.500
		Rb K $\beta$	14.96-15.29	0.087
Cd-109	EC	Ag K $\alpha$	21.99-22.16	0.821
		Ag K $\beta$	24.93-25.60	0.173
Am-241	$\alpha$ -decay	Np L $\alpha$	13.93	0.132
		Np L $\beta$ $\eta$	17.61	0.194
		Np L $\gamma$	20.99	0.049
	$\gamma$ -decay	$\gamma$ -ray	26.34	0.024

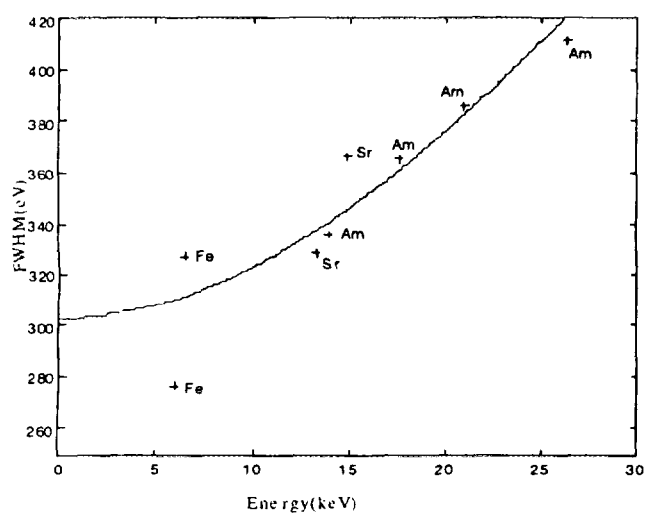


**Fig. 1 :** The result of FWHM vs energy .

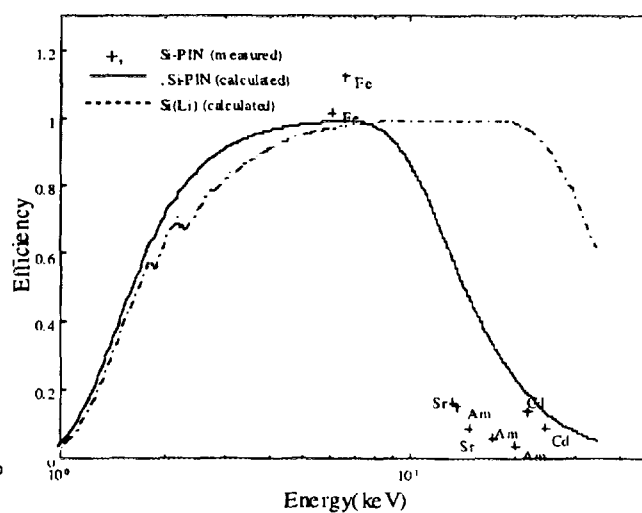


**Fig. 2 :** The result of efficiency for the Si-PIN photodiode and conventional Si(Li) detector.

### 3. APPLICABILITY TO PIXE

Applicability of the detector to PIXE has been studied in an in-air PIXE condition. The Si-PIN photodiode detector was mounted in a specially manufactured assembly for the beam exit of ViaPIXE (Vertical beam in-air PIXE system of Cyclotron Radioisotope Center, Tohoku University)<sup>(3)</sup>. In Fig. 3, the set up of ViaPIXE with the Si-PIN photodiode detector is shown. A typical spectrum of PIXE measured by the detector is shown for a sample of ZnS layer on aluminium foil which has been used for the beam monitor at the sample position (see Fig.4). In the spectrum, several peaks of aluminum, argon, iron, zinc, and other minor elements were observed, and lastly cadmium contained as an activator in the ZnS in the higher energy range was. The peak of argon was due to the bombardment of protons on the air between the beam exit foil (Kapton film) and sample. An inspection of the spectrum does not indicate a significant difference, especially in the separability of peaks from that measured by a conventional Si(Li) detector. However we could notice the low counts of peaks for cadmium as mentioned before. Fig.5 shows a spectrum of a serum sample. It also indicated that the separability of peaks which we interested in was enough good for PIXE analysis.

### 4. SUMMARY

The basic characteristics of a Si-PIN photodiode detector were examined by a set of X-ray sources, and rather consistent with the catalogue data given by the manufacture. Feasibility of this detector in the PIXE experiment was also investigated. This type of detector can be applied to PIXE experiment except for the samples which contain high Z elements above 40 because of the low efficiency of the detector to corresponding higher energy X-rays or if the analysts are not interested in heavier elements in samples to be studied. If they want to know the concentration of the heavier elements, they should take an alternative way to compensate for the low efficiency of the detector. For example, it can be solved by using a high Z semiconductor detector CdZnTe which is operable in the same way of the Si-PIN photodiode detector, and shows relatively good energy resolution of about 300eV. Another method is use of an array of the Si-PIN photodiode detectors because the cost of the detector is not so expensive. Relatively lower energy resolution of the detector is not significant drawback compared to the conventional Si(Li) detector, if we apply the pattern analysis method proposed by our group<sup>(4)(5)(6)</sup>.

### References

- (1) A. C. Huber, et al., Nucl.Instr.and.Meth.in.Phys.Res.**B99**(1995) 655.
- (2) Nuclear Data Standards For Nuclear Measurements(1991),NEANDC/INDC Nuclear Standard File.
- (3) S. Iwasaki, K. Ishii, K. Yoshizaki, H. Fukuda, K. Murozono, J. Inoue, M. Kitamura, H. Yokota, Y. Iwata, and H. Orihara, Vertical Beam In-Air PIXE System at CYRIC, to be appeared in *IJPIXE*.
- (4) K. Yoshizaki, S. Iwasaki, H. Fukuda, M. Kitamura, K. Ishii, KEK Proceedings, **95-1** (1995)330.
- (5) S. Iwasaki, H. Fukuda, K. Yoshizaki, M. Kitamura, K. Ishii, *IJPIXE*, **4** (1994)131.
- (6) K.Murozono, in this symposium.

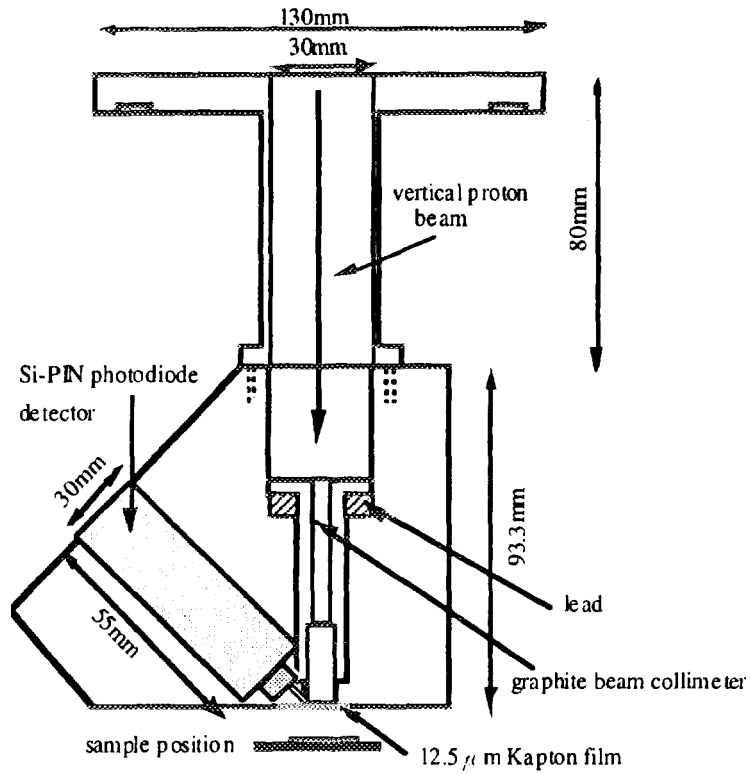


Fig. 3 :Schematics of the beam exit assembly of ViaPIXE for Si-PIN photodiode detector.

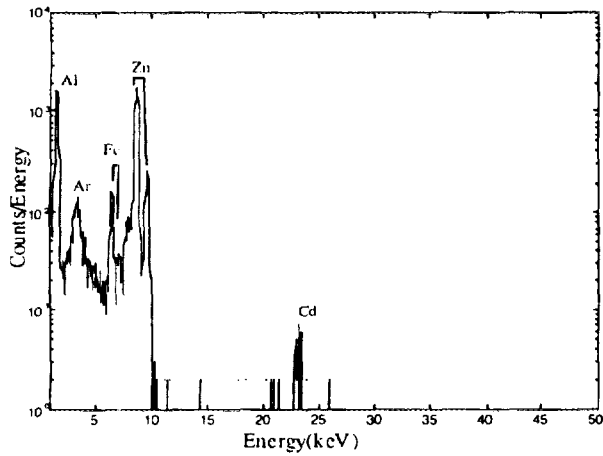


Fig.4 :PIXE spectrum from ZnS sample using Si-PIN photodiode.

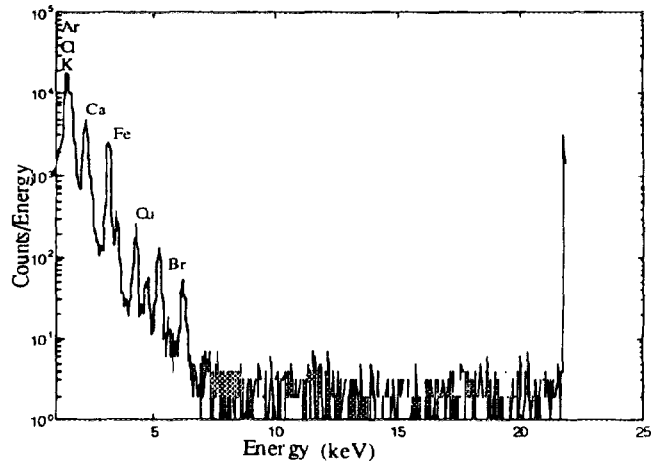


Fig. 5 : PIXE spectrum from serum sample using Si-PIN photodiode.

# GAS GAIN CHARACTERISTICS OF PARALLEL PLATE AVALANCHE COUNTER

Katsuhisa Nishio, Hideki Yamamoto, Ikuo Kanno, Itsuro Kimura

*Department of Nuclear Engineering, Kyoto University, Yoshida, Sakyo-ku, Kyoto, 606-01, Japan*

Y. Nakagome

*Research Reactor Institute, Kyoto University, Kumatori-cho, Sennan-gun, Osaka 590-04, Japan*

## 1. INTRODUCTION

A parallel plate avalanche counter (PPAC) is widely used for nuclear fission study due to its large detection area, position sensitivity and good timing resolution. When a PPAC is applied to the fission fragment detection, the pressure of its working gas is controlled to be as low as a few torr. As the gas gain is very sensitive to the gas pressure ( $p$ ), its characteristics with respect to  $p$  is important to develop a new PPAC. There have been many works so far to investigate the gas multiplication of a conventional proportional counter. In these measurements, typical gas pressure in the counter is about atmospheric value or a few hundreds torr. In the low gas pressure region, Tsumaki<sup>(1)</sup> obtained the Townsend primary ionization coefficient ( $\alpha$ ) between  $p = 10$  and 30 torr using a PPAC sealed with isobutane. But scarce works can be found in the region below 10 torr, so we have measured the gas multiplication in this region.

In the conventional gas gain theory, the Townsend primary ionization coefficient is expressed as a function of  $S$ , which is the ratio of the electric field strength ( $E$ ) to the gas density ( $N$ ). In this paper, an experimental form of  $\alpha$  is derived from the data and is compared with the formula so far.

## 2. STRUCTURE OF PPAC

The configuration of the PPAC is shown in Fig. 1. This PPAC consists of a central cathode and two grounded anodes with active area of  $20 \times 10 \text{ cm}^2$ . The cathode is made of a mylar film of  $1.5 \text{ }\mu\text{m}$ , on which gold is evaporated about  $50 \text{ }\mu\text{g/cm}^2$  in thickness on both sides, and the film is glued to a epoxy frame by using a vacuum grease and silver paint. The

negative bias is applied to the cathode, . The anodes, which are positioned 0.25 cm apart on both sides of the cathode, are designed to determine the fragment incident position two dimensionally. They consist of serial subelectrodes of 1.0 cm in width, and each subelectrode is made of evaporated gold of  $50 \mu\text{g}/\text{cm}^2$  thick on  $1.5 \mu\text{m}$  mylar so as to face the cathode. The neighboring subelectrodes are connected with each other through a 450 ohm resistance. The fragment incident position is determined by the charge ratio induced on both ends of the serial subelectrodes. The PPAC is mounted in a chamber made of aluminum. Isobutane is flowed in the chamber and the gas pressure is controlled by two valves. In order to detect the fission fragment, the PPAC is connected to a vacuum flight chamber by an entrance window which is made by a  $1.5 \mu\text{m}$  mylar film.

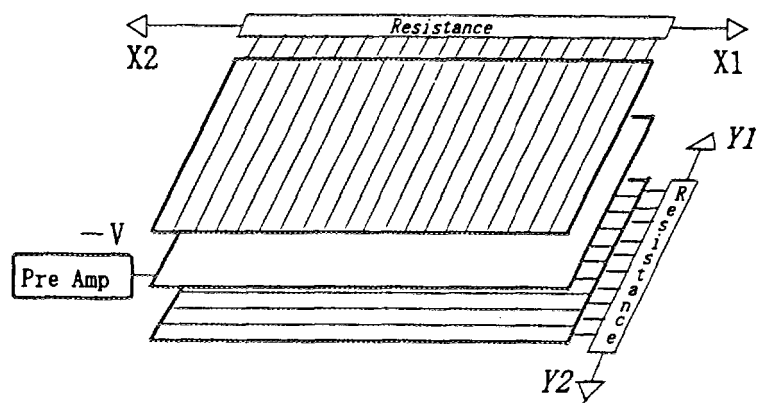


Fig. 1 Structure of PPAC

### 3. GAS GAIN MEASUREMENT

The PPAC was filled with isobutane to a desired pressure ( $p$ ) and a negative voltage ( $V$ ) was applied on the cathode through a preamplifier (ORTEC 142A). The fission fragments from the spontaneous fission of  $^{252}\text{Cf}$  were used as projectiles. A pulse of the avalanche electrons initiated by the fission fragment was generated on the cathode. After the amplification of the pulse signal, it was sent to a pulse height analyzer. Figure 2 shows the pulse height spectrum with a condition of  $p = 6$  torr and  $V = -450$  V, from which the peak channel of the pulse height spectrum was determined. In this way, the peak channels with respect to  $p$  and  $V$  were determined, and the results were shown in Fig. 3. In this figure, it is

seen that the pressure which yields the highest pulse height channel exists for all bias voltages except  $V = -450$ . From the same figure, as the peak channel increases exponentially with respect to  $V$  at a given pressure, the gas multiplication of the PPAC is operated in the proportional region. In the following section, we derive the Townsend primary ionization coefficient by using this data.

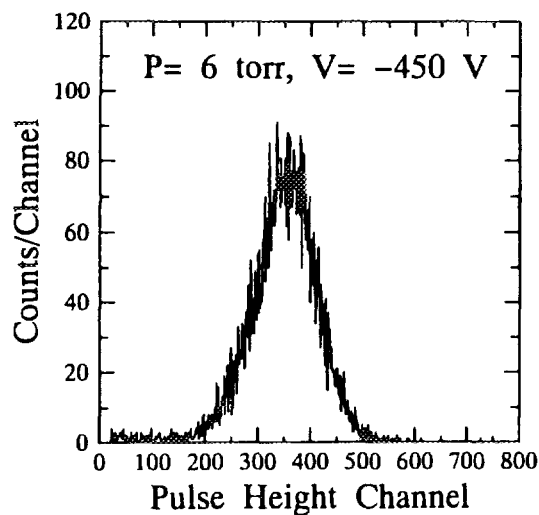


Fig. 2 Pulse height spectrum for the fission fragment of  $^{252}\text{Cf}(\text{sf})$

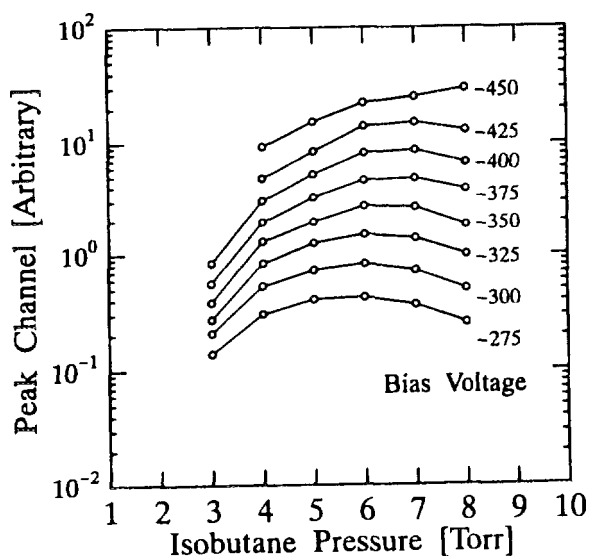


Fig. 3 Observed peak channel in the pulse height spectrum at a given pressure ( $p$ ) and applied bias voltage ( $V$ )

#### 4. TOWNSEND PRIMARY IONIZATION COEFFICIENT

The gas multiplication is described by the Townsend primary ionization coefficient  $\alpha$ . The increase of the number of electrons per path  $dx$  is given by,

$$dn = n \alpha dx \quad , \quad (1)$$

where  $n$  is the number of electrons. In the framework of the conventional gas gain theory, the  $\alpha$  over  $N$  is expressed by the function of  $S$  as follows (2).

$$\alpha / N = f(S) \quad . \quad (2)$$

Several expressions of  $f(S)$  proposed so far are listed in Table. 1.

Next we derive the  $\alpha/N$  from the present data. From the structure of the PPAC, the electric field strength  $E$  is assumed to be constant in any region of the PPAC. Then we obtain the  $\alpha$  for a given pressure  $p$  and  $E$ .

$$\alpha = \log(n / n_0) / X = \log G / X \quad , \quad (3)$$

where  $X$  is the distance from the cathode to the anode, and  $n_0$  is the initial number of electrons. As the experimentally obtained pulse height  $P_h$  is proportional to  $n$ , Eq. (3) becomes

$$\alpha = \log(k_1 P_h / n_0) / X \quad , \quad (4)$$

where  $k_1$  is constant. The initial number of electrons  $n_0$  is proportional to  $p$ , because the energy loss of the fission fragments in the PPAC increases linearly by  $p$ . Then the  $n_0$  becomes

Table 1 Analytical forms for  $\alpha/N$  used by different authors.

Authors	$\alpha/N$
Rose and Korff (3)	$H S^{1/2}$
Diethorn (4)	$D S$
Williams and Sara (5)	$A \exp(-B / S)$
Zastawny (6)	$G (S - Q)$
Charles (7)	$I \exp(-J / S^{1/2})$
Aoyama (8)	$K S^m \exp(-L / S^{1-m})$ , $0 \leq m \leq 1$

$$n_0 = k_2 p , \quad (5)$$

where  $k_2$  is constants. Inserting Eq. (5) into (4),  $\alpha$  becomes

$$\alpha = \log(k P_h / p) / X = \log(P_h / p) / X + A , \quad (6)$$

where  $k$  and  $A$  are also constants. The experimental value of  $P_h$  shown in Fig. 3 is substituted to Eq. (6) and the  $\alpha$  is obtained. From the analysis, it is found that the  $\alpha$  is a function of not only  $S$  but also  $p$  and that the following equation satisfactorily represents the experimental data

$$\alpha / N = r_0 (1 - p_0 / p) (S - S_0) + A_0 \quad (7)$$

Parameters  $r_0$ ,  $p_0$  and  $S_0$  for isobutane are determined by the fitting procedure. Then we obtain,

$$r_0 = 3.02 \times 10^{-18} \text{ [cm}^2\text{/Td]} , \quad (8)$$

$$p_0 = 1.56 \text{ [torr]} , \quad (9)$$

$$S_0 = -5.00 \times 10^{-2} \text{ [Td]} . \quad (10)$$

The value of  $A_0$  in Eq. (7) is determined to be  $-1.93 \times 10^{-16} \text{ cm}^2$  by comparing the present expression with the following one proposed by Tsumaki<sup>(7)</sup> when  $p = 10$  torr.

$$\alpha / N = 7.29 \exp(-1343 / S) \times 10^{-16} \text{ [cm}^2\text{]} . \quad (11)$$

In Fig. 4, the value of  $\alpha/N$  obtained from the experiment and that predicted by Eq. (7) are shown by solid circle and solid line, respectively. The curve given by Tsumaki is also shown in this Figure. The N.P in this figure is the normalization point to determine the  $A_0$ . The  $\alpha/N$  predicted by Eq. (7) for all of the gas pressure intersect at a point ( $S_0, A_0$ ), if it is extrapolated to the negative  $S$  value. We named this point as P.O.F (pivot of fun). But the negative values of  $S$  and  $\alpha/N$  have no physical meaning. The dotted line in the same figure shows the asymptote of  $\alpha/N(S)$  when  $p$  increases to infinity or sufficiently large value compared to the  $p_0$  and is expressed as

$$\alpha / N = r_0 (S - Q) . \quad (12)$$

This is the analytical form of Zastawny (see Table 1) with  $Q = 1.38 \times 10^2$  Td.

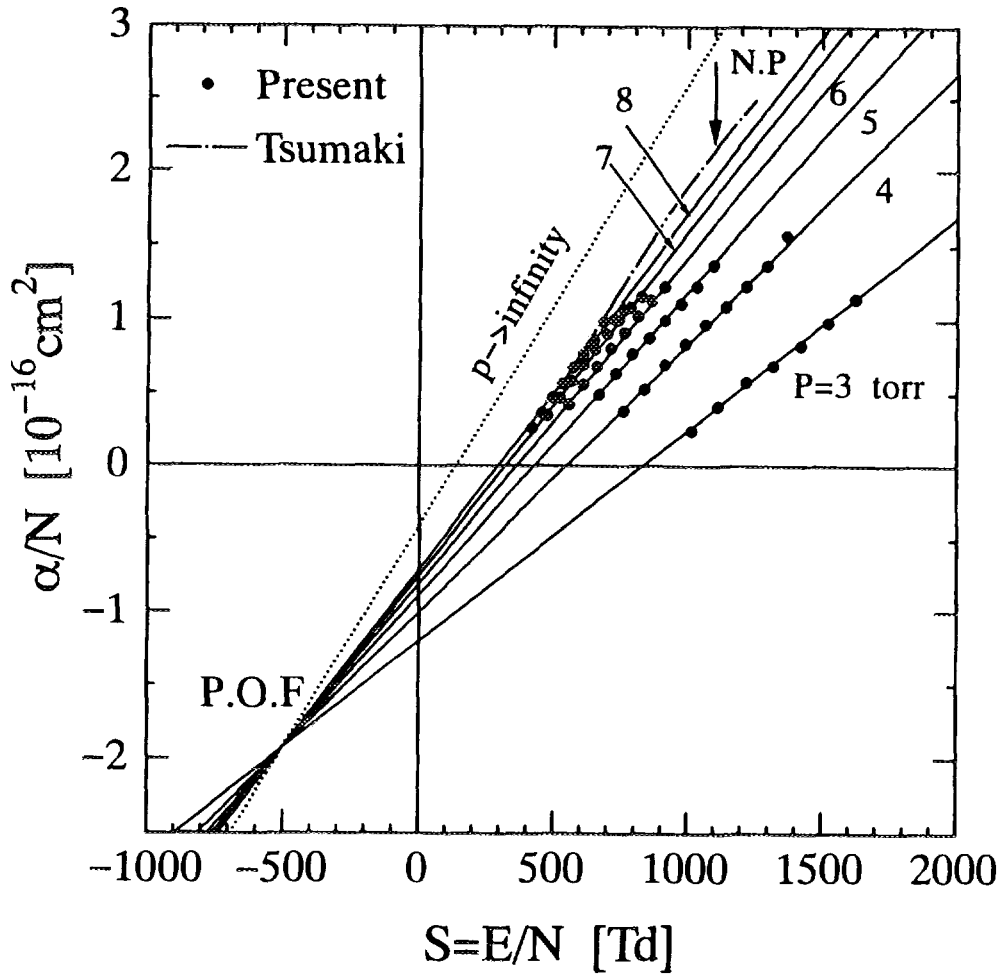


Fig. 4 Townsend primary ionization coefficients over  $N$  versus  $S$  for several gas pressure

### 5. CONCLUSIONS

The PPAC operated in low gas pressure region (less than 8 torr) was manufactured and its Townsend primary ionization coefficient  $\alpha$  was measured. It has been found that the  $\alpha/N$  value depends not only on  $S$  but also on  $p$ . We have obtained an experimental formula of  $\alpha/N$  with four constants. In this formula, the  $\alpha/N$  value converges to the form of Zastawny, if the gas pressure is large enough compared to the constant  $p_0$ .

## 6. ACKNOWLEDGEMENT

Sincere thanks are due to Mr. T. Ebisawa of Research Reactor Institute for his experimental support to make PPAC. This work was supported by a Grant-in-Aid for Scientific Research of the Ministry of Education, Science and Culture of Japan. The experiment was performed under the Cooperative Research Program of Research Reactor Institute, Kyoto University.

## REFERENCES

- (1) K. Tsumaki, *Jpn. J. Appl. Phys.*, **27** (1988) 393.
- (2) F. Bonaudi and C. W. Fabjan, " Particle Detection with Drift Chamber", p.131, Springer-Verlag (1993).
- (3) M. E. Rose and S. A. Korff, *Phys. Rev.*, **59** (1941) 850.
- (4) W. Diethorn, US Atomic Energy Commission Report NYO-6628 (1956).
- (5) A. Williams and R. I. Sara, *Int. J. Appl. Radiat. Isotopes* **13** (1962) 229.
- (6) A. Zastawny, *J. Sci. Instrum.* **43** (1966) 179.
- (7) M. W. Charles, *J. Phys.* **E5** (1972) 95.
- (8) T. Aoyama, *Nucl. Instrum. Meth.* **A234** (1985) 125.

# ESR (electron spin resonance) Radiation Dosimeter

Yoshihisa KINOSITA, Syunji TAKAKI, Chihiro YAMANAKA and Motoji IKEYA

Department of Earth and Space Science, Faculty of Science,  
Osaka University, 1-1 Machikaneyama, Toyonaka, Osaka 560, Japan

## 1. Introduction

Electron spin resonance (ESR) was discovered by Zavoisky (1945). ESR is a physical method of observing resonance absorption of microwave power by unpaired electron spins under a magnetic field. The concentration of radiation - induced radicals i.e., ESR signal intensity can be used in radiation dosimetry. The information on the cumulative radiation dose is unaltered in ESR dosimetry by repeated measurements, but it is destroyed in a similar method of thermoluminescence (TL) dosimetry.

The sensitivity of ESR is unfortunately several orders of magnitude less than that of TL at the moment; only the intermediate to high dose ranges can be measured with ESR. However, recent technological development has increased the sensitivity for the intensity measurement of ESR. The detection of about ten mGy exposure has been demonstrated for aragonitic corals in ESR dating and also human tooth enamel in accident dosimetry<sup>1)</sup>. A dosimeter of alanine combined with paraffin<sup>2)</sup> or polystyrene<sup>3)</sup> is commercially available to an intermediate dose range ( $5 \sim 10^5$  Gy) higher than radiotherapy level.

Sulfates have been studied for TL dosimeters and are now commercially available as  $\text{CaSO}_4$  doped with rare earth elements. The sensitivity of  $\text{MgSO}_4$  for use in ESR dosimetry seems promising<sup>4,5)</sup>.

In this work, new materials for ESR radiation dosimeter have been developed using radiation - sensitive sulfates such as  $\text{MgSO}_4$  and  $\text{Li}_2\text{SO}_4$ .

## 2. Experimental

Powdered sulfates of Li, Mg, Na and K (10 g) were prepared for the first samples as ESR radiation dosimeter material. These samples were mixed with the other sulfates since divalent cation impurities in monovalent cation lattice enhance the formation efficiency of

defects by ionizing radiation. Third group were sulfates mixed with additional sulfur powder (43 mg) not to be oxidized by heating in air. Remained oxygen in the glass tube was consumed for the reaction with S by heating. These samples were heated at 550 °C for Li sulfates, at 750 °C for Mg and K sulfates and at 580 °C for Na sulfates to diffuse thermally for two hours.

The following three samples were investigated in details.

$\text{MgSO}_4$  :  $\text{MgSO}_4$

$\text{Li}_2\text{SO}_4(\text{Mg})$  :  $\text{Li}_2\text{SO}_4$  mixed with  $\text{MgSO}_4(0.5 \text{ mol}\%)$  and fired with S

$\text{Li}_2\text{SO}_4(\text{K,Na})$  :  $\text{Li}_2\text{SO}_4$  mixed with  $\text{K}_3\text{Na}(\text{SO}_4)_2(1.0 \text{ mol}\%)$  and fired with S

Irradiation was carried out using a  $^{60}\text{Co}$   $\gamma$ -ray source. The dose rate was corrected by a commercial alanine dosimeter. Irradiation time and distance from the source were changed to obtain low exposed samples. Each sample of 100 mg was measured at room temperature in a standard quartz sample holder using a commercial X-band (9.5 GHz) ESR spectrometer (JEOL-ESR-REIX) with a cylindrical cavity of  $\text{TE}_{011}$  and 100 kHz field modulation. The height of the main peak to peak amplitude was used as the intensity.

### 3. Results and Discussion

$\text{MgSO}_4$ ,  $\text{Li}_2\text{SO}_4(\text{Mg})$  and  $\text{Li}_2\text{SO}_4(\text{K,Na})$  were suitable as a dosimeter material according to ESR spectra and dose dependence under the same measurement condition.

Figure 1 shows the ESR spectra with an absorbed dose of 100 Gy. The g-factors of radicals are indicated in the figure based on our tentative assignment following the published works tabulated in the text book<sup>1)</sup>. The signal at  $g = 2.0030$  is due to  $\text{SO}_3^-$ .

ESR spectrum and the signal amplitude depend on the microwave power and the field modulation width. When we use the ESR dosimetry, we should give priority to a high signal-to-noise ratio rather than to a high resolution of the spectrum. Therefore,

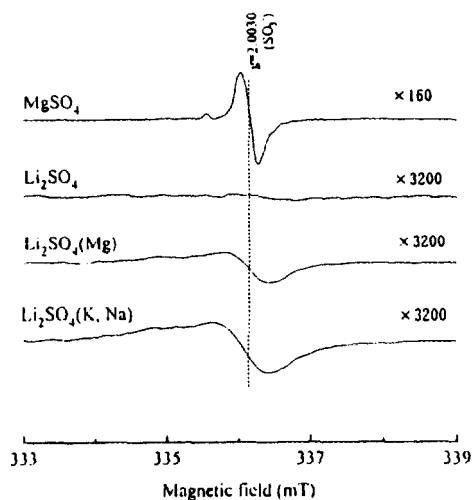


Fig. 1. ESR spectra of sulfates irradiated by  $\gamma$ -rays to the dose of 100 Gy. Microwave power is 1 mW and field modulation width is 0.05 mT.

Table 1 The most appropriate measurement conditions that gave the largest signal amplitude.

	MgSO <sub>4</sub>	Li <sub>2</sub> SO <sub>4</sub> (Mg)	Li <sub>2</sub> SO <sub>4</sub> (K,Na)
Microwave power (mW)	0.4	10.0	0.6
Field modulation width (mT)	0.79	1.0	1.0

we determine the most appropriate measurement conditions with the dependence of the signal amplitude on the microwave power and the field modulation width. Table 1 shows the best measurement condition with each materials.

The dependence of the signal amplitude on  $\gamma$  -ray dose under the most suitable condition is shown in Fig. 2. The signal amplitude is proportional to the low dose. Noise levels are at about 70 mGy for MgSO<sub>4</sub>, at about 200 mGy for Li<sub>2</sub>SO<sub>4</sub>(Mg) and Li<sub>2</sub>SO<sub>4</sub>(K,Na), respectively.

The defects have been annealed thermally. As the result the signal amplitude has decreased. Isochronal annealing is shown in Fig. 3. Samples were heated for 900 s at each temperature. The signal amplitude began to decrease at 620 K in MgSO<sub>4</sub>. The annealing curves have two stages in Li<sub>2</sub>SO<sub>4</sub>(Mg) and Li<sub>2</sub>SO<sub>4</sub>(K,Na). First decay began at 430 K and the curve reached a plateau at 550 K. Second decay began at 620 K. The signal of MgSO<sub>4</sub> is very stable. The signals of Li<sub>2</sub>SO<sub>4</sub>(Mg) and Li<sub>2</sub>SO<sub>4</sub>(K,Na) involve two different ones.

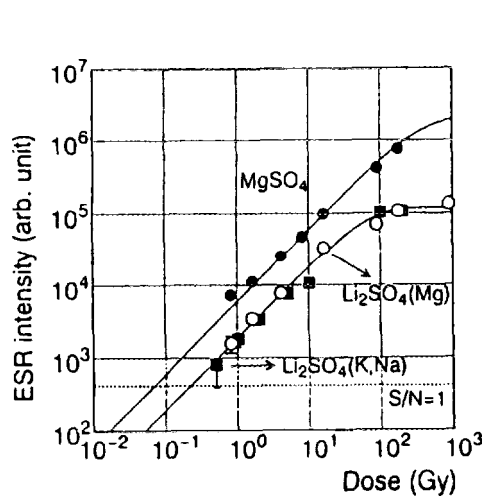


Fig. 2. The dose dependence of the signal amplitude under the most appropriate measurement conditions. The intensities increase linearly at a low dose range and then saturated as  $I_0(1-\exp(-D/D'))$  where  $D' = 350$  Gy, 60 Gy and 80 Gy for MgSO<sub>4</sub>, Li<sub>2</sub>SO<sub>4</sub>(Mg) and Li<sub>2</sub>SO<sub>4</sub>(K, Na) respectively.

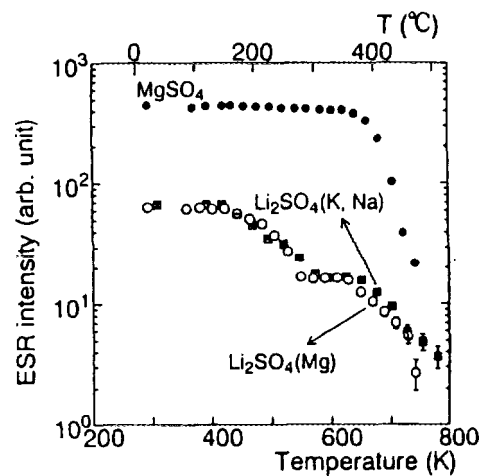


Fig. 3. The isochronal annealing curves of the radicals at various temperatures.

The lifetimes of the signals were calculated based on Fig. 3. Each temperature where the signal intensity decreased to  $1/e = 0.3679$  was taken assuming that the defects decreased by the first-order decay. The lifetimes were plotted as a function of the reciprocal temperature as Arrhenius plot and then extrapolated to room temperature as shown in Fig. 4. The activation energy was also calculated. The obtained lifetimes and activation energy were shown in Table 2. All signals may be used as a radiation dosimeter.

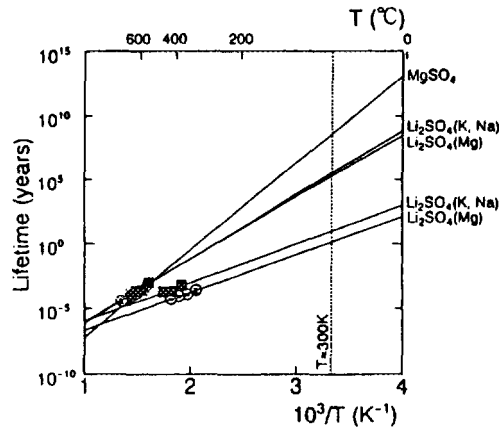


Fig. 4. Lifetime of the signals at the temperature assuming the first order decay.

The second decreased signals of

$\text{Li}_2\text{SO}_4(\text{Mg})$  and  $\text{Li}_2\text{SO}_4(\text{K,Na})$  and signal of  $\text{MgSO}_4$  resemble each other in the spectrum and began to decrease at the same temperature in Fig. 3. The activation energy is also similar. We consider that the same  $\text{SO}_3^-$  radical is annealed out.

Table 2 Lifetimes and activation energy calculated based on Fig. 4.

	$\text{MgSO}_4$	$\text{Li}_2\text{SO}_4(\text{Mg})$	$\text{Li}_2\text{SO}_4(\text{K, Na})$
Lifetime (years)	$3.9 \times 10^8$	1.4 $3.3 \times 10^5$	8.4 $1.2 \times 10^6$
Activation energy (eV)	1.3	0.9 1.6	1.0 1.6

#### 4. Summary

The doses where the signal-to-noise ratio is equal to one were about 70 mGy for  $\text{MgSO}_4$  and about 200 mGy for  $\text{Li}_2\text{SO}_4(\text{Mg})$  and  $\text{Li}_2\text{SO}_4(\text{K,Na})$  respectively. The noise level can be reduced by signal averaging with a computer and by increasing the time constant from 0.3 s to 1.0 s in ESR measurement. Hence, the minimum detectable dose limits will be further reduced to about less than one-tenth.

The lifetimes of the signal of  $\text{MgSO}_4$  and the stable one of  $\text{Li}_2\text{SO}_4(\text{Mg})$  and  $\text{Li}_2\text{SO}_4(\text{K},\text{Mg})$  are sufficiently long for the use as ESR dosimeter materials, while the lifetimes of the first one of  $\text{Li}_2\text{SO}_4(\text{Mg})$  and  $\text{Li}_2\text{SO}_4(\text{K},\text{Na})$  are relatively short, but still usable.

This paper is only confined to the use of  $\gamma$ -rays dosimetry. Further works to detect neutrons with  $\text{MgSO}_4$ ,  $\text{Li}_2\text{SO}_4(\text{Mg})$  and  $\text{Li}_2\text{SO}_4(\text{K}, \text{Na})$  using  $(n, \alpha)$  reaction of  ${}^6\text{Li}$  are going on.

### Acknowledgments

We would like to thank Dr. T. Ikeda, the Institute of Science and Industrial Research for  $\gamma$ -irradiation.

### References

- (1) M.Ikeya. New Applications of Electron Spin Resonance - Dating, Dosimetry and Microscopy-, ed. M.R. Zimmerman and N.Whitehead (World Scientific, Singapore, 1993), Chap.13.
- (2) D.F.Regulla and U.Deffner, Appl. Radiat. Isot. **33** (1982) 1101-1114.
- (3) T.Kojima, R.Tanaka, Y.Morita and T.Seguchi, Appl. Radiat. Isot. **37** (1986) 517-520.
- (4) M.Ohta and M.Sato, Radioisotopes **42** (1993) 439-440 [in Japanese].
- (5) J.R.Morton, F.J.Ahlers and C.C.Schneider, Radiat. Prot. Dosim. **47** (1993) 263-266.

# ANALYSIS OF TIME VARIANT FILTERS BY MEANS OF THE FOURIER TRANSFORM

K. Husimi

I. N. S. University of Tokyo, Tanashi, Tokyo 188, Japan

M. Kuwata

JEOL Engineering Co., 3-1-2 Musashino, Akishima, Tokyo 196, Japan

## 1. INTRODUCTION

The pulse forming network should be designed to minimize the influence of noises generated in the preamplifier. These noises which are originated by two noise sources, the detector and the field effect transistor (FET) are classified into three types namely the detector leakage current noise, the FET channel noise and the FET  $1/f$  noise. The step noise index, the delta noise index and the  $1/f$  noise index are measures of the quality of pulse forming network representing the effect of these noises upon the energy resolution of radiation to be measured.

The transfer function of time invariant filter is easily obtained by the classical circuit theory. The frequency domain analysis is performed based on this transfer function and is used to obtain these noise indices of time invariant filter. While the time variant has no transfer function, so that the frequency domain analysis is not applicable to this type of filter.

The time domain analysis is performed based on the waveform of pulse forming network, therefore it is applicable to obtain noise indices of pulse forming network not only of the type of time variant filter but also of the type of time invariant. The most important drawback of this method is the difficulty to calculate the  $1/f$  noise index. The  $1/f$  noise is defined not by the voltage spectrum but the power spectrum, therefore it is necessary at first to obtain the voltage response of a voltage noise having a  $\sqrt{1/f}$  frequency spectrum. This calculation is not easy even in the case of time invariant filter and is hopelessly difficult in the case of time variant filter.

The weighting function is defined in the time domain analysis for calculating the effect of noise filtering on the energy resolution. This frequency spectrum of the filter is obtained from the weighting function by means of the Fourier transform. This can be converted to the transfer function of the pulse forming network and is used in the time domain analysis.

This method is applied on the calculation of the finite cusp waveform as an example.

## 2. THE METHOD OF NOISE INDEX ANALYSIS

The time variant filter has no transfer function because it has time variant circuit components. Therefore, the time domain analysis is mainly used based on the weighting function of the filter. The Fourier transform of the weighting function of the pulse forming network is the frequency spectrum of noises which degrades the energy resolution to be measured. Using this Fourier transform, evaluation of pulse forming network can be performed by means of the frequency domain analysis. At first, we will make a brief introduction of the frequency domain analysis.

A model of noise sources of the detector-preamplifier combination used in the frequency domain analysis is shown in Figure 1.<sup>1)</sup> The current noise power shown by  $I_p^2$  is the parallel noise

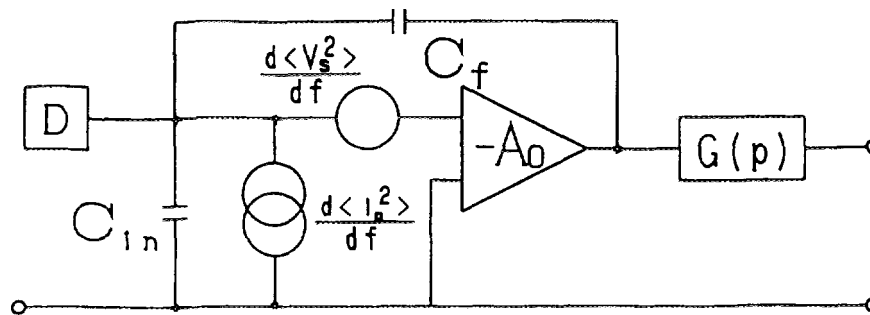


Fig.1 Noise sources of the detector preamplifier system

and is expressed as

$$\frac{d\langle I_p^2 \rangle}{df} = \frac{4kT}{R_p} \quad (1)$$

The resistance  $R_p$  is the equivalent noise resistance which represents the total amount of current noises due to detector leakage current and FET gate current. The voltage noise power  $V_s^2$  is the series noise and is expressed as

$$\frac{d\langle V_s^2 \rangle}{df} = 4kTR_s + A_f / f \quad (2)$$

where  $R_s$  represents the equivalent series noise resistance of FET channel noise and  $A/f$  shows the amount of FET  $1/f$  noise power.

The output noise power  $V_n^2$  delivered from the preamplifier is expressed as

$$d\langle V_n^2 \rangle = \left\{ \frac{d\langle V_s^2 \rangle}{df} \frac{(C + C_f)^2}{C_f^2} + \frac{d\langle I_p^2 \rangle}{df} \frac{1}{\omega^2 C_f^2} \right\} d\omega \quad (3)$$

where the gain  $A_0$  in Fig. 1 is assumed to be very large. The frequency component of these noise powers is filtered by the pulse forming network having a transfer function  $G(\omega)$ . The equation (3) is simplified as

$$d\langle V_n^2 \rangle = \left( a^2 + \frac{b^2}{\omega^2} + \frac{c^2}{\omega} \right) \cdot d\omega \quad (4)$$

where  $a^2$ ,  $b^2$  and  $c^2$  are given by

$$\begin{aligned} a^2 &= \frac{(C + C_f)^2}{C_f^2} \cdot 4kTR_s \\ b^2 &= \frac{1}{C_f^2} \frac{4kT}{R_p} \\ c^2 &= \frac{(C + C_f)^2}{C_f^2} \cdot 2\pi A_f \end{aligned} \quad (5)$$

The noise power  $V_n^2$  is given by

$$\begin{aligned} V_n^2 &= \int G(\omega)^2 \cdot d\langle V_n^2 \rangle \\ &= \frac{1}{2\pi} \int_{-\infty}^{\infty} \left( a^2 + \frac{b^2}{\omega^2} + \frac{c^2}{\omega} \right) \cdot G(\omega)^2 d\omega \\ &= a^2 \cdot N_d^2 + b^2 \cdot N_s^2 + c^2 \cdot N_f^2 \end{aligned} \quad (6)$$

The noise power is the weighted sum of noise components  $a_2$ ,  $b_2$  and  $c_2$ , and these weighting

coefficients  $N_d^2$ ,  $N_s^2$  and  $N_f^2$  are called delta noise index, step noise index and 1/f noise index. These indices are given by following equations

$$N_d^2 = \frac{1}{2\pi} \int_{-\infty}^{\infty} G(\omega)^2 \cdot d\omega$$

$$N_f^2 = \frac{1}{2\pi} \int_{-\infty}^{\infty} \frac{G(\omega)^2}{\omega} \cdot d\omega \quad (7)$$

$$N_s^2 = \frac{1}{2\pi} \int_{-\infty}^{\infty} \frac{G(\omega)^2}{\omega^2} \cdot d\omega$$

In this Fourier transform method, the function  $G(\omega)$  is derived from the weighting function  $h(t)$  of the pulse forming network as follows. The Fourier transform  $H(\omega)$  of the time variable  $h(t)$  is given as

$$H(\omega) = \int_{-\infty}^{\infty} h(t) \exp(-j\omega t) \cdot dt \quad (8)$$

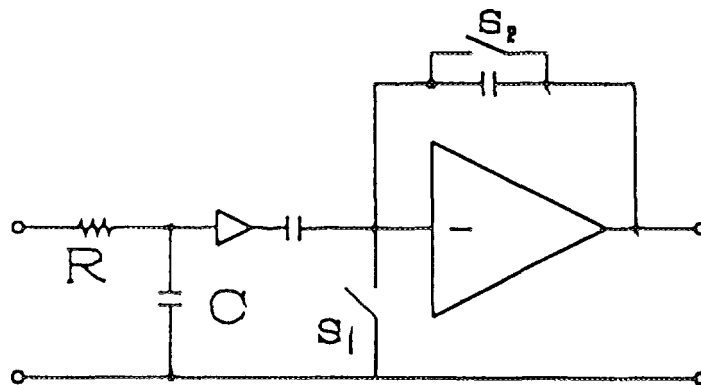


Fig.2 Block diagram of a time variant filter simulating the finite duration cusp

The resulting function  $H(\omega)$  is the frequency spectrum of the filter response to the input delta impulse. The output waveform of preamplifier is not the delta impulse but the step impulse, therefore the transfer function  $G(\omega)$  of the step response can be derived from the frequency spectrum  $H(\omega)$  of the weighting function as

$$G(\omega) = j\omega \cdot H(\omega) \quad (9)$$

where  $s=j\omega$  is the differential operator.

### 3. NOISE INDICES OF THE FINITE DURATION CUSP WAVEFORM

The infinite duration cusp pulse which is derived from the matched filter theory has been considered as the ideal waveform that gives the best S/N ratio. However, it is not practical because of its infinitely long wave tail. Approximating this infinite duration cusp, the finite duration cusp has been introduced. Noise indices of this finite duration cusp waveform will be considered here, as an example of the noise index analysis using the Fourier transform method.

The time variant filter which has an output pulse approximating the cusp waveform is shown in Fig. 2.<sup>2)</sup> The build-up waveform of this filter is expressed as follows

$$h_-(t) = (t + T) - CR \left\{ 1 - \exp\left(-\frac{t+T}{CR}\right) \right\} \quad (10)$$

The peak value  $h_-(0)$  of this waveform is given by

$$h_-(0) = T - CR \left\{ 1 - \exp\left(-\frac{T}{CR}\right) \right\} \quad (11)$$

The finite duration symmetrical cusp waveform is shown in Fig. 3, where the decay waveform  $h_+(t)$  is given from Eq. (10) as

$$h_+(t) = (T - t) - CR \left\{ 1 - \exp\left(-\frac{T-t}{CR}\right) \right\} \quad (12)$$

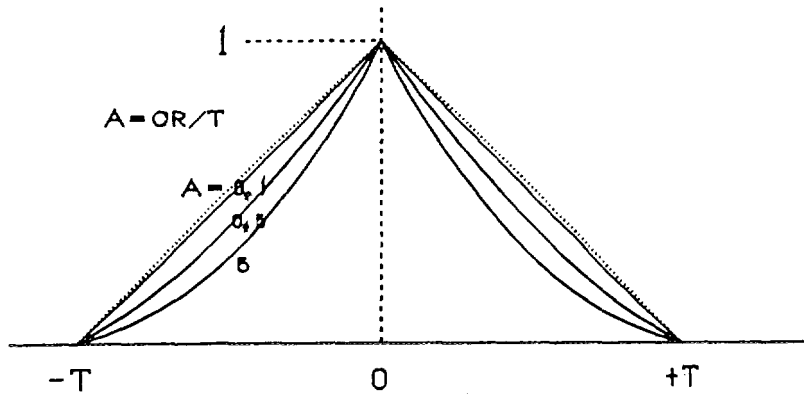


Fig. 3 The symmetrical finite duration cusp

The weighting function is normalized by the factor  $h_-(0)$ . The Fourier transform  $H_-(\omega)$  of

the build-up waveform  $h_-(t)$  is given using Eq.(5) as

$$H_-(\omega) = \left( \frac{CR}{j\omega} - \frac{T}{j\omega^2} + \frac{1}{\omega^2} \right) \left\{ -\frac{CR}{j\omega} - \frac{1}{\omega^2} + \frac{(CR)^2}{1+j\omega CR} \right\} \exp(j\omega T) - \frac{(CR)^2}{1+j\omega CR} \exp\left(-\frac{T}{CR}\right) \quad (13)$$

The Fourier transform  $H_+(\omega)$  of the decay waveform  $h_+(t)$  is given as the complex conjugate of  $H_-(\omega)$  and is

$$H_+(\omega) = \left( \frac{CR}{-j\omega} - \frac{T}{-j\omega^2} + \frac{1}{\omega^2} \right) \times \left\{ -\frac{CR}{-j\omega} - \frac{1}{\omega^2} + \frac{(CR)^2}{1-j\omega CR} \right\} \exp(-j\omega T) - \frac{(CR)^2}{1-j\omega CR} \exp\left(-\frac{T}{CR}\right) \quad (14)$$

The transfer function of the finite duration cusp is given by the equation

$$G(\omega) = j\omega \left\{ \frac{H_-(\omega)}{h_-(0)} + \frac{H_+(\omega)}{h_+(0)} \right\} \quad (15)$$

From this equation, the final result of  $G(\omega)$  is obtained as

$$G(\omega) \cdot h_-(0) = j(2CR) \left\{ \frac{1}{\omega CR} + \cos(\omega T) \right\} \left\{ -\frac{1}{\omega CR} + \frac{\omega CR}{1+(\omega CR)^2} \right\} - \sin(\omega T) \left\{ 1 - \frac{(\omega CR)^2}{1+(\omega CR)^2} \right\} - \frac{\omega CR}{1+(\omega CR)^2} \exp\left(-\frac{T}{CR}\right) \quad (16)$$

Noise indices can be obtained from the equation  $G(\omega)$  using the relationship of Eq.(7) and the results are shown in Table. 1, where  $A = CR/T$  is the parameter of curvature of the finite duration cusp pulse as shown in Fig.3.

Table 1 A versus Noise Indices

A	0.01	0.1	0.5	1/1.333
$N_d^2 \times T$	1.9845	2.2276	3.3988	3.6524
$2\pi N_r^2$	5.5440	6.6411	6.8441	7.1791
$N_s^2 / T$	0.6595	0.6084	0.4755	0.4504

The parameter A is smaller, the delta noise index  $N_d^2$  and the 1/f noise index  $N_f^2$  become better as shown in Table 1. Each of these noise indices tends to that of the triangular waveform in the case of A=0.

#### 4. CONCLUSIONS

The Fourier transform method for analysing the pulse forming network is introduced. This method was once applied to analyze a time variant filter,<sup>3)</sup> but was not widely used up to now. However, this is especially useful for calculation of 1/f noise index, because the time domain analysis requires a complicated calculation of the inverse Laplace transform containing the factor  $\sqrt{1/s}$ .

The finite duration cusp waveform has been thought to be an improvement of the infinite duration cusp pulse, but the triangular waveform has been proved to be the best in the case of the finite duration pulse waveform owing to this Fourier transform analysis.

#### REFERENCES

- 1) R. Kowalski, Nuclear Electronics, Springer-Verlag, 369 (1970)
- 2) K. Kandiah, Nucl. Instr. & Meth. 95, 289 (1971)
- 3) H. Koeman, Nucl. Instr. & Meth. 123, 161 (1975)

# PERFORMANCE COMPARISON OF VARIOUS TIME VARIANT FILTERS

M. Kuwata

JEOL Engineering Co., 3-1-2 Musashino, Akishima, Tokyo 196, Japan

K. Husimi

I. N. S. University of Tokyo, Tanashi, Tokyo 188, Japan

## ABSTRACT

This paper describes the advantage of the trapezoidal filter used in semiconductor detector system comparing with the other time variant filters. The trapezoidal filter is the compose of a rectangular pre-filter and a gated integrator. We indicate that the best performance is obtained by the differential-integral summing type rectangular pre-filter. This filter is not only superior in performance, but also has the useful feature that the rising edge of the output waveform is linear. We introduce an example of this feature used in a high-energy experiment.

## 1. INTRODUCTION

Recently low energy detecting limit has been expand up to K line X-ray from beryllium owing to the development of the low noise FETs. In high energy field, low energy events i.e. kaonic hydrogen X-ray experiment has been investigated. In the case of measuring low energy X or gamma rays with high throughput maintaining high resolution, considerable point for the filter amplifier is the compromise of resolution and dead time. Using a long filter time constant is the easy way to get a good resolution. However, it produces degradation of count rate performance. When the sufficiently cooled semiconductor detector is used, its leak current which generates the step noise is negligibly small. Therefore, considerable noise is delta and  $1/f$  noise. F. S. Goulding and D. A. Landis previously proposed the product of delta noise index and dead time as the performance index of various kinds of filter circuits for semiconductor detectors<sup>(1)</sup>. Before their work, filter performance was only evaluated in terms of signal-to-noise ratio at noise-corner frequency. That is inconvenient for practical use by the reason that the dead time of each filter is different at the optimum point.

It has been believed that the best performance is obtained by the integrator type time variant filter because its output waveform is close to the cusp shape. We indicated that the best value of the product of delta noise index and dead time is obtained by the trapezoidal filter which was composed of a real rectangular pre-filter and a gated integrator<sup>(2)</sup>. In order to realise the real rectangular pre-filter, we developed the circuit which forms a rectangular waveform by means of adding the differentiated step signal and its integration<sup>(3)</sup>. We compare the performance of this trapezoidal filter with the other time-variant filters and introduces an application of this filter for high-energy experiment.

## 2. CIRCUIT AND NOISE INDICES

Figure 1 indicates typical time variant filter circuits these are compose of a pre-filter and a gated integrator. Generally, long filter time constant is used in order to get good resolution and that is switched short after AD conversion to prevent the increase of dead time. A simple switching time constant (an integrator or a differentiator) pre-filter was reported by K. Kandiah et al.<sup>(4)</sup> and G. White<sup>(5)</sup>. We presented rectangular pre-filter type<sup>(3)</sup>. In the figure, the series switch timing for avoiding the influence of ballistic deficit is neglected. There are other circuits that use a time invariant pre-filter or without gated integrator type. However the performances of these filters are worse than the circuits indicated in figure 1.

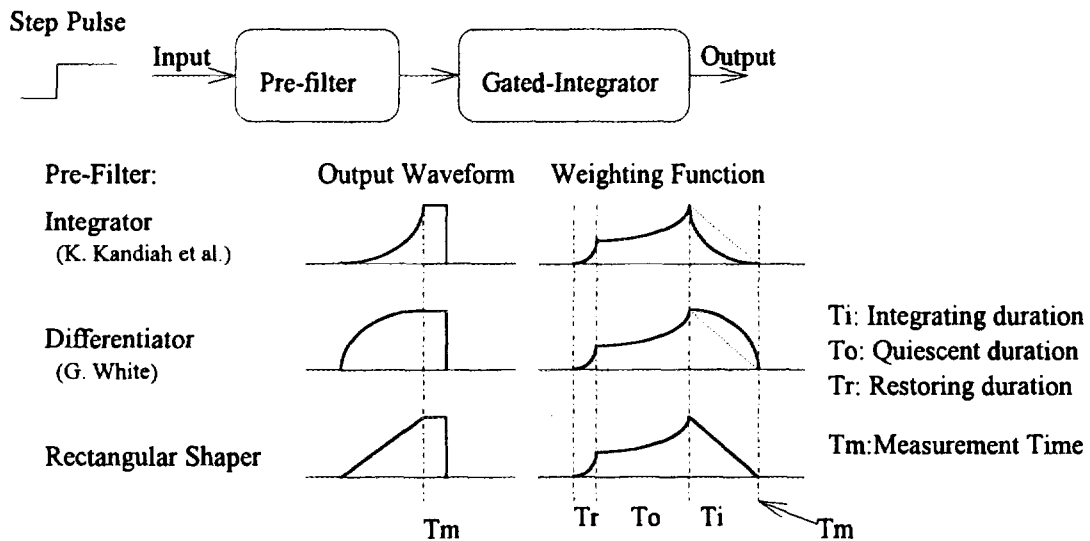


Fig. 1 Typical time variant filter circuits and its weighting functions.

The noise indices are calculated by time domain method. Step and delta noise index can be obtained respectively as follows:

$$N_s^2 = (1/S^2) \int_0^{\infty} \{R(t)\}^2 dt \quad (1)$$

$$N_d^2 = (1/S^2) \int_0^{\infty} \{R'(t)\}^2 dt \quad (2)$$

where weighting function (residual function)  $R(t)$  is the effect of a noise that generated prior to the measurement time and  $S$  is the amplitude at the measurement time ( $T_m$ ).  $R(t)$  is represented in three parts by considering integrating duration of the gated integrator ( $T_i$ ), restoring duration ( $T_r$ ) and quiescent duration ( $T_o$ ). Therefore, noise indices are represented as:

$$N_s^2 = \int_0^{T_i} \{R_1(t)\}^2 dt + \int_0^{T_o} \{R_2(t)\}^2 dt + \int_0^{\infty} \{R_3(t)\}^2 dt \quad (3)$$

$$N_d^2 = \int_0^{T_i} \{R'_1(t)\}^2 dt + \int_0^{T_o} \{R'_2(t)\}^2 dt + \int_0^{\infty} \{R'_3(t)\}^2 dt. \quad (4)$$

In the case of the integrator pre-filter,  $R_1(t)$  is:

$$R_1(t) = [t - \tau_0 \{1 - \exp(-t/\tau_0)\}] / [T_i - \tau_0 \{1 - \exp(-T_i/\tau_0)\}], \quad (5)$$

in the case of the differentiator pre-filter:

$$R_1(t) = \{1 - \exp(-t/\tau_0)\} \tau_0 / \{1 - \exp(-Ti/\tau_0)\}, \quad (6)$$

in the case of the rectangular pre-filter:

$$R_1(t) = t/Ti. \quad (7)$$

The weighting functions of these three circuits during restoring and quiescent duration are the same that is indicated as follows:

$$R_2(t) = \exp(-t/\tau_0), \quad (8)$$

$$R_3(t) = \exp(-T_0/\tau_0) \exp(-t/\tau_1). \quad (9)$$

The best step noise index is obtained by the integrator pre-filter and the best delta noise index is obtained by the rectangular pre-filter.

We give an example of the calculation process with trapezoidal filters. The step noise index of the trapezoidal filter is given by:

$$N_s^2 = \frac{Ti}{3} + \frac{\tau_0}{2} \cdot \left\{ 1 - \exp\left(-\frac{2T_0}{\tau_0}\right) \right\} + \exp\left(-\frac{2T_0}{\tau_0}\right) \cdot \frac{\tau_1}{2}. \quad (10)$$

The delta noise index is given by

$$N_d^2 = \frac{1}{Ti} + \frac{1}{2\tau_0} \cdot \left\{ 1 - \exp\left(-\frac{2T_0}{\tau_0}\right) \right\} + \exp\left(-\frac{2T_0}{\tau_0}\right) \cdot \frac{1}{2\tau_1}. \quad (11)$$

In the case of time variant filter in which a gated integrator is used, the end of processing pulse is defined as the point that the integrated value of the output waveform tail becomes smaller than the AD converter resolution. Thus we obtain following relations:

$$\exp\left(-\frac{Ti}{\tau_0}\right) \cdot \exp\left(-\frac{Th}{\tau_1}\right) \cdot \int_0^\infty \exp\left(-\frac{t}{\tau_0}\right) dt \leq \frac{Ti}{1024}, \quad (12)$$

$$\frac{\tau_0}{Ti} \exp\left(-\frac{Ti}{\tau_0} - \frac{Th}{\tau_1}\right) \leq \frac{1}{1024}. \quad (13)$$

Assuming  $Th = 0.2Ti$  for an example, in the case of  $\tau_0 = Ti$ , the maximum restoration time constant is represented as  $\tau_1 = 0.0281Ti$  from eq. (13). The delta noise index is obtained by substituting  $\tau_1$  into equation (11) as follows:

$$N_d^2 \cdot Ti = 1.5 + 14.33 \exp\left(-\frac{2T_0}{Ti}\right), \quad (14)$$

in the case of  $\tau_0 = 0.5Ti$ :

$$N_d^2 \cdot Ti = 2.0 + 4.898 \exp\left(-\frac{4T_0}{Ti}\right), \quad (15)$$

in the case of  $\tau_0 = 2Ti$ :

$$N_d^2 \cdot Ti = 1.25 + 17.56 \exp\left(-\frac{T_0}{Ti}\right). \quad (16)$$

The results are shown in figure 2 as a function of  $T_0/Ti$ . The step noise indices are calculated in a similar way and results are shown in figure 3.

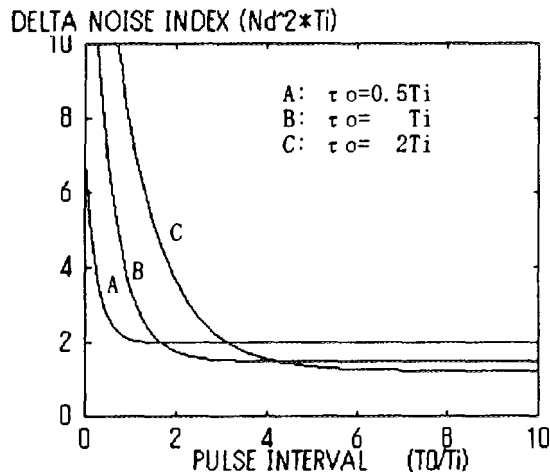


Fig. 2 Delta noise indices as a function of pulse interval.

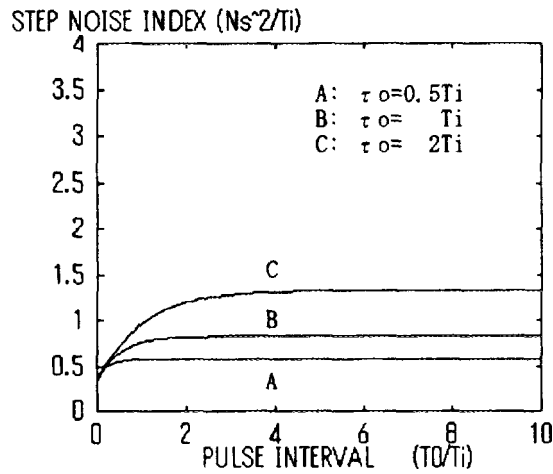


Fig. 3 Step noise indices as a function of pulse interval.

When the interval of signal pulses becomes short, step noise index decreases and delta noise index increases by the influence of the reset time constant of the preceding pulse.

### 3. DEAD TIME AND OPTIMUM FILTER PARAMETERS

F. S. Goulding and D. A. Landis reported that the dead time of the gated integrator type time variant filter was two times of the integration time (pulse width)<sup>(1)</sup>. However, that is the case of the circuit which uses a time invariant pre-filter. If the time variant pre-filter is used, the dead time becomes pulse width from the view point of pile-up. When the pile-up occurs, all of the time constant is restored and it can process next pulse immediately. It is clear from figure 2, if the pile-up rejection is done during only pulse width, resolution degrades at high input rate. The protection time is settled after restoring and pile-up rejection is also done during protection time.

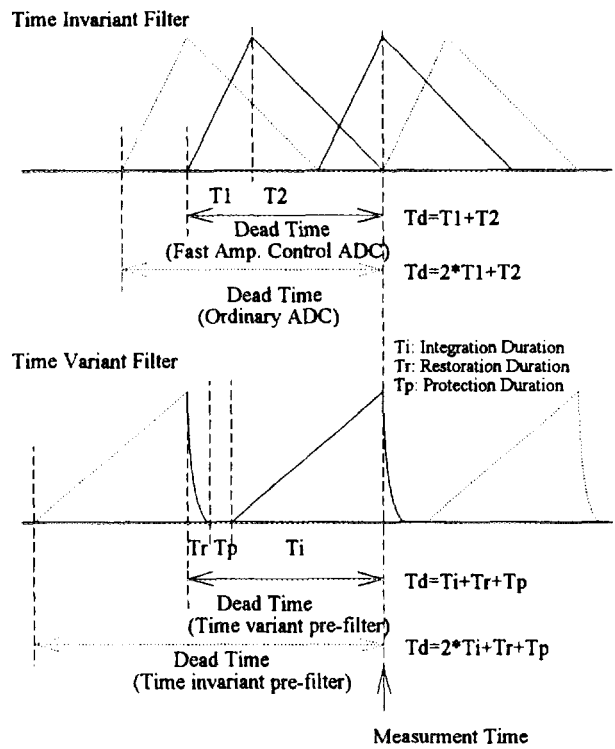


Fig. 4 Dead time of the filter circuit. The dead time varies by means of pile-up rejector.

Therefore, dead time of the time variant filters is pulse width plus protection time. Even if the output pulse shape is the same, dead time varies according to the circuit construction. Figure 5 indicates the output waveforms of the differentiator that has the same dead time considering the protection time. When the long filter time constant is used, the delta noise index is improved. However, it requires short restoration time constant in order to be the same pulse width. This requires long protection time and dead time becomes longer.

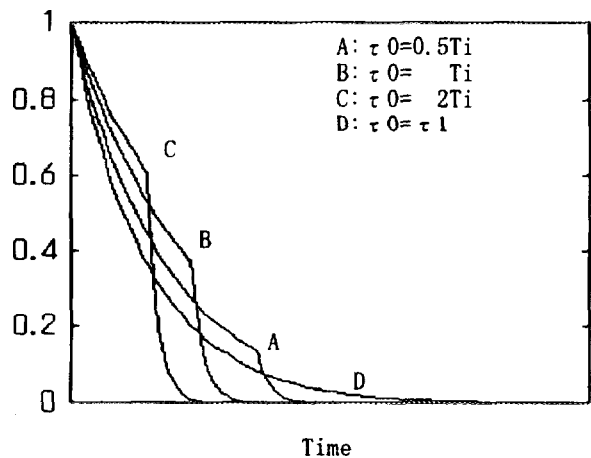
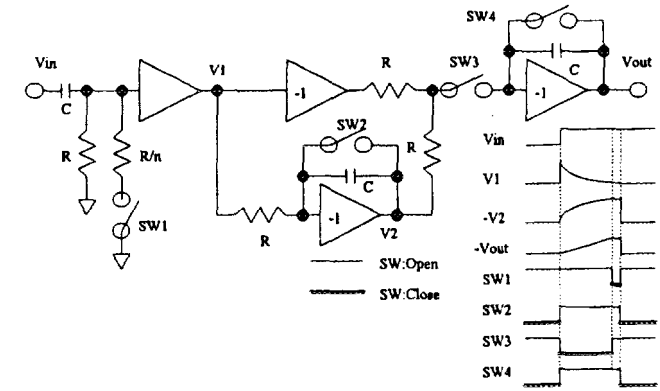
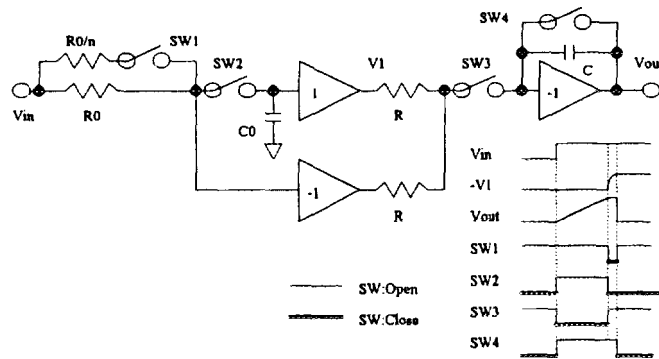


Fig. 5 Output waveforms of the switched time constant differentiator.  $\tau_0$  and  $\tau_1$  are the filter and restoration time constant respectively and  $T_i$  is the time of  $\tau_0$  duration. Considering the protection time, A, B and C has the same dead time as the pulse width of D.



(a) Differential-Integral Summing Type Trapezoidal Filter



(b) FFBLR Type Trapezoidal Filter

Fig. 6 Trapezoidal filter circuits.

There are several circuits to form a trapezoidal waveform. Figure 6 indicates the example of trapezoidal filter circuits. The output waveform of both circuits are the same. However, dead time of the circuit (a) is shorter than (b) by the reason that the voltage to be restored is low at the measurement time and circuit (b) requires shorter restoration time constant than (a).

The optimum filter parameter is obtained to minimize the product of delta noise index and dead time. The dead time  $T_d$  of the trapezoidal filter should be written as

$$T_d = T_i + T_h + T_p = T_i(1 + a + b), \quad (17)$$

where  $a$  is given by  $T_h/T_i$  and  $b$  is given by  $T_p/T_i$ . In the case of  $\tau_0 = T_i$ , the restoration time constant is represented as  $\tau_1 = aT_i / (5.932 - a)$  and the delta noise index becomes

$$N_d^2 \cdot T_d = 1.5 + \frac{5.932 - a}{2a} 7.41 \exp\left(-\frac{2T_0}{T_i}\right). \quad (18)$$

Let  $T_p$  be the time  $T_0$  at which the delta noise index increases 10 percent. Put 0.15 into the second term of right side of eq. (18), we obtain:

$$b = -0.5 \ln\left(\frac{0.3a}{5.932 - a}\right) \quad (19)$$

From eq. (17), we have

$$N_d^2 \cdot T_d = 1.5 \left[ 1 + a - 0.5 \ln\left(\frac{0.3a}{5.932 - a}\right) \right] \quad (20)$$

in the case of  $\tau_0 = 0.5T_i$ :

$$N_d^2 \cdot T_d = 2.0 \left[ 1 + a - 0.25 \ln \left( \frac{0.4a}{4.238 - 2a} \right) \right] \quad (21)$$

in the case of  $\tau_0 = 2T_i$ :

$$N_d^2 \cdot T_d = 1.25 \left[ 1 + a - \ln \left( \frac{0.25a}{7.125 - 0.5a} \right) \right] \quad (22)$$

The calculated result is shown in figure 7. The optimum restoration time constant that related with the filter time constant  $\tau_0$  is obtained by the minimum point of the curve.

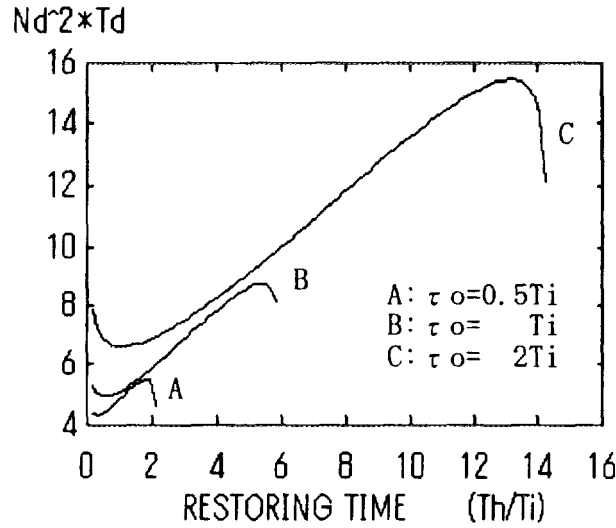


Fig. 7 Performance index as a function of  $T_h/T_i$ .

#### 4. PERFORMANCE COMPARISON

Table 1 shows the performance of the typical filter circuits. The integrator, differentiator and rectangular pre-filter are calculated in the case of  $\tau_0 = 0.5T_i$ . The best product of delta noise index and dead time is obtained by the rectangle pre-filter type time variant filter.

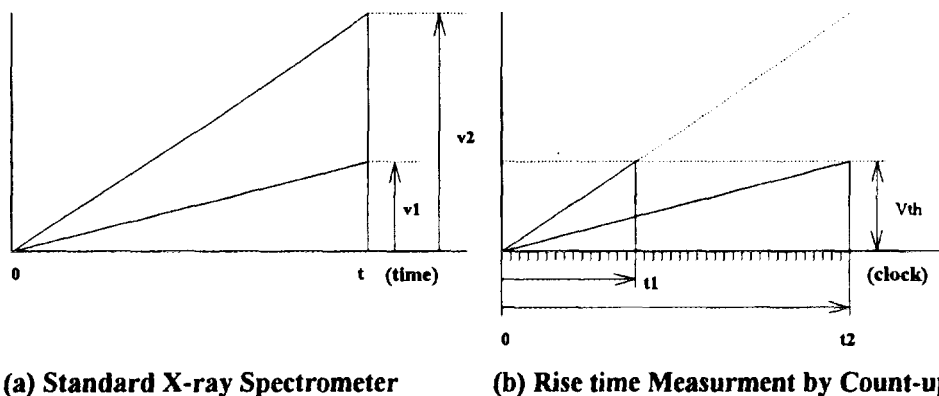
Table 1 The performance of the various time variant filters.

	(1) Triangle	(2) Gauss (7th order)	(3) Gauss + G.I.	(4) Quasi- Rectangle + G.I.	(5) Integrator + G.I.	(6) Differen. + G.I.	(7) Rectangle + G.I.
Refer.	(1)	(1)	(1)	(2)			(3)
$N_s^2$	$0.67T_p$	$0.67 \tau_0$	$2.08 \tau_0$	$0.74T_i$	$0.49T_i$	$0.76T_i$	$0.58T_i$
$N_d^2$	$2/T_p$	$2.53/\tau_0$	$1.47/\tau_0$	$1.98/T_i$	$2.2/T_i$	$2.3/T_i$	$2.0/T_i$
$\sqrt{N_s^2 N_d^2}$	1.16	1.30	1.74	1.21	1.04	1.32	1.08
$T_d$	$3T_p$	$4.1 \tau_0$	$5 \tau_0$	$2.57T_i$	$2.12T_i$	$2.12T_i$	$2.12T_i$
$N_d^2 \cdot T_d$	6	9.4	7.35	5.07	4.66	4.88	4.25

G.I.: Gated Integrator,  $T_p$ : Peaking Time,  $\tau_0$ : Filter Time Constant,  $T_i$ : Integration Time of the G.I.

## 5. APPLICATION OF THE TRAPEZOIDAL SHAPER

The trapezoidal shaper which has the real rectangular pre-filter is not only superior in noise index and dead time performance, but also has the remarkable feature that rising edge of the output waveform is linear. This provides the new concept pulse amplifier for high energy experiments. We presented an application of this for observing low-energy events in accelerator experiment<sup>(6)</sup>.



(a) Standard X-ray Spectrometer

(b) Rise time Measurement by Count-up ADC

Fig. 8 A new concept pulse amplifier that measures the rise time of trapezoidal waveform instead of peak height.

When the low energy events are measured in high energy experiment, large quantity of background that originates from the high-energy gamma rays and charged particles some times cause degradation of the signal-to-noise ratio and signal count rate. Figure 8 (a) is the conventional processor that measures the pulse height. This type processor has the same processing time even a high energy background pulse. Figure 8 (b) is the new processor that measures the rise time of the trapezoidal waveform. This is just the reverse action of the Wilkinson ADC.

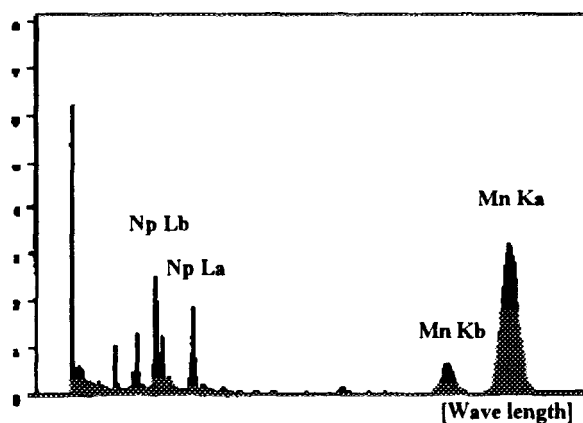


Fig. 9 <sup>241</sup>Am and <sup>55</sup>Fe spectrum taken with a Si(Li) detector. The abscissa represents the reciprocal of the energy.

The rise time of the trapezoidal waveform is inversely proportional to the height of the input step pulse. Therefore, processing time for a high-energy pulse is shorter than that for low-energy one.

Consequently, the pile-up loss of the low-energy X-rays appearing in a background of high-energy pulses is reduced. The pulse-processor is unsuitable for general purposes, such as element analyzing. However, it is very useful for measuring low-energy X-rays or gamma rays as its high throughput with high resolution in accelerator experiments. Figure 9 shows the spectrum response of a Si(Li) detector using the processor. The abscissa represents the reciprocal of the energy.

## 6. CONCLUSION

The time variant filter has a relatively simple and compact circuit configuration. It has the flexibility to design its delta noise and throughput performance according to the purposes by changing one or two components. Among them, the trapezoidal shaper that is composed of the differential-integral summing type rectangular pre-filter and gated integrator is the best for cooled semiconductor radiation detector.

## 7. REFERENCE

- (1) F. S. Goulding and D. A. Landis, *IEEE Trans. Nucl. Sci.*, NS-29, No.3, pp. 1125-1141, 1982.
- (2) K. Husimi, S. Ohkawa, M. Nakanishi, S. Hayashida, M. Taira, M. Kuwata, H. Maeda, and T. Ikeda, *IEEE Trans. Nucl. Sci.*, NS-36, No.1, 396-400, 1989.
- (3) M. Kuwata, H. Maeda and K. Husimi, *IEEE Trans. Nucl. Sci.*, NS-42, No. 4, pp. 705, 1995.
- (4) K. Kandiah, A.J. Smith and G. White, *IEEE Trans. Nucl. Sci.*, NS-22, No. 5, pp. 2058-2065, 1975.
- (5) Graham White, *IEEE Trans. Nucl. Sci.*, NS-35, No. 1, pp. 125-130, 1988.
- (6) M. Kuwata, H. Maeda, K. Husimi, S. Ohkawa, M. Iwasaki, S.N. Nakamura, T.M. Ito, T. Terada, *IEEE Nucl. Sci. Symposium*, San Francisco, 1995.

# **A response of the imaging plate to radiation properties and a discriminated radiation image**

M. TAKEBE, K. ABE, Y. KONDO, Y. SATOH, M. SOUDA, Y. KOKUBUN,  
M. MIYAZAKI, Y. HORI, Y. MURAKAMI  
Tohoku Univ. Faculty of Eng.

## **1. INTRODUCTION**

We have reported that the imaging plate (IP) varies its excitation spectra to radiation properties<sup>1-3</sup>). The effect may be based on two reasons. One is responsible for the LET effect of the IP and another is ranges of radiations in IP. The excitation spectra may be affected by depth of light emission if it is colored. Actually, the IP (type UR) we used before is colored with a dye to obtain higher space resolution. Three types of IP are available, UR, TR and 2000. Type TR is also colored but thickness of fluorescent substance is only 50  $\mu\text{m}$ , instead of 150  $\mu\text{m}$  of UR. On the other hand, type 2000 is not colored and has same thickness of fluorescent substance. This paper report that the experiment using three type IPs and two type radiations and preliminary test of discrimination of radiation properties with using two wavelength readout method.

## **2. Experiment and Calculation**

The IPs were irradiated with raging 1.5, 2.0, 2.6, 3.2 MeV of proton beam by  $3 \times 10^9$  C/cm<sup>2</sup> at Tohoku Univ. Fast Neutron Facility and with raging 40 to 1250keV of electron beam by  $3 \times 10^9$  C/cm<sup>2</sup> at Tohoku Univ. 1 MeV Electron Microscope Facility. Optical attenuation coefficients from 450 to 750 nm were measured by cutting IP with microtome. Energy deposition in IP were calculated with TRIM code for proton and EGS4 for electron.

## **3. Results and Discussion**

According to exp. results, only UR shows a response to radiation properties. It is too thin for TR to show a same response. We derived optical attenuation coefficients of IP by curve-fitting the calculated energy deposition with the ratio of light emission (photo-stimulated luminescence, PSL) intensity 18hrs after irradiation read out by 600 to 500 nm (Fig. 1). The coefficients obtained are roughly in agreement with the ones from optical measurement of IP cut by microtome. The attenuation lengths are found to be 27  $\mu\text{m}$  for 500nm, 62  $\mu\text{m}$  for 600nm. Experimental energy response for electron beam is in good agreement with calculated values based on the estimated attenuation length. We concluded

that the dye in IP works to discriminate radiation properties and energies.

## **4. Discriminated image measurement**

No instrument is available for two wavelength readout. We constructed a preliminary apparatus for this purpose to demonstrate the discrimination ability. The apparatus consists of 40W W-lamp, spectrometer, a low-pass filter (450nm), a band pass filter (390nm) and a PMT. Readout lights from the spectrometer introduced to a piece of IP through a optical fiber and emitted lights were transmitted to the PMT through a optical fiber. A set of optical fiber mounted on a pen-holder of a drawing pen plotter which can be moved by a personal computer.

A part of an IP sheet was irradiated with 100  $\mu$  Ci, Am-241 apart 8mm from the surface of the IP for 10min. Another part was exposed to about 300 Ci Co-60 gamma source with setting a lead brick having a hole 30mm dia between the gamma source and the IP apart 300mm from the source for 10min. The thickness of the brick was 50mm.

The irradiated IP was read out by the apparatus by 3mm step with 500 nm and 600 nm.(Fig. 3 lower image) The image shows two peaks of almost same height. With applying PSL ratio discrimination the image formed by Co-60 was disappeared and the alpha image was not (Fig. 3. upper image). The test apparatus remains several problems such as a smaller discriminated alpha image than the real one because of low small S/N ratio, a long measuring time ( it took 30s for one point) and a bad reproducibility.

## **5. Conclusion**

We concluded that the IP having a blue dye discriminate radiation properties and energies with detecting radiation ranges in fluorescent substance. The original purpose of the blue dye is to get higher space resolution and not for radiation discrimination. We believe that some improved IP will be useful in various fields.

## **6. References**

1. Masahiro Takebe, Ken Abe, Nucl. Instr. and Meth, A345 (1994) 606-608
2. Masahiro Takebe, Ken Abe, Manabu Souda, Yoshiyuki Satoh and Yasuhiro Kondo, Nucl. Instr. and Meth, A359 (1995) 625-627
3. M.Takebe, Ken Abe, Yasuhiro Kondo, Yoshiyuki Satoh and Manabu Souda Jpn. J. Appl. Phys. 34(1995) 4197-4199.

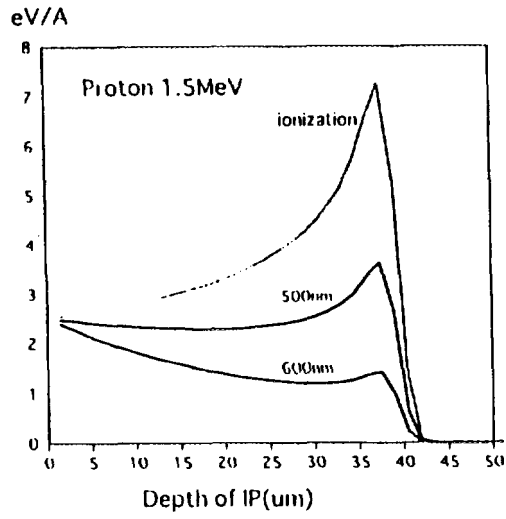


Fig. 1 Energy deposit and readout PSL

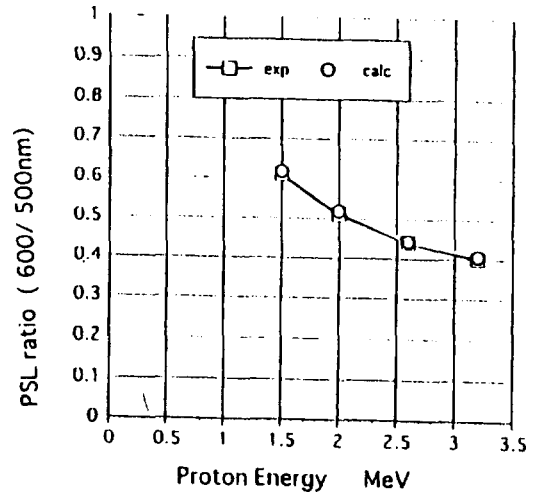


Fig.2 Comparison of exp PSL ratio with calculated value

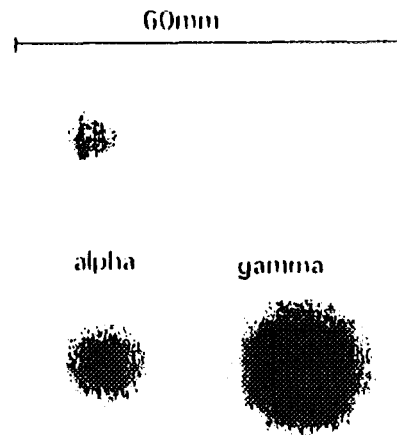


Fig. 3 Lower picture shows IP image irradiated alpha and gamma radiation. Upper picture shows IP image discriminated by two wavelength readout.

# IMAGING PLATE-ASSISTED RADIOGRAPHIES WITH 3.7MBq OR LESS SOURCES

Ken Abe, Masahiro Takebe, Yasuhiro Kondo, Yoshiyuki Satoh,  
Manabu Souda, Yasunori Kokubun, Mikiya Miyazaki,  
Yasuyuki Hori and Yasuo Murakami  
Faculty of Engineering, Tohoku University  
Sendai 980-77, Japan

## 1. INTRODUCTION

The imaging plate (IP, here BAS-UR<sup>(1)</sup>, BaFBr<sub>0.85</sub>I<sub>0.15</sub>:Eu<sup>2+</sup> based imaging plate) has many striking performances of radiation detection, such as a large detection area, long time dose accumulation, low cut-off energy (of several electron volts after passing the surface protection layer<sup>2)</sup>), wide dynamic range of exposure dose (linear over more than 5 decades, with no S-figure response characteristic to photo and X-ray films) and a high sensitivity (detectable even very weak radioactivity of 10<sup>-4</sup> Bq in a spot of 1mm<sup>2</sup> or less in area with several hours of exposure<sup>3)</sup>). Imaging simply using the IP in place of the X-ray film have been done so far by many people. They have encountered, however, unexpected difficulties turning out the adverse effects of those striking performances; 1) the high sensitivity even for cosmic rays against which effective shielding is very hard, 2) nearly no energy cut-off and 3) wide latitude of exposure dose, the two being similar to usages of nuclear emulsion plates sensitive even to minimum ionization particles or photo films of superhigh sensitivity, or superhigh gain amplifiers with no window filters. Effectual measures for such a little troublesome IP have not been found, then X-ray film or solid film methods are still often employed in various radiographies. We pointed out that an arrangement of some kind of ROI (region of interest) windows on particle energy and/or exposure dose, and/or an equipment of particle discrimination can strongly reduce both the background noises (PSL/mm<sup>2</sup>) and the forward scattering overlapping and highly improve the S/N (signal-to-noise) ratios<sup>4)</sup>, for which a new type of IP reader should be

developed<sup>5)</sup>.

The features of the image accumulation, wide dynamic range and high detection sensitivity will give us a new world of static radiography if being backed up by a full use of the detectability of extremely low specific radioactivities with the further increased S/N ratio, which will surpass the usual one with the conventional substitution of X-ray films for IP's. However, here we do not present radiographies with such a new equipment but do restrictedly the low activity radiographies using both the conventional IP and conventional IP reader. Recent low level radioactivity imaging of some kind of vegetables and ceramic ware pictures<sup>(6)</sup> and neutron imaging by use of Gd-containing IP<sup>7)</sup> show a step ahead of these radiographies.

Enhancement of the signal S or the S/N ratio on the IP as well as reduction of the fading of images due to both temperature and time elapsing is quite important to low activity radiography because the radiography requires the long time accumulation of exposure dose. Truth to say, improvement of image S/N ratio to the extremely high level makes available, for example, the neutron radiography with very weak neutron sources and/or a rather easy radiography with various radiations of usual radioisotopes. Really, low activity radiography forms the fundamentals common to any type of radiation imaging using the IP. We thereby can expect to realize the radiographies with weak sealed gamma or neutron sources of 100 $\mu$ Ci (3.7MBq) or less, necessitating no controlled area of radiation handling.

Low activity radiographies generally require simultaneous solution of many problems such as reduction of the fading of the latent images annexed to long time exposure, good shielding against the earth-origin radiations, cosmic rays and radiations from the shielding material itself, good detection geometries, improved data-taking efficiency of the target signals and so on. No means seems to be left after recent enforcement of such policies using well-known equipments and procedures. Then we have tried some extraordinary and a little absurd experiments to break the ceiling, and found unexpectedly that some useful policies on IP-assisted radiographies are still left.

Does IP make really to be of practical use the low level radiography with weak radioactive sources in no need of the radiation regulations? What quality is given by such radiographs although highfine graphs are not expected? Getting easily radiographs in an

everyday laboratory room having no relation to reactors, accelerators, X-ray generators nor controlled area, or in a museum, at excavation spots of historic interest, at small industrial works in town or at building construction fields and so on means a realization of a new type of so-called "u-tsu-run'desu (film with lens) for radiation" as long as getting useful informations in its own way. Both the background reduction and high improvement of S/N ratios in a long time period are decisive of all. The exposed IP's can be processed and printed in color with PSL/mm<sup>2</sup> densitometry data when sent to an IP handling agency by a cooled package, in the same way as DPE of photo films. The IP's are comparatively of low price and can be easily erased on the spot for a fresh use or reuse without a commercial IP eraser. Then, in the field where cosmic ray radiography is effective, a poor man's radiography may be realizable at the investment cost of only ¥10,000.

## 2. GAMMA-RAY RADIOGRAPHY (<sup>60</sup>Co, 100μCi, a point source)

The background fog noises of IP's (PSL/mm<sup>2</sup>) are reduced by ① an all-out shielding against environmental radiations including cosmic rays, ② setting some ROI windows, ③ a particle discrimination and ④ some post treatments. Special shielding materials, e.g. iron plates formed out of the ancient sunken battleship named Mutsu completed in 1921 or lead bricks fabricated 25 years or more ago, are not becoming here, but a few commonplace materials such as common lead bricks (5x10x20cm<sup>3</sup>), various thickness of lead or bismuth sheets, polyethylene bricks, metacrylic acid resin plates, oxgen-free copper plates and others are suitable for the simple, easy and cheap radiographies. We tested various materials and methods for shielding and found that the shielding efforts bear little effect over a limit. Background reduction by 10<sup>-1</sup> in fog density is easily attained, but it is rather good to think no more of effect over it. On the other hand, intensifying the IP is much effective to increase the S/N ratio although the IP is already very high in sensitivity. The imaging picture as shown in fig.1 can be obtained easily by the help of an backward intensifying screen of 2mm thick lead sheet.

## 3. NEUTRON RADIOGRAPHY (<sup>252</sup>Cf, 100μCi)

For neutron radiography using usual IP's, neutron converters are indispensable such as  ${}^6\text{Li}$ ,  ${}^{10}\text{B}$ ,  ${}^{157}\text{Gd}$ , polyethylene or their compounds. It has been well known that the converters for IP's should not be phosphorescent because that latent images of the IP's are fully erased by visible light. We found, however, that X-ray intensifying screens mainly containing  $\text{Gd}_2\text{O}_2\text{S:Tb}$  scintillators are more effective than the Gd metal foils for thermal neutron radiography and of more easy use and very much cheaper. Fig.2 shows the test images using the  $\text{Gd}_2\text{O}_2\text{S:Tb}$  screen (Fuji Grenex HR-16), indicating from bottom to upper, 0.5mm thick lead plate, 5mm thick metacrylic acid resin plate and 2mm aluminum plate (common plate supporting the former two). Neutron fluence of the  ${}^{252}\text{Cf}$  source was  $3/\text{cm}^2/\text{sec}$  at 1m. After thermalization the fluence was reduced by about  $10^{-2}$ . The keys are a howitzer construction to produce rich thermal neutrons and an intensifying screen to get a high S/N ratio at IP imaging.

#### 4. COSMIC RAY RADIOGRAPHY

Sendai district is a weak place of Japan in environmental radiation level, the radiation amounting to about  $0.06\mu\text{Sv/h}$ , and producing background fogs of about  $1.7 \text{ PSL}/\text{mm}^2/\text{day}$  in the IP. Then the long time accumulation of IP images is expected to realize a sourceless radiography with the half space of environmental radiations and/or cosmic rays. Fig.3 shows a cosmic ray radiography of a 5mm thick copper loading disk of a 300MeV electron linear accelerator and a cadmium block put at the right hand using the  $\text{Gd}_2\text{O}_2\text{S:Tb}$  screen (Fuji Grenex HR-16).

#### References

- (1) K.Takahashi and J.Miyahara, J.Crystallographic Soc.Japan, **35** (1993)256. [in Japanese.]
- (2) M.Katto, R.Matsumoto, K.Kurosawa, W.Sasaki, Y.Takigawa and M.Okuda, Rev.Sci.Instr. **64** (1993)319.
- (3) C.Mori, A.Matsumura, T.Suzuki, H.Miyahara, T.Aoyama and K.Nishizawa, Nucl.Instr.Meth. **A339** (1994)278.
- (4) M.Takebe et al., Nucl.Instr.Meth. **A345** (1994)606, **A359** (1995)626, **A363** (1995)614. Jpn.J.Appl.Phys. **34** (1995)4197.
- (5) Y.Hori, M.Miyazaki, M.Souda, K.Abe, Y.Kondo, Y.Satoh and M.Takebe,

Extended Abstract of 19th Meeting of Tohoku Branch of Atomic Energy Society of Japan (1995)9. [in Japanese.]

- (6) C.Mori, S.Koido, T.Suzuki, J.Miyahara and K.Takahashi, Radioisotopes 44 (1995)433. [in Japanese.]
- (7) N.Niimura, Y.Karasawa, I.Tanaka, J.Miyahara, K.Takahashi, H.Saito, S.Koizumi and M.Hidaka, Nucl. Instr. and Meth. A349 (1994)521.

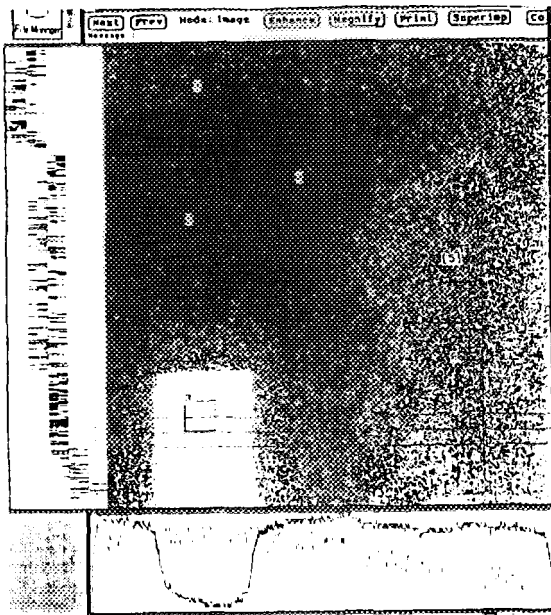
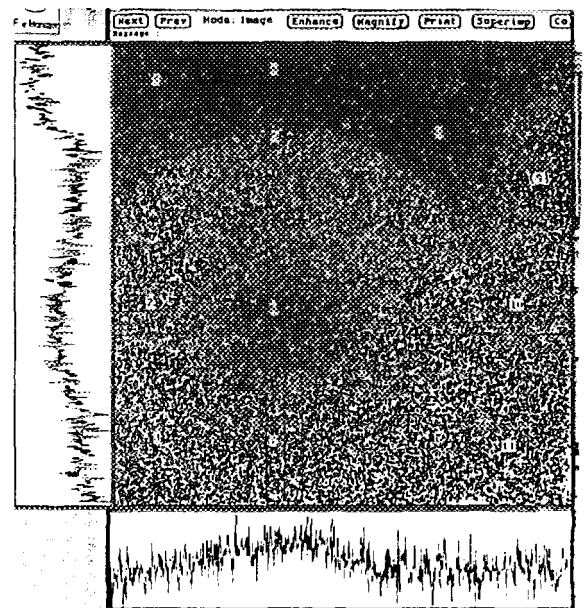
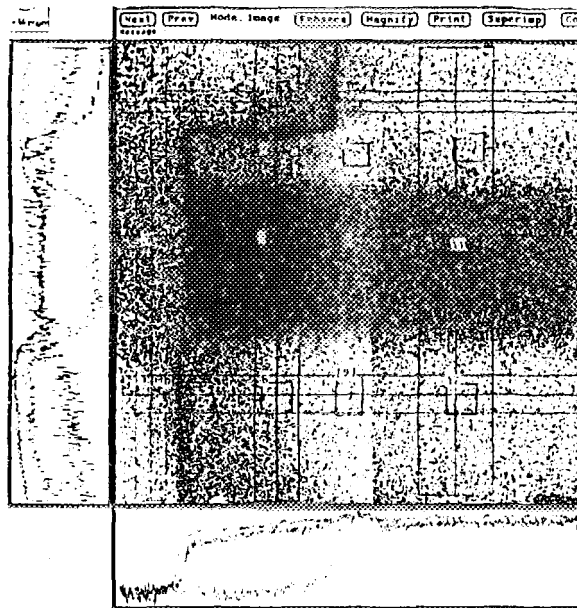


Fig.1(left upper). A ceramic doll and a lead block by 100 $\mu$ Ci  $^{60}$ Co gamma rays. Left and bottom insets show PSL curves of densitometry.

Fig.2(left below). Thermal neutron radiograph of a combination of lead, metacrylic acid resin and aluminum plates by the help of Gd<sub>2</sub>O<sub>2</sub>S:Tb screen by 100 $\mu$ Ci  $^{252}$ Cf source. Left and bottom insets show PSL curves of densitometry.

Fig.3(below). Radiograph of a copper disk by natural environmental radiation at 20m height from the ground surface.



# HIGH GAMMA-RAY MEASUREMENT USING OPTICAL EMISSION OF CERAMIC MATERIAL

**Tsunemi Kakuta, Kaoru Sakasai and Hideshi Yamagishi**

*Advanced Science Research Center, Research Group for Quantum Radiation measurement,  
Japan Atomic Energy research Institute (JAERI)  
2-4 Shirakata-shirane, Tokai-mura, Naka-gun, Ibaraki-ken, 319-11, Japan*

**Masaharu Nakazawa**

*Department of Quantum Engineering & System Science,  
University of Tokyo  
7-3-1 Hongo, Bunkyo-ku, Tokyo, 113, Japan*

## 1. INTRODUCTION

To measure the high level ionizing radiation, fluorescence phenomena in ceramic material, is used for a sensor. It is known that the ceramic material occurs optical emission under the exposure to ionizing radiation. In previous investigation, we have observed fluorescence at the wavelength of 690 nm band in Zr-O ceramic<sup>(1)</sup>.

On the other side, research and development of radiation resistant optical fibers have been actively continued resulting in clarification of radiation effects on various optical fibers. From these studies, it has been make sure that the pure silica core fibers have good radiation resistance. Besides the newest investigation, the fluorine to the silica core as a dopant improves its radiation resistivity more strong. The pure silica with fluorine doped core fiber can be used in severe radiation environment under doses exceeding  $10^7$ - $10^9$  Gy<sup>(2)</sup>. The new optical diagnosing systems using radiation resistant optical fibers are now applied to expanding in more severe radiation environments.

This paper describes the fluorescence phenomena in Zr-O ceramic under expose to high gamma-ray and fission neutron source. In addition, the paper also discusses the possibility of ionizing radiation detection in the core region of reactor.

## 2. MEASURING SETUP

A Zr-O ceramic is used for this experiment as a sensor material. Outer diameter and length of Zr-O sensor are 1.4 and 2.0 mm, respectively. The sensor has 200 $\mu$  m of center hole for

connecting to an optical fiber. A pure silica with fluorine doped core fiber, which shown in Table 1, is connected to Zr-O sensor. Figure 1 shows an outline of the measuring procedure.

Table 1 Fluorine Doped Radiation Resistant Optical Fiber

Type	Core		Clad		$\Delta n$ (%)
	Composition	Outer Diameter	Composition	Outer Diameter	
S. 1.	SiO <sub>2</sub> -F F:1.6 wt%	200 $\mu$ m	SiO <sub>2</sub> -F F:5.6wt%	250 $\mu$ m	1.1

Table 2 Irradiation and Measurement Conditions

Items	Fission neutron	Gamma-ray
Facility	JRR-4, No.1Pool	<sup>60</sup> Co Facility
Atmosphere	Free Air	Free Air
Temperature	Room temperature	Room temperature
Flux/Exp.rate	1.0 x 10 <sup>12</sup> n/cm <sup>2</sup> s	2.7 x 10 <sup>6</sup> R/hr
Fluence/Exp.	>2.0 x 10 <sup>15</sup> n/cm <sup>2</sup>	>1.0 x 10 <sup>8</sup> R
Measurement	In-situ measurement for optical spectrum	

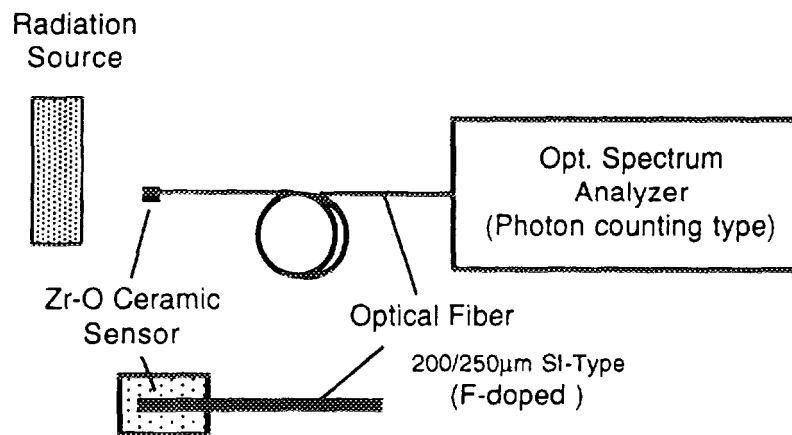


Fig. 1 Measuring procedure for high gamma-ray radiation

A <sup>60</sup>Co irradiation facility in JAERI and a JRR-4 reactor is used for this experiment as a Gamma-ray and fission neutron source. Irradiation condition of the sensor and optical fiber is listed in Table 2. The ceramic sensor is examined on its fluorescence phenomena during

expose to both radiation sources.

In case of  $^{60}\text{Co}$  measurement, the ceramic sensor is exposed under exposure rate between  $7.7 \times 10^4$  and  $2.7 \times 10^6$  R/hr. Total dosage of gamma-ray during this experiment is up to about  $10^8$  R. Fission neutron irradiation with a JRR-4 reactor is examined under flux level up to  $10^{11}$  n/cm $^2$ -s (3.5MW), concurrent with high gamma-ray dose rate.

An optical spectrum analyzer, PMA-11 manufactured by Hamamatsu-Photonics, is used for this fluorescence measurement. The optical wavelength from 300 to 800 nm can be measuring its spectrum analyzer by photon counting method.

#### 4. RESULTS AND DISCUSSION

##### 4.1 Gamma-Ray Observation

Figure 2 shows the spectral fluorescence of Zr-O ceramic sensor during irradiation to a  $^{60}\text{Co}$  gamma-ray. Gamma-ray induced fluorescence is observed at the wavelength from 300 to 800 nm. The fluorescence can be divided into two part. One is, small optical intensity part at the wavelength region from about 300 to 700 nm, which seems to a cherenkov radiation.

The optical intensity of its phenomena is proportional to the second power of inverse of wavelength. Other part is, strong optical intensity at wavelength 650 to 750 nm band, which have a narrow peak of 690 nm. The value of full width half maximum (FWHM) of 690 nm peak is about seven nm. Relation of the gamma-ray exposure rate and optical intensity of 690 nm peak

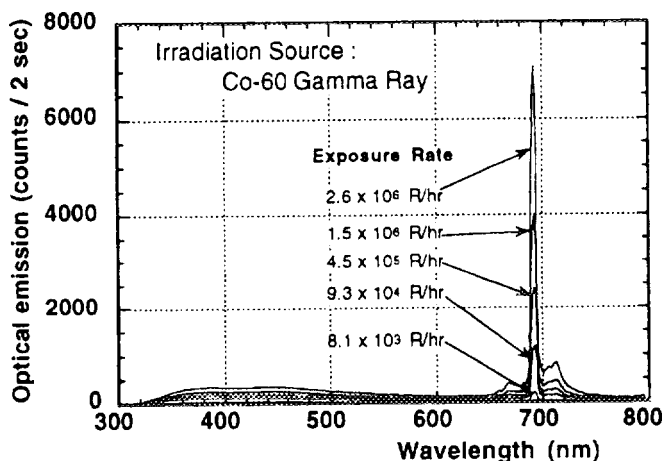


Fig. 2 Spectral optical emission under gamma-ray irradiation

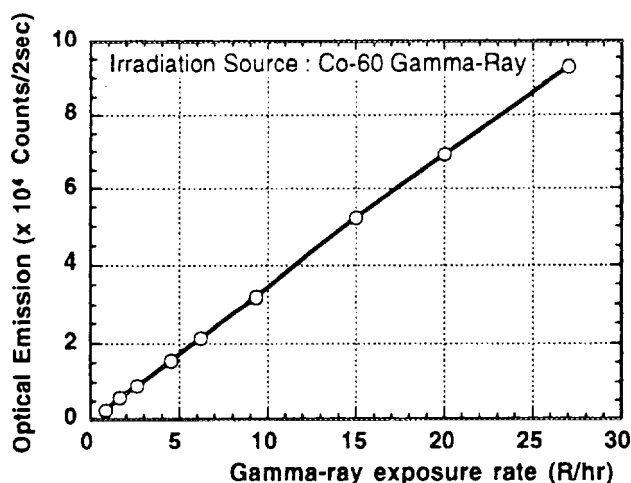


Fig.3 Linearity of optical emission

is shown in Fig. 3.

Optical intensity of 690 nm peak is directly proportional to the exposure rate. These fluorescence phenomena are maintained during irradiation up to  $10^8$  R.

#### 4.2 Fission Neutron Observation

Fission neutron irradiation test is carried out with JRR-4 reactor. Ceramic sensor is exposed fast and thermal neutrons concurrent with high gamma-ray.

Figure 4 shows the fluorescence spectrum of Zr-O ceramic sensor during irradiation to a fission neutron. The observed spectrum at the wavelength from 300 to 800 nm is quite similar to a gamma-ray irradiation test. Therefore, the fluorescence of Zr-O ceramic is appeared by an interaction of gamma-ray.

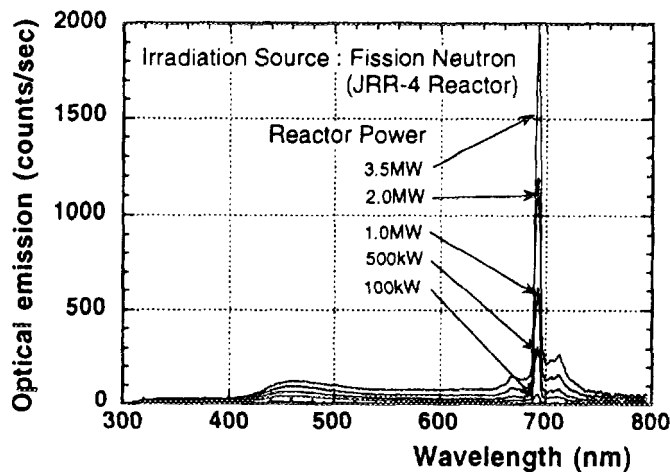


Fig. 4 Spectral optical emission under fission neutron irradiation

#### 5. CONCLUSION

High level ionizing radiation measuring tests are carried out using ceramic sensor and radiation resistant optical fiber. The fluorescence phenomena in ceramic material are used for a sensor. Induced fluorescence is observed at the wavelength from 300 to 800 nm. A Zr-O ceramic sensor appeared strong fluorescence at wavelength 650 to 750 nm band that have a narrow peak of 690 nm. The optical intensity of 690 nm peak is directly proportional to the exposure rate up to  $2.7 \times 10^6$  R/hr. The fluorescence phenomena are maintained during irradiation to a  $^{60}\text{Co}$  gamma-ray source and fission neutron source of JRR-4 reactor. Ceramic sensor can be applied to new radiation measuring systems for severe radiation environment of reactor.

## REFERENCES

- (1) Kakuta. T., Sakasai K., Yamagishi H., et al. "Measurement of high gamma-ray using fluorescence phenomena in ceramics", 1995 Fall Mtg. Atomic Energy Society of Japan, C2, Tokai, 17-20 Oct. (1995)
- (2) Kakuta T., Shikama T., et al. "Development of in-core monitoring measuring method using optical techniques", KEK Proceedings 94-7, Radiation Detectors and Their Uses, 109-113(1994)

# IS RADIATION DOSIMETRY POSSIBLE USING SUGAR DECOMPOSITION ?

Hiroshi Kawai  
Hiroshige Morishima  
Taeko Koga  
Katsuichi Nakamura

Atomic Energy Research Institute, Kinki University

## 1. INTRODUCTION

It is well known that cane sugar (sucrose) in acid solution decomposes into glucose and fructose as shown in Fig.1. We have studied how much radiation accelerate this sugar decomposition, which may suggest that an acid sugar solution can be used for radiation dosimetry.

## 2. EXPERIMENTAL

Sucrose, glucose and fructose are optically active substances. When plane-polarized light falls on these substances, the plane of light oscillation rotates. As the specific rotary powers  $[\alpha]_D^{20}$  of sucrose, glucose and fructose are  $66.5^{(1)}$ ,  $52.7^{(1)}$  and  $-92^{(1)}$ , respectively, the angle of rotation becomes  $-20^{(1)}$  after whole decomposition of sucrose. The superscript 20 of the bracket shows the temperature of the solution and the subscript D the monochromatic light, sodium D-line. Then it is estimated that the rotation angle indicates the degree of sucrose decomposition. To measure the rotation angle a Laurent saccharimeter, which includes two Nicol prisms, was used. The light source was Na lamp which

produced D-line. The samples were 22.5% or 34.7% granulated cane sugar dissolved in HBr acid solution of pH 1.5. The samples were irradiated with Co-60  $\gamma$ -rays or ultra-violet rays (UV) of 0.00258 w/l and 0.145 w/l, of which wave lengths were 185 nm and 254 nm, respectively. The rotation angles were measured ten times, from which the mean values and standard deviations were determined. The rotation angle of the non-irradiated sample for subtraction(control) was also measured at the same time.

### 3. RESULTS AND DISCUSSION

Fig.2 shows the relation between  $\gamma$ -radiation doses and the rotation angles which were the differences between the rotation angles of control and those of the irradiated samples. Fig.3 is the semi-log plots of Fig.2. Fig.4 shows the relation between UV radiation doses expressed in irradiated hours and the rotation angles. The shape of the curve in Fig.2 is convex to the horizontal axis until 8 Gy, but that of UV in Fig.4 is concave. This suggests that sugar decomposition mechanism by  $\gamma$ -rays is different from that by UV.

No  $\gamma$ -ray and UV influence was observed on sugar dissolved in distilled water. No decomposition was also seen in sugar irradiated with  $\gamma$ -rays or UV before dissolving in distilled water or HBr solution.

Further study on the above phenomena would be necessary for practical dosimetry.

#### **4. ACKNOWLEDGMENT**

The authors wish to acknowledge instructor Takashi Chikaike in Department of Science and Technology of Kinki University for preparing Laurent saccharimeter for us.

#### **5. References**

- (1) Rikagaku Jiten, 4th ed.(Iwanami-shoten, Tokyo, 1987).

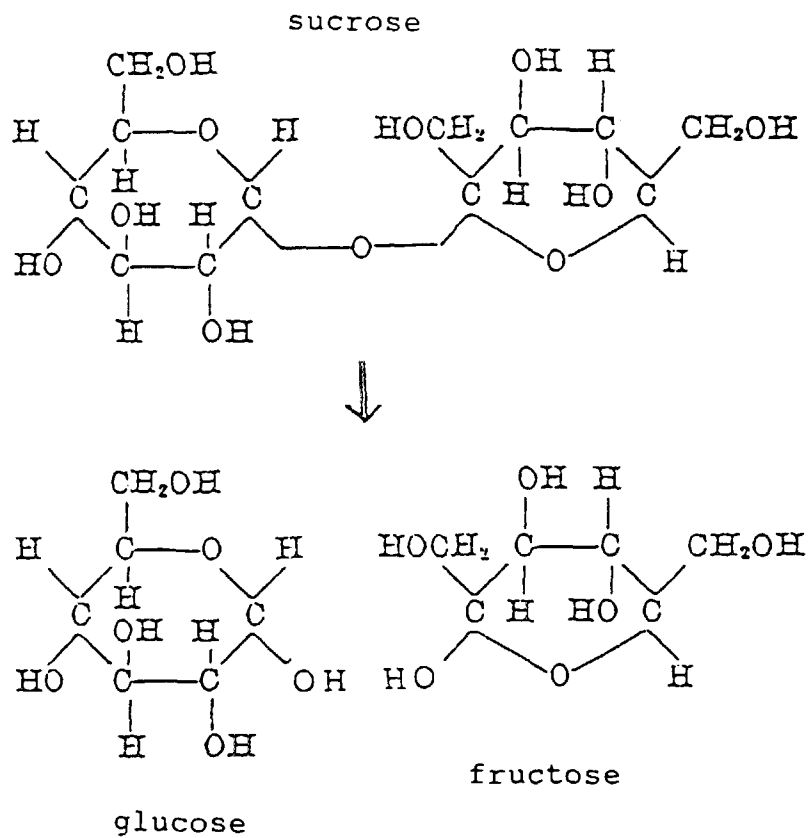


Fig.1 Decomposition of sucrose into glucose and fructose

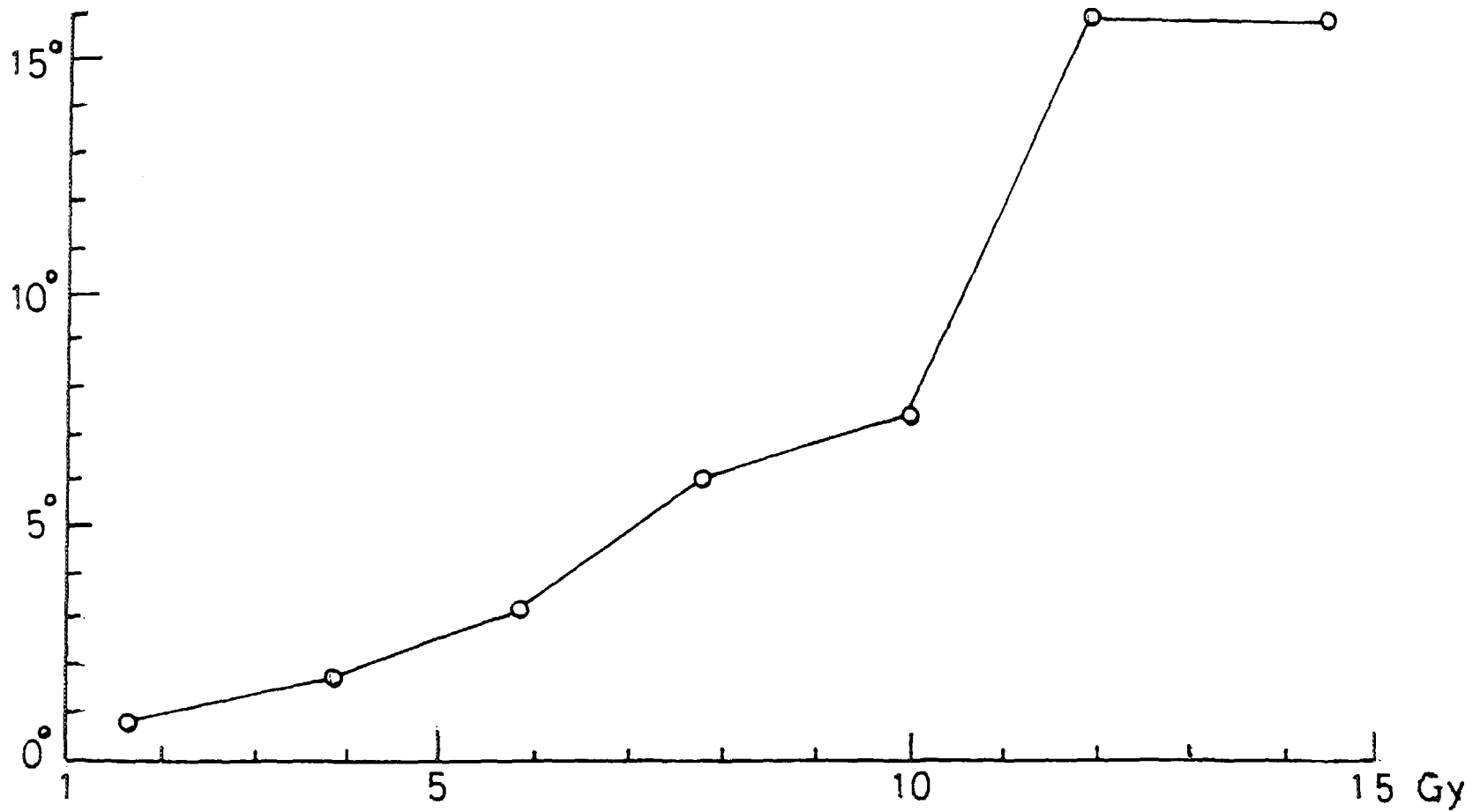


Fig.2 Relation between  $\gamma$ -radiation doses and rotation angles

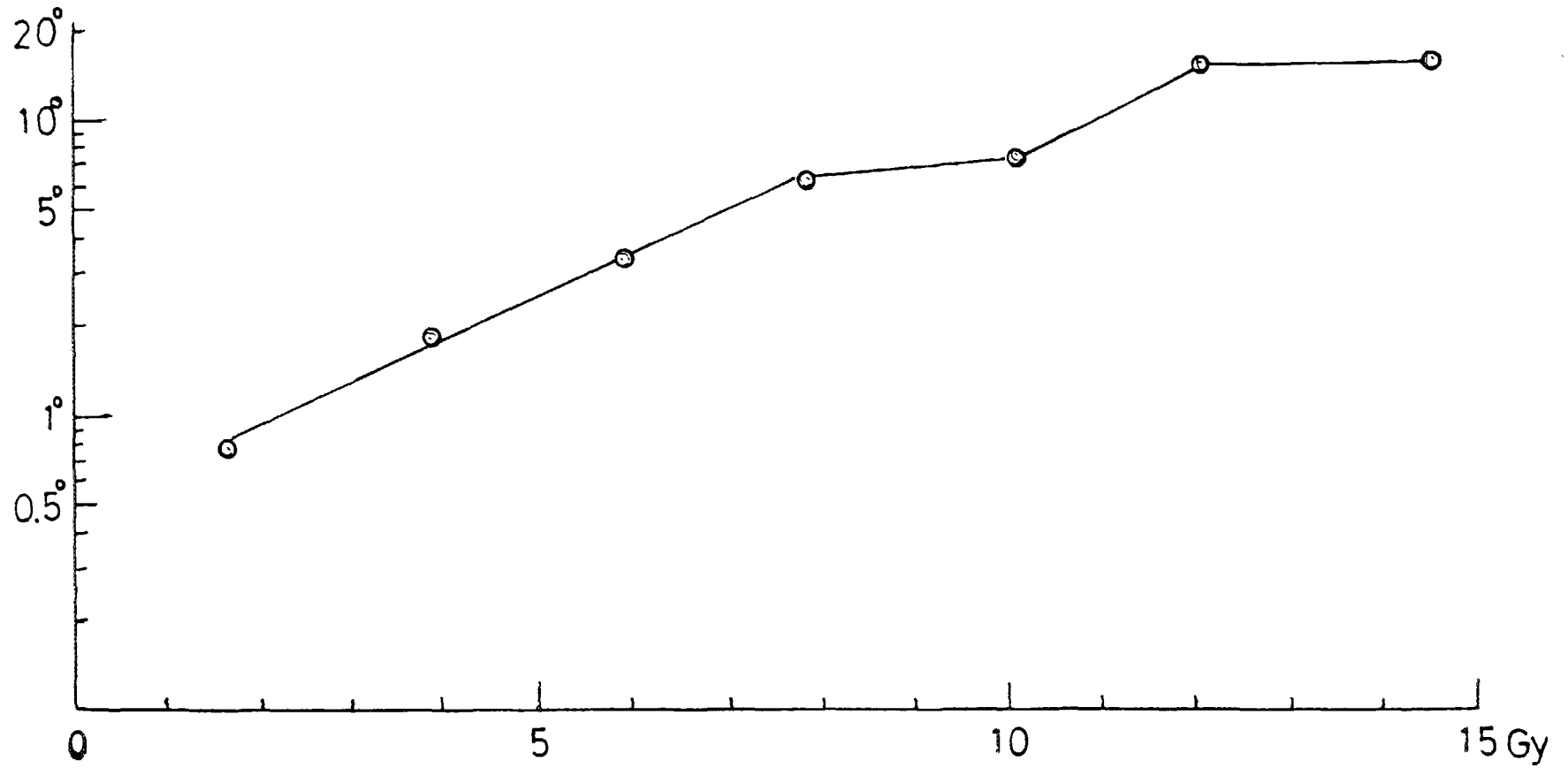


Fig.3 Relation between  $\gamma$ -radiation doses and log-scale rotation angles

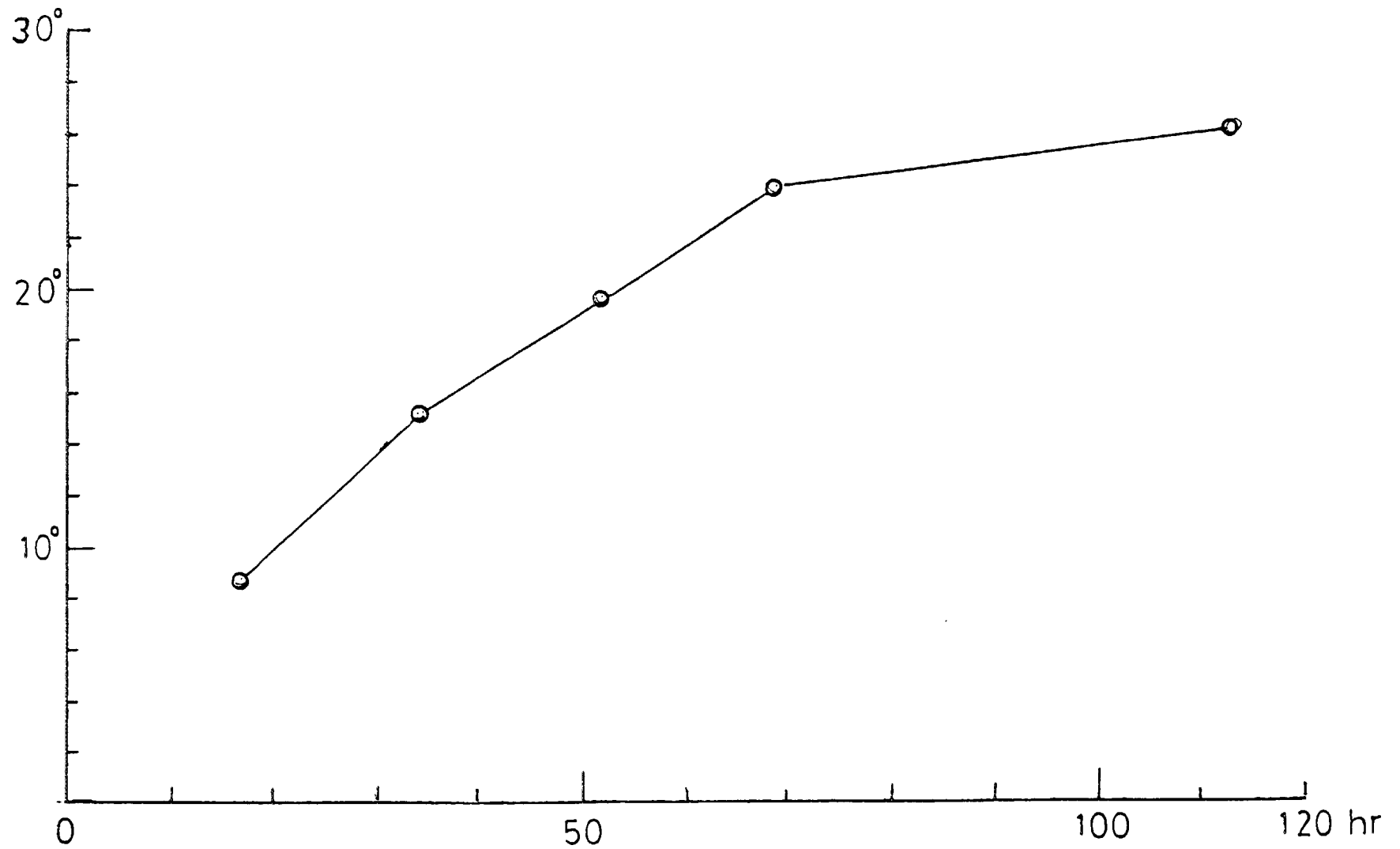


Fig.4 Relation between UV radiation doses expressed in irradiated hours and rotation angles

# **PopTop-Type Germanium Detector Cooled by Stirling Refrigerators**

Masaki Katagiri and Yoshii Kobayashi  
Japan Atomic Energy Research Institute (JAERI)

Koji Takahashi  
SEIKO EG&G CO. LTD.

Yoshito Taguchi and Toshio Uchida  
Sumitomo Heavy Industry LTD.

## **1. INTRODUCTION**

A germanium gamma-ray detector is very useful to gamma-ray spectroscopy applications. However, this detector needs a dewar for keeping liquid nitrogen because of the operation at the temperature near 77K. Therefore, a small maintenance-free germanium detector system has been required from various research fields.

For this purpose, we developed a small electric-cooled germanium gamma-ray detector using a Stirling refrigerator for cooling the detector element<sup>1)2)</sup>. Moreover, a germanium detector system, in which the detector element can be easily exchanged with consideration of radiation damage, is required by researchers using the detector in accelerators. On the other hand, in a PopTop Ge detector system that was developed by ORTEC<sup>3)</sup>, a PopTop Ge capsule can be easily exchanged without a vacuum pump, heater tapes, or other equipment.

Therefore, we have developed a PopTop-type germanium detector cooled by three Stirling refrigerators.

## **2. DESCRIPTION OF THE DETECTOR**

Schematic structure of developed PopTop-type germanium detector with the Stirling refrigerators is illustrated in Fig. 1. Three Stirling refrigerators are used to cool down a PopTop Ge capsule to temperature near 80K instead of a dewar containing liquid nitrogen. A Model SRS-2110 fabricated by Sumitomo Heavy Industry LTD. was used as the Stirling refrigerator<sup>4)</sup>. The cooling ability of the refrigerator is 1.5 W at 80K when it works with operation condition of AC

17V and 3.5A. Three cold heads of the cooling system cooled by the displacer are connected by an inverse-T shape fitting.

Figure 2 shows a detailed structure of a PopTop-type capsule system that consists of a Ge detector

capsule and a cooling connection mechanism. The PopTop-type cooling connection mechanism is attached at the center of the fitting. The Ge detector capsule is installed to the cooling connection mechanism. A closed-end high purity germanium detector element having the relative efficiency of 17% is mounted in the capsule. Moreover, the first stage circuit of a preamplifier is installed near the germanium detector element to reduce microphonic noises induced by vibration of the Stirling refrigerators.

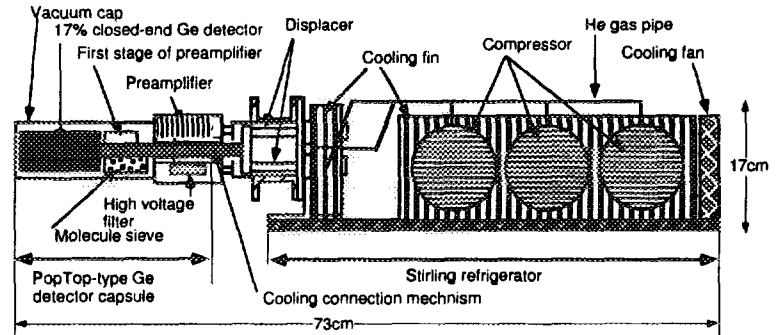


Fig. 1 Schematic structure of developed PopTop-type germanium detector with three Stirling refrigerators

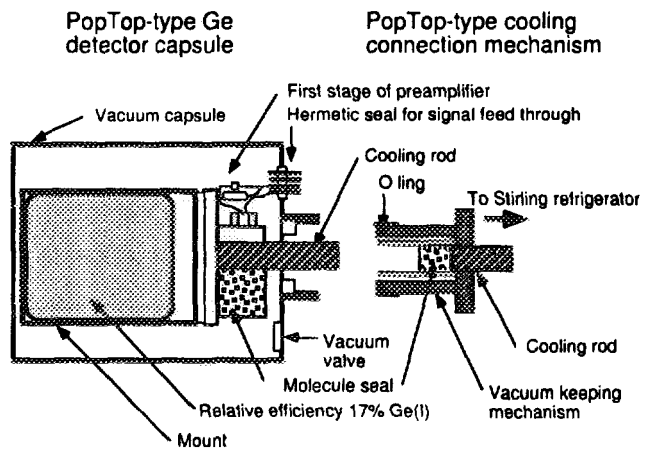


Fig. 2 Detailed structure of a PopTop-type capsule system

The developed PopTop-type germanium detector with the Stirling refrigerators is shown in Photo. 1. A size of the detector is 73cmh x 17cmh x 17cmw.

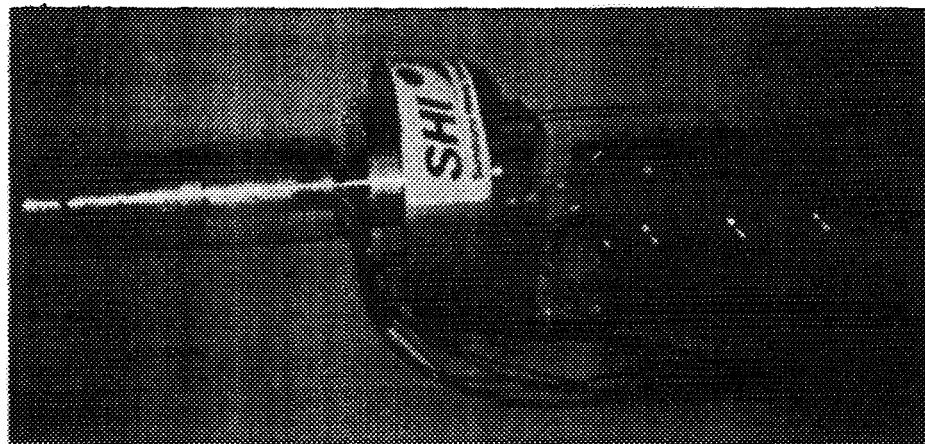


Photo. 1 PopTop-type germanium detector with three Stirling refrigerators

### 3. PERFORMANCE OF THE DETECTOR

The measurement of cooling characteristics was carried out by operating three Stirling refrigerators with AC 17V of the rated voltage. The temperature at a cooling rod in the capsule was measured. The result is shown in Fig. 3. The lowest cooling temperature, 82K, was obtained after operation of 8 hours.

The performance of the detector was measured by a  $^{60}\text{Co}$  gamma-ray source. A typical gamma-ray spectrum for the  $^{60}\text{Co}$  source is shown in Fig. 4. The dependency of FWHM energy resolution on shaping time of a spectroscopy amplifier(CANBERRA-2021) was measured at the range of  $1\mu\text{sec}$  to  $10\mu\text{sec}$ . The results are shown in Fig. 5.

The best FWHM energy resolution is obtained when the shaping time is  $2\mu\text{sec}$ . The energy resolution for 1.33MeV gamma-rays is 2.43keV and that for the pulser is 1.87keV. On the other hand, the energy resolution for 1.33MeV gamma-rays is 2.40keV and that for the pulser is 1.80keV if the AC power supply of the refrigerators is stopped for a short time.

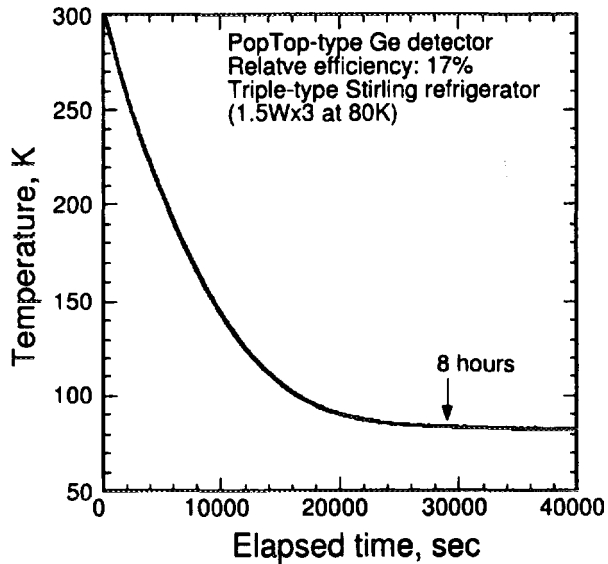


Fig. 3 Cooling characteristics of PopTop-type Ge detector with Stirling refrigerators

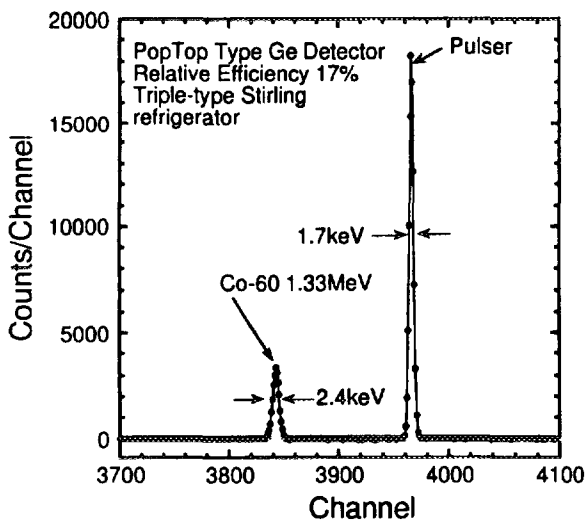


Fig. 4 Typical gamma-ray spectrum for  $^{60}\text{Co}$  source

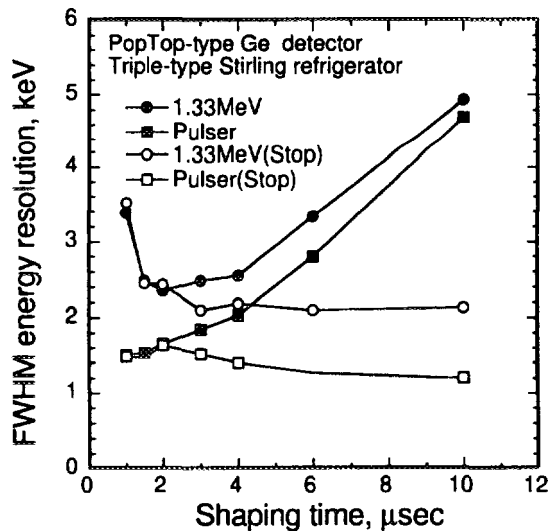


Fig. 5 Dependency of energy resolution on shaping time of a spectroscopy amplifier

#### 4. ANALYSIS OF MICROPHONIC NOISE

From the above-mentioned shaping time dependency, it is revealed that the FWHM energy resolution of this PopTop-type Germanium detector is affected by microphonic noises induced by three refrigerators. Noise spectra were measured by a spectrum analyzer in order to investigate the cause of wrong energy resolution at shaping time more than  $3\mu\text{sec}$ .

At first, noise levels of a preamplifier output signal were measured when the Stirling refrigerator is operated and stopped. The results are shown in Fig.6. One can see that the spectrum for operation-mode have small peaks at frequency of 3kHz, 6.5kHz and 15kHz. Next, noise levels of a spectroscopy amplifier output signal were measured at shaping time of  $2\mu\text{sec}$  and  $5\mu\text{sec}$  when the Stirling refrigerator is operated and stopped. The results are shown in

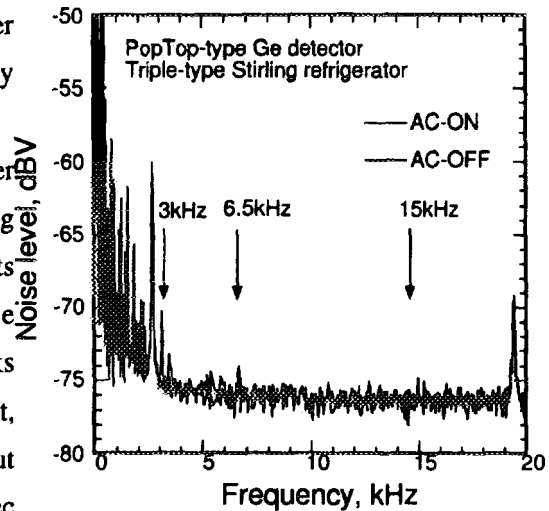


Fig. 6 Noise spectrum of a preamplifier output signal

Fig. 7 and Fig. 8, respectively. Two spectra are distributed in the range from 1kHz to 15kHz. One can see that noise level measured at the shaping time of  $2\mu\text{sec}$  is less than that of  $5\mu\text{sec}$ . By these results, it is revealed that the FWHM energy resolution of this detector is affected by the microphonic noise when the shaping time of the spectroscopy amplifier is more than  $3\mu\text{sec}$ .

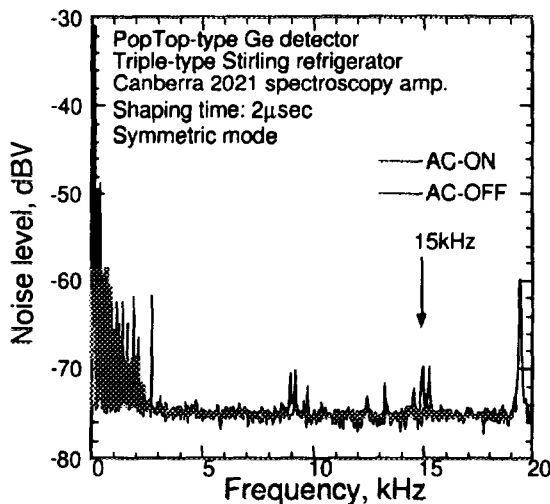


Fig. 7 Noise spectrum of a spectroscopy amplifier output signal were measured at shaping time of  $2\mu\text{sec}$

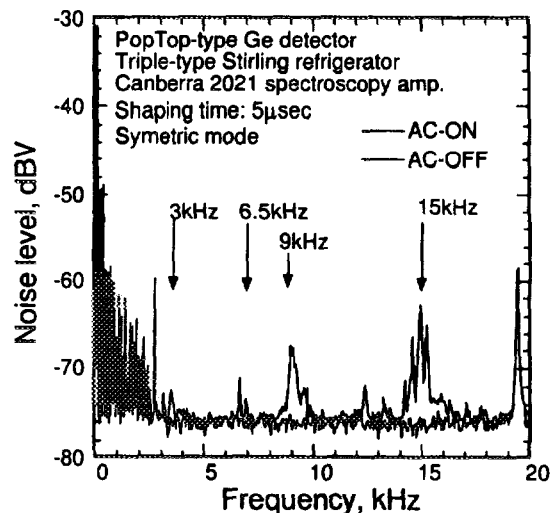


Fig. 8 Noise spectrum of a spectroscopy amplifier output signal were measured at shaping time of  $5\mu\text{sec}$

## 5. CONCLUSION

A PopTop-type germanium detector cooled by three Stirling refrigerators was developed. The relative detection efficiency of the Ge detector is 17%. The FWHM energy resolution at the gamma-ray energy of 1.33MeV is 2.43keV when the shaping time of a spectroscopy amplifier is set up at 2 $\mu$ sec. The energy resolution at this shaping time is almost as same as that of a commercial germanium detector cooled by liquid nitrogen. It is concluded that this germanium detector can be applied to various gamma-ray spectroscopy.

## References

- (1)M. Katagiri et al.: KEK Proceeding 94-7, Radiation Detector and Their Uses, 174-178(1994).
- (2)M. Katagiri et al.: KEK Proceeding 95-1, Radiation Detector and Their Uses, 219- 224 (1995).
- (3)EG&G ORTEC: Catalog of Detector & Instruments for Nuclear Spectroscopy.
- (4)Sumitomo Heavy Industry LTD.: Stirling refrigerator Model SRS-2110 manual.

# Correction of diagnostic x-ray spectra measured with CdTe and CdZnTe detectors

M. Matsumoto

School of Allied Health Sciences, Faculty of Medicine,  
Osaka University, Toyonaka, Osaka 560, Japan

H. Kanamori

Department of Electronics & Information Science,  
Kyoto Institute of Technology, Matsugasaki,  
Sakyo-ku, Kyoto 606, Japan

T. Toragaito and A. Taniguchi

Engineering Laboratory of Toyo Medic Co., LTD.

## 1. INTRODUCTION

Theoretical and experimental investigation of diagnostic x-ray spectra have been made over a long period by many authors. Twidell<sup>(1)</sup>, Sundararaman et al<sup>(2)</sup> and Stanton et al<sup>(3)</sup> have carried out reconstructions based on Monte Carlo methods for primary radiation (absorption, scattering, etc., of electrons on the target) and bremsstrahlung radiation (absorption and scattering in the target and in the filters). The most diffuse experimental method for determination of x-ray spectral composition is attenuation analysis (e.g., Stanton et al<sup>(4)</sup>, Ardran et al<sup>(5)</sup>, Soole and Jager<sup>(6)</sup>). Peale and Burt<sup>(7)</sup>, Seelentag and Panzer<sup>(8)</sup>, Birch and Marshall<sup>(9)</sup>, Kanamori et al<sup>(10)</sup>, Matsumoto et al<sup>(11, 12)</sup> and Kubota et al<sup>(13, 14)</sup> introduced another experimental method for direct measurement of x-ray spectra using nuclear detectors such as NaI and Ge. This last method works under the real operating conditions of an x-ray machine, but requires unsuitable geometries due to the high counting rates: they need source-detector distances of up to several meters and very narrow collimation of the beam. A collection of spectra from 10 to 300 kV, have been published by Seelentag et al<sup>(15)</sup> and from 30 to 150 kV, by

Birch et al<sup>(16)</sup>.

E. Di. Castro et al<sup>(17)</sup> have attempted to perform the direct measurement of x-ray spectra using a low-efficiency CdTe detector. Photon spectra produced by a portable diagnostic x-ray machine from 45-100 kV have been analyzed. We have attempted to perform the direct measurement of x-ray spectra using low-efficiency CdTe and CdZnTe detectors, which have been developed recently. Photon spectra produced by a single-phase 2-pulse diagnostic x-ray machine from 50-100 kV have been analyzed. Since detected spectra do not coincide with the true photon spectra, a correction by stripping procedure is applied. This procedure has been determined by an evaluation of spurious effects using a Monte Carlo method elaborated on an Epson personal computer. The obtainable results with CdTe and CdZnTe detectors are less exact than those with a Ge detector, because of the lower resolution and the higher background due to several spurious effects.

## 2. METHOD

We modified the stripping formula presented by E. Di. Castor et al.<sup>(17)</sup> in the following formula:

$$N_t(E_0) = \left( N_d(E_0) - \sum_{E=E_0+1}^{E_{max}} R(E_0, E) N_t(E) \right) / \epsilon(E_0)$$

where

$N_t(E_0)$  = true number of photons of energy  $E_0$ ,

$N_d(E_0)$  = number of photons detected of energy  $E_0$ ,

$E_{max}$  = maximum photon energy of the spectrum,

$R(E_0, E)$  = Monoenergetic response function of events of energy (E)

due to spurious effects included incomplete charge collection.

$\epsilon(E_0)$  = full energy peak efficiency.

Monoenergetic response functions and full energy peak efficiencies for CdTe and CdZnTe detectors have been determined by an evaluation of spurious effects, which are K-escape, coherent scattering and incoherent(Compton) scattering, using a Monte Carlo method elaborated on a Epson personal computer. The functions are shown by

Fig.1. In Fig.1 (a) and (b) are the functions for CdTe and CdZnTe detectors respectively. In Fig.1 (c) and (d) are the functions broadened for  $\text{FWHM}(\text{full width at half maximum for Ge detector}) \times 4.0$  and  $\text{FWHM} \times 2.0$  for CdTe and CdZnTe detectors respectively. The efficiencies for Ge, CdTe and CdZnTe detectors, and the calculated efficiency from attenuation coefficient of CdTe detector are shown by Table 1 and Fig.2. Incomplete charge collection is the dominant mechanism that produces a continuous background. The correction factor for this continuous background incident photon per keV has been added as constant for every photon energy. (17) At present the correction factors for CdTe and CdZnTe detectors have been evaluated as 0.006 respectively.

Using these functions, efficiencies and factors, the correction is applied step by step starting from the highest energy for measured  $\gamma$ -ray spectra of isotope  $^{241}\text{Am}$  and diagnostic x-ray spectra of tube voltage 50kV to 100kV with Ge, CdTe and CdZnTe detectors.

### 3. RESULT AND DISCUSSION

The comparison of measured and corrected  $\gamma$ -ray spectra of isotope  $^{241}\text{Am}$  for Ge(solid line), CdTe(dotted line) and CdZnTe(broken line) detectors are shown by Fig.3. In Fig.3 (a) and (b) are measured and corrected spectra for Ge, CdTe and CdZnTe detectors respectively. In Fig.3 (c) and (d) are corrected spectra by using the functions included incomplete charge collection and the functions broadened for  $\text{FWHM} \times 4.0$  and  $\text{FWHM} \times 2.0$  for CdTe and CdZnTe detectors respectively. The corrected spectra are improved in order of (b), (c) and (d). The corrected spectra for CdZnTe detector coincide with those for Ge detector. But the corrected spectra for CdTe detector do not coincide with those for Ge detector.

The comparison of measured and corrected diagnostic x-ray spectra(object 4mmAl) of tube voltage 50kV to 100kV for Ge(solid line), CdTe(dotted line) and CdZnTe(broken line) detectors are shown by Figs.4-9. In Figs.4-9 legends of (a), (b), (c) and (d) are the same as shown in Fig.3. The corrected spectra at higher tube voltage than 70kV are improved in order of (b), (c) and (d). The corrected spectra for CdTe and CdZnTe detectors coincide with those for Ge detector at lower tube voltage than 70kV. But the corrected spectra at higher tube voltage

than 70kV do not coincide with those for Ge detector. The reason is incomplete correction for full energy peak efficiencies of real CdTe and CdZnTe detectors.

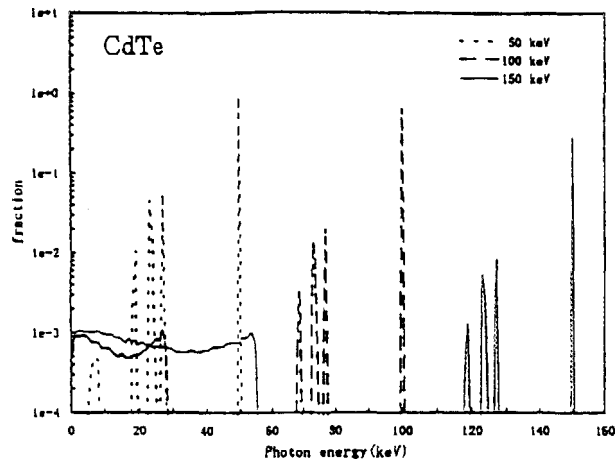
#### 4. CONCLUSION

We modified the formula of stripping procedure presented by E. Di. Castor et al. We added the Compton scattering and separated K<sub>a</sub> radiation of Cd and Te (23 and 27keV, respectively). Using the new stripping procedure diagnostic x-ray spectra(object 4mm-Al) of tube voltage 50kV to 100kV for CdTe and CdZnTe detectors are corrected with comparison of those spectra for the Ge detector. The corrected spectra for CdTe and CdZnTe detectors coincide with those for Ge detector at lower tube voltage than 70kV. But the corrected spectra at higher tube voltage than 70kV do not coincide with those for Ge detector. The reason is incomplete correction for full energy peak efficiencies of real CdTe and CdZnTe detectors.

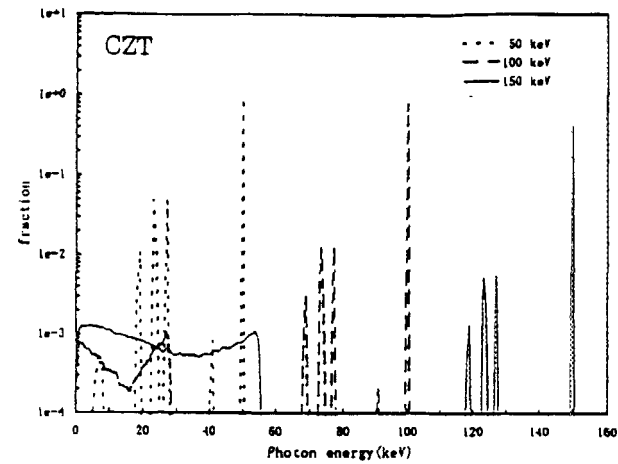
#### References

- (1)J. W. Twidell, Phys. Med. Biol. 15(1970)529.
- (2)V. Sundararaman, M. A. Prasad and R. B. Vora, Phys. Med. Biol. 18(1973)208.
- (3)L. Stanton, J. L. Day, D. A. Lightfoot, Theodore Villafana and P. L. Rauch, Radiology 130(1979)477.
- (4)L. Stanton, D. A. Lightfoot and S. Mann, Radiology 87(1966)87.
- (5)G. M. Ardran, A. K. Burt, H. E. Crooks and L. H. Peuple, Br. J. Radiol. 42(1969) 757.
- (6)B. W. Soole and W. F. Jager, Phys. Med. Biol. 15(1970)107.
- (7)L. H. Peuple and A. K. Burt, Phys. Med. Biol. 14(1969)73.
- (8)W. W. Seelentag and W. Panzer, Phys. Med. Biol. 24(1979)767.
- (9)R. Birch and M. Marshall, Phys. Med. Biol. 24(1979)505.
- (10)H. Kanamori, M. Matsumoto and N. Nakamori, Med. Biol. Eng. Comput. 23, Suppl. Part 2(1985)1334.
- (11)M. Matsumoto, H. Kubota, H. Hayashi and H. Kanamori, Med. Phys. 18(1991)921.
- (12)M. Matsumoto, H. Kubota, Y. Ozaki and H. Kanamori, Med. Biol. Eng. Comput. 33 (1995)48.

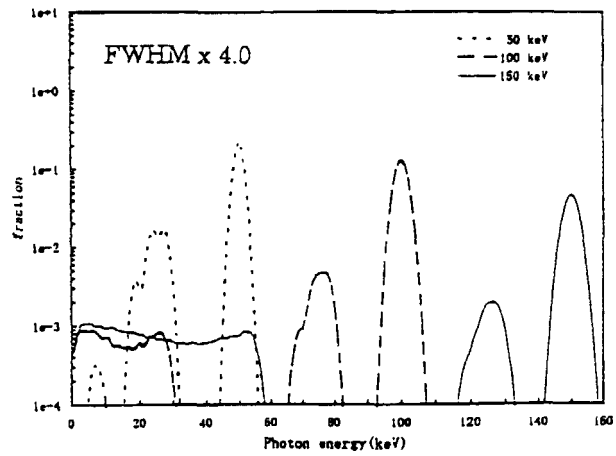
- (13)H. Kubota, Y. Ozaki, M. Matsumoto and H. Kanamori, Med. Phys. 20(1993)1023.
- (14)H. Kubota, Y. Ozaki, M. Matsumoto and H. Kanamori, Med. Biol. Eng. Copmul. 32 (1994)468.
- (15)W. W. Seelentag, W. Panzer, G. Drexler, L. Platz and F. Santner, GSF Report S-560 (1979).
- (16)R. Birch, M. Marshall and G. M. Ardran, Catalogue of Spectral Data for Diagnostic X-rays SRS 30(Hospital Physicists' Association, 47 Belgrave Square, London SW1X 8QX, 1979).
- (17)E. Di. Castor, R. Pani, R. Pellegrini and C. Bacci, Phys. Med. Biol. 29(1984) 1117



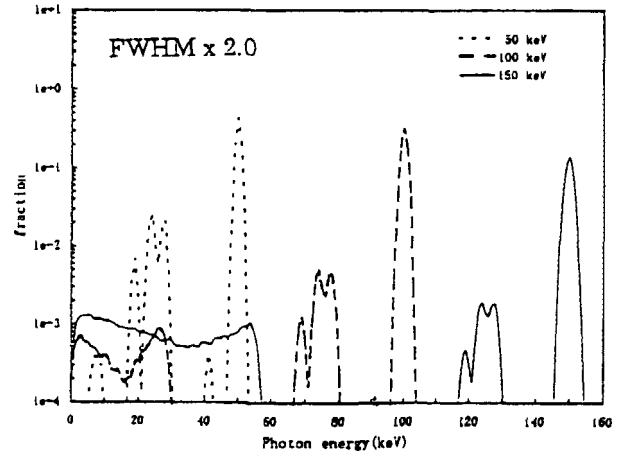
(a)



(b)



(c)



(d)

Fig.1 Monoenergetic response functions for CdTe and CdZnTe detectors. (a)for CdTe detector, (b)for CdZnTe detector, (c)the functions broadened by FWHM(full width at half maximum for Ge detector) $\times 4.0$  for CdTe detector, (d) the functions broadened by FWHM $\times 2.0$  for CdZnTe detector.

Table 1 Full energy peak efficiencies for Ge, CdTe and CdZnTe detectors.

Photon energy (keV)	Ge	CdTe	CZT	$\epsilon = 1 - \exp[-\mu t]$ *)
10	99.67	99.81	93.73	100.00
20	90.36	99.57	98.29	100.00
30	95.51	82.34	83.93	100.00
40	97.57	81.93	82.86	100.00
50	98.29	87.15	88.05	100.00
60	98.46	89.53	91.34	99.20
70	98.32	87.70	92.60	-
80	97.76	81.45	91.18	89.40
90	96.32	72.37	86.44	-
100	93.78	62.71	79.43	71.20
110	90.01	53.59	71.28	-
120	85.23	45.54	63.00	-
130	79.68	38.59	55.16	-
140	74.29	32.77	48.09	-
150	68.83	28.01	41.94	36.30

\*) CdTe

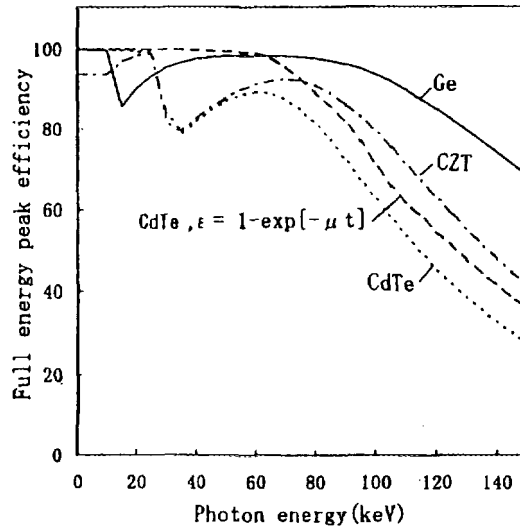


Fig. 2 Full energy peak efficiencies for Ge, CdTe and CdZnTe detectors and calculated efficiency from attenuation coefficient of CdTe detector.

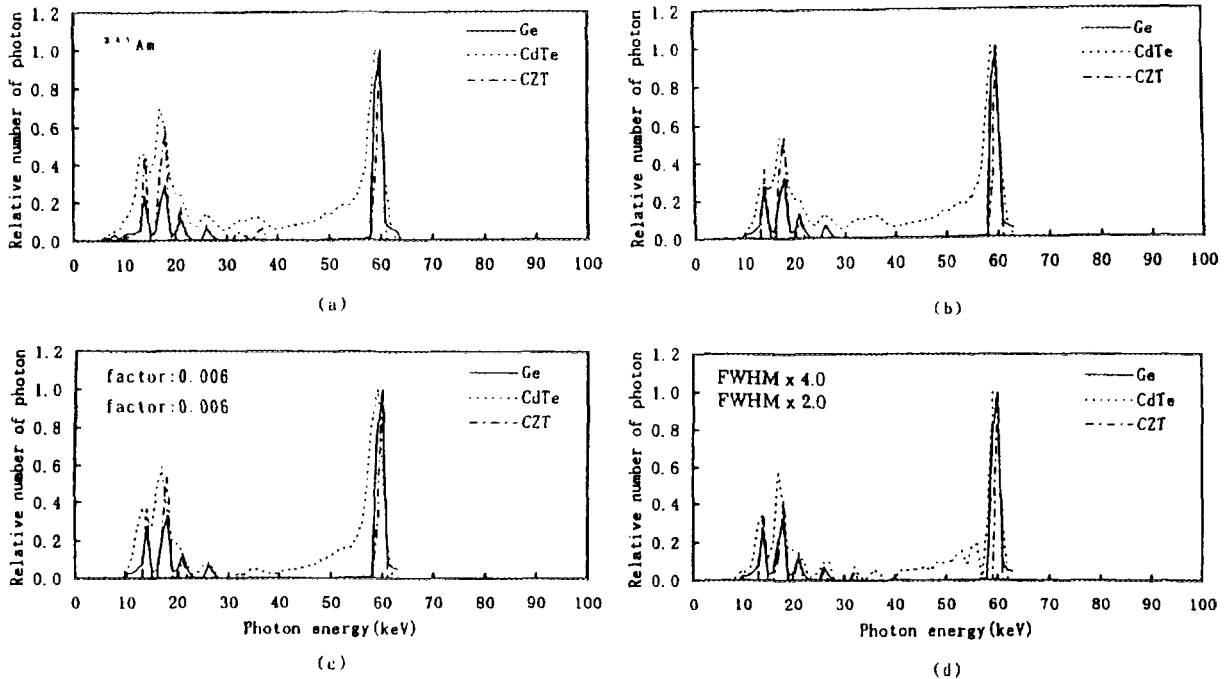


Fig. 3 Comparison of  $\gamma$ -ray spectra of isotope  $^{241}\text{Am}$ . (a) measured, (b) corrected, (c) corrected with added incomplete collection factor 0.006 for CdTe and CdZnTe detectors respectively, (d) corrected with FWHM (full width at half maximum for Ge detector)  $\times 4.0$  for CdTe and FWHM  $\times 2.0$  for CdZnTe detectors respectively.

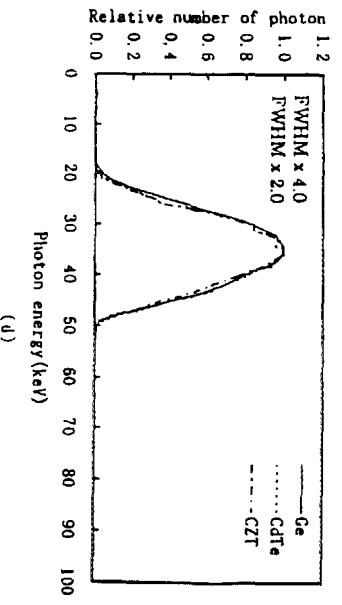
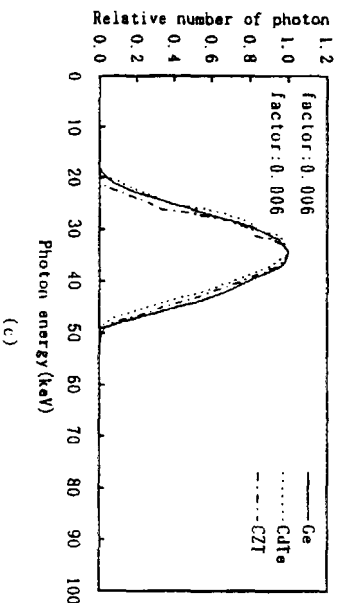
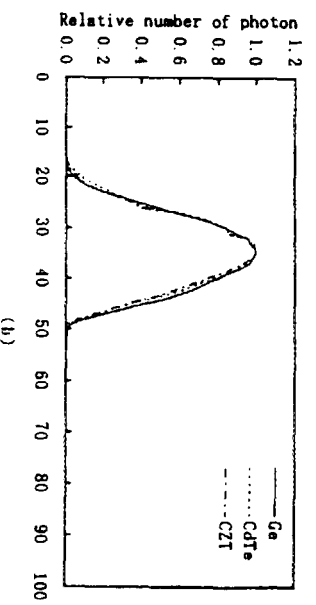
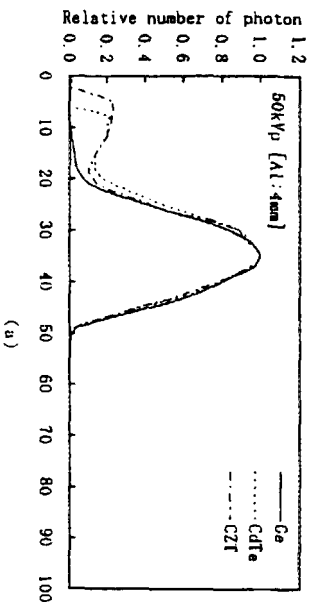


Fig. 4 Comparison of diagnostic x-ray spectra for tube voltage 50kV. The legends of (a), (b), (c) and (d) are the same as shown in Fig. 3

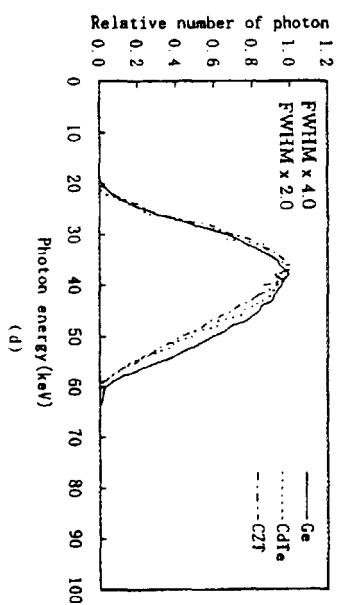
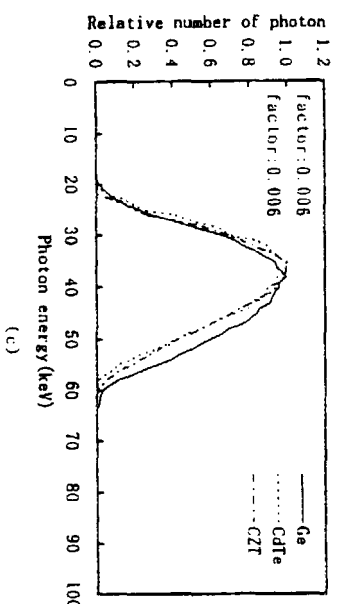
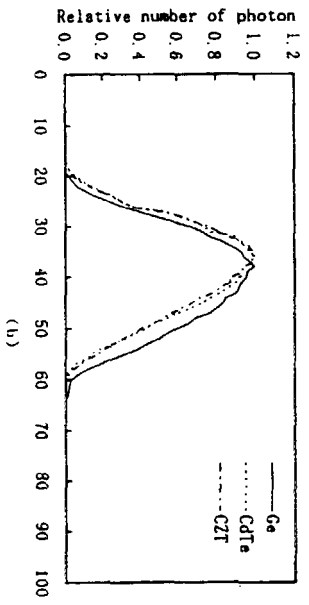
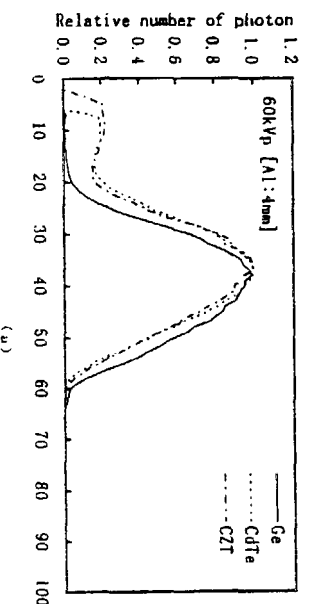


Fig. 5 Comparison of diagnostic x-ray spectra for tube voltage 60kV. The legends of (a), (b), (c) and (d) are the same as shown in Fig. 3

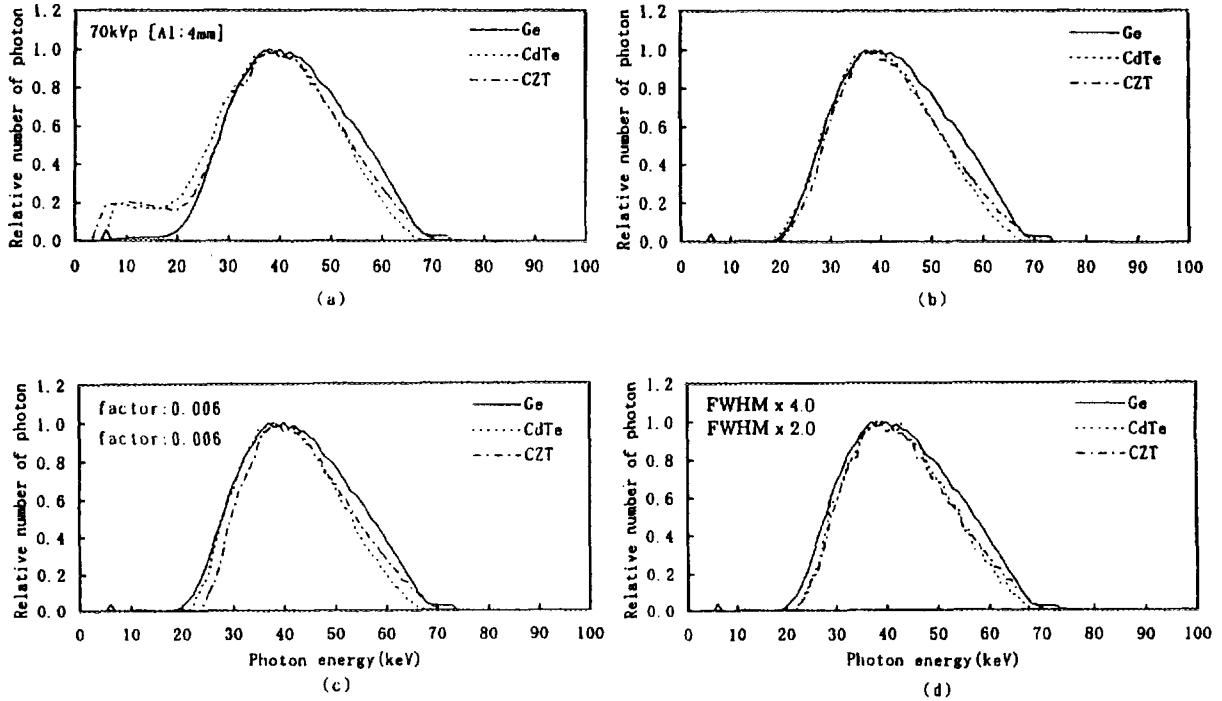


Fig.6 Comparison of diagnostic x-ray spectra for tube voltage 70kV.  
 The legends of (a),(b),(c) and (d) are the same as shown in Fig.3

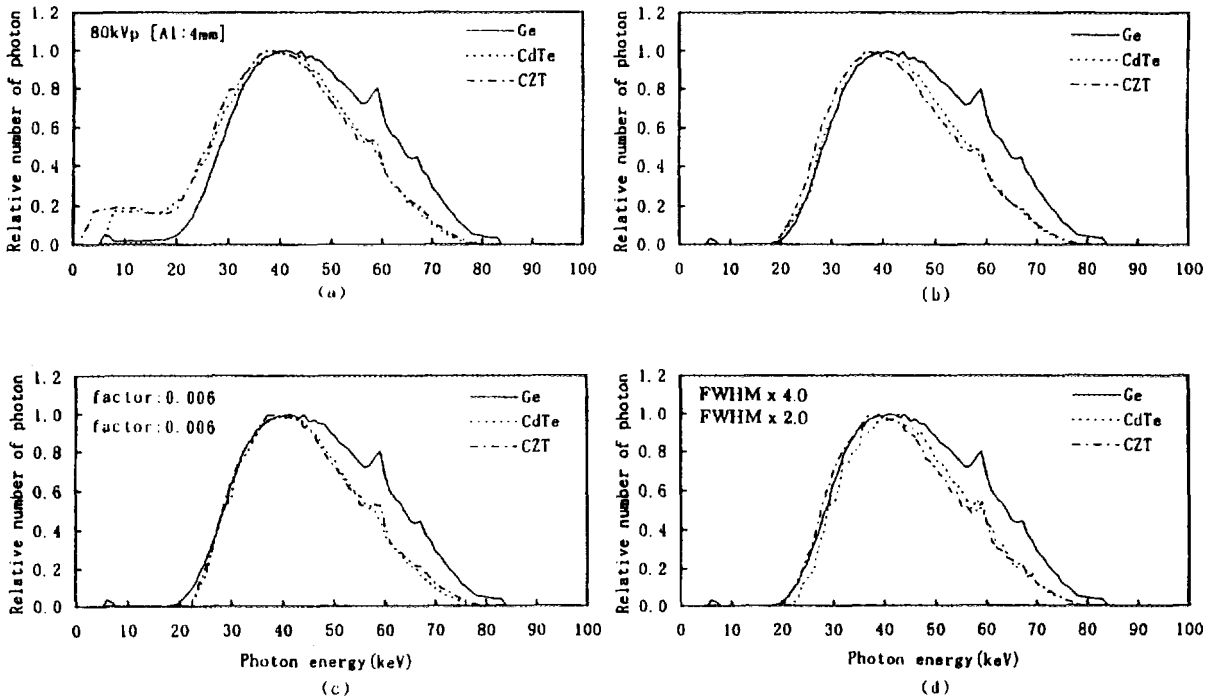


Fig.7 Comparison of diagnostic x-ray spectra for tube voltage 80kV.  
 The legends of (a),(b),(c) and (d) are the same as shown in Fig.3

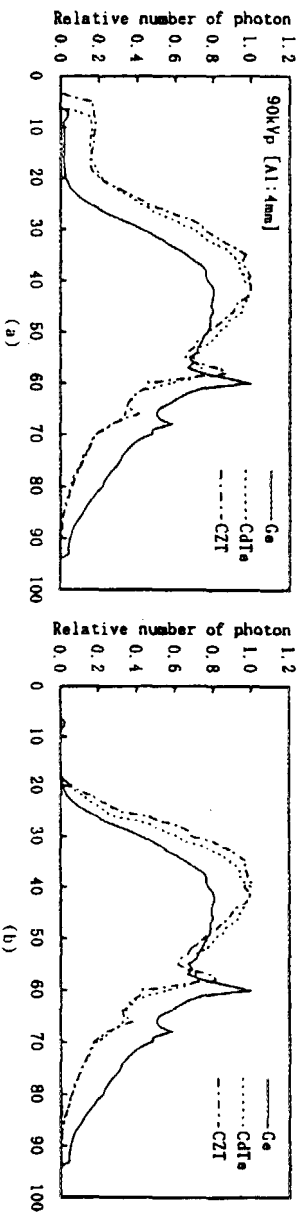


Fig. 8 Comparison of diagnostic x-ray spectra for tube voltage 90kV. The legends of (a), (b), (c) and (d) are the same as shown in Fig. 3

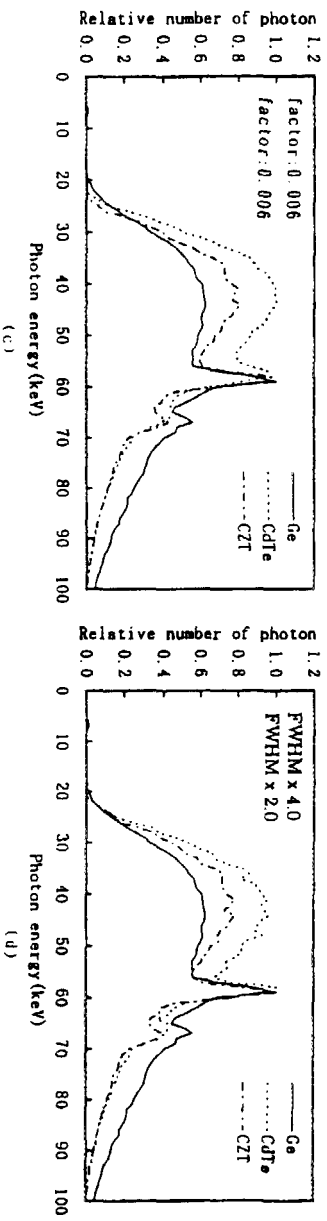
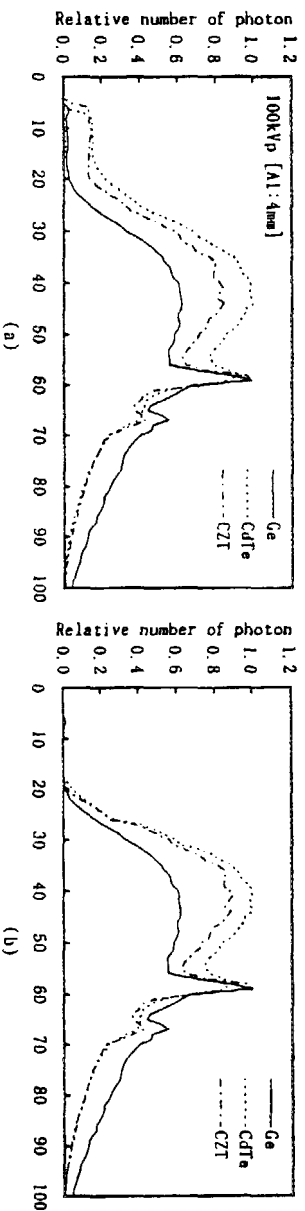
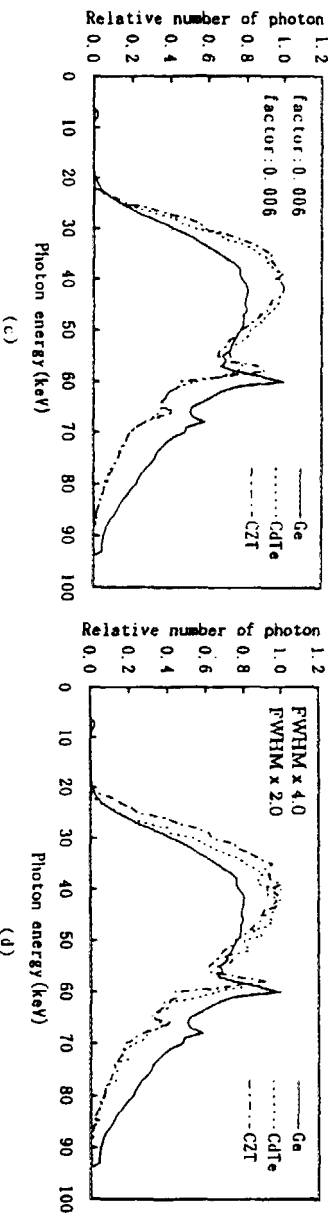


Fig. 9 Comparison of diagnostic x-ray spectra for tube voltage 100kV. The legends of (a), (b), (c) and (d) are the same as shown in Fig. 3

# FABRICATION OF RADIATION DETECTOR USING $\text{PbI}_2$ CRYSTAL

T.Shoji, K.Sakamoto, K.Ohba, T.Suehiro and Y.Hiratate

## 1.INTRODUCTION

Lead iodide ( $\text{PbI}_2$ ) crystal is a promising material for use as a nuclear radiation detector which can be used at the room temperature. It is also possible to fabricate X-ray and low energy  $\gamma$ -ray radiation detectors of small size, because this material has a high atomic number (Pb:82, I:53) and a wide band gap (2.55 eV). The development in technology concerning the  $\text{PbI}_2$  radiation detector has been discussed by Roth [1], Manfredotti [2] and Lund [3]. Recently, Lund [4], Roth[5] and Shoji [6] discussed the  $\text{PbI}_2$  crystal growth method and its characteristics. An accurate value for the carrier mobility in the  $\text{PbI}_2$  crystal, however, has not yet been obtained experimentally. We have reported performances of the  $\text{PbI}_2$  radiation detector fabricated from crystals grown by a zone melting method. In this case, the average energy for the production of electron-hole pair of the  $\text{PbI}_2$  detector has been estimated to be about 8 eV, which is in agreement with the value expected from the formula proposed by Klein.

In this paper, we will discuss the  $\text{PbI}_2$  radiation detector fabricated from a crystal grown by the zone melting method and by the vapor phase method, together with characteristics of the crystal obtained by a XPS analyzer.

## II. EXPERIMENTAL PROCEDURES

$\text{PbI}_2$  powder with nominal purity of 4 nines is used for the single crystal growth. In this experiment, crystals were grown by two different methods i.e., the 50 pass zone melting method (zone melting method), and the vapor phase method.

Fig.1 shows a typical temperature profile of the electric furnace for growing the single crystal in the vapor phase method. In the case of the zone melting method, the experimental set up was almost the same as the one reported in the previous reports [6].

In the fabrication of  $\text{PbI}_2$  radiation detectors, the ingots were cleaved into small pieces of  $2 \times 2 \times 0.3 \sim 0.6 \text{ mm}^3$ . The surfaces of these pieces were not polished mechanically nor etched chemically. The electrodes are formed on both side of the piece by painting the with colloidal graphite (aquadag).

The leakage current of the detector were ranging from  $10^{-9}$  to  $10^{-10}$  A for the bias voltage of 10 V at the room temperature.

The crystal was characterized by a X-ray Photoelectron Spectroscopy (XPS) measurement and response properties by using the  $\alpha$ - and  $\gamma$ -rays. The  $\alpha$  and  $\gamma$ -rays with an energy of 5.48

MeV and 59.5 keV emitted from the  $^{241}\text{Am}$  source impinge on the detector and created electron-hole pairs along the trajectory in the crystal. Electric charges collected on the electrodes were supplied to a charge sensitive preamplifier. The output pulse was amplified and pulse-shaped with an appropriate time constant ranging from 0.5 to 6.0  $\mu\text{s}$ . The output signals were analyzed and stored in a 1024 channel pulse height analyzer.

The characteristics of these crystals were carried out by using an XPS apparatus of PHI-model 5600 which enables precise determination of the photo electron energy. A Mg X-ray anode was operated at an acceleration voltage of 10 keV, emission being about current 40mA. The characteristic X-rays corresponding to Mg-K $\alpha$  has an energy of 1253.6 eV. The XPS measurements were performed in the vacuum chamber evacuated to about  $5 \times 10^{-9}$  Torr and the data from the analyzer were directly stored in SHIMAZU model VX8100 Module computer.

### III. RESULTS AND DISCUSSION

The crystal grown by the vapor phase method is expected to have a higher quality compared with the one produced by the Bridgman growth method or zone melting methods because the vapor phase method has the advantage over growth methods in that no contact with the crucible is required, thus minimizing thermal stresses on the growing crystal.

Fig.2 shows pulse-height spectra for the 5.48 MeV  $\alpha$ -particles impinging on the positive electrode. Fig.2-(a) shows a pulse-height spectrum for a detector fabricated from the crystal grown by the vapor phase method. The  $\alpha$ -peak was not observed, as shown in this figure. On the other hand, fig.2-(b) shows the detector fabricated from a crystal grown by the vapor phase method applied to a material refined by 50 pass zone melting. The  $\alpha$ -peak was clearly observed with an applied detector bias of 10V. When the bias voltage was increased beyond of 10V, the detector broke down, resulting in extra leakage currents. The breakdown voltage of 10V is much smaller than the value expected from the wide band-gap of  $\text{PbI}_2$  crystals at room temperature. This seems to suggest that the optimization of growth conditions such as the growth temperature and the growth rate is highly necessary to obtain crystals of higher quality with the vapor phase method.

Fig.3 shows the variation of 59.5keV  $\gamma$ -ray spectra as a function of the shaping time of the main amplifier for the detector fabricated from a crystal grown by the zone melting method. The photopeak has been gradually improved by increasing the shaping time at the bias voltage of 250V.

A wide-range photoelectron spectrum obtained by XPS analysis is depicted in fig.4 for the  $\text{PbI}_2$  crystal grown by the vapor phase method. Attention should be paid for the peaks corresponding to photoelectrons from  $4f_{5/2}$  and  $4f_{7/2}$  electron shells in the Pb atoms, and also for the peaks corresponding to  $3d_{3/2}$  and  $3d_{5/2}$  shells in iodine atoms. As for the former, there can be seen in fig.5 a marked difference between the energy spectrum obtained for the surface of the crystal and that for the inner part of the crystal. This figure shows the variation of the expanded XPS spectrum in the neighbor of the 4f peaks from Pb as going from the surface layer to the inner layers of the crystal. So far as the crystal surface is concerned, the peak corresponding

to each shell is basically single, while in the spectra obtained for the inner layers of the crystal each peak is split into two peaks with comparable intensities. The binding energy of the  $4f_{7/2}$  electrons is found to be about 140 eV for the single peak at the crystal surface. This value is far removed from the value 136.4 eV of the single Pb atom [7], and closer to the value 138.9 eV for the compounds PbO reported in the literature [8]. Our tentative assumption is, therefore, to attribute this single peak to the formation of PbO on the surface of the  $PbI_2$  crystal. The peak corresponding to the  $4f_{7/2}$  shell splits into two peaks in the interior of the crystal, one located at 141.0 eV and the other at 139.5 eV. The peak separation, 1.5 eV, is nearly in agreement with the binding energy difference 1.8 eV of electrons from Pb in  $PbI_2$  and from Pb. We tentatively assign these as originating from  $PbI_2$  and from Pb atoms coexisting in the interior.

The photoelectron spectra from iodine atoms are displayed in fig.6 for each layer of the  $PbI_2$  crystal. The peak corresponding to the  $3d_{5/2}$  shell or the one corresponding to the  $3d_{3/2}$  shell in iodine atoms is single in every layer of the crystal and the peak shape does not change, contrary to the case of Pb atoms. The binding energy observed is always 621.9 eV. Consequently the iodine atoms seem to exist as  $PbI_2$  in the crystal and excessive  $I_2$  or iodine atoms are apparently not contained.

The above-mentioned phenomena were equally observed both for crystals grown by the vapor phase method and by the zone melting method.

#### IV. SUMMARY

The  $PbI_2$  crystals were grown by two different methods. The  $\alpha$ -peak was not observed by the  $PbI_2$  detectors fabricated from the crystal grown by the vapor phase method. By use of the detector fabricated from the crystal grown by the vapor phase method following 50-pass zone refining, the  $\alpha$ -peak was clearly observed with the applied detector bias voltage of 10 V. The detector fabricated from the sample grown by the 50-pass zone melting method successfully yielded a photopeak for  $^{241}Am$   $\gamma$ -rays (59.5 keV). The shape of the photopeak of  $\gamma$ -rays gradually improved by increasing the shaping time constant at the bias voltage of 250 V. The crystals grown by the two methods (vapor phase method and zone melting method) are characterized and compared by using the XPS analysis. A marked difference was observed for the photoelectron spectrum from Pb atoms in the surface region and those in the interior region. No such difference was observed for photoelectrons from iodine. The difference in XPS characteristics was not observed between two crystal-growth methods.

## REFERENCES

- 1) Roth and W.R.Willing; *Apple. Phys. Letter*, 18 (1971) p.328
- 2) C.Manfredotti, R.Murri, A.Quirini and L.Vasanelli; *IEEE. Tras. Nucl. Sci.* Vol.24 (1977) p.126
- 3) J.C.Lund, K.S.Shah, M.R.Squillante and F.Sinclair; *IEEE. Trans. Nucl. Sci.* Vol.35 (1988) p.89
- 4) J.C.Lund et al: 9th International Workshop on Room temp. Semiconductor X and  $\gamma$ -Ray Detector Conf. (1995)
- 5) V.Deich and M.Roth: 9th International Workshop on Room temp. Semiconductor X and  $\gamma$ -Ray Detector Conf. (1995)
- 6) T.Shoji et al: 9th International Workshop on Room temp. Semiconductor X and  $\gamma$ -Ray Detector Conf. (1995)
- 7) L.Ley, S.P.Kowalozyk, F.R.McFeely, R.A.Pollak, D.A.Shirley; *Phys. Rev.* 138 (1973) p.2392
- 8) K.S.Kim, J.T.O'Leary, N.Winograd; *Anal. Chem.* 45 (1973) p.2214

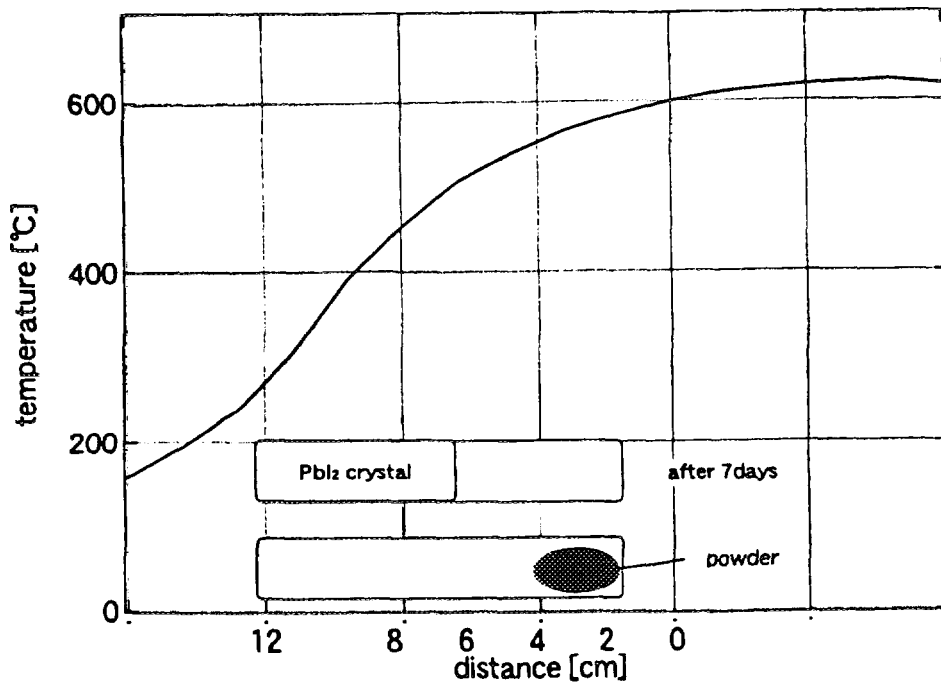


fig.1: A typical temperature profile of electric furnace for growing single crystal in vapor phase method

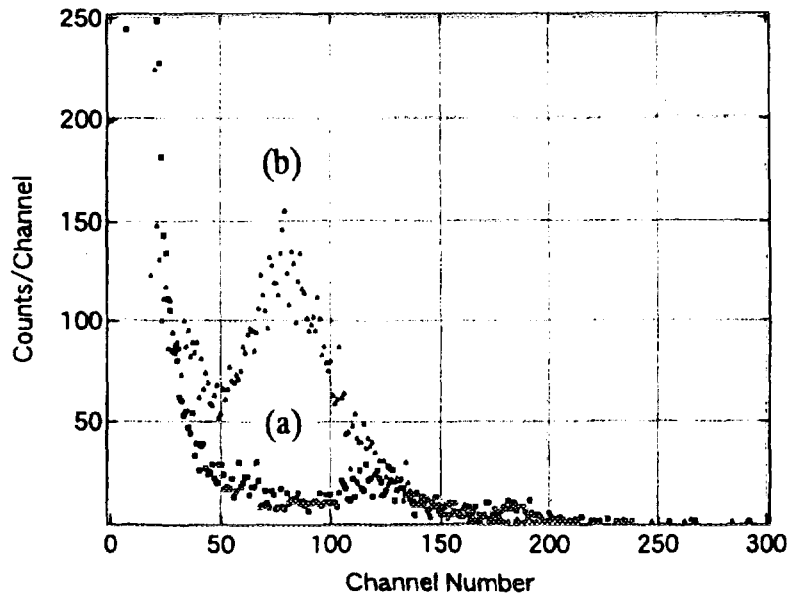


fig.2: The pulse-height spectra for the 5.48 MeV  $\alpha$ -particles.  
 a) For the detector fabricated from crystal grown by the vapor phase method  
 b) For the detector fabricated from crystal grown by the vapor phase after 50 pass zone refining

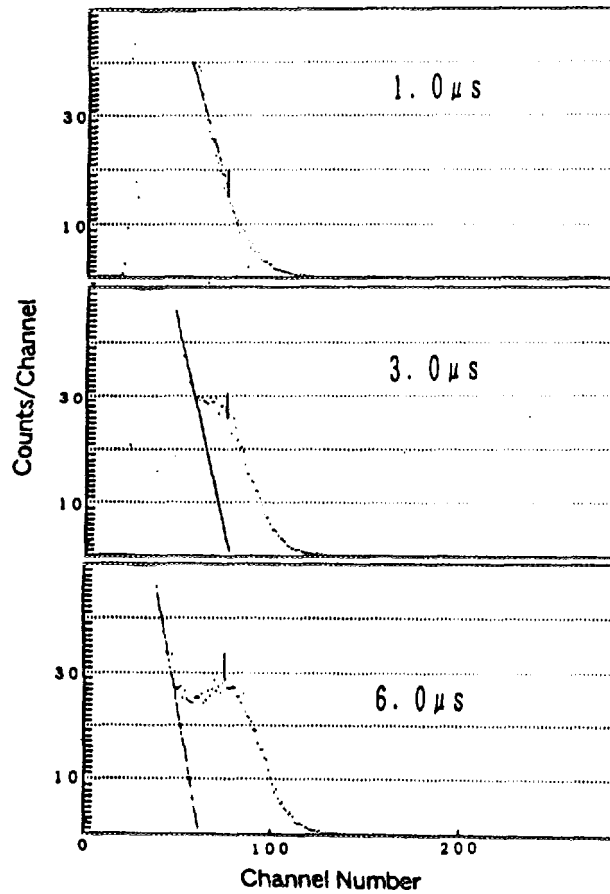


fig.3: The variation of 59.5 keV  $\gamma$ -rays spectra as a function of the shaping time of main amplified system for the  $PbI_2$  detector

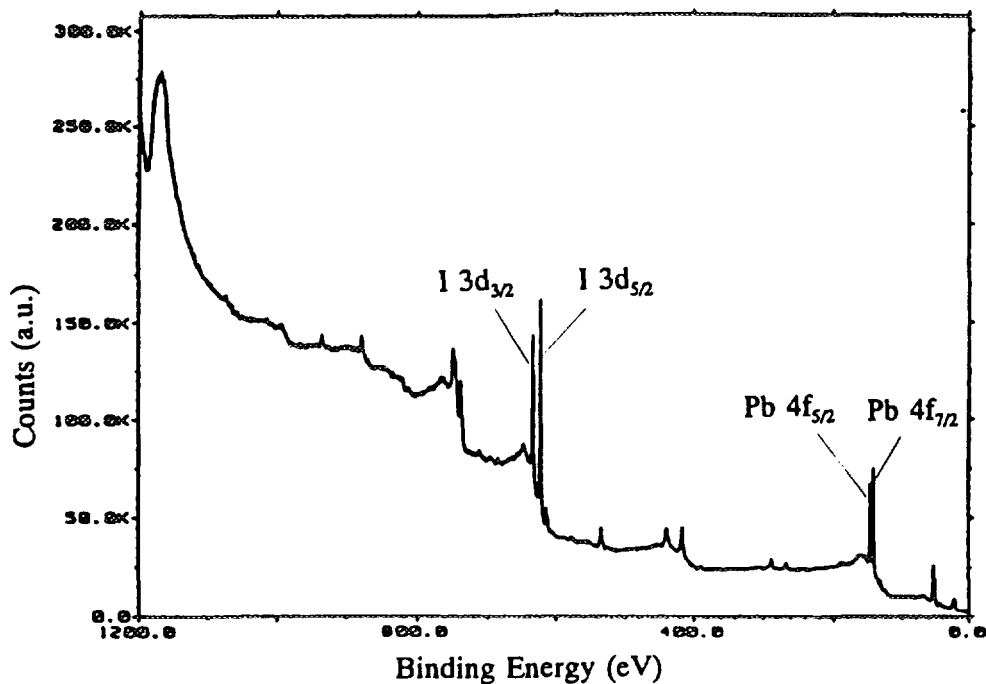


fig.4: A wide-range photoelectron spectrum obtained by XPS analysis for the  $\text{PbI}_2$  crystal

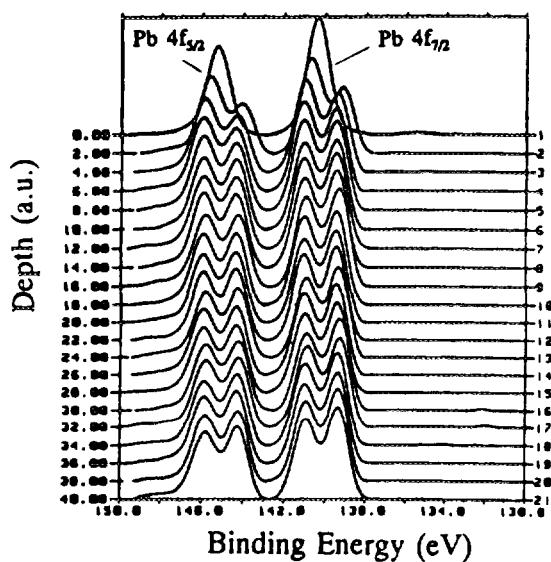


fig.5: The variation of the expanded XPS spectrum in the 4f peaks from lead as going from the surface layer to the inner layer of the  $\text{PbI}_2$  crystal

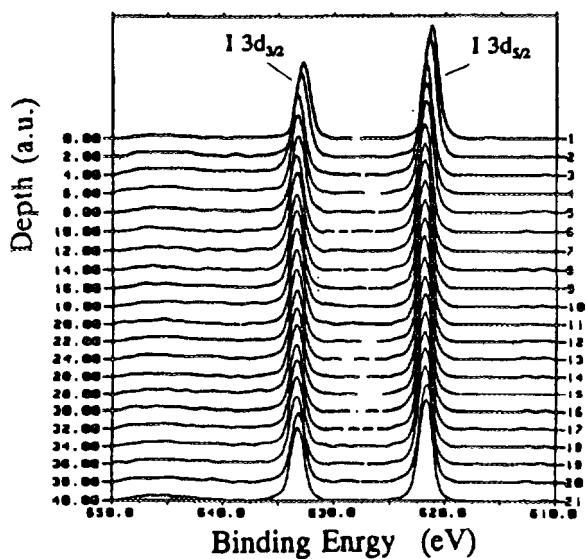


fig.6: The variation of the expanded XPS spectrum in the 3d peaks from iodine as going from the surface layer to the inner layer of the  $\text{PbI}_2$  crystal

# IMPROVEMENT OF THE SENSITIVITY OF CdTe DETECTORS IN THE HIGH ENERGY REGIONS

Hiroshi NISHIZAWA, Kazunori IKEGAMI, Kazuo TAKASHIMA and Teruo USAMI  
Mitsubishi Electric Corporation  
8-1-1, Tsukaguchi-Honmachi, Amagasaki, Hyogo 661, Japan

Takayoshi YAMAMOTO  
Radioisotope Research Center, Osaka University  
2-4, Yamadaoka, Suita, Osaka 565, Japan

## 1. INTRODUCTION

Cadmium Telluride, CdTe, semiconductor detectors have sufficient band gap energy (1.47eV) to use at room temperature, and their atomic number are so large (48 and 52) that their photon detection efficiency is more excellent than that of Si or Ge. Recently CdTe crystals have become easily available because of improvement in the crystal growth method<sup>(1)</sup> and novel CdZnTe detectors whose thicknesses are a few centimeters have been developed. However, the CdTe detector has disadvantages in that the mobility of charge carriers in CdTe is much smaller than in Si and Ge and it is difficult to produce a large volume element. When the incident photon energy is less than a few hundred keV, the CdTe detector has good energy resolution and high efficiency of the full energy peak because the photon interaction occurs so near to the detector surface that the charge collection efficiency is high. When the incident photon energy is over a few hundred keV and the photon interaction occurs at random locations in the detector, the charge collection efficiency becomes low because of hole trapping phenomena. Therefore the efficiency of the full energy peak becomes much worse, and it is very difficult to distinguish the full energy peak above 1 MeV.

In order to improve the efficiency of the full energy peak in the high energy regions, we had previously suggested a multi-layered structure of CdTe elements and have since confirmed the sensitivity improvement of the full energy peak<sup>(2)</sup>. And furthermore, we have suggested a new type structure of multi-layered elements in this paper and we confirmed that the efficiency of the full energy peak became higher and that more proper energy spectra were obtained by our current experiment than by the detector with the conventional structure.

This paper describes a simulation and experiment to improve the efficiency of the full energy peak and to obtain the more proper energy spectra of <sup>137</sup>Cs (662keV) and <sup>60</sup>Co (1.17 and 1.33MeV) using the new structure of CdTe detector.

## 2. METHOD OF SENSITIVITY IMPROVEMENT

It is common to increase the detector volume in order to improve the efficiency of the full energy peak in the high energy regions. However, the charge carrier mobility of CdTe, particularly in holes, is much smaller than that of Si and Ge<sup>(1), (3)</sup>. When the detector volume is too large, most holes drifting in the CdTe detector are trapped at trapping centers, for example lattice defects, and their mean free path is shorter than the thickness of the detector. Therefore most of the holes can not reach the collecting electrode and hence all the energy deposited in the detector by photon interaction does not contribute to the output pulse height.

The mean free path  $\lambda$  of charge carriers, that is electrons and holes, in semiconductor detectors is estimated as

$$\lambda = \mu \tau F \tag{1}$$

where  $\mu$ ,  $\tau$  and  $F$  are the mobility, the mean lifetime and the electric field respectively. For example, the typical values of mobility-lifetime products  $\mu\tau$  for hole is  $5 \times 10^{-5} \text{ cm}^2/\text{V}$ . When the electric field  $F$  is 500 V/cm, the mean free path  $\lambda$  of holes in the CdTe detector can be estimated to be 0.25 mm. Because the thickness of the typical CdTe detector is 1 or 2 mm, the thickness of the detector is longer than the mean free path of holes and most holes drifting in the CdTe detector are trapped and can not reach the collecting electrode. The output pulse height is proportional to the collected charge on the electrodes and the collected charge depends on the sum of the drifting distances of the electron and hole. Figure 1-1 shows the average collected charge dependent on the interaction position, where  $q_0$ ,  $x$  and  $d$  are the amount of created charge, the distance from the collection electrode and the detector thickness, respectively. When the distance from the collected electrode is longer than  $\lambda$ , the collected charge decreases because of the charge carrier trapping, especially hole trapping, in the CdTe detector.

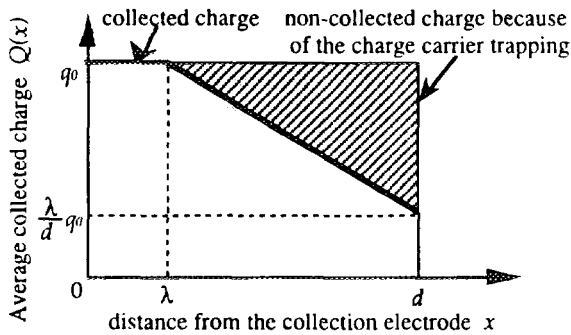


Fig. 1-1 Average collected charge of the conventional one element detector.

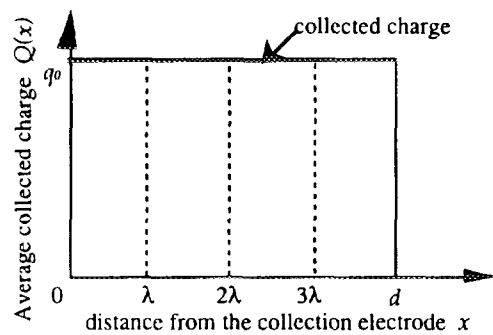


Fig. 1-2 Average collected charge of the layered element detector.

In order to collect most of charge carriers, it is necessary for the thickness of detector elements to be as thin as the mean free path of holes so that the holes are not trapped in the CdTe detector. So we propose that plural elements which are as thin as the mean free path of holes be layered in order to satisfy both the large detector volume and high charge collection efficiency. By means of the multi-layered structure, the collected charge will be sufficient as shown in Fig. 1-2 and the detector volume can be increased. Therefore the output pulse from each element will be superimposed by connecting them in parallel as shown in Fig. 2-A. By this method only one amplifier is needed, therefore minimizing the cost to improve sensitivity.

In order to improve the performance of the multi-layered detector, new layering methods have been proposed as shown in Fig. 2-B and C. In the case of A, each CdTe element is layered simply as we have previously suggested. New type structures of multi-layered elements are described as below. The CdTe elements layered with each other are wired so that the polarities of electric fields imposed on the elements alternately change between positive and negative polarities as in the case of B. An improvement of the energy resolution can be expected since no electric fields are formed between the elements and the total electric capacitance of the detector becomes small. Besides, because the electric field between elements are removed, insulation between the elements becomes easy and space between elements can be even smaller. Furthermore, in the case of C, the collecting electrodes are put between elements layered on top of each other and the electrodes are respectively wired so that the electric potential imposed on the electrodes is alternately changed between positive and negative voltages. Therefore no non-sensitive regions between elements exist completely because of no spaces between elements and, consequently, the sensitivity in the high energy regions is further enhanced. Besides, whereas single detector elements are thin and fragile, elements layered on top of each other through some electrodes have enlarged mechanical strength and as a whole are not fragile.

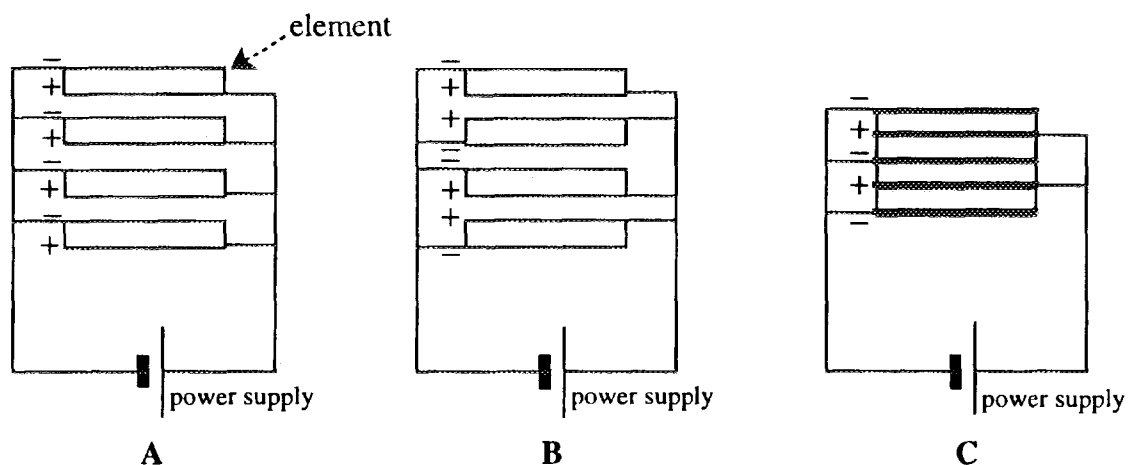


Fig. 2. Multi-layered CdTe detector.

### 3. SIMULATION

#### 3.1 Calculation of Response Function

The response function of the CdTe detector was predicted by simulation using the Monte-Carlo calculation code, EGS4 (Electron Gamma Shower Version 4)<sup>(4)</sup> to evaluate the degree of sensitivity improvement. It is common to calculate the amount of energy absorption in the detector when the response function of the detector is simulated. Although EGS4 can calculate the energy absorption, it has been considered that the charge carrier trapping and response function of a semiconductor detector whose charge carriers have been trapped can not be simulated. If the charge carriers drifting in the semiconductor detector are trapped and can not reach the collecting electrode, the output pulse height is dependent on the sum of the drifting distance of the charge carriers. In this simulation the charge carrier trapping in the CdTe detector had to be considered as follows.

In the case of planar type detector, the collected charge  $Q(t)$  on the electrode is presented as<sup>(5)</sup>

$$Q(t) = \frac{q_0}{d} \left[ \text{drifting distance of electron} + \text{drifting distance of hole} \right] \quad (2)$$

where  $d$  is the thickness of the detector, and  $t$  is the time from creation of charge carriers  $q_0$  by photon interaction. In Fig. 3, the charge carriers are created at the interaction position and the distance from this point to the cathode is indicated by  $x$ .

If the mean free path of electron and hole are  $\lambda_e$  and  $\lambda_h$  respectively, there are four cases of the average collected charge  $Q(x)$ , and  $Q(x)$  becomes the function of  $x$ .

[1] In the case of  $\lambda_e > d$  and  $\lambda_h > d$ ,

$$Q(x) = q_0 \quad (3)$$

[2] In the case of  $\lambda_e > d$  and  $\lambda_h < d$ ,

$$Q(x) = q_0 \left[ \frac{d-x}{d} + \frac{\lambda_h}{d} \right] \quad (4)$$

[3] In the case of  $\lambda_e < d$  and  $\lambda_h > d$ ,

$$Q(x) = q_0 \left[ \frac{\lambda_e}{d} + \frac{x}{d} \right] \quad (5)$$

[4] In the case of  $\lambda_e < d$  and  $\lambda_h < d$ ,

$$Q(x) = q_0 \left[ \frac{\lambda_e}{d} + \frac{\lambda_h}{d} \right] \quad (6)$$

The energy deposition in the CdTe detector calculated by EGS4 was multiplied by the weight functions, which are defined in the brackets of equations (3) to (6). Therefore, except for the case [1], the energy multiplied by the weight function is less than the energy when the charge carrier trapping is not considered. In this way, response function can be simulated considering the charge carrier trapping in the CdTe detector. The simulated results of  $^{137}\text{Cs}$  and  $^{60}\text{Co}$  using this model of the one element CdTe detector whose size is  $2 \times 2 \times 2 \text{ mm}^3$  are shown in Fig. 4-1 and 4-2, respectively. The simulated results concurred well with the experimental results and indicate that the simulation model was correct.

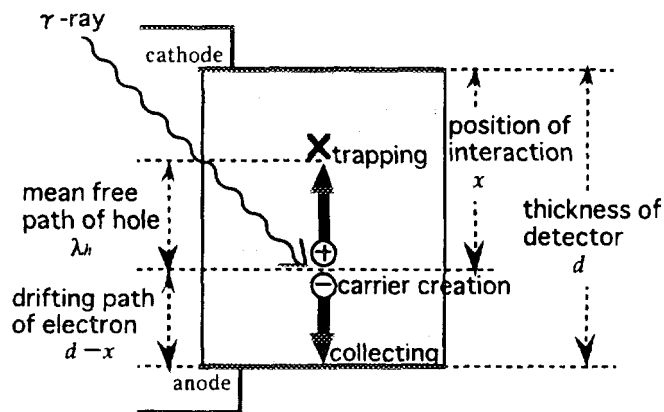


Fig. 3. Simulation model considering the carrier trapping in the semiconductor detector

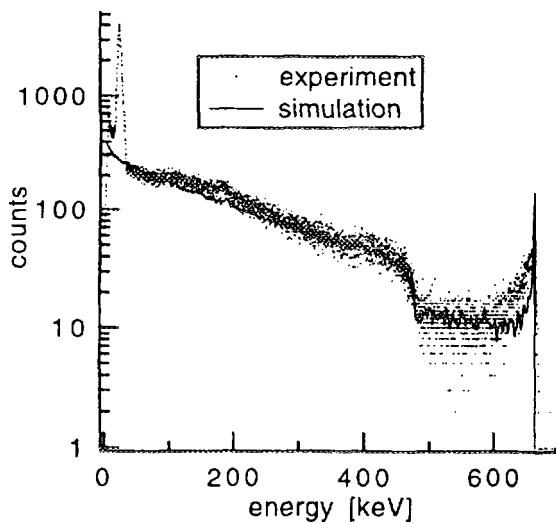


Fig. 4-1 Simulation result compared with experiment. ( $^{137}\text{Cs}$ )

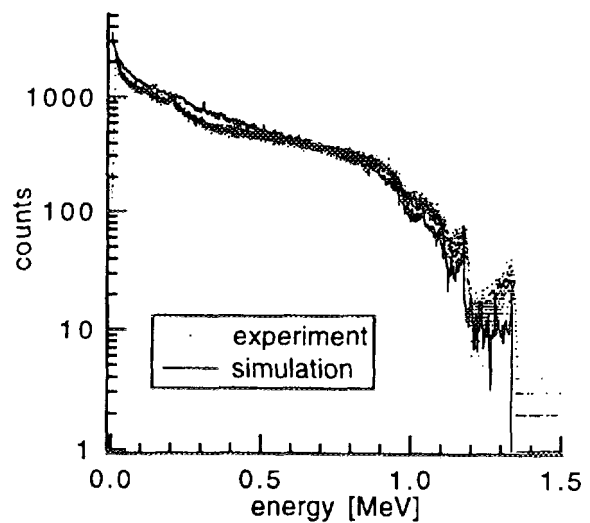


Fig. 4-2 Simulation result compared with experiment. ( $^{60}\text{Co}$ )

### 3.2 Prediction of the Sensitivity Improvement

By using this model, we predicted the energy spectrum and the degree of sensitivity improvement of a multi-layered CdTe detector whose layered type is as shown in Fig.1-C. Figure 5-1 is the result of the one element CdTe detector whose size is  $2 \times 2 \times 2 \text{mm}^3$  shown here for comparison. The assumed detector of this simulation was the 4 layered CdTe detector whose each element size was  $2 \times 2 \times 0.5 \text{mm}^3$  and whole detector size was  $2 \times 2 \times 2 \text{mm}^3$ . Figure 5-2 shows the simulated result of the 4 layered detector in the case of 662 keV incident photon energy. It was predicted that the efficiency of the full energy peak at 662 keV of the 4 layered detector would be about 3.6 times that of the one element detector and that the Compton edge would be clearer. And the simulated result in the case of perfect charge collection is shown in Fig. 5-3. In this case, it was predicted that the full energy peak at 662 keV would be about 15 times that of the one element detector, which indicated that high charge collection efficiency would be indispensable for improving the energy spectrum in the high energy region.

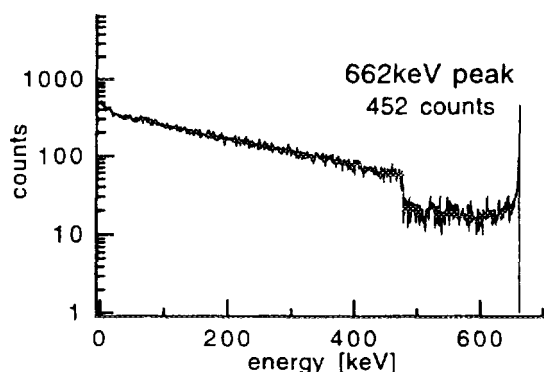


Fig. 5-1 Simulated result of the one element detector.

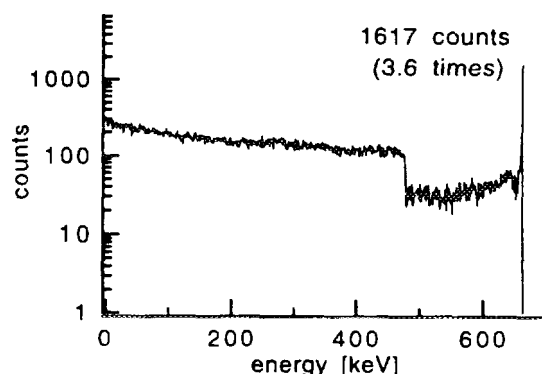


Fig. 5-2 Simulated result of the 4 layered layered detector.

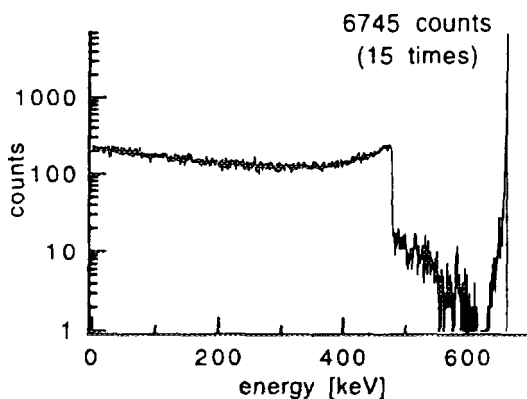


Fig. 5-3 Simulated result of the 4 layered detector in the case of the perfect charge collection.

## 4. EXPERIMENT

The structure type of the 4 layered CdTe detector in the present experiment is the type shown in Fig. 1-C. The whole size was  $2 \times 2 \times 2 \text{ mm}^3$ , and the size of each element was  $2 \times 2 \times 0.5 \text{ mm}^3$ . Figure 6 shows a block diagram of the present experiment. This system was the same as the normal measurement of the energy spectrum except that the practical voltage between electrodes of the CdTe elements was also measured. About 25 minutes was needed to fix the measured voltage of the 4 layered CdTe detector as shown in Fig. 7. Therefore the practical voltage between electrodes of the CdTe elements was measured at 25 minutes after the bias power supply had been turned on. Figure 8 shows the relation between the voltage of the bias power supply and the practical voltage, comparing the 4 layered detector with the one element detector whose size is  $2 \times 2 \times 2 \text{ mm}^3$ . The practical voltage of the 4 layered detector rose to only 65 V when the voltage of the bias power supply was 100 V, where the practical voltage of the one element detector rose to 94 V.

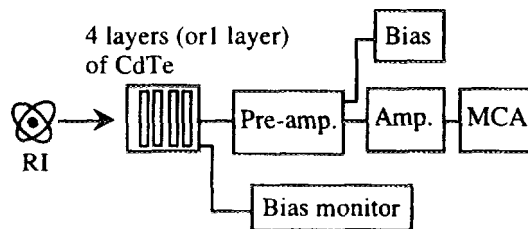


Fig. 6 A block diagram of the experiment.

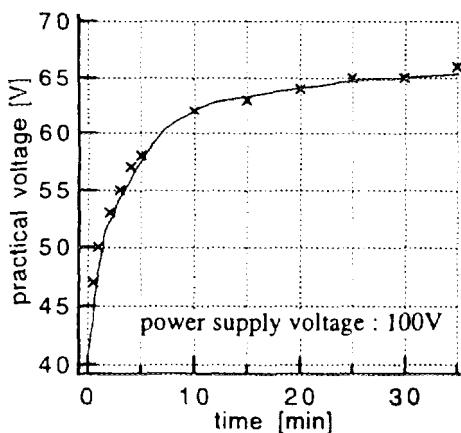


Fig. 7 The practical voltage between electrodes of the 4 layered CdTe detector dependent on time.

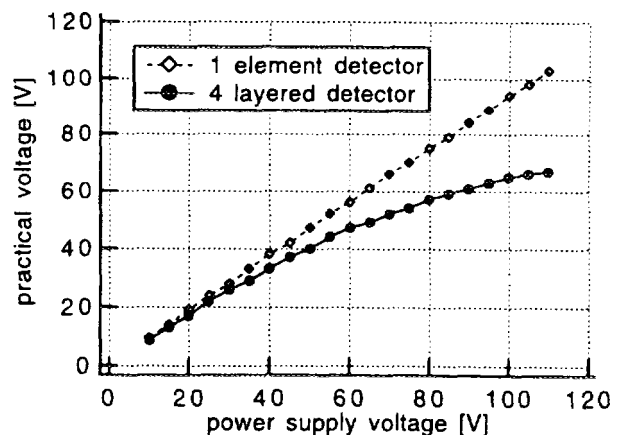


Fig. 8 The voltage of bias power supply and the practical voltage between electrodes of detectors.

In this experiment, the energy spectrum measured by the 4 layered CdTe detector was compared with that of the one element CdTe detector having the same whole size,  $2 \times 2 \times 2 \text{mm}^3$ . The experimental conditions of both the detectors were the same and their details are shown in Table 1. The practical voltage between electrodes of the CdTe elements are different from each other, although the bias power supply voltage of both detectors are 100 V. The energy axis was calibrated by using the check source of  $^{137}\text{Cs}$  and  $^{60}\text{Co}$ .

Table 1. Experimental Condition

$\gamma$ -ray source	$^{137}\text{Cs}$ (3.29MBq), $^{60}\text{Co}$ (2.70MBq)
detector size	one element detector : $2 \times 2 \times 2 \text{mm}^3$ 4 layered detector : $2 \times 2 \times 2 \text{mm}^3$ (four $2 \times 2 \times 0.5 \text{mm}^3$ )
measuring time	3600 sec
shaping time of amplifier	2 $\mu\text{sec}$
power supply voltage	100V
voltage between electrodes	one element detector : 94V 4 layered detector : 65V

## 5. RESULT AND DISCUSSION

The energy spectra of  $^{137}\text{Cs}$  were obtained by the one element detector and the 4 layered detector as shown in Fig. 9-1 and 9-2, respectively. These figures show obviously that the intrinsic peak efficiency of 662 keV of the 4 layered detector was about 3.3 times that of the one element detector in spite of the same detector volume. The part of tail at the energy region under the 662 keV peak decreased relatively. The Compton edge at 477keV and the back scattering peak at about 200 keV appeared more clearly than in the case of the one element detector. Consequently, the detector performance was improved as indicated by the high efficiency of the full energy peak and the proper shape of the Compton continuum.

The energy spectra of  $^{60}\text{Co}$  were also obtained as shown in Fig. 10-1 and 10-2. There were few counts of the full energy peak at 1.33 MeV measured by the one element detector as shown in Fig. 10-1. On the other hand, a 1.33 MeV peak measured by the 4 layered detector was distinguished. The Compton continuum was more even and the energy spectrum of  $^{60}\text{Co}$  was improved. These results indicate that the full energy peak efficiency in the high energy regions becomes high in spite of the same detector volume

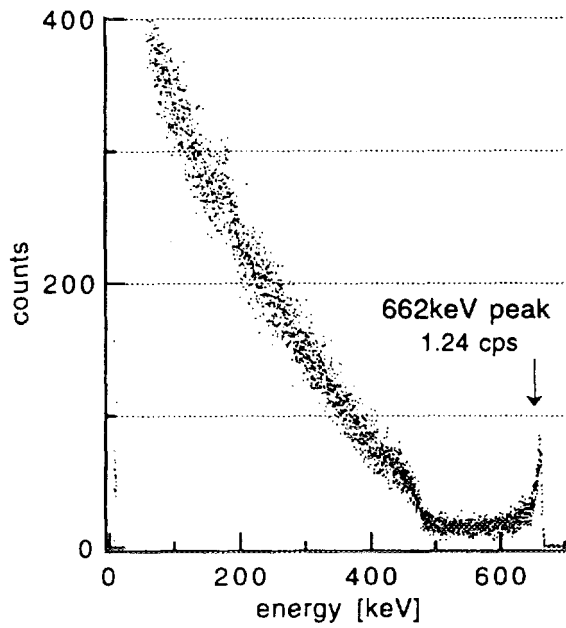


Fig. 9-1 The experimental result by the one element detector ( $^{137}\text{Cs}$ ).

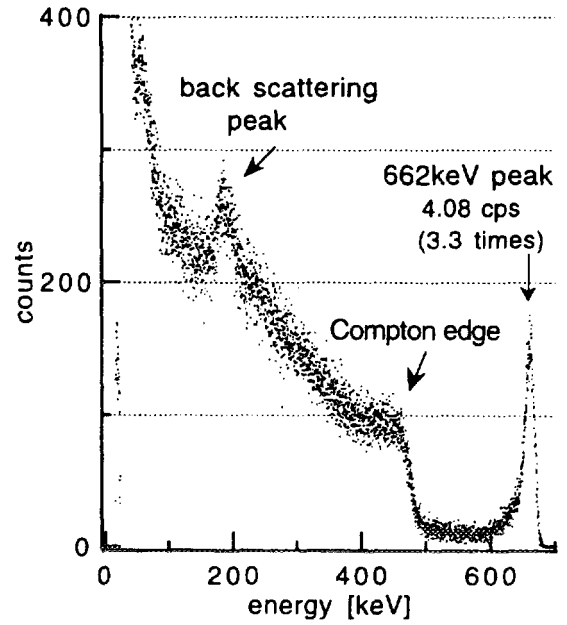


Fig. 9-2 The experimental result by the 4 layered detector ( $^{137}\text{Cs}$ ).

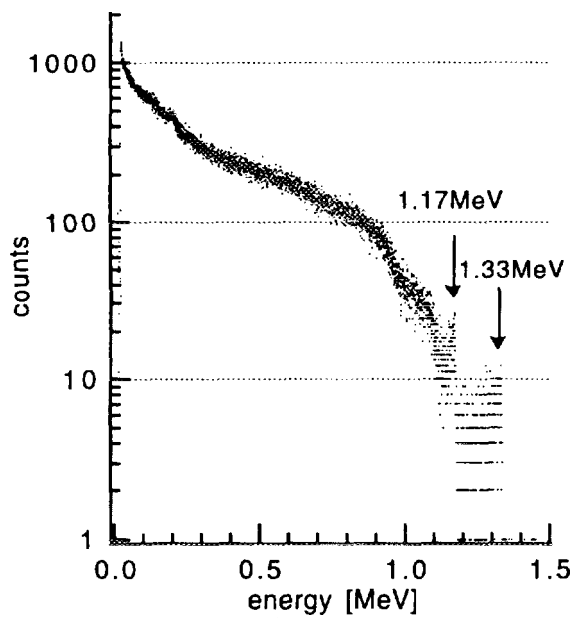


Fig. 10-1 The experimental result by the one element detector ( $^{60}\text{Co}$ ).

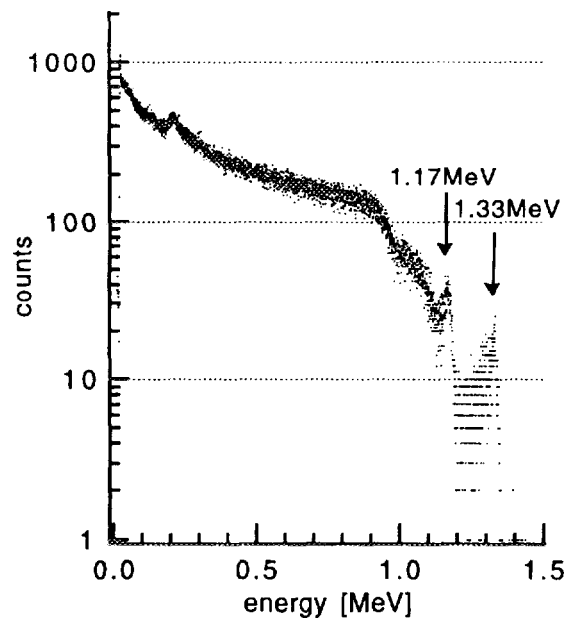


Fig. 10-2 The experimental result by the 4 layered detector ( $^{60}\text{Co}$ ).

and the energy spectrum can be improved by means of the multi-layered structure of detector elements.

The improvement degree of the full energy peak efficiency at 662 keV by this experiment agreed well with the simulated result. Since in the simulation the improvement degree in the case of perfect charge collection was predicted to be 15 times that of the one element detector as mentioned above, this experimental result predicted that the charge collection was not perfect yet. In order to improve the sensitivity in the high energy regions still more, the higher charge collection efficiency is indispensable. It is thought that the thinner elements should be used and the semiconductor whose carrier mobility is larger should be used.

## 6. CONCLUSION

A new type structure of multi-layered elements has been proposed in order to improve the sensitivity of CdTe detectors in the high energy regions. The response function of a semiconductor detector whose charge carrier mobility is as small as CdTe could be simulated, and the degree of sensitivity improvement in the high energy regions could be predicted by using this model. The experimental result indicates that the full energy peak efficiency in the high energy regions can become high in spite of the same detector volume and the energy spectrum can be improved by means of the multi-layered structure of detector elements.

## References

1. Y.Iwase, R.Ohno, et al., Mat. Res. Soc. Symp. Proc. Vol.302, 225-230 (1993)
2. K.Ikegami, H.Nishizawa, et al., 11th Int. Conf. on SSD, Budapest, Hungary (1995)
3. R.O.Bell and F.V.Wald, IEEE Trans. on Nucl. Sci. Vol.NS-22, 241-245 (1975)
4. W.R.Nelson, H.Hirayama and D.W.O.Rogers, The EGS4 Code System, SLAC-265 (1985)
5. G.F.Noll, Radiation Detection and Measurement Second Edition, The Nikkan Kougyou Sinbun Ltd. pp.430-434 (1991) [in Japanese]

# **DISCRIMINATION OF THE WALL EFFECT IN A THIN COUNTER WITH MICRO-GAP STRUCTURE FOR NEUTRON POSITION SENSING**

Takeji SAKAE, Tohru MANABE, Yasunori KITAMURA, Akihiro NOHTOMI  
*Kyushu Univ. Fukuoka 812, Japan*

and Sigeyasu SAKAMOTO  
*Tokai Univ., Kanagawa, Japan*

## **Abstract:**

Simulation by the Monte Carlo method is applied to estimate the wall effect in a thermal neutron counter having a new function for discriminating the effect. The counter is designed to have paralleled electrodes with micro-gap structure. A resistive anode is used for position sensing on the center of a set of the three electrode. The structure can be made by simple arrangement of anode and cathode wires on an insulator plane. The calculation shows discrimination of the wall effect can be achieved by coincident counting of two or three elements included in the counter. By using the coincident counting, the thickness of the neutron counter can be made into 1 mm with the information of the total energy created in the neutron detection.

## **1. INTRODUCTION**

Measurements of a neutron flux distribution are performed effectively under the condition with no modification of the field medium and no perturbation of the flux by the existence of the sensor. The accuracy and the quickness of the measurements are also important for the reactor physics experiments and the subcriticality monitoring. In order to advance the measuring method, a long and slender neutron counter for position sensing was recently studied by Uritani et al.<sup>1)</sup>. This type of neutron counter is suitable for quick and rough measurements of neutron flux distributions. In the measurements by using a position sensitive counter with a small-size cross section, one of the unavoidable problems is the wall effect on the pulse height distribution of the counter signal. By decreasing the counter diameter to suppress the perturbation of the neutron field, the wall effect is made to a strict problem. In order to realize a slender counter with sufficient performance, the discrimination of pulses changed by the wall effect is needed as a function of the counter.

Micro structure for a particle tracking counter system has been investigated recently, because of good space resolution, good time resolution and high rate capability

2,3, for example). If the wall effect in the neutron counter is controlled, the structure should be useful for a slender neutron counter.

In this work, an idea of the structure that realizes a thin neutron counter is proposed. The counter has a function to discriminate the wall effect by using a coincident counting technique. The discrimination of the wall effect in the counter is estimated by a simulation using the Monte Carlo method.

## 2. MICRO-GAP STRUCTURE AND WALL EFFECT DISCRIMINATION

The micro gap for a gas-filled counter is made of micrometrical structures of insulators and conductors. The structure realized by the techniques for the production of semiconductor devices (photo lithograph), chemical etching, micro printing, micro painting and micro machining. The gas discharges on the gap bring us the information of energy, incident position and counting rate about the radiation that triggers the discharge. By using a resistive electrode in the structure, a position sensitive counter which has a very small cross section can be made as shown in Figure 1(a) schematically. As the first step of investigating this type of neutron counter, a simple structure is adopted to make a discharge gap in the counter. This is not depending on the sophisticated techniques described above. The schematic cross section view of the counter is shown in Figure 1(b).

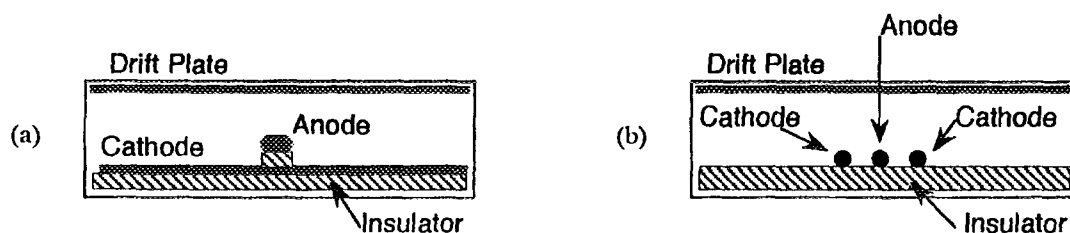


**Figure 1.** Schematic view of the micro-gap structure.

In this counter, wire electrodes which work as anode and cathode are fixed on an insulator plate. Discharge gaps which measure less than 1 mm are made on the surface of the insulator. Two cathode wires and one resistive anode wire make an element that works as a position sensitive counter. This arrangement of the electrodes is derived from the original structure shown in Figure 1(a), through some changes and modifications of the arrangement. The field near the insulator in the new arrangement should not be steep in comparison with the original one because of the curved surface of wires.

A typical case of the wall effect is shown in Figure 2(a). In this case, a part of energy carried by the proton vanishes in the wall. The charge signal is coming from only the central element of the counter. The discrimination of the wall effect is achieved by a coincident count for plural counters. The coincidence means that the particles (proton

and triton for  $^3\text{He}$  gas) go through two or three elements without wall incidence. The situation in which we can get the coincidence of three elements is shown in Figure 2(b). The total charge produced by the particles is obtained by summation of the signals from the elements at the same time.

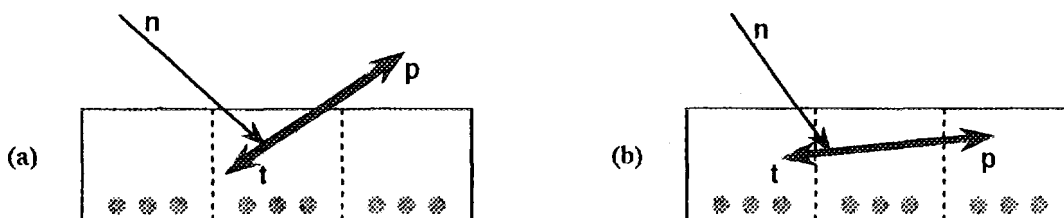


**Figure 2.** Typical cases of the neutron detection with and without the wall effect.

The detection without the wall effect can be picked up by using detectors paralleled each other. The counter should be made of paralleled elements for neutron detection. The expected characteristics of the counter are followings.

- (i) In a neutron field assembled by using plane elements, the thin cross section of the counter is useful for setting. The accurate measurement of neutron flux distribution without perturbation of the field can be achieved.
- (ii) Because of using the wire electrodes, the uniformity of the field for discharges is easily achieved. And the resistive electrode can be introduced easily.
- (iii) The information of the direction of the particle emission for the neutron reaction can be obtained by the parallel arrangement of the counter elements. The spectrum without the wall effect should have more discriminating power to the continuum of  $\gamma$  background counting. In this discrimination, the counting efficiency is wasted.
- (iv) The density of energy loss along the track of the particles will give us the information of the correct position of the reaction. The counter with very high position resolution can be realized by progressing this method.

### 3. SIMULATION OF THE WALL EFFECT

Numerical calculations are applied in order to investigate the function of the neutron counter. As the counter gas, a gas mixture contains  $\text{CF}_4$  and a small amount of  $^3\text{He}$  is assumed for the simulation. The particles emitted by (n, p) reaction are tracked numerically from the reaction to stopping of the particles. The data of stopping power for proton and triton are used in the calculation. The pressure of the mixture is assumed to be atmospheric. The detector is divided in three regions on the cross section plane as shown in Figure 3. Energy losses in each region are calculated separately in the numerical tracking of the particles. The equipotential lines for an element in the counter

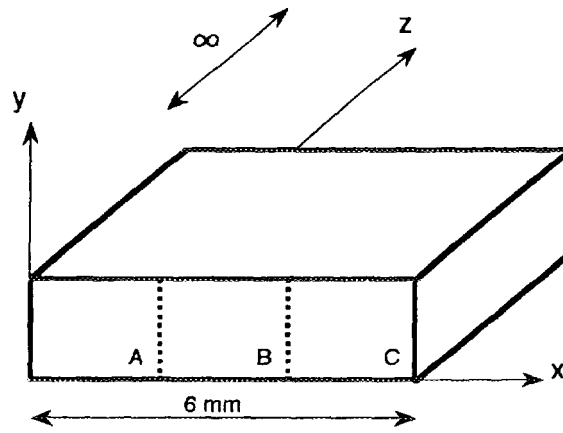


**Figure 3.** Geometrical boundary conditions for the simulation.

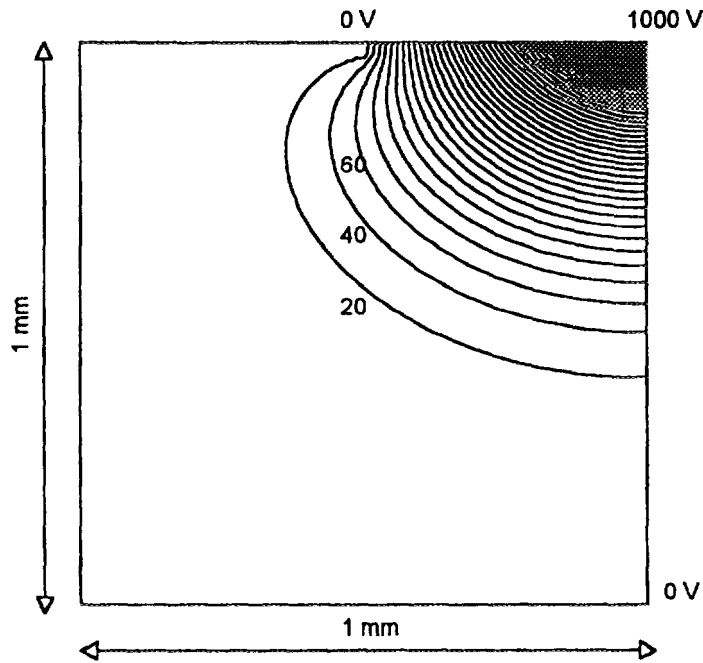


**Figure 4.** Equipotential lines in an element of the counter. The potential on the drift plate is 0 V.

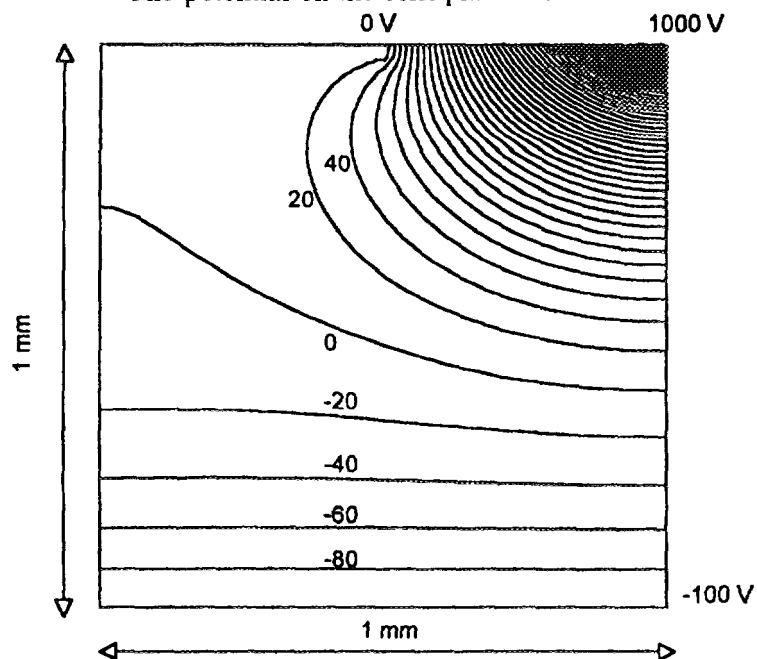


**Figure 5.** Equipotential lines in an element of the counter. The potential on the drift plate is -100 V.

are calculated in Figure 4 and 5 by using the relaxation method. In this calculation, the anode potential is set to 1000 V and the diameters of the wires are set to 20  $\mu\text{m}$ . The thickness of the counter is 1 mm. The drift plate potential is set to 0 V (Figure 4) or -100 V (Figure 5). The lines show that the weak field region appears in the Figure 4 can be easily reinforced by a small potential on the drift plate. Therefore, the sensitive region in the counter can be assumed to cover the full space of the counter for simplicity. If the particle reaches on the wall or has no energy in a step of the calculation for an infinitesimal length advanced in the tracking, the summation of the energy loss for the event is terminated. The sensitive region of the element is assumed to have infinite length in the axial dimension (dimension for position sensing). That is the particle goes out the calculating region is moved to the opposite side as a particle goes in the region again.

The Monte Carlo technique is used in the calculation in which the direction of the proton emission is determined isotropically in 3-dimensional space by using random numbers. Spherical coordinates  $(r, \theta, \phi)$  are used to convert to Cartesian coordinates for simplicity in making the probability distribution of the direction. The azimuthal angle  $\phi$  in spherical coordinates is set by using a normal random number  $t_1$ .

$$0 < t_1 < 2\pi.$$

The polar angle  $\theta$  is calculated by a normal random number  $t_2$ .

$$\theta = \cos^{-1}(1 - 2t_2), \quad 0 < t_2 < 1$$

Another particle triton is emitted in the opposite direction of that for proton. As the results of the calculation, the charges provided by the particle stopping in the counter elements is calculated in succession for the infinitesimal length of the tracking. The charges are integrated to make pulse height spectra listed in Table 1.

**Table 1.** Pulse height spectra obtained by the simulation.

	Coincidence	Charge signal
Spectrum-1	-	A
Spectrum-2	-	B
Spectrum-3	-	C
Spectrum-4	-	A + B + C
Spectrum-5	2 (any pair)	A + B + C
Spectrum-6	3	A + B + C

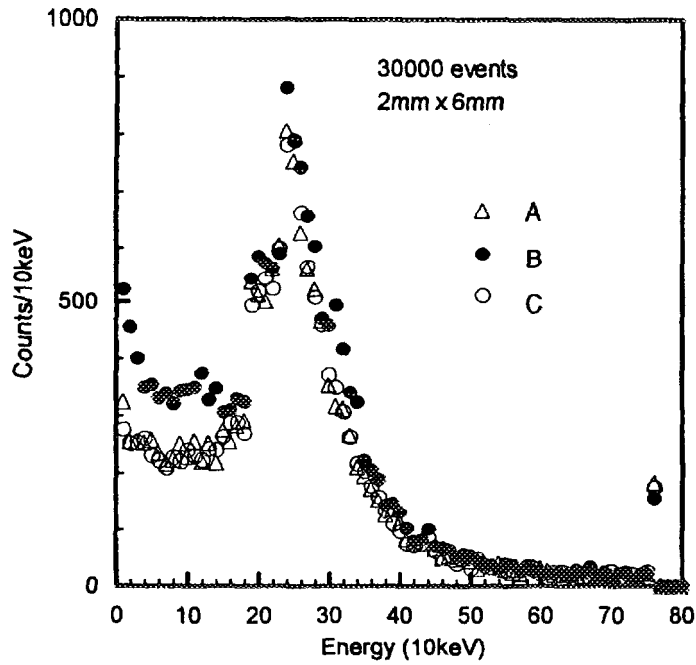


Figure 6. Pulse height spectra obtained by using the elements of the counter.

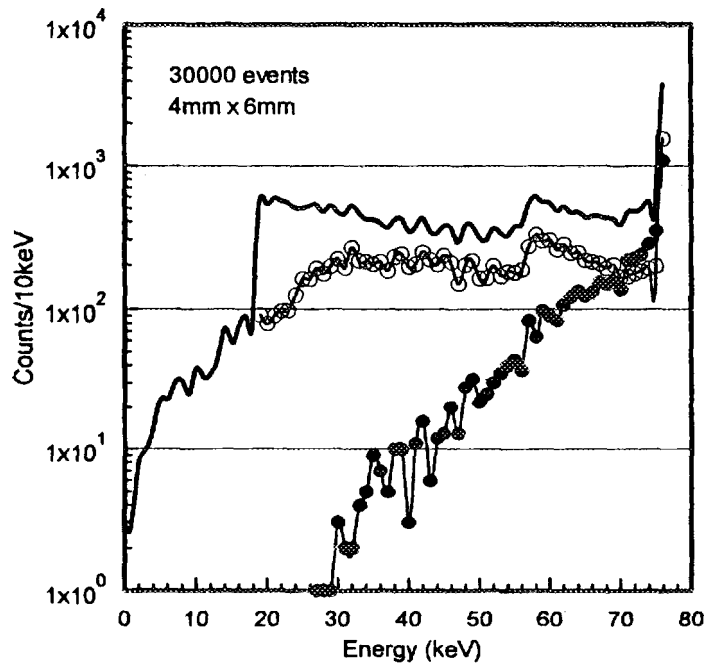
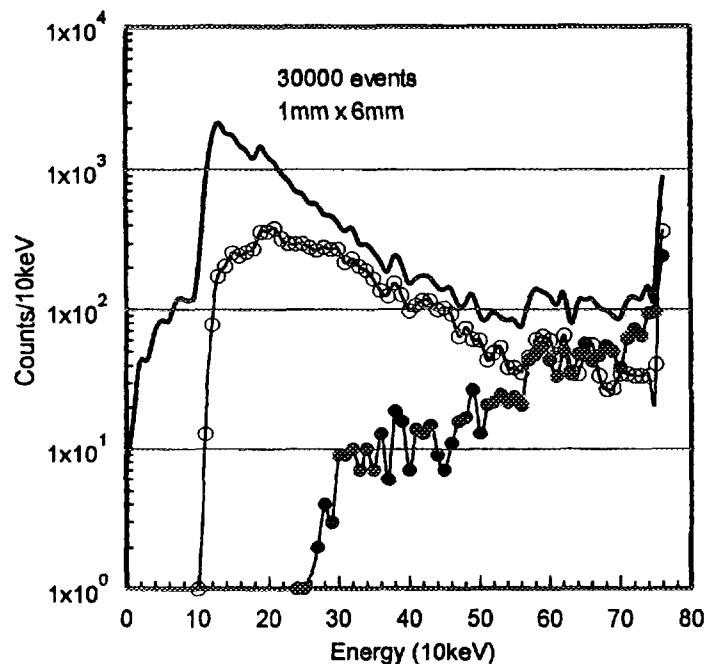


Figure 7. Pulse height spectra made by the summation of the counter signals. The thickness of the counter is 4 mm.

#### 4. RESULTS AND DISCUSSION

The results by the calculation are shown in Figures 6, 7, 8 and 9. The spectrum-1, 2 and 3 in the Table 1 are drawn in Figure 6 for the counter thickness of 2 mm. In the calculations, 30000 events of neutron detection are evaluated and all of the charges created in the sensitive region of the counter are considered to be collected by the anodes. The small peaks of 765 keV in these three spectra are the full energy peaks of the reaction. The case with the wall effect by the vanishing of proton energy appears in

the broad peak of about 200 keV. In these spectra, the information of full energy of the (n, p) reaction is distorted by the wall effect. The spectra using summation and coincidence technique are shown in Figure 7 for the counter thickness of 4 mm. The solid line is the spectrum-4 in the Table 1. The wall effects by vanishing of proton energy and by vanishing of triton energy appears clearly in the spectra. The full energy peak is comparatively higher than the wall effect continuum for this counter thickness. The spectra-5 and 6 are also shown in the figure as open circles and closed circles. By the coincidence method, the continuum of the wall effect is rejected. The spectra for the thickness of 1 mm are shown in Figure 8. The full energy peak is smaller than the continuum of wall effect in the spectrum-4 for the thickness of 1 mm. The discrimination of the wall effect is achieved in all cases. Especially, in the spectrum-6 using coincidence of three elements, the continuum of the wall effect is reduced to one percent at low energy region of the spectrum. The counting of full energy peak is reduced to about a quarter by the coincidence of three counters. The function of the discriminating the wall effect in the pulse height spectrum is confirmed in the calculations.



**Figure 8.** Pulse height spectra made by the summation of the counter signals. The thickness of the counter is 1 mm.

## 5. CONCLUSION

A new idea for a thin neutron counter with a function of discriminating the wall effect is proposed. The discrimination of the wall effect in the counter can be achieved by the coincident counting technique using signals from paralleled elements that is made with micro-gap structure. Simulation by the Monte Carlo method is applied to estimate

the wall effect in the new counter. The calculation shows discrimination of the wall effect can be achieved by the coincident counting of two or three counting elements. The total energy peak created by the (n, p) reaction appears clearly in the pulse height spectrum for a very thin counter with 1 mm thickness.

### Reference

- (1) A. Uritani, Y. Kuniya, Y. Takenaka, H. Toyokawa, Y. Yamane, C. Mori, K. Kobayashi, S. Shiroya and C. Ichihara, *J. Nucl. Sci. And Tech.*, Vol.32 (1995) 719.
- (2) R. Fang, R. Blaes, J. M. Brom, W. Geist, A. Michalon, J. L. Riester, R. Seltz and C. Voltolini, *Nucl. Instr. And Meth. In Phys. Res.*, Vol. A 361 (1995) 85.
- (3) F. Angelini, R. Bellazzini, M. Bozzo, A. Brez, M. M. Massai, R. Raffo, G. Spandre, M. Spezziga and A. Toropin, *Nucl. Instr. And Meth. In Phys. Res.*, Vol. A 362 (1995) 273.

# A NRESPG Monte Carlo Code for the Calculation of Neutron Response Functions for Gas Counters

K. Kudo, N. Takeda and A. Fukuda

Quantum Radiation Division, Electrotechnical Laboratory,  
1-1-4 Umezono, Tsukuba-shi, Ibaraki-ken 305, Japan

T. Torii and M. Hashimoto

Power Reactor and Nuclear Fuel Development Corporation,  
4002 Narita, Oarai, Ibaraki-ken 311-13, Japan

T. Sugita

Science System Laboratory  
1342-6 Sumiyoshi, Tomobe-cho, Ibaraki-ken 309-17, Japan

X. Yang

Radiometrology Center, China Institute of Atomic Energy,  
P.O.Box. 275-20, Beijing, 102413, P.R. of China

G. Dietze

Department 6, Physikalisch-Technische Bundesanstalt  
Bundesallee 100, 38116 Braunschweig, Germany

## I. INTRODUCTION

A  $^3\text{He}$  proportional counter is known to have good characteristics for neutron spectroscopy in a wide energy range using the  $^3\text{He}(n,p)\text{T}$  and  $^3\text{He}(n,n)^3\text{He}$  reactions. In the energy range below 3 MeV, the  $^3\text{He}(n,p)\text{T}$  reaction yields a clear peak on its pulse height spectrum corresponding to the incident neutron energy plus the Q value of 764 keV for this reaction if commercially available detectors are used. The latter reaction of  $^3\text{He}(n,n)^3\text{He}$  becomes more pronounced as the neutron energy becomes higher than 5 MeV. A hydrogen or methane proportional counter plays an important role in the absolute measurements of monoenergetic neutron fluences due to the knowledge of its precise scattering cross section of  $\text{H}(n,n)\text{H}$  reaction. In order to calculate the neutron response functions and detector efficiencies of gas counters, we have developed a Monte Carlo code "NRESPG" by modifying the NRESP code<sup>(1)</sup>, which was originally developed by G. Dietze and H. Klein for the calculation of the response functions and efficiencies for NE213 scintillation detectors for monoenergetic neutrons over the energy range from 0.02 MeV to 20 MeV.

In this paper, we show the outline of the NRESPG and some typical results of the response functions and efficiencies of several kinds of gas counters. The cross section data for the several kinds of filled gases and the wall material of stainless steel or aluminum are taken mainly from ENDF/B- IV<sup>(2)</sup>. The ENDF/B- V for stainless steel is also used to investigate the influence on pulse height spectra of gas counters due to the difference of nuclear data files.

## II. DESCRIPTION OF NRESPG CODE FOR GAS COUNTERS

The NRESPG (Version- I) code calculates the response functions for cylindrical gas counters, which are composed by two regions of gas and cylindrical housing. Two kinds of filled gases were included as; (1) a mixture of <sup>3</sup>He+<sup>4</sup>He+Kr gases and; (2) a mixture of H<sub>2</sub>+CH<sub>4</sub>+<sup>3</sup>He+Kr gases. Similarly, an option for two types of wall materials. i.e. aluminum and stainless steel were added as input data to the code. The initial energy distribution of incident neutrons can be selected as monoenergetic or continuous one having isotropic angular distribution or parallel beam distribution. The program determines the energies as well as directions of the scattered neutrons and the induced charged- particles which are produced as a result of neutron interactions with the constituents of the gas. The energy loss of the induced charged particles in the sensitive and insensitive volume of a gas counter is taken into account separately to calculate the effective energy deposition from the charged particle to the gas. We assumed a W value of the gas to be constant, i.e. the deposition energy equals to the output energy to be measured in the gas counter. Stopping power data for the filled gas have been included in the program. The stopping power for methane was determined by combining the partial stopping powers of hydrogen: S<sub>H</sub> and that of carbon: S<sub>C</sub> in the following form; S<sub>CH<sub>4</sub></sub> = 0.75 x S<sub>C</sub> + 0.25 x S<sub>H</sub>. The output energy distributions calculated by the NRESPG code are stored as a total spectrum and partial spectra depending on the first interaction of an incident neutron. The difference between the total spectrum and the summed partial spectra shows the effect of neutron scattering at the wall material on the response function.

For the comparison of a measured response spectrum with a calculated one, the calculated spectrum must be transferred into a spectrum with an energy calibrated scaling and then folded by a Gaussian function, taking into accounts the real energy resolution of the gas detector. Such numerical procedures was carried out by an additional program SPEKT on the basis of a personal computer.

## II. RESULTS AND DISCUSSION

The response functions have been calculated by the NRESPG Monte Carlo code for gas

proportional counters at different neutron energy points. Calculations were performed for three different types of filled gases and two types of wall material as mentioned earlier. The schematic drawing for the calculational arrangements is illustrated in Fig.1. The detector had an active length of 15 cm with a diameter of 2.5 cm and a wall thickness of 0.5 cm, which was placed at 30 cm apart from a neutron source such that the top flat end of the cylinder is facing the source.

In Fig.2, calculated response functions for the same type of filled gas mixed by  $^3\text{He}$  (0.4MPa) and Kr (0.2MPa) but for two different types of wall materials, i.e. stainless steel and aluminum, have been compared at several energy points of 25 keV, 1.2 MeV and 14 MeV. A very little difference was seen between the two response functions. The detector efficiencies were compared by integrating each pulse height spectrum. The difference between the efficiencies of the counters are summarized in Table 1. In general, the efficiency of the counter with stainless steel wall is slightly larger than that of aluminum wall. This may be attributed to the larger scattering cross section of neutrons by the stainless steel which results in relatively more neutron scattering to the inside of the detector. However, at 25 keV, the response of the counter with stainless steel wall becomes lower than the counter with aluminum wall. This is because iron has a neutron window at this energy and has the total cross section close to zero. Therefore, most of incident neutrons can penetrate the stainless steel wall without scattering at 25 keV. In the case of  $\text{CH}_4$  filled gas, carbon and hydrogen recoil edges can be clearly seen in the Fig.3. It can be easily found from the Table 1 that the wall materials cause about 1 % difference in the detector efficiency.

In order to study the scattering effect of stainless steel wall at an energy point of 2.413 MeV, the neutron cut-off energy was changed from 500 keV to 2.413 MeV in the calculations. If a neutron energy becomes below this cut-off energy, the one neutron history will be terminated and a new seed of incident neutrons will be generated. Making the cut-off energy equal to the incident neutron energy implies that the scattered neutrons in the detector are neglected in the response calculations. By lowering the cut-off energy level to 500 keV, all the possible secondary interactions are taken into account. The difference between the response functions obtained with the above cut-off levels will give us the contribution of the scattered neutrons due to the wall material of stainless steel. This effect was found to be the order of 1.1 %.

In order to compare the ENDF/B- IV with the recent cross section data of the ENDF/B-V, the response functions were calculated by using the NRESPG with the stainless steel cross section data of the ENDF/B- IV or the ENDF/B- V. The response obtained with the data version V was about 0.7% smaller than that of obtained with the data version IV.

The peak-region spectra induced by the reaction of  $^3\text{He}(n,p)\text{T}$  at 2.413 MeV are shown in Fig.4- a. The calculated spectrum assuming the constant gas gain within the effective volume in

the gas proportional counter showed the agreement with the experimental one, except for a discrepancy in the vicinity of a valley following closely to the lower energy tail of the full energy peak. In order to improve the discrepancy in the valley region, the space- dependent gas multiplication factor was included in the NRESPG code. The relative gas multiplication along the cylindrical anode wire of a  $^3\text{He}$  proportional counter was measured by using a slit beam of thermal neutrons<sup>(3)</sup>. The measured gas gain depending on the anode wire position was taken in the SPEKTG program. The better agreement was obtained as shown in Fig.4-b.

The calculated spectrum was fitted to the measured one at the full energy peak region at 2.413 MeV. The significant deviation of 120 keV to the lower energy was found at the helium recoil edge as shown in Fig.5, because of the nonlinear effects such as the space charge effect and the recombination effect. In order to reconstruct the calculated spectrum referring to the experimental spectrum, first, the partial pulse height spectrum of  $^3\text{He}(n,p)\text{T}$  was fitted to the experimental one as shown in Fig.6-a and subtracted. Second, the partial pulse height spectrum of  $^3\text{He}(n,n)^3\text{He}$  was fitted to the subtracted spectrum as shown in Fig.6-b. Finally, thermal neutron peak was fitted with the same manner as shown in Fig.6-c. The reconstructed spectrum by summing the partial spectra showed the better agreement with the experimental one in Fig.7.

## V. CONCLUSION

In the foregoing, we have described the development of the NRESPG code and have then successfully applied the code for the calculation of the response functions and efficiencies of different types of cylindrical gas proportional counters. The NRESPG code is expected to play an important role in the precise determination of neutron fluences where the effect of secondary neutrons produced in the detector housing is not ignored. The NRESPG code is being developed to include the sphere geometry of a detector and the graphic representation of the output spectra..

## References

- (1) G. Dietze and H. Klein: PTB-Bericht ND-22 (1982).
- (2) Evaluated Nuclear Data File ENDF/B-IV, BNL, Upton, New York (1973).
- (3) N. Takeda and K. Kudo: IEEE Trans. Nucl. Sci., NS-41, 880 (1994).

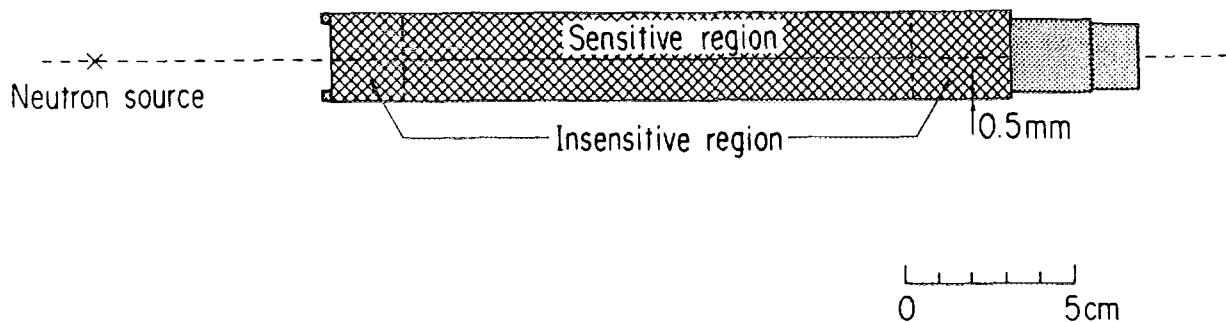


Fig.1 Schematic drawing of a gas proportional counter for the calculational arrangements.

The detector have active length of 15 cm with a diameter of 2.5 cm and a wall thickness of 0.5 cm.

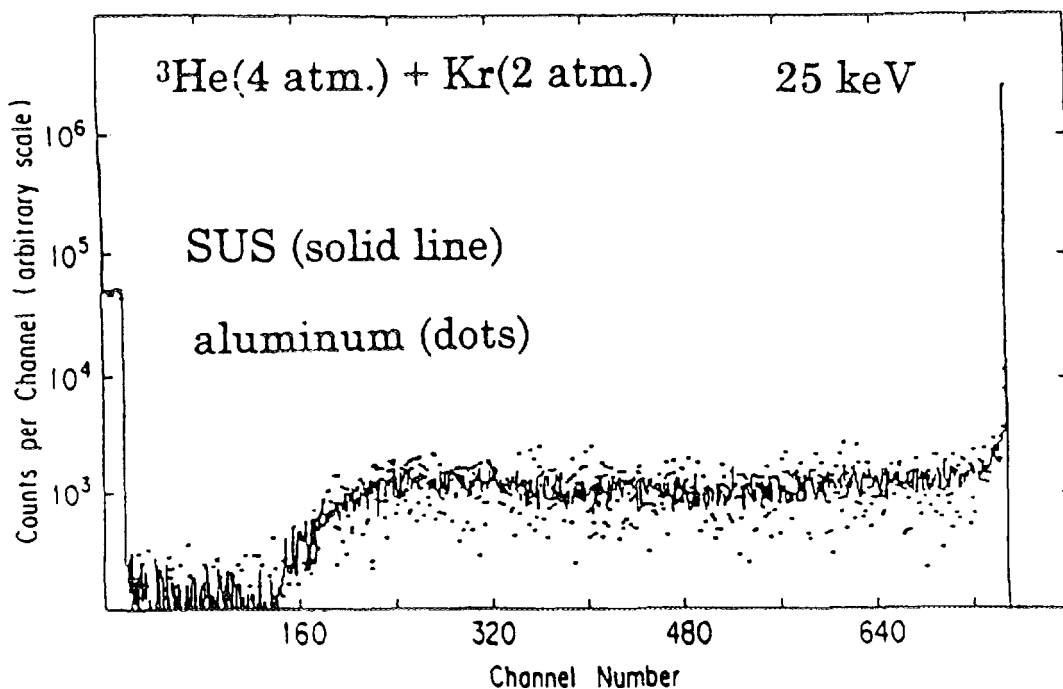


Fig.2-a Comparison of pulse height spectra for the same type of filled gas mixed by  $^3\text{He}$  (0.4MPa) and Kr (0.2MPa) but for two different types of wall materials, i.e. stainless steel (solid line) and aluminum (dots) at several energy points of (a) 25 keV, (b) 1.2 MeV and (c) 14 MeV, respectively.

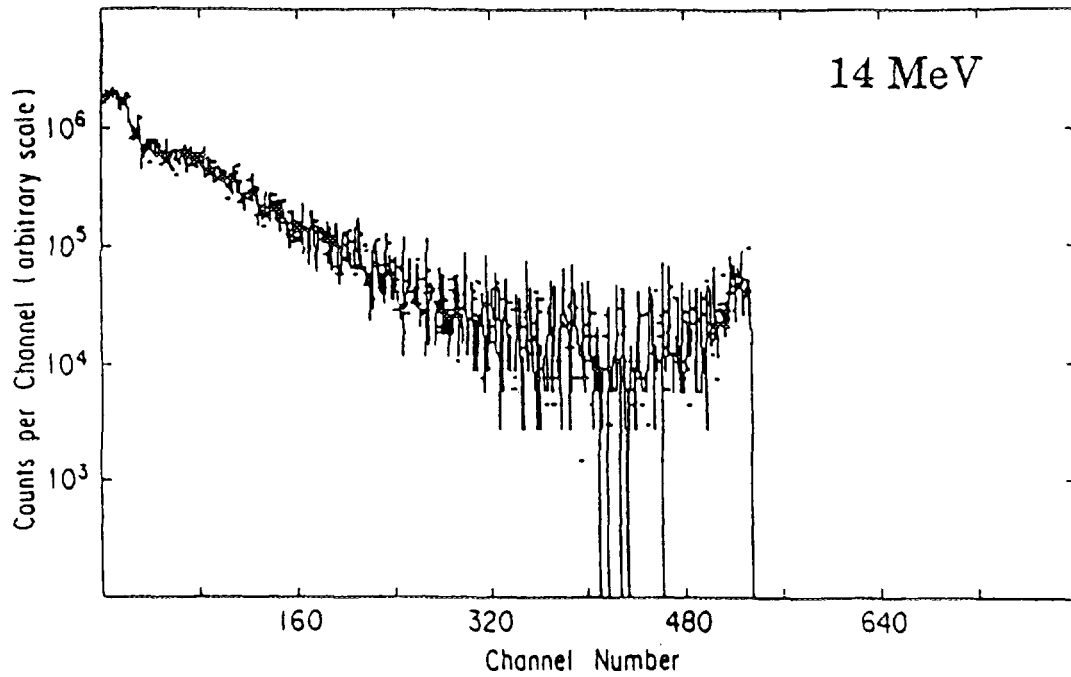
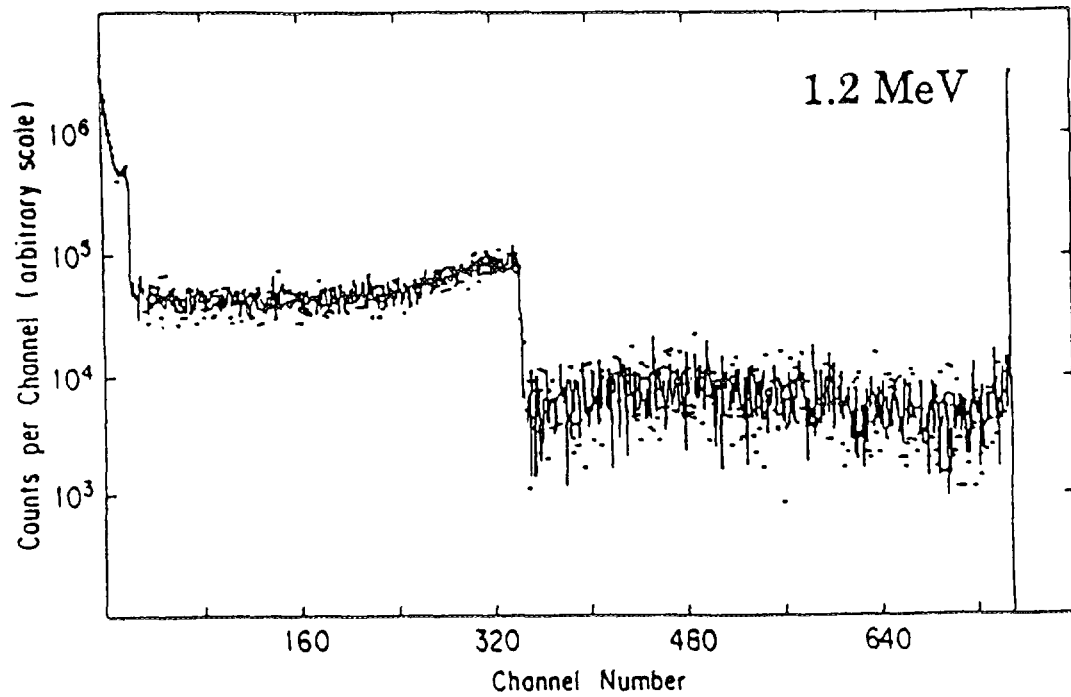


Fig.2-b & 2-c Comparison of pulse height spectra for the same type of filled gas mixed by <sup>3</sup>He (0.4MPa) and Kr (0.2MPa) but for two different types of wall materials, i.e. stainless steel (solid line) and aluminum (dots) at several energy points of (a) 25 keV, (b) 1.2 MeV and (c) 14 MeV, respectively.

Table 1 Ratio of efficiencies of the counters with stainless steel and aluminum walls at the listed neutron energies and filled gases.

ENERGY	WORKING GAS PRESSURE (MPa)				RATIO OF EFFICIENCIES (SUS/AL)
	<sup>3</sup> He	Kr	H <sub>2</sub>	CH <sub>4</sub>	
25 keV	0.4	0.2	0.0	0.0	0.985
565 keV	0.0	0.0	0.4	0.0	1.005
565 keV	0.0	0.0	0.0	0.2	1.003
1.2 MeV	0.4	0.2	0.0	0.0	1.007
2.413 MeV	0.4	0.2	0.0	0.0	1.012
14 MeV	0.4	0.2	0.0	0.0	1.007

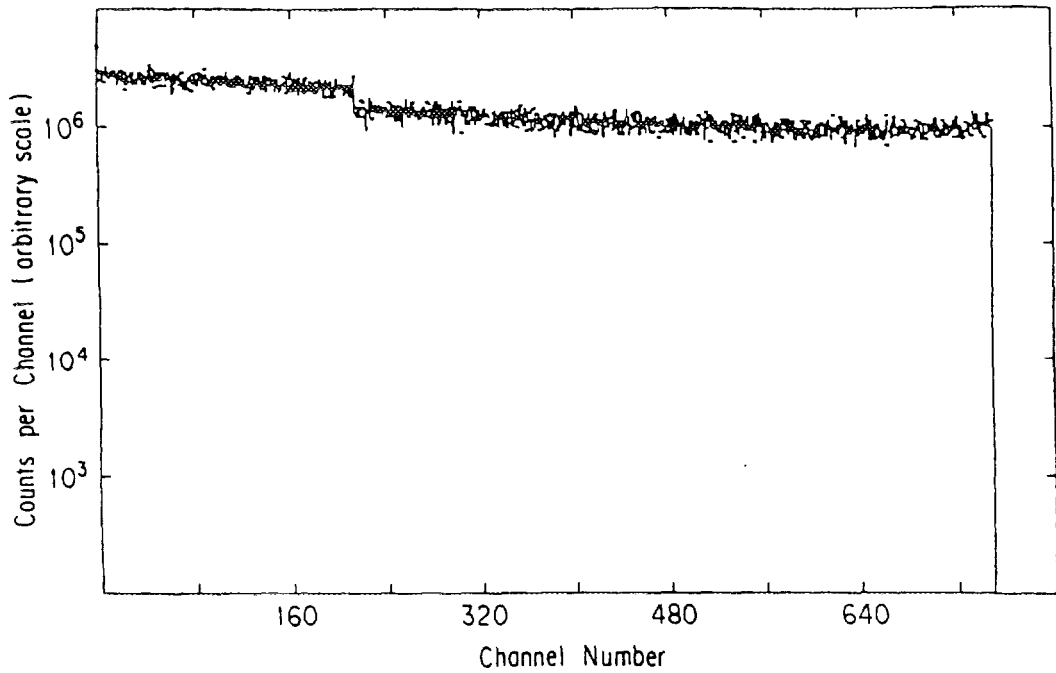


Fig.3 Comparison of pulse height spectra in CH<sub>4</sub> proportional counter with stainless steel (solid line) and aluminum (dots) wall materials at 565 keV.

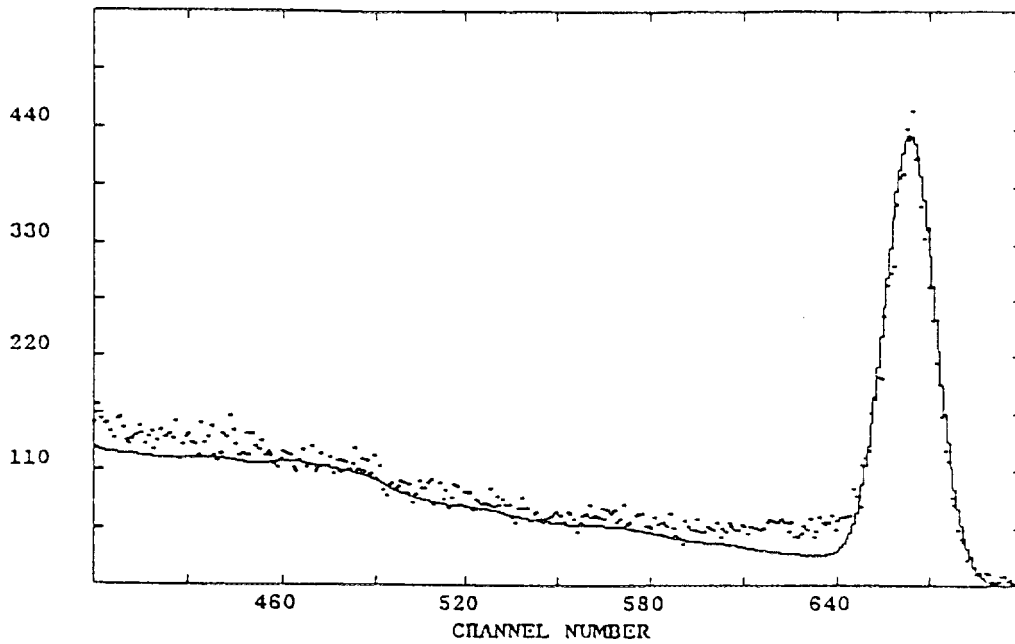


Fig.4-a The peak-region spectra induced by the reaction of  ${}^3\text{He}(n,p)\text{T}$  at 2.413 MeV assuming a constant gas gain within the effective volume in the gas proportional counter.

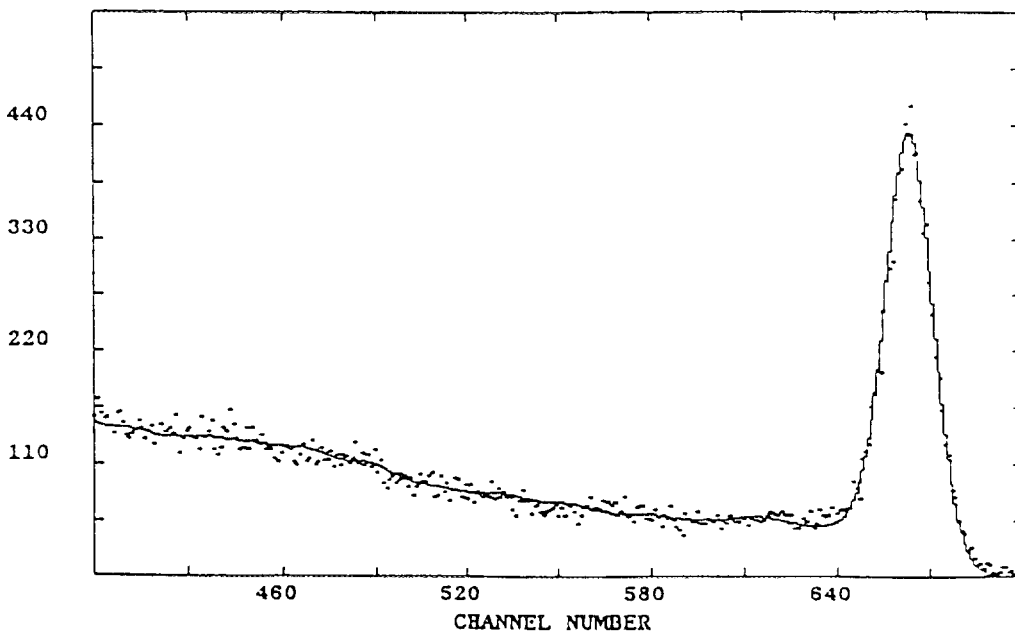


Fig.4-b The peak-region spectra induced by the reaction of  ${}^3\text{He}(n,p)\text{T}$  at 2.413 MeV assuming a position-dependent gas gain within the whole volume in the gas proportional counter.

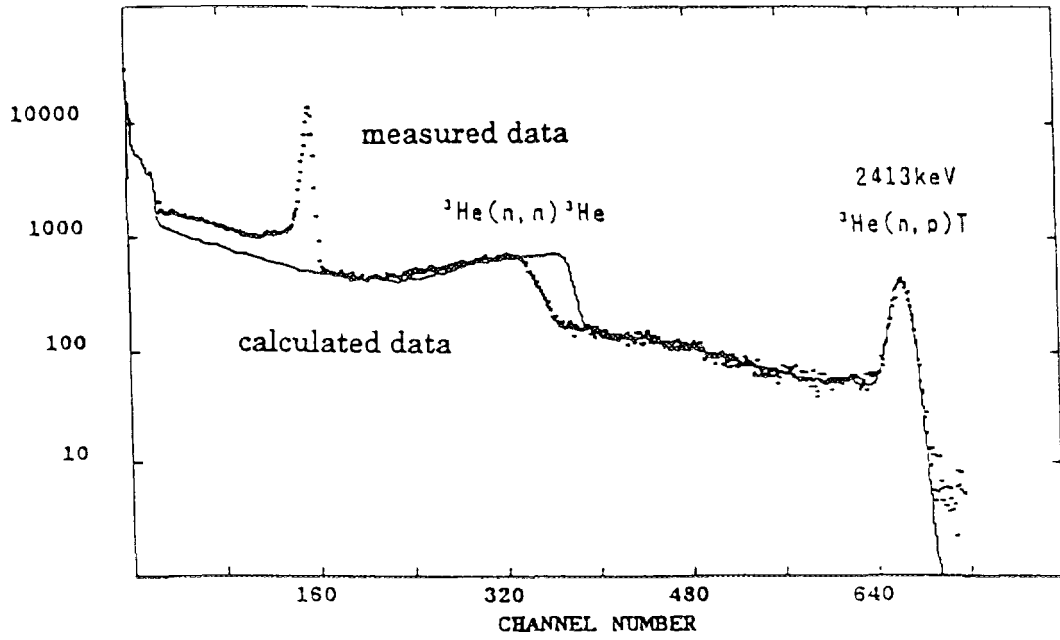


Fig.5 Comparison of pulse height spectra obtained by an experiment (dots) and a calculation (solid line) in a  $^3\text{He}$  proportional counter at 2.413 MeV.

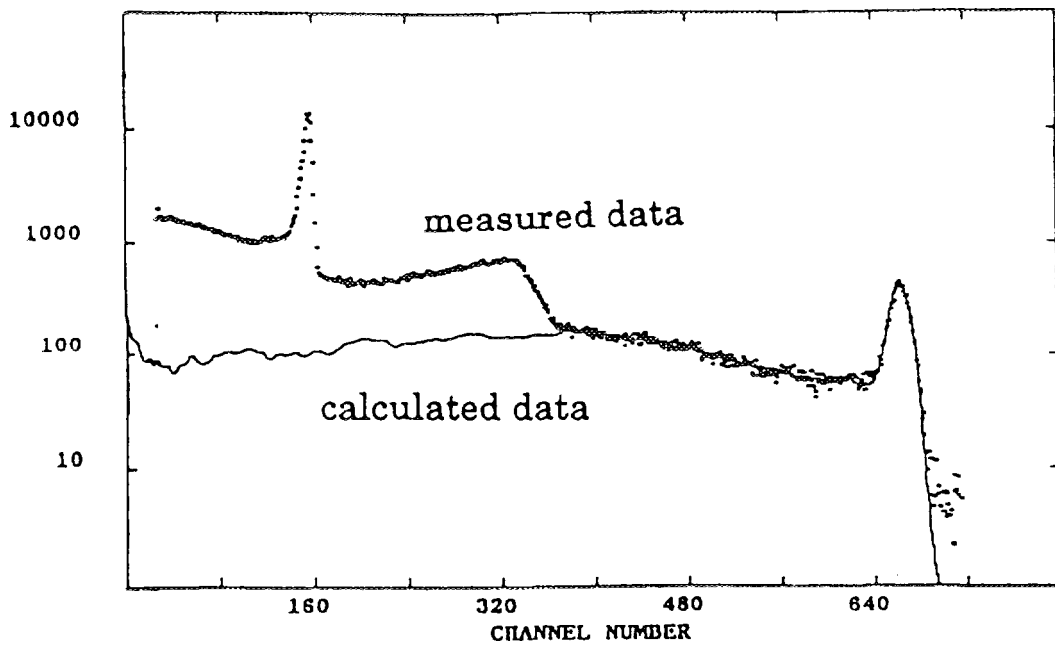


Fig.6- a Fitting of the calculated partial pulse height spectrum (solid line) of  $^3\text{He}(n,p)\text{T}$  reaction to the experimental one (dots) at 2.413 MeV.

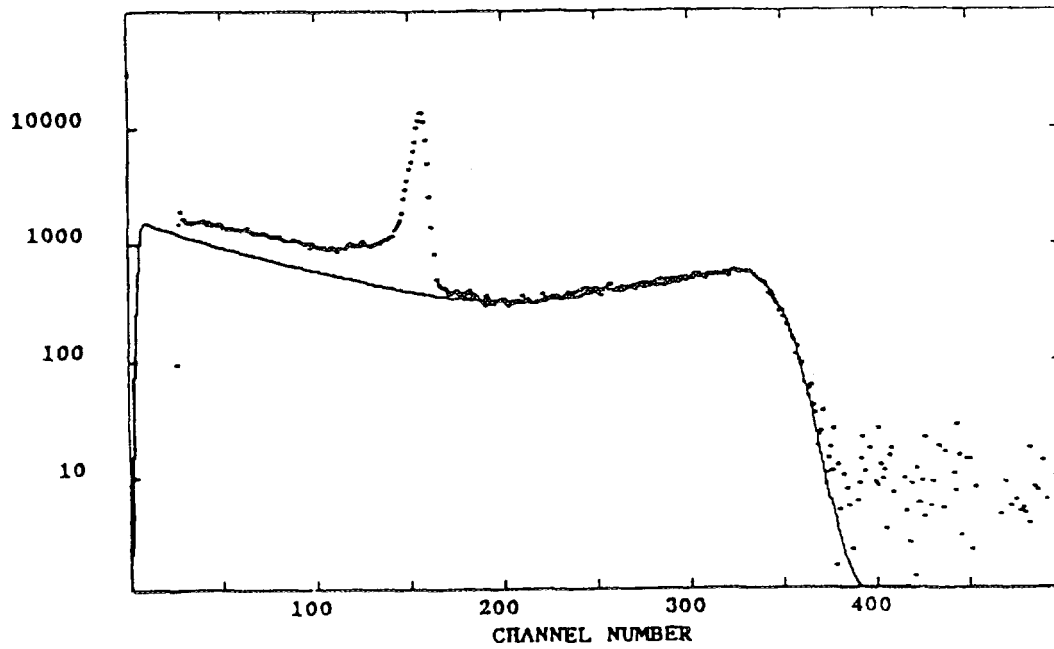


Fig.6- b Fitting of the calculated partial pulse height spectrum (solid line) of  ${}^3\text{He}(n,n){}^3\text{He}$  reaction to the experimental one (dots) after subtracting the contribution of partial pulse height spectrum of  ${}^3\text{He}(n,p)\text{T}$  reaction.

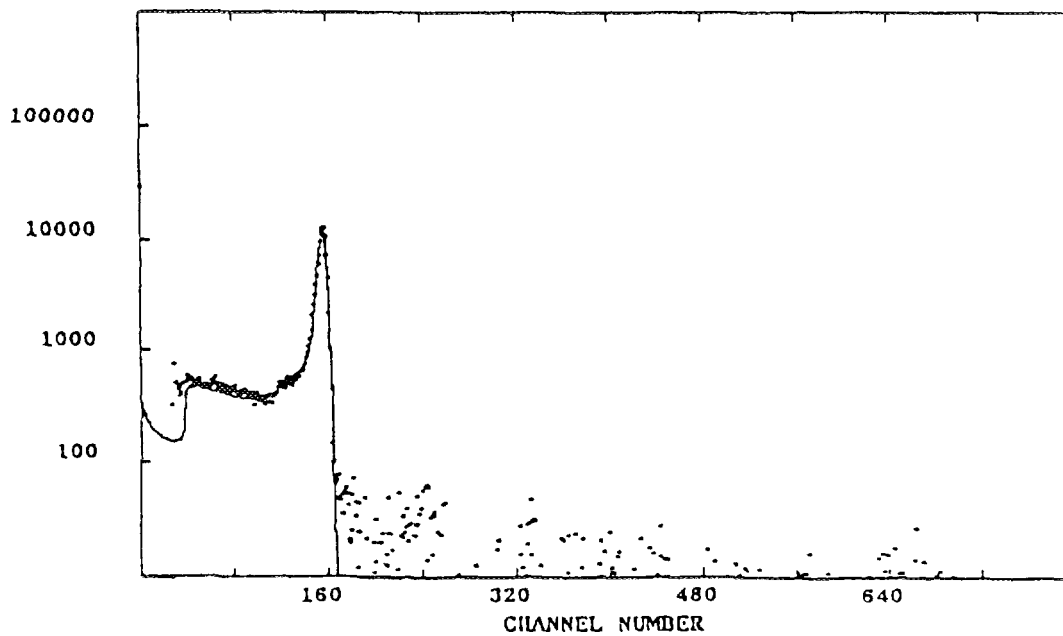


Fig. 6- c Fitting of the calculated partial pulse height spectrum (solid line) of  ${}^3\text{He}(n,p)\text{T}$  reaction to the experimental one (dots) at the thermal neutron peak region.

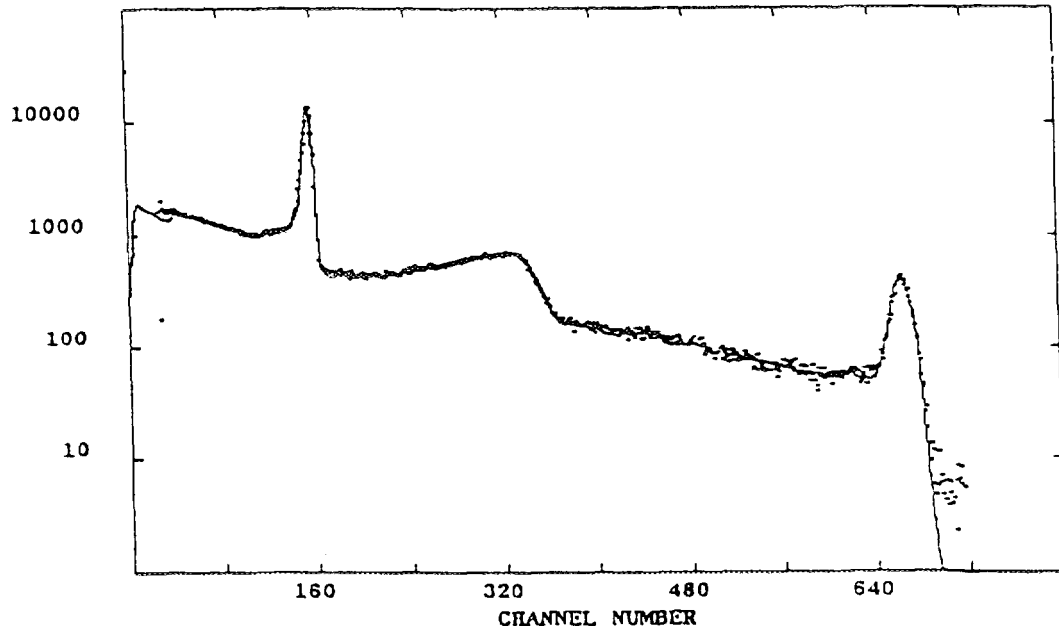


Fig.7 Comparison of pulse height spectra obtained by an experiment (dots) and a reconstruction (solid line) in a  $^3\text{He}$  proportional counter at 2.413 MeV .

# Development of a Directional Neutron Detector for Neutron Emission Profile Monitor

Junichi Kaneko, Masaki Katagiri, Yujiro Ikeda, Katsuyuki Ara  
Department of Reactor Engineering, Japan Atomic Energy Research Institute  
Tokai-mura, Ibaraki, 319-11 Japan

Tetsuo Iguchi and Masaharu Nakazawa  
Department of Quantum Engineering & Systems Science  
The University of Tokyo, Hongo 7-3-1, Bunkyo, Tokyo, 113 Japan

## 1. Introduction

Neutron emission profile monitors are used on fusion plasma diagnostics<sup>(1), (2), (3)</sup> and nuclear fuel safety research<sup>(4)</sup>. This diagnostic system needs huge multiple channel neutron collimators and neutron detectors. In these systems, especially in plasma diagnostics, only a few multiple channel neutron collimators can be adopted to an experimental device because of its size and weight. It means that enough number of view points and lines of sight cannot be used. This limitation sometime corrupts contrast and spatial resolution on reconstructed neutron emission profiles, and makes unreal images in the worst case<sup>(5)</sup>.

Directional neutron detectors are one method to improve this sever problems on reconstructed neutron emission profiles. These detectors are possible to reduce the size of multiple channel neutron collimator or omitting it, and increase the number of view points and lines of sight. For 14-MeV neutron, directional neutron detectors using plastic scintillating fibers or scintillators were investigated in reference (6) and (7). In this research, the authors evaluated a recoil proton telescope type directional neutron detector that is possible to adopt not only to 14-MeV but also fission and 2.4-MeV neutrons.

## 2. Detectors and experimental

Fig. 1 shows the principle of directional neutron detection. This detector is a kind of recoil proton telescope, consists of three parts, a radiator including hydrogens, a recoil proton collimator and a charged particle detector. The recoil proton collimator limits the scattering angle that allows recoil protons to enter the charged particle detector, then this

detector achieves the directionality by setting energy discrimination threshold. A charged particle detector that has no sensitivity to neutron nor gamma rays is ideal for this system.

The components of the detector are written in Table 1. The detector does not have any vacuum vessel, and all channels of a recoil proton collimator were filled with air. In this experiment a CsI(Tl) scintillator and a photomultiplier tube were used as a charged particle detector. A CsI(Tl) scintillator was chosen for rise time pulse shape discrimination (8), (9). The thickness of the scintillator was decided from the 14-MeV proton's range in a CsI crystal. A photo diode is suitable for a CsI(Tl) scintillator than a photomultiplier tube in quantum efficiency(10). This detector will be used in high neutron and gamma ray environment, so a photomultiplier tube was chosen in the advantage of radiation hardness and low level of the noise caused by direct reaction in a photo detector.

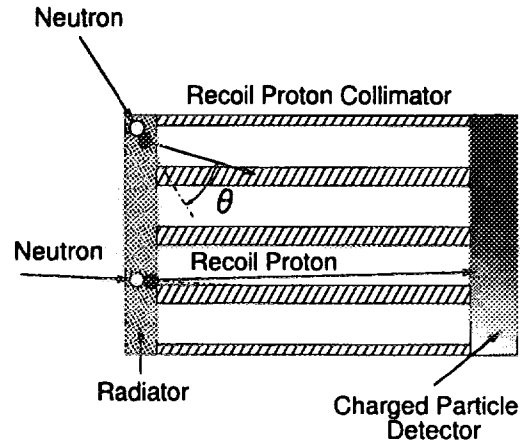


Fig. 1 Principal of directional neutron detection.

Table 1 Detector components

Radiator; Polyethylen,	30mm × 30mm × 1mm, 0.2mm
Recoil Proton Collimator;	
#1 Aluminum,	25mm × 25mm × 2mm, φ 1.4mm × 188 holes
#2 Aluminum,	30mm × 30mm × 2mm, φ 0.8mm × 492 holes
#3 Lead,	25mm × 25mm × 2mm, φ 1.4mm × 188 holes
Photo Detector;	
Photomultiplier tube + CsI(Tl) scintillator,	25mm × 25mm × 2mm

The response function measurement for 14-MeV and 2.4-MeV neutrons was done at the Fusion Neutron Source (FNS) Facility, and the Yayoi Fast Reactor was used to the measurement for fission neutrons. The response functions were measured by rotating the detector against the target (FNS) or the neutron beam (Yayoi reactor).

### 3. Experimental results and discussion

Fig. 2 shows response functions of the directional neutron detector to 14-MeV, fission and 2.4-MeV neutrons. In Fig. 2a, for 14-MeV neutron, there are three regions, alphas, protons and background gamma rays. For 14-MeV neutron, the thin scintillator

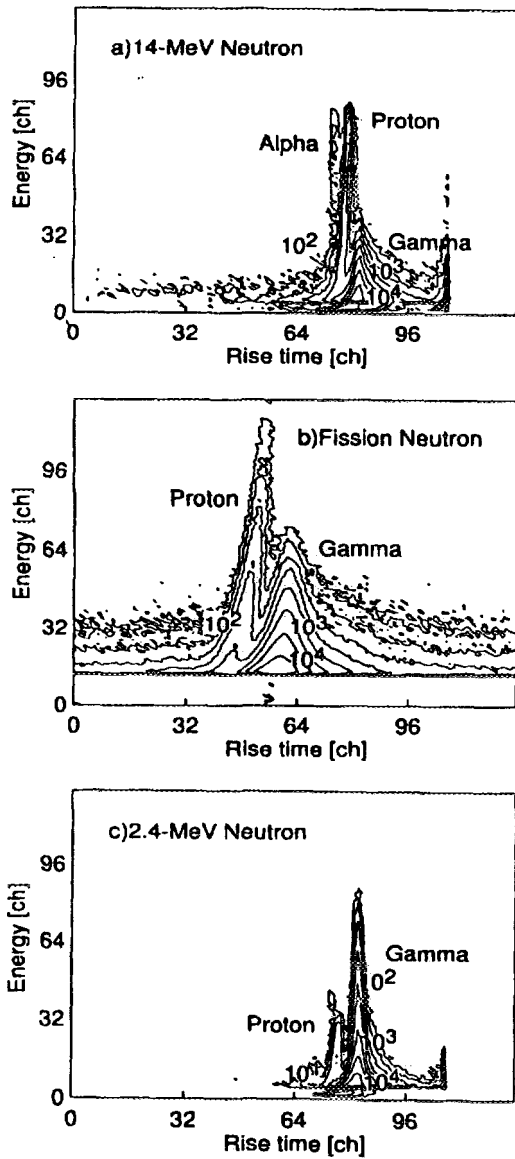


Fig. 2 Response functions for 14-MeV, fission and 2.4-MeV neutrons.

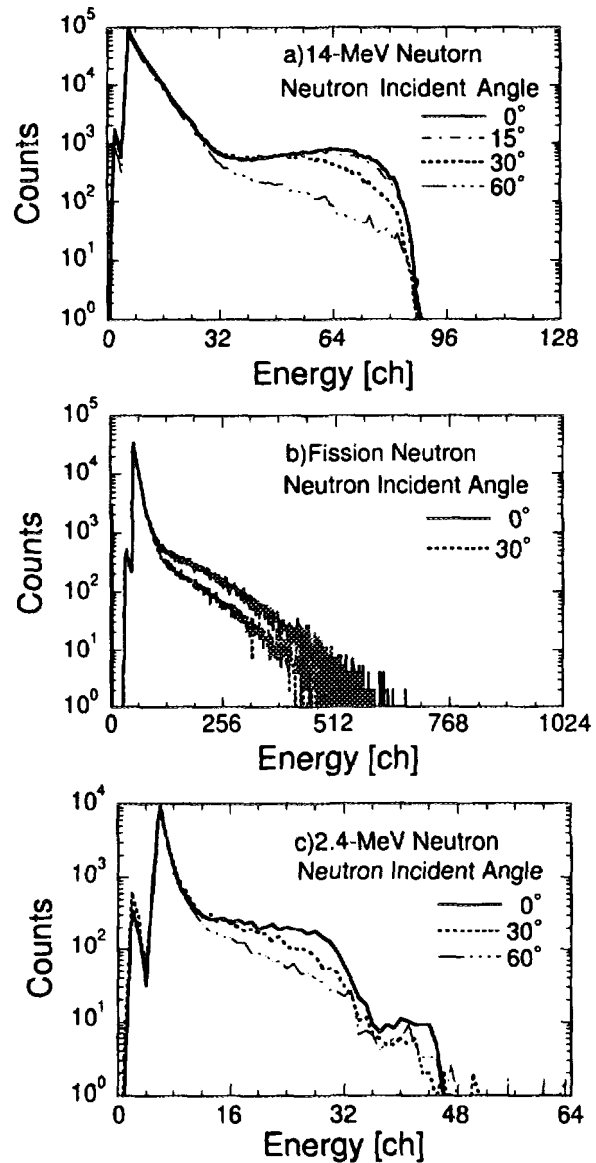


Fig. 3 Proton spectra's dependence on neutron incident angles measured for 14-MeV, fission and 2.4-MeV neutrons.

geometry achieved big protons' light outputs and small gamma rays' light outputs relatively. Although this detector was designed for 14-MeV neutron, Fig. 2b and c show that it is possible to get a recoil proton energy spectrum in high gamma ray background by rise time pulse shape discrimination

Fig. 3 shows proton energy spectra that measured to several neutron incident angles for 14-MeV, fission and 2.4-MeV neutrons. These spectra were measured by using the pulse shape discrimination technique with the window decided by proton signal's rise time. It is clearly, the counts decrease at the high energy region with increasing of

the neutron incident angle for three different neutron energy distributions. In Fig. 3a and c, for 14-MeV and 2.4-MeV neutrons, the spectra for 60 degrees were almost same level as background. Although the cross section of (n, p) reactions in Pb for 14-MeV neutron is about  $10^{-2}$  smaller than the cross section in Al<sup>(11)</sup>, there were no differences in proton energy spectra for 14-MeV neutron between detectors using Al and Pb recoil proton collimator. It means that the (n, p) reactions in the CsI(Tl) scintillator govern the noise level. The protons caused by (n, p) reaction in the scintillator become the most important noise that corrupts the signal-to-noise ratio. There are no differences between 14-MeV, fission, 2.4-MeV neutrons in the origin of noise protons.

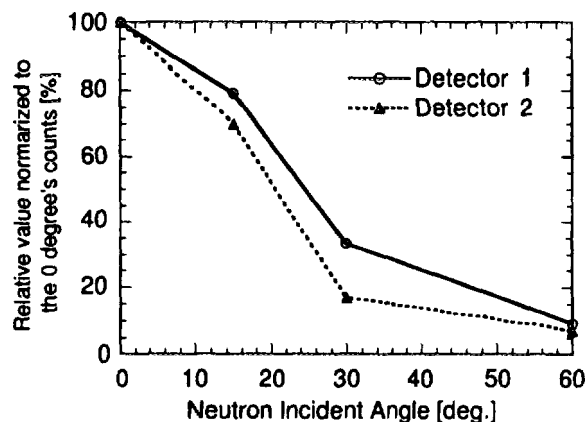


Fig. 4 Directional sensitivity; Detector 1 (Radiator 1.0mm in thickness, Recoil Proton Collimator #1 Al  $\phi$  1.4mm), Detector 2 (Radiator 0.2mm in thickness, Recoil Proton Collimator #2 Al  $\phi$  0.8mm).

The directionality resolution for 14-MeV neutron is shown in Fig. 4. These values are calculated by summing up all counts beyond the energy threshold, then normalized to the counts number at 0 degrees. The count number became half of the 0 degrees' counts at 25 degrees for the detector one, and at 21 degrees for detector two. The signal-to-noise ratio was 6.85 and 5.9 respectively. If background counting was done, it improves the directionality a little. It makes the number of detectors double. Several ten to a hundred neutron detectors need for a real system, so background counting is not realistic.

#### 4. Conclusion

As a result of this experiment, it was proved that the recoil proton telescope type directional neutron detector has a directionality for 14-MeV, fission and 2.4-MeV neutrons. For 14-MeV neutron, it is possible to achieve the directional performance just setting the energy discrimination by adopting thin scintillator geometry. Although a pulse shape discrimination technique is effective for fission and 2.4-MeV neutrons, it makes limitation to countrates. A Gas scintillator is one choice to improve this problem by using thin scintillator geometry like for 14-MeV neutron. From the discussion on the (n, p) reactions

in CsI(Tl) scintillator, a fast scintillator consisting of light elements that have high energy threshold and low cross section to  $(n, p)$  and  $(n, \alpha)$  reactions is suitable for this system. Fig. 5 illustrated one concept for this detector. Side read out geometry allows multiple of the radiator -recoil proton collimator - scintillator layers, then it can control the efficiency.

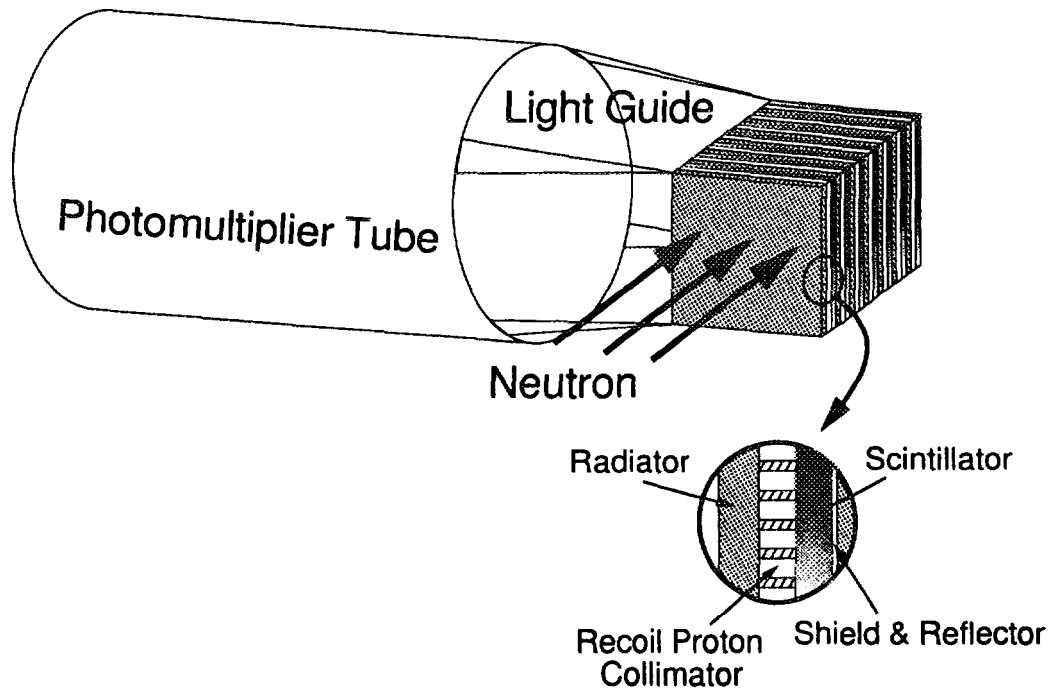


Fig. 5 A concept of recoil proton telescope type directional neutron detector

#### References

- (1) J. M. Adams et al., Nucl. Instrum. and Meth., A329, (1993), 277
- (2) K. Baumung et al., Nuclear Technology, Vol. 71, (1985), 353
- (3) ITRE DIAGNOSTICS, ITER Documentation Series No. 33, ( IAEA, Vienna, 1991), 51
- (4) A. L. Roquemoire et al., Rev. Sci. Instrum., Vol. 61, No. 10, (1990), 3163
- (5) Y. Nagayama, Kakuyugo Kenkyu, Vol. 62, No. 6, (1989), 427, in Japanese
- (6) E. L. Chupp and D. J. Forrest, IEEE Trans. Nucl. Sci., NS-13, (1966), 468
- (7) G. A. Wurden, et al, Rev. Sci. Instrum., Vol. 66, No. 1, (1995), 901
- (8) S. Keszthelyi-Landori and G. Hrehuss, Nucl. Instrum. and Meth., (1969), 9
- (9) S. Usuda, A. Mihara and H. Abe, Nucl. Instrum. and Meth., A321, (1992), 247
- (10) Z. Bian, J. Dobbins and N. Mistry, Nucl. Instrum. and Meth., A239, (1985), 518
- (11) T. Nakagawa et al, JAERI-M, 90-099, (1990)

## LIST OF PARTICIPANTS

S.Sakamoto, (Faculty of Engineering, Tokai University)  
N.Saito, (Electrotechnical Laboratory)  
K.Kondo, (Radiation Safety Control Center, National Laboratory for High Energy Physics)  
S.Takeuchi, (Faculty of Engineering, Saitama University)  
M.Hasegawa, (Electrotechnical Laboratory)  
K.Katoh, (Ibaraki Prefectural University of HS)  
T.Sugita, (SSL)  
K.Sato, (Faculty of Science and Technology, Nihon University)  
M.Katagiri, (Japan Atomic Energy Research Institute)  
M.Miyajima, (Radiation Safety Control Center, National Laboratory for High Energy Physics)  
M.Matsumoto, (Medical School, Osaka University)  
A.Nunoko, (Nuclear Engineering Ltd.)  
T.Emoto, (Radiation Control Section, OEC P.N.C.)  
H.Hirayama, (Radiation Safety Control Center, National Laboratory for High Energy Physics)  
T.Ohama, (Physics Department, National Laboratory for High Energy Physics)  
T.Ozaki, (Japan Energy Corporation)  
H.Takahasi, (Faculty of Engineering, The University of Tokyo)  
K.Miyasita, (Earthnics Corporation)  
S.Honda, (Tokushima University)  
S.Ban, (Radiation Safety Control Center, National Laboratory for High Energy Physics)  
S.Iwasaki, (Faculty of Engineering, Tohoku University)  
Y.Amemiya, (Photon Factory, National Laboratory for High Energy Physics)  
A.Mutoh, (Faculty of Engineering, Hosei University)  
I.Suzuki, (Electrotechnical Laboratory)  
K.Abe, (Faculty of Engineering, Tohoku University)  
M.Takebe, (Faculty of Engineering, Tohoku University)  
K.Kikuchi, (Seiko E.G&G. Inc.)  
Y.Kitamura, (Faculty of Engineering, Kyushu University)  
A.Yamaguchi, (Toyo Medic Co.Ltd.)  
Y.Katoh, (Tokyo Metropolitan College of Allied Medical Sciences)  
T.Miura, (Radiation Safety Control Center, National Laboratory for High Energy Physics)  
H.Onabe,(Raytech Corporation)  
Y.Kinosita, (Faculty of Science, Osaka University)  
H.Yoshida, (Faculty of Engineering, Kyushu University)  
M.Numajiri, (Radiation Safety Control Center, National Laboratory for High Energy Physics)  
F.Shiraishi, (Institute for Atomic Energy, Rikkyo University)  
M.Takada, (Cyclotron and Radioisotope Center, Tohoku University)  
T.Aoyama, (Nagoya University College of Medical Technology)  
S.Koyama, (Nagoya University College of Medical Technology)  
T.Kobayashi, (Shiga University of Medical Science)  
T.Sakae, (Faculty of Engineering, Kyushu University)

H.Tawara, (Radiation Safety Control Center, National Laboratory for High Energy Physics)  
K.Mori, (CLEAR-PULSE)  
H.Nishimura, (E.G.&G. Japan)  
K.Oda, (Kobe University of Mercantile Marine)  
H.Nishizawa, (Mitsubishi Electric Corporation)  
Y.Oki, (Radiation Safety Control Center, National Laboratory for High Energy Physics)  
A.Taniguchi, (Toyo Medic Co., Ltd. Engineering Laboratory)  
H.Shibuya,(Toyo Medic Co., Ltd., Engineering Laboratory)  
T.Tsuruta, (Atomic Energy Research Institute, Kinki University)  
T.Suda, (Japan Atomic Energy Research Institute)  
T.Hamano, (Japan Atomic Energy Research Institute)  
T.Kamiya, (Japan Atomic Energy Research Institute)  
Y.Namito, (Radiation Safety Control Center, National Laboratory for High Energy Physics)  
Than Win, (Faculty of Engineering, Tohoku University)  
T.Tanoue, (Medical Engineering Laboratory, Toshiba Co., Ltd.)  
H.Murakami, (College of Science, Rikkyo University)  
H.Sekiguchi, (Electrotechnical Laboratory)  
T.Shouji, (Tohoku Institute of Technology)  
Y.Kanda, (Radiation Safety Control Center, National Laboratory for High Energy Physics)  
M.Kuwata, (JEOL Engineering Co., Ltd.)  
K.Hushimi, (Institute for Nuclear Study, The University of Tokyo)  
K.Hasegawa, (College of Engineering, Hosei University)  
T.Suzuki, (Radiation Safety Control Center, National Laboratory for High Energy Physics)  
N.Ujiie, (Physics Department, National Laboratory for High Energy Physics)  
N.Oshima, (Graduated University for Advanced Studies)  
S.Sasaki, (Radiation Safety Control Center, National Laboratory for High Energy Physics)  
N.Toyoshima, (Radiation Safety Control Center, National Laboratory for High Energy Physics)  
M.Nakazawa, (Faculty of Engineering, The University of Tokyo)  
T.Matsuzaki, (Japan Radiation Engineering Co., Ltd.)  
N.Miyazaki, (Japan Radiation Engineering Co., Ltd.)  
Y.Asano, (Japan Atomic Energy Research Institute)  
K.Hozumi, (Radiation Safety Control Center, National Laboratory for High Energy Physics)  
T.Michikawa, (Japan Radiation Engineering Co., Ltd.)  
H.Ono, (Seiko E.G.&G. Inc.)  
K.Itoh, (Photon Factory, National Laboratory for High Energy Physics)  
K.Kotani, (National Institute for Research in Inorganic Materials)  
M.Taira, (Radiation Safety Control Center, National Laboratory for High Energy Physics)  
T.Iguchi,(Faculty of Engineering, The University of Tokyo)  
C.Takahata, (Seiko E.G.&G. Inc.)  
T.Sakai, (Japan Atomic Energy Research Institute)  
J.Kaneko, (Japan Atomic Energy Research Institute)  
K.Nishio, (Department of Nuclear Engineering, Kyoto University)  
S.Takahara, (Radiation Safety Control Center, National Laboratory for High Energy Physics)  
K.Murozono, (Department of Nuclear Engineering, Tohoku University)  
K.Fukumura, (Department of Physics, Shiga University of Medical Science)

J.Inoue, (Department of Nuclear Engineering, Tohoku University)  
T.Kakuta, (Japan Atomic Energy Research Institute)  
K.Kudo, (Electrotechnical Laboratory)  
K.Kimura, (The Institute of Physical and Chemical Research)  
K.Iijima, (Radiation Safety Control Center, National Laboratory for High Energy Physics)  
A.G.Prokopets, (Department of Accelerator Science, The Graduate University for Advance Science)  
H.Nakamura, (Radiation Safety Control Center, National Laboratory for High Energy Physics)  
M.Yamamoto, (National Institute of Radiological Sciences)  
T.Sawamura, (Faculty of Engineering, Hokkaido University)  
H.Kawai, (Atomic Energy Research Institute, Kinki University)  
S.Matsuura, (Hamamatsu Photonics K.K.)  
H.Matsumoto, (Kobe University of Mercantile Marine)  
M.Ukibe, (Faculty of Engineering, The University of Tokyo)  
D.Fukuda, (Faculty of Engineering, The University of Tokyo)  
J.Frederik, (Faculty of Engineering, The University of Tokyo)  
H.Yoshida, (Faculty of Engineering, Kyushu University)